ADDRESSING ELECTRODE DEGRADATION AND MICROSTRUCTURE EFFECT IN ENERGY STORAGE

A Dissertation

By

CHIEN-FAN CHEN

Submitted to the Office of Graduate and Professional Studies of
Texas A&M University
In partial fulfillment of the requirements for the degree of

DOCTOR OF PHILOSOPHY

Chair of Committee,	Partha P. Mukherjee
Committee Members,	Perla Balbuena
	Hong Liang
	Philip Park
	Choongho Yu
Head of Department,	Andreas A. Polycarpou

August 2016

Major Subject: Mechanical Engineering

ABSTRACT

Recent years have witnessed a phenomenal increase in research efforts in energy storage for vehicle electrification. Lithium batteries, such as lithium-ion and lithium-sulfur batteries are leading the race towards meeting the energy and power requirements for the next generation of hybrid and electric vehicles. Majority of the research focused on the performance improvement and degradation analysis of lithium batteries. Since the electrode microstructure affects the electrode properties, such as effective ionic conductivity and solid-phase diffusion, the cell performance and degradation phenomena (*i.e.* formation microcrack and solid electrolyte interphase) vary with the microstructure design. The objective of this dissertation is to develop a microstructure-aware electrochemical model to conduct a fundament study of microstructural effects on cell performance and degradation. The influence of microstructure was observed from the cell performance and electrochemical impedance spectroscopy (EIS).

In the study of lithium-ion batteries, the proposed model successfully captures the influence of active particle morphology on the SEI formation and corresponding impedance characteristics. Different electrode realizations with microstructural and compositional variations have been considered. The critical influence of active material morphology, mean particle size, binder and electrolyte volume fractions on the SEI formation and impedance behavior reveals the underlying interdependences of the interfacial and transport resistance modes. Moreover, a systematic investigation of the influence of mechanical degradation on the resistance to diffusion and charge transport is

provided. In this regard, a modeling approach combining fracture formation and electrochemical impedance is presented, which predicts the mechanical damage induced impedance response and resistance evolution in the electrode. Besides the degradation phenomena, the microstructure-aware electrochemical model also captures the microstructural effects on the heat generation and electrode optimization design. With this model, the electrode microstructure has been proven to have an influence on the cell temperature under different discharge rate and ambient temperature. The variation of cell temperature has been analyzed and discussed by the time evolution and spatial distribution of different heating sources (i.e. joule heating, reaction heating, and reversible heating).

In the study of lithium-sulfur batteries, due to the influence on precipitation, the degradation of lithium-sulfur batteries can be controlled by the electrode microstructure fabrication. A microstructure-aware impedance model is proposed to observe the microstructure evolution and the influence of microstructure on the impedance response. The microstructure-aware impedance model adopted the method of three-dimension (3D) virtual microstructure reconstruction to take the varied microstructure properties (due to precipitation or solid sulfur loading), such as porosity, tortuosity, and interfacial electrochemical area, into account. Besides the properties required for the impedance prediction, the pore-size distribution, transport path, and pore closure were also observed and discussed from the reconstructed microstructure. According to the prediction of impedance response, the impedance evolution during the discharging process can be detail addressed and a strategy of electrode microstructure design is proposed.

This thesis is dedicated to my parents, sister and my lovely wife Chung-Wen Shih.

ACKNOWLEDGEMENTS

I express my sincere gratitude to my Ph.D. adviser and mentor, Prof. Partha Mukherjee, for his continuous encouragement as well as technical and financial support during my Ph.D. career. I would also like to thank my committee members, Prof. Perla Balbuena (Chemical Engineering), Prof. Hong Liang (Mechanical Engineering), Prof. Philip Park (Civil Engineering), and Prof. Choongho Yu (Mechanical Engineering), for their guidance and support throughout the course of this research.

Thanks also go to my colleagues for helping me in research at ETSL in Texas A&M University. Thanks also go to my friends and colleagues and the department faculty and staff for making my time at Texas A&M University a great experience.

Finally, thanks to my mother, father and sister for their encouragement and to my wife for her patience and love.

NOMENCLATURE

a	Specific surface area (cm^{-1})
c_e	Electrolyte concentration (mol cm^{-3})
$c_{i,max}$	Maximum Li^+ concentration in the solid phase (mol cm-3)
C_{dl}	Double layer capacitance (F cm^{-2})
$C_{dl,1}$	Capacitance of the double layer between solid phase and SEI (F cm^{-2})
$C_{dl,2}$	Capacitance pf the double layer between SEI and electrolyte (F cm^{-2})
C_{film}	SEI capacitance for LIB, and Layer capacitance (Li_2S precipitation or $S_{8(s)}$) for Li-S battery (F cm^{-2})
C_i	Concentration of species i in Li-S battery (mol m^{-2})
$C_{i,ref}$	Reference concentration of species i (mol m^{-2})
C_T	Theoretical capacity (mAh/g)
D_s	Solid phase diffusion coefficient for Li^+ for each electrode (cm^2 s^{-1})
D_i	Diffusivity of species i in the electrolyte (cm^2 s^{-1})
f_{bb}	Fraction of broken bounds
F	Faraday's constant
$I_{i,0}$	Exchange current density for each electrode
I_{app}	Applied current (A)
i_{of}	Exchange current density for the formation of film (A cm^{-2})
$i_{0.ref}$	Reference exchange current density (A cm^{-2})
J_i	Current density for each electrode (A cm^{-2})

J_s	Side reaction current (A cm^{-2})
k_p	Rate constant for cathode (A $cm^{2.5}$ $mol^{-1.5}$)
k_n	Rate constant for anode (A $cm^{2.5}$ $mol^{-1.5}$)
k_f	Rate constant for SEI formation (A $cm^{2.5}$ $mol^{-1.5}$)
k_N	Spring stiffness along the axial direction
k_s	Spring stiffness along the shear direction
L	Length of electrode (cm)
M_f	Molecular weight of SEI (g mol^{-1})
n_j	Number of electron transfer in reaction *j*
N_{cycle}	Total number of cycles
Q_p	Charge capacity (Ah)
Q_s	Capacity loss (Ah)
r_i	Generating/consuming of species *i* due to electrochemical reaction
R	Gas constant
$R_{contact}$	Contact resistance
R_i	Generating/consuming of species *i* due to dissolution/precipitation
R_{ct}	Charge transfer resistance (Ω cm^2)
$R_{ct,1}$	Charge transfer resistance between solid phase and SEI (Ω cm^2)
$R_{ct,2}$	Charge transfer resistance between SEI and electrolyte (Ω cm^2)
R_{film}	SEI resistance (Ω cm^2)
R_s	Active material particle radius in electrode
$s_{i,j}$	stoichiometric coefficient of species *i of reaction j*

S_i	Effective electroactive surface area for each electrode (cm^2)
T	Temperature (K)
U_i	Open circuit potential of each electrode (V)
$U_{ref,f}$	Open circuit potential for SEI (V)
$U_{j,ref}$	Reference open-circuit potential of reaction j (V)
$U_{j,eq}$	Equilibrium open-circuit potential of reaction j (V)
$x_{i,avg}$	Ratio of average Li^+ concentration to the maximum Li+ concentration for each electrode
$x_{i,surf}$	Ratio of surface Li+ concentration to the maximum Li+ concentration for each electrode
Y	Admittance on the interface (Ω^{-1} cm^{-2})
Z	Impedance for the porous electrode (Ω cm^2)
$\alpha_{a,i}$	Anodic transfer coefficient
$\alpha_{c,i}$	Cathodic transfer coefficient
$\alpha_{c,f}$	Cathodic transfer coefficient for the SEI formation
ε	Porosity of electrode
ε_{SEI}	SEI permittivity (F cm^{-1})
ε_{Film}	Layer permittivity (Li-S) (F cm^{-1})
δ_{SEI}	SEI thickness (cm)
δ_{Film}	Layer thickness (Li-S) (cm)
η_i	Overpotentials for the Li^+ intercalation for each electrode (V)
η_s	Side reaction overpotential (V)
σ	Electrical conductivity of solid phase (S/cm)
σ^{eff}	Effective electrical conductivity of solid phase (S/cm)

κ	Ion conductivity of electrolyte (S/cm)
κ^{eff}	Effective ionic conductivity of electrolyte (S/cm)
ρ_f	SEI density (g cm^{-3})
ρ_{SEI}	SEI resistivity (Ω m)
ρ_{Film}	Layer resistivity (Li-S) (Ω m)
ϕ_i	Potential for each electrode
ϕ_s	Solid-phase potential
ϕ_s	Electrolyte potential
τ	Tortuosity of void (electrolyte phase)

TABLE OF CONTENTS

Page

LIST OF FIGURES

Page

LIST OF TABLES

Page

CHAPTER I

INTRODUCTION, MOTIVATION AND OBJECTIVE

1.1 Lithium Energy Storage System

Today the world faces a serious risk due to the high demand of fossil fuels, the depletion of non-renewable energy sources, and the high emission of CO_2. The earth's greenhouse effect, which mainly from burning the fossil fuels, causes the temperature and climate changes. To slow down the pollution from fossil fuels, shifting electricity production to renewable energy sources and electrification the ground transportation, such as using electric vehicles, become two main research direction. To achieve the goals, suitable technology for energy storage is necessary. The development of energy storage system, such as batteries, which has high long-term stability, life, and high energy capacity become more and more important. Moreover, to fully replace the internal combustion engines, the requirement of high power capability and energy density still a huge challenge to overcome.

1.1.1 Lithium-ion Battery

Lithium-ion batteries (LIBs), due to their favorable energy density, power capability, light weight, and environmental friendly are considered as the candidate of choice for vehicle electrification [1-4]. To improve the capacity and power of LIBs, the anode material, which has a large theoretical capacity and high solid-phase diffusion rate, such as nano carbon material has been studied. [5] The anode of LIBs also can be alloyed

with Sn, Si, and Al to improve the capacity and safety. However, the mechanical damage inside the electrode due to the volume change is a huge drawback. For the cathode material of LIBs, $LiFePO_4$, $LiCoO_2$, and $LiNi_{0.33}Mn_{0.33}Co_{0.34}O_2$ (NMC) are the three common materials for the positive electrode. $LiFePO_4$ has the disadvantage of poor electronic conductivity (~10^{-9} S cm^{-1}). [6] $LiCoO_2$ has been adopted as cathode material because of high specific capacity, long cyclic stability, and easy preparation. [7-10]. However, it has the disadvantages of low thermal stability and high cost. To overcome the disadvantage, nickel and manganese have been added to $LiCoO_2$, which becomes NMC. NMC shows the most promising properties, such as operating voltage, high specific capacity, cyclic stability, and structural stability. [11, 12] , the low conductivity still an issue for NCM, many researches works on the dispersion of the active material in a high conductivity matrix, especially carbon material, would improve the conductivity, such as Al_2O_3[13] $LiAlO_2$[14] and carbon material[15, 16] **.** Besides the material design, different efforts have been undertaken to study the microstructural characteristics. Particularly, the influence of electrode microstructure on charge (i.e. electron and ion) transport, and solid phase diffusion is critical, which ultimately affects the cell performance. Moreover, significant efforts are focusing on predicting and extending the life, performance and safety of LIBs to satisfy the increasing demand of LIBs. Mechanical and chemical degradation modes, such as fracture in the electrode active particles due to diffusion induced stress [17-20] and the solid-electrolyte interphase (SEI) formation, [21, 22] pose a significant bearing on the LIB life and performance decay in terms of capacity fade and impedance rise.[23, 24]

1.1.2 Lithium-sulfur Battery

Lithium-sulfur battery, which has a high specific energy (2600 Wh kg^{-1}) and specific capacity (1675 mAh g^{-1}),[25, 26] which is five times higher than the $LiCoO_2$ cathode, [27] is a promising candidate for the high energy storage system. Therefore, significant interesting is rising to develop or improve a rechargeable lithium-sulfur battery,[28, 29] such as discharge capacity,[25, 30, 31] self-discharge,[32] and cycling.[33] In addition, elemental sulfur also has an advantage in the sense of safety due to its non-toxicity and intrinsic protection from overcharge.[34, 35] The poor cycle life of lithium-sulfur batteries has been a significant drawback for commercialization. The capacity fade during cycles is due to (a) precipitation of intermediate lithium polysulfides products in the electrolyte (b) large volume expansion of sulfur during cycling (c) insulating nature of Li_2S. In general, during discharge, the elemental sulfur in solution is reduced to S_8^{2-} , then to S_6^{2-}, S_4^{2-}, S_2^{2-} and to S^{2-} in the end.[36, 37] During operation, the sulfur anion reacted with lithium ion and form lithium polysulphides with the form of Li_2S_n. The product of polysulphides precipitates on the surface of the positive electrode surface and decreasing effective surface and decrease the porosity of electrode.[28, 38] Moreover, polysulfides are soluble in the electrolyte and could diffuse to the lithium anode, resulting in undesired shuttle effect. The shuttle effect also leads to random precipitation of Li_2S_2 and Li_2S on the negative electrode, which dramatically changes the electrode morphology and thus results in capacity fading. [28] Nanostructured composite materials, is a possible solution to prevent to shuttle effect by retaining the polysulfides at the cathode region. [39] Although

there are plenty researches focus on studying microstructure effect on lithium ion batteries, the microstructure effect on lithium sulfur batteries has not been well discussed. Many efforts have been done from experimental approaches, which focus on the modification or utilization of different cathode microstructure or material, such as the usage of microporous carbon[40], multi-walled carbon nanotube[41], carbon nanofiber[42], mesoporous carbon[43]. However, there are lack of mathematical approaches to detail address the influence of microstructure, such as ionic transport in the electrolyte and the change of active surface area, on the performance of lithium-sulfur batteries.

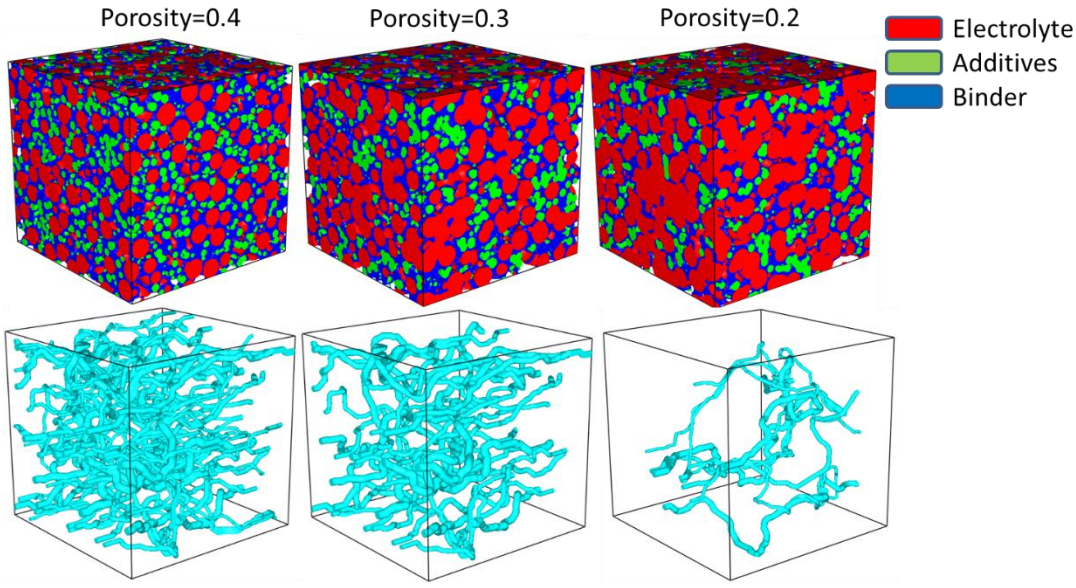

Figure 1.1. *The microstructure effect on the ionic transport path. The line corresponding the path particle can transport through the void space of microstructure.*

1.2 Microstructure Effect

Microstructure design is a method used to increase the performance of cells. Different microstructural designs have been studied to improve the energy density, power density, and degradation behavior. A majority of these studies focused on several microstructure characteristics, including electrode thickness [44], porosity [45], particle size [46], conductive additives [47] and composition .[48] As a part of a composite material, interactions with the other components of the electrode should also play a role in the pathway formation as shown in Figure 1.1. Due to the decrease of porosity, the number of the pathway for ionic transport decrease. The decrease of pathway hinder the ionic transport in the electrolyte and hence the effective conductivity. Several studies by Sastry [49] and Liu [48] have been performed that analyze the impact of conductive additive shape, material contents, and even, to an extent, active material morphology on the effective conductivity of LIB electrodes. However, one apparent shortcoming of these studies is the lack of consideration of the influence of the multiphase (active particle, additive, binder, electrolyte) electrode microstructural attributes, such as nano-/microscale particles morphology, anisotropy, and orientation on the short-range (interfacial resistance to charge transfer) and long-range (effective electronic, ionic, diffusive transport due to underlying tortuosity) interactions on the electrode performance and concomitant design and optimization strategies.

As mentioned, the electrode microstructure has an influence on the tortuosity and porosity for ionic transport. The tortuosity is the degree to which the lithium ion path is curved or twisted as a result of the solid phase materials that the ions must travel around

[50, 51]. The tortuosity is dominated by microstructural heterogeneity,[52, 53] electrode architecture,[54] and anisotropic of the active particle.[55] Due to the influence of particle morphology, the conventional Bruggeman ideal relation ($\tau = \varepsilon^{-0.5}$) is no longer sufficient. The porosity is a measure of the amount of space available for ion transport or space not occupied by the solid phase materials. An addition of active material decreases the porosity due to a decreased number of pathways for lithium ion transport and increases the transport distance due to the increase in tortuosity, thereby increasing the difficulty of ion transport and impacting the performance and power capability of LIBs [51, 56, 57]. Owing to the fact that the active material is the primary component in LIBs, the influence of active material particle size distributions and morphology on microstructure tortuosity has been previously studied [52, 53, 58, 59]. There are also many recent studies focused on predicting and calculating the tortuosity more accurately via mathematical methods [53, 60-62]. Besides the pathway for the ionic transport in the electrolyte, the non-uniform particle size distribution can affect the degradation phenomena of lithium-ion batteries since the degradation phenomena are mainly taking place in the active particles or on the electrolyte/active particle interface.

The influence of microstructure on the time evolution temperature was presented in the study of Ji and Wang *et al.*[63] However, there is a lack discussion and the detail reason of the interaction between microstructure properties and thermal behavior is still unclear. In addition, the model from Ji and Wang *et al.*[63] did not consider the complexity of microstructure, which may underestimate the tortuosity and heat generation.

In the cathode of lithium-sulfur batteries, the precipitation of lithium polysulfide varies the cathode microstructure significantly, which the high volume fraction of precipitation decrease the porosity and change the pore morphology of cathode electrode microstructure.[64, 65] The change of microstructure affects the properties of the electrode, such as active surface area, porosity, and tortuosity.

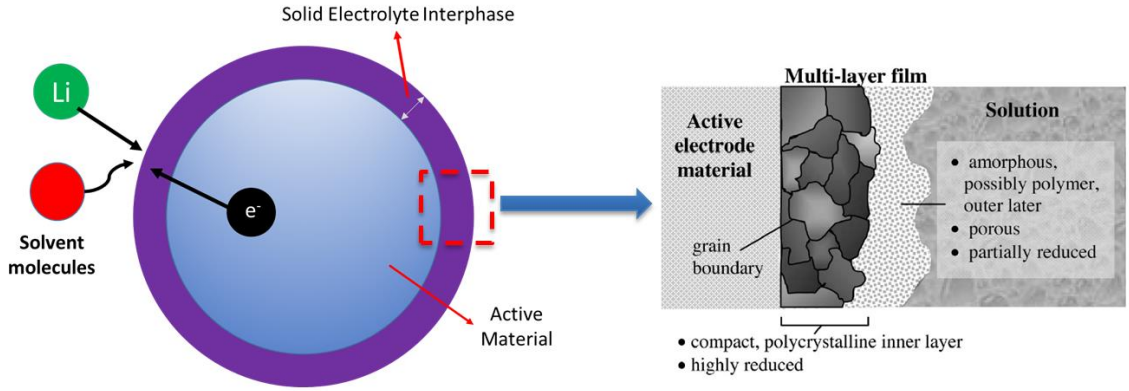

Figure 1.2. *The mechanism of solid electrolyte interphase formation and the composition in the SEI layer.[66]*

1.3 Thermal Behavior of Lithium-ion Battery

According to previous studies, increase LIBs cell temperature can diminish the energy lost and increase the power ability[63, 67, 68] since the transport properties (i.e. ionic conductivity, ionic diffusivity, and solid phase diffusivity) increase with temperature.[69] In addition, temperature increase also can ease the mechanical degradation (i.e. microcrack formation)[23] and prevent the lithium deposition in the anode.[70] However, the overheating of the cell can cause the decomposition of solid-

electrolyte interphase (SEI) layer, anode, and cathode. The heat generation due to the decomposition can further trigger the electrolyte decomposition and combustion.[71, 72] The cell temperature can increase from internal sources or external sources. The external sources refer to the devices, such as oven and heater. The cell temperature due to the internal sources is so called self-heating. The internal sources include (i) joule heat, which comes from the ohmic heating due to the internal resistance, (ii) reaction heat, which comes from the electrochemical reaction, (iii) reversible heat, which due to the change of thermodynamic properties.

The fully coupled electrochemical-thermal (ECT) modeling of LIBs incorporating thermal aspects can provide insights into the effect of varying operating conditions and battery electrode microstructure on its performance. The seminal works on the electrochemical model (EC) based on porous electrode and concentrated solution theory[73, 74] is given by Newman and coworkers[75-77] . It is an isothermal, one-dimensional model with additional complexity of solving solid phase transport in spherical coordinates and has been used as a stepping stone for further models in literature[78-93]. The electrodes are considered as two-phase structures consisting of solid active material, conductive additive, binder and liquid electrolyte. The separator is sandwiched in between the anode and the cathode and allows for the diffusion of lithium ions while hindering electron transport through the electrolyte. The model accounts for the Lithium intercalation kinetics, mass conservation in the solid and electrolyte phase and charge conservation in the solid and electrolyte phase. Building on it, Gu and Wang[84] developed the fully coupled ECT framework which solves the energy conservation

equation in conjunction with the electrochemical model and is capable of predicting internal temperature distribution as well as cell temperature evolution for large size lithium-ion cell for electric vehicle applications. ECT models have been analyzed further and the accuracy is increased by the incorporation of temperature and concentration dependent kinetic and transport properties and inclusion of state of charge dependent entropic heat term in the energy conservation equation. Electrolyte diffusivity, ionic conductivity and thermodynamic factor relations reported by Valoen and Reimers [69] for $LiPF_6$ based electrolytes have been used to investigate different battery chemistries and get better match with experimental data. The ECT model together with microstructure dependent parameters can provide a good understanding of thermal issues within the LIBs.

1.4 Degradation in Energy Storage System

1.4.1 Chemical Degradation in Lithium-ion Battery

The solid electrolyte interphase (SEI) is a thin layer (5 nm ~ 300 nm) [94] which forms at the interface between the active material and electrolyte, especially on the negative electrode (anode), during the charging process of LIBs.[95] The SEI formation is a side electrochemical reaction between the solvent of electrolyte and lithium ion as shown in Figure 1.2. Although the SEI formation protects battery components (electrode and electrolyte) from undesired reduction and oxidation,[96, 97] it also comes with several disadvantages. The SEI formation consumes the active lithium ions and solvent,[98, 99] and leads to capacity fade due to the compact layer (Figure 1.2) in SEI film. In addition, the thin layer also hinders the intercalations of lithium ion between the electrolyte and the

active material, and increases the cell resistance.[100-103] The SEI layer thickness varies with the operation condition (temperature and charge rate) and the morphology (i.e. size and shape) of the active material particles in the anode.[104-107] Therefore, particle size distribution and morphology of the active material inside the electrode microstructure become an important factor to control the chemical degradation level under the same operation condition.

The macroscopic models are a useful method to predict the SIE formation, and its influence on the capacity lost and cell performance. The models solved charge and species conservation equations to predict the species concentration and electric potential profiles, which can further be used to calculate the side reaction (*i.e.* SEI formation).[66, 108-111] The SEI prediction model has two branches of modeling strategy. One simplified the SEI formation chemistry, which can decrease the computational expense but lost some of the accuracy of the model. One includes detail SEI growth chemistry, but the finding of the parameters the model need is difficult.

As mentioned, sometimes the model, which includes the detail SEI growth chemistry, can meet the difficulty of finding the parameters the model need. Therefore, a simpler version of SEI growth model was proposed by Ploehn et al.[109] In this model, the SEI growth model is treated as a 1-D continuum model. The SEI growth depends on a two-electron reaction of the reactive solvent component in the interface between SEI and graphite. According to this model, the capacity lost was found to be proportion to square root of time, which fit with the experimental data. With a reasonable assumption of the SEI composition, this solvent diffusion model is a good candidate for calculating capacity

loss and SEI growth. With the similar concept, Rahimian *et al.* [105, 112] proposed a more simplified model that assumed the SEI layer as a thin conduct layer, and the diffusion of species through the SEI layer is ignored. The side reaction to from SEI layer is obtained from the irreversible Butler-Volmer equation, and the SEI layer thickness is predicted from this side reaction rate. The influence of SEI is treated as an additional resistance in the electrochemical reaction and implemented into the Butler-Volmer equation. Although this model ignores the diffusion of species inside the SEI layer and the detail SEI chemistry, the low computational expense can help to do a long cycle and optimization studies. Based on their method, they proposed the methods to maximize the life and find the optimal charge rate of lithium ion battery. [105, 112] From their results, by applying different charging rate at different cycles, the life of lithium-ion batteries can be maximized.

Although the simplified model can capture the capacity loss and SEI thickness evolution, the simplified SEI growth chemistry makes the model cannot obtain a more detail information during the SEI formation, such as the change of electrolyte. Christensen and Newman developed an electrochemical model, which considered SEI as a conductor and including the detailed chemistry of SEI formation, to model the growth of SEI on a planar graphite surface.[66] In this model, the Butler-Volmer equations were used to calculate all the electrochemical reactions, and the nonequilibrium interfacial kinetic were used as film boundary condition. Based on the work from Christensen and Newman, Colclasure and Kee improved the model by coupling the electrolyte reduction and the growth of SEI layer.[110, 111] The growth of SEI layer is predicted according to the side

reaction rate, which forms the SEI layer. Compare to the model developed by Christensen and Newman, the model developed by Colclasure and Kee can study SEI film growth and resistance under cycling conditions. Their results suggest that the SEI film growth rate and interfacial resistances highly depend on the intercalation of lithium, but weakly depend on the cycling conditions.

The mathematical continuum models show a good ability to capture the SEI growth and capacity fade. However, the assumption of uniform charge density distribution ignores the interaction between double layer and SEI. To include the influence of double layer on SEI growth, Deng *et al*. [108] proposed a phase field model that takes the non-zero charge density into account. In this model, the SEI formation is treated as a phase transformation process, where the SEI phase is transformed to the SEI phase due to the side electrochemical reaction. This model has the potential of including more species and can be extended to higher dimensional space. From this model, the SEI growth was found to be a diffusion-limited process. This study also found that the growth rate of SEI varied with the initial state of charge of an anode.

1.4.2 Mechanical Degradation in Lithium-ion Battery

Fracture in active materials due to the diffusion induced stress (DIS) causes mechanical degradation in LIB electrodes. The intercalation induced fracture has been identified as a major source of capacity fade and impedance rise in LIB electrodes.[113] In reality, the electrode active particles contain imperfections and defects which form either during the fabrication process or during operation caused by the DIS.[114] For

example, microscopic cracks (2 – 50 nm) have been observed in the graphite anode.[115] The fracture happens because the tensile stress inside the active material, which induced by the lithium ion diffusion in the active material. During the intercalation process, the intercalation of lithium causes the displacement of atoms and the strain energy stores in the bonds between atoms as shown in Figure 1.3. When the strain energy exceeds the fracture threshold, the bond broke and microcrack forms inside the active particle. The initial flaws can start to propagate or new microcracks can form inside the active material.[116] In previous studies, the critical size of the initial imperfection that can propagate during lithiation and delithiation have been investigated.[117, 118] In addition, the orientation of the initial pre-existing crack[119] and particle size[120-122] can affect the probability of fracture propagation or formation during lithiation and delithiation. In general, stress generation and fracture in LIB electrode active particles received significant attention in the last few years.[123, 124]

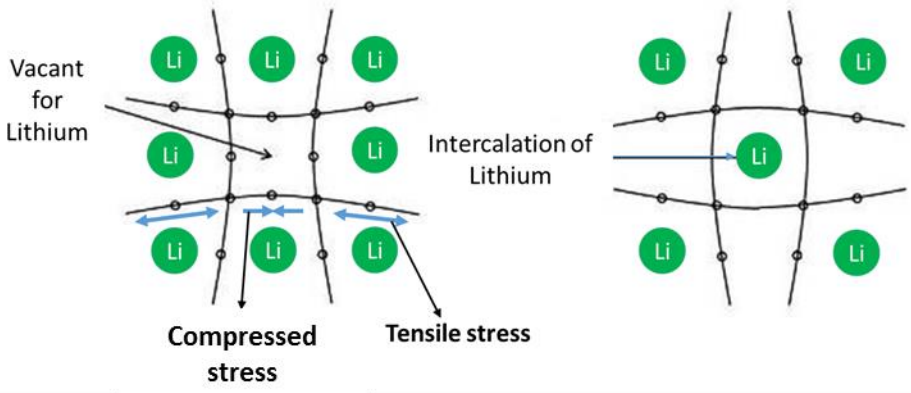

Figure 1.3. *The deformation of crystal structure and the accumulation strain energy.*

To the best of authors' knowledge, although scaling analysis have been implemented to better understand the damage happened in material, such as scaling analysis of avalanche precursors[125, 126] and the roughness of fracture surface[127, 128], the scaling study for the damage evolution in LIB electrodes has not been well established. Since the formation of microcracks inside the active particle is affected by the strain energy, which induced by the lithium diffusion and is proportional to the concentration gradient inside the active particle, the correlation between concentration gradient, cumulative strain energy (CSE), and microcrack formation is worth studying. Moreover, although the microcrack formation has been successfully predicted from our previous work,[24] the computational expense is still an obstacle we need to overcome. The scaling analysis of diffusion induced damage can significant decrease the simulation time.

1.5 Measure Methods

1.5.1 Electrochemical Impedance Spectroscopy

Electrochemical impedance spectroscopy (EIS) is a powerful technique to analyze the response of an electrochemical system, which is subjected to a small perturbation of voltage or current.[129-131] The cell resistances (i.e. charge transfer resistance, solid-phase diffusion resistance, and SEI resistance) can be quantified and studied via the impedance response.[130, 132-139] From previous studies, the microstructure has been proven to have an influence to the charge transfer resistance and diffusion resistance.[140, 141]In the context of impedance modeling, the mathematical EIS model for active particles was originally proposed by Tribollet *et al*.[142, 143] Based on the active particle

impedance model, the EIS response of porous electrodes was further developed by Meyers *et al*. and Huang *et al*. [130, 144] The porous electrode EIS model combines the porous electrode theory [73, 145, 146] with the phenomenological approach of active particles to describe the impedance of a homogeneous electrode. Figure 1.4 shows an example of EIS. The diameter of first semi-circle can be used to observe the resistance contributed by the SEI formation. The second semi-circle can be used to observe the resistance of charge transfer. The slope of impedance tail can be used to determine the solid-phase diffusivity.

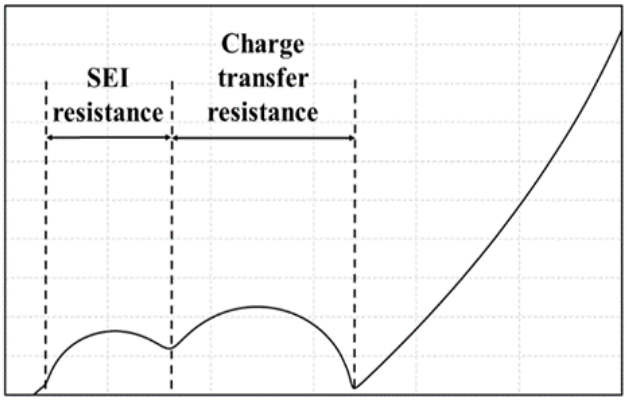

Figure 1.4. *An example of electrochemical impedance spectroscopy.*

Previous numerical EIS simulation for SEI studies which based on the porous electrode theory (developed by Meyers *et al.*[130] and Huang *et al.*[144]) did not consider the fact that the SEI thickness varies with the morphology of carbon active materials. Since the side reaction rate and time vary with the morphology of active material,[112]

the SEI thickness inside the electrode is not uniform and hence the impedance response. To include the morphological effect, we proposed a microstructure-aware impedance model to improve the impedance prediction. In this model, the electrochemical properties of each active particle in the electrode, such as SEI thickness, were evaluated during the charging process. Subsequently, according to the evaluated electrochemical properties, the corresponding impedance response for the electrode microstructure can be predicted.

In the electrochemical impedance spectra, the influence of chemical degradation, e.g. thin SEI layer formation, can be observed directly from the change in the Nyquist plot. The influence of fracture formation on the impedance response is, however, difficult to discern and extract. The microcracks affect the concentration distribution inside the active material, which in turn depends on the cycling and environmental conditions (e.g. temperature, charge/discharge rate) and active particle characteristics (e.g. morphology, size distribution, connectivity). The mathematical model in this dissertation enables us to observe and quantify the effect of fracture formation and propagation on the impedance response by directly comparing the EIS spectra with and without the diffusion induced damage. Furthermore, the influence of mechanical degradation on the impedance response for different electrode microstructural characteristics and operational conditions can be probed. The electrode microstructure of lithium-ion batteries has been proven to have an influence on the impedance response.[140, 141] However, to the best of authors' knowledge, although Wang et al.[147] and Kolosnitsyn et al.[148] reported the change of impedance response during charge and discharge process, there is a lack of detail study on the microstructure effect on the impedance response of lithium-sulfur batteries.

1.6 Objective

1.6.1 Microstructure Effect on the Performance and Thermal Behavior of Lithium-ion Battery

Due to the trade-off between the improvement of electrical conductivity and decrease in ion transport, there should exist an optimal electrode design, which balances the electrical conductivity and tortuosity. Beside the microstructural effect on the performance of LIBs, since the heat generation is mainly contributed by the joule heating, which mainly contributed by the effective ionic conductivity and effective electrical conductivity, the microstructure of electrode also has an influence on the cell self-heating. The objective of this research is to conduct a fundamental study of the microstructural effect on the electrode energy density, power capability, and the temperature of the cell. In addition, the detailed study of the relation between the cell temperature and microstructure properties can help us to better control the temperature of cell and improve the safety of LIBs. With the understanding, the optimize design of electrode with the consideration of power, capacity, and safety can be found. The electrode with different (a) solid phase composition (i.e. active material, additives, and binder) (b) thickness (c) particle morphology will be studied. The electrochemical performance has been simulated to study the discharge rate capability of different microstructure designs under different operation condition.

1.6.2 Degradation in Lithium-ion Battery

The objective of this task is to conduct fundamental investigation of the degradation of the anode in the lithium-ion battery due to mechanical degradation (e.g. microcrack formation) and chemical degradation (e.g. formation of solid electrolyte interphase (SEI))

Chemical Degradation: Solid electrolyte interphase (SEI) formation, due to the electrochemical reaction between the salt and solvent in the electrolyte, is a key contributor to the electrode performance decay in lithium-ion batteries. The active particle morphology and electrode microstructure affect the side reaction rate and hence the SEI induced interfacial transport and impedance behavior. The change resistance due to the variation of SEI thickness can be inferred from the electrochemical impedance spectroscopy. In this study, we proposed a microstructure-aware impedance model to predict the effect of electrode microstructure on impedance response. The objective of this study is to capture the influence of active particle morphology on the SEI formation and corresponding impedance characteristics. Different electrode realizations with microstructural and compositional variations have been considered. The critical influence of active material morphology, mean particle size, binder and electrolyte volume fractions on the SEI formation and impedance behavior reveals the underlying interdependencies of the interfacial and transport resistance modes.

Mechanical Degradation: Solid state diffusion of lithium ions in the active particles causes concentration gradients, which results in stress generation and formation of microcracks or propagation of preexisting cracks. Formation and propagation of

microcracks, in turn, affect the solid state transport of lithium ions and the interfacial charge transfer resistance. In this study, our objective is to(a) execute a systematic investigation of the influence of mechanical degradation on the resistance to diffusion and charge transport (b) damage evolution under different operation condition. In this regard, a modeling approach combining fracture formation and electrochemical impedance is presented, which predicts the mechanical damage induced impedance response and resistance evolution in the electrode. The impact of particle size, charge/discharge rate and operating temperature on the electrode impedance response is illustrated. In addition, a scaling analysis is implemented to understand the mechanism of damage evolution in the active particle of LIB electrodes under different operation conditions (i.e. temperature, particle size, and C-rate) by tuning the correlation between concentration gradient, cumulative strain energy, and microcrack formation.

1.6.3 Degradation in Lithium-sulfur Battery

The cathode architecture plays an important role in determining the performance of the Li-S battery. The deposition of Li_2S on the substrate affects the porosity of the cathode microstructure, which increases the tortuosity and decreases effective ionic conductivity and diffusivity. The objective of this study is understanding the cathode microstructure evolution during the discharge and optimizes cathode design to reduce disadvantages from Li_2S precipitation. In this study, we develop a mesoscale model to fundamentally understand the morphology evolution of Li_2S precipitations and the related electrode microstructure variation during the discharge process. An upscaling strategy is employed to fundamentally understand physicochemical interplay during the Li_2S precipitation. In

this study, the effect of ambient environment (spices concentration), operating condition (temperature), and cathode geometrical properties (porosity and specific surface area) on the kinetics of Li_2S film growth. A mesoscale model is proposed to investigate Li_2S morphology evolution in a large temporal-spatial scale. Based on the chemical reaction rate, the time evolution of the thickness of Li_2S precipitation layer can be evaluated. Since the side reaction rate is depended on temperature and lithium ion concentration, the time evolution of the thickness varied accordingly. With the thickness got from mesoscale simulation, the time evolution of the porosity of electrode microstructure can be predicted by reconstructing a virtual 3D microstructure. The variation of porosity can be affected by the original substrate surface area, pore size, and morphology of discharge product and carbon base. Moreover, since the thickness of discharge product is a function of lithium ion concentration and temperature, the variation of porosity also depended on lithium ion concentration and temperature. The time evolution of microstructure porosity can further be used to evaluate the effective electrochemical properties, such as effective electrical conductivity, ionic conductivity, and ionic diffusivity. From the mesoscale model and systematic simulations, an optimal design of lithium-sulfur electrode microstructure can be found.

A brief overview of what is being presented in this thesis provided below. The background of the microstructure effect on the performance of energy storage system and the degradation phenomena in energy storage system is presented in this section. Chapter II expressed the microstructure-effect on the chemical degradation (*i.e.* SEI formation) and its influence on the impedance response. Chapter III provides the microstructure-

effect on the mechanical degradation (*i.e.* microcrack formation), and its effect on the impedance response. Chapter IV expressed that there is a global relation between the strain energy and mechanical damage. Chapter V talks about the microstructure effect on the thermal behavior of LIBs. Chapter VI includes the Li-S cathode microstructure variation during the discharging process and the corresponding impedance response. In the end, the thesis will be concluded and the future research goals will be presented in Chapter VII.

CHAPTER II

PROBING THE MORPHOLOGICAL INFLUENCE ON SOLID ELECTROLYTE INTERPHASE AND IMPEDANCE RESPONSE IN INTERCALATION ELECTRODES

Previous numerical EIS simulation for SEI studies which based on the porous electrode theory (developed by Meyers *et al.*[130] and Huang *et al.*[144]) did not consider the fact that the SEI thickness varies with the morphology of carbon active materials. Since the side reaction rate and time vary with the morphology of active material,[112] the SEI thickness inside the electrode is not uniform and hence the impedance response. To include the morphological effect, we proposed a microstructure-aware impedance model to improve the impedance prediction. In this model, the electrochemical properties of each active particle in the electrode, such as SEI thickness, were evaluated during the charging process. Subsequently, according to the evaluated electrochemical properties, the corresponding impedance response for the electrode microstructure can be predicted.

In this study, the canonical mode of chemical degradation (i.e. SEI formation) and concomitant impedance response are studied for different electrode microstructural and compositional variations.

---

*Reprinted with permission from "Probing the morphological influence on solid electrolyte interphase and impedance response in intercalation electrodes" by C. -F. Chen and P. P. Mukherjee, 2015, PCCP, **17**, 9812, Copyright 2015, The Royal Society of Chemistry.

In particular, the influence of active particle morphology, size distribution, binder, and electrolyte volume fractions is investigated. The microstructure-aware computational model predictions are envisioned to provide fundamental insight into the influence of electrode microstructures on the chemical degradation mode and virtual diagnosis of impedance response.

2.1 Computational Methodology

As mentioned, in order to include the morphological effect of active material to the impedance response, the electrochemical properties of each active particle should be evaluated accordingly. The schematic diagram of our microstructure-aware impedance model is as shown in Figure 2.1. First, microstructures with different particle-size distribution and composition were constructed, which affect the active interfacial area and porosity. The primary components in the generated microstructures are the active material, electrolyte, and binder. The active materials are generated using the sequential generation method of piling in the active material particles and then randomly distributing the particles within the void space. All particles are prohibited from overlapping in the domain. The binder was added to a structure in the shape of a concave meniscus in locations where material surfaces got close together. The amount of binder utilized was varied by volume fraction. Based on the assigned active particle morphology in the microstructure, the lithiation/delithiation and side reaction (SEI formation) of active particles were simulated during cycling accordingly. With the evaluated electrochemical properties, such as SEI thickness and state of charge (SOC), the corresponding impedance response can be evaluated from the analytical solution of EIS of porous electrode.[130] It

is important to note that, in this study, the active particles are considered to homogeneously disperse throughout the electrode microstructure. The aggregation of active material and hence the effect on the structure of SEI film[149] is not taken into account. The active particle aggregation will be included in the future development of this impedance model.

2.1.1 Impedance Response of a Porous Microstructure

The analytical solution of microstructure-aware impedance model was based on the model developed by Meyers *et al.* [130]. The schematic diagram of different active material morphologies is shown in Figure 2.2 (a). The aspect ratio α and β are set to make the side surface area much smaller than the reactive surface area (10 times smaller). In Figure 2.2 (b) and (c), an equivalent circuit of the interface and a sample of the impedance response are displayed. The first semicircle of the high frequency accounts for the SEI resistance and the second semicircle of the middle frequency accounts for the charge transfer resistance.

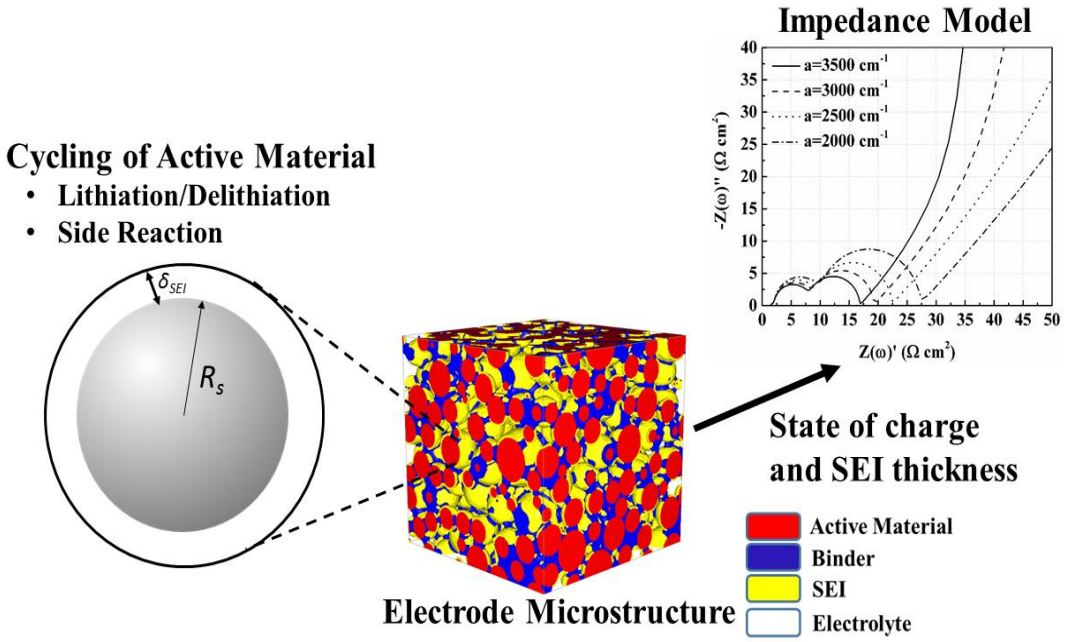

Figure 2.1. *Schematic diagram of the microstructure-aware impedance model, which considers the morphological effect of active material.*

Larger diameter of semicircle corresponds to larger resistance. The slope of the impedance tail corresponds the solid-phase diffusion resistance. Higher sloped of this tail corresponds to smaller diffusion resistance and lower values of the slope signify enhanced solid phase diffusion resistance. In this study, we considered an electrode-only model, specifically for a representative anode active particle. Therefore, all the parameters in the following EIS model refer to a typical graphite active material. It is important to note that since graphite is chosen as the representative active material, the effect of active particle volume change on the SEI formation and corresponding impedance response is neglected in this study. This important effect of volume change is left as a future exercise.

From the equivalent circuit (Figure 2.2(b)), the impedance Z of active particles can be expressed as follows. The admittance Y for active particle can be expressed as Eq. (2.1)

.

$$Y = \frac{1}{Z} = \frac{1}{\dfrac{R_{ct,1} + \dfrac{R_{part}}{Y_s}}{1 + j\omega C_{dl,1}\left(R_{ct,1} + \dfrac{R_{part}}{Y_s}\right)} + R_{film} + \dfrac{R_{ct,2}}{1 + j\omega R_{ct,2} C_{dl,2}}} + j\omega C_{film} \qquad (2.1)$$

where $R_{ct,1}$ and R_{part}/Y_s are the charge transfer and diffusion resistance between the solid phase and SEI layer which can be calculated from Eq. (2.2) – (2.3) when particle radius $r = R_s$.

Table 2.1. *SEI capacitance and resistance*

Morphology	**The SEI Capacity C_{film} (F/cm²)**	**The SEI Resistance R_{film} (Ω cm²)**
Spherical	$\dfrac{\varepsilon_{SEI}(R_s + \delta_{SEI})}{\delta_{SEI} \cdot R_s}$	$\dfrac{\rho_{SEI} \cdot \delta_{SEI} \cdot R_s}{R_s + \delta_{SEI}}$
Cylinder	$\dfrac{\varepsilon_{SEI}}{R_s} \cdot \dfrac{1}{\ln((R_s + \delta_{SEI})/R_s)}$	$\rho_{SEI} \cdot R_s \cdot \ln((R_s + \delta_{SEI})/R_s)$
platelet	$\dfrac{\varepsilon_{SEI}}{\delta_{SEI}}$	$\rho_{SEI} \cdot \delta_{SEI}$

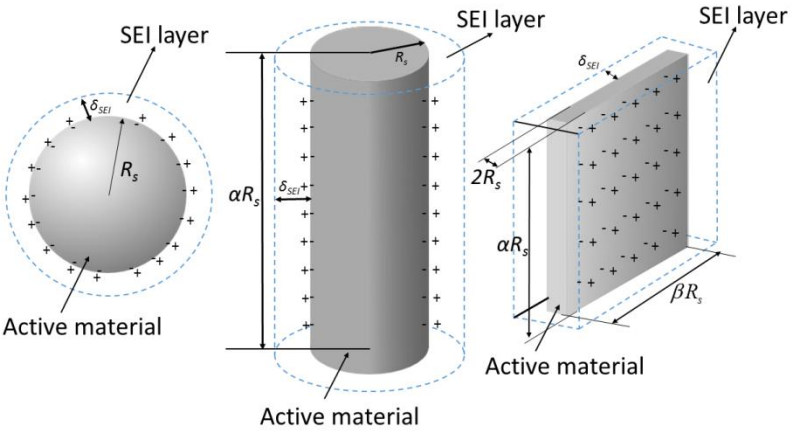

(a)

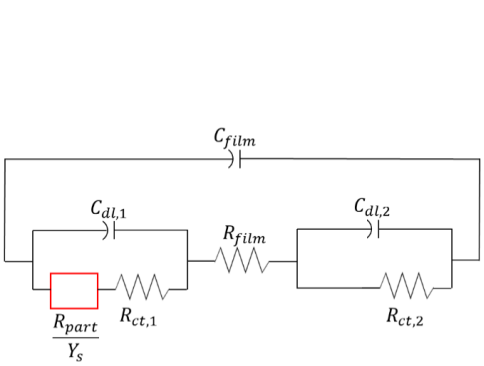

(b)

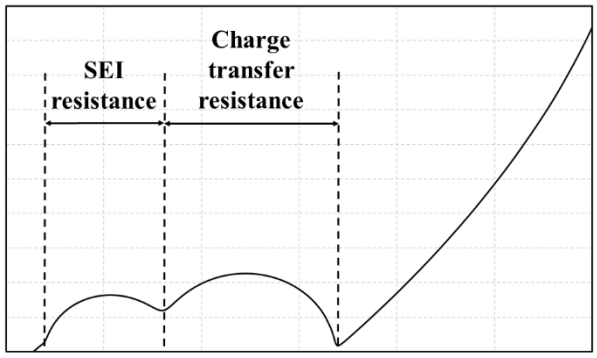

(c)

Figure 2.2. *(a)The morphology of spherical, cylinder and platelet active materials. Cylinder particles: α=5. Platelet particles: α=10 and β =10. (b) Equivalent-circuit diagram. (c) Sample of Electrochemical impedance spectroscopy. The first semicircle on the left accounts for the SEI resistance. The second semicircle accounts for the charge transfer resistance. The slope of the impedance tail account for the solid-phase diffusivity.*

The SEI resistance R_{film} and capacitance C_{film} can be calculated from

$$R_{ct,1} = \frac{RT}{I_0(r)\left(\alpha_a + \alpha_c\right)F} \tag{2.2}$$

$$R_{part} = \left(-\frac{\partial U}{\partial c_s}\right)\frac{R_s}{FD_s} \tag{2.3}$$

with the slope of open circuit potential ($\partial U/\partial c_s$) can be expressed as Eq.(4) [150]**;** the exchange current density $I_{i,0}$ is a function of state of charge $x_{i,surf}$ as Eq. (2.5).

The state of charge $x_{i,surf}$ is defined as the ratio between surface concentration and the maximum surface concentration $c_{surf} / c_{\max}$

$$\frac{\partial U}{\partial c_s} = -\frac{0.63562}{\left[\left(22.523x_{i,surf} - 3.653\right)^2 + 1\right]} - \frac{0.37}{\left[\left(28.348x_{i,surf} - 13.44\right)^2 + 1\right]} \tag{2.4}$$
$$-49.9789\,\mathrm{e}^{\left(49.9789x_{i,surf} - 43.3789\right)} - 33.9111\mathrm{e}^{-49.2036x_{i,surf}} - 106.6\,\mathrm{e}^{-254.4x_{i,surf}}$$

$$I_{i,0} = k_i\left(c_{i,\max} - x_{i,surf}c_{i,\max}\right)^{0.5}\left(x_{i,surf}c_{i,\max}\right)^{0.5}c_e^{0.5} \tag{2.5}$$

The value of Y_s for the diffusion resistance in Eq. (2.1) can be calculated from Eq. (2.6) – (2.8) for spherical, cylinder and platelet particles.

$$Y_s = \frac{R_s\sqrt{\frac{jw}{D_s}} - \tanh\left(R_s\sqrt{\frac{jw}{D_s}}\right)}{\tanh\left(R_s\sqrt{\frac{jw}{D_s}}\right)} \text{ for sphere} \tag{2.6}$$

$$Y_s = \frac{R_s\sqrt{\frac{jw}{D_s}}I_1\left(R_s\sqrt{\frac{jw}{D_s}}\right)}{I_0\left(R_s\sqrt{\frac{jw}{D_s}}\right)} \text{ for cylinder} \tag{2.7}$$

$$Y_s = R_s\sqrt{\frac{jw}{D_s}}\tanh\left(R_s\sqrt{\frac{jw}{D_s}}\right) \text{for platelet} \tag{2.8}$$

According to the previous study, $R_{ct,1}$ is the major factor, which determines the charge transfer resistance (diameter of right semicircle in Fig. 2(c)) and is dominated by the exchange current density I_0 and temperature T. The change in the slope of the low-frequency tail (solid-phase diffusion resistance) is due to the variation of diffusivity D_s and $\partial U/\partial c_s$. The SEI resistance (diameter of left semi-circle in Fig. 2(c)) is only affected by the SEI thickness as shown in Table 2[130, 144].

By implementing the admittance Y calculated from Eq.(2.1), we can evaluate the EIS for the porous microstructure. The impedance Z for the porous microstructure can be expressed as Eq. (2.9).

$$Z = \frac{L}{\kappa+\sigma}\left[1+\frac{2+\left(\frac{\sigma}{\kappa}+\frac{\kappa}{\sigma}\right)\cosh\upsilon}{\upsilon\sinh\upsilon}\right] \tag{2.9}$$

where

$$\frac{L}{\upsilon} = \left(\frac{\kappa\sigma}{\kappa+\sigma}\right)^{1/2}\left(\overline{aY}\right)^{-1/2} \tag{2.10}$$

The average of single particle admittance $\overline{aY}$ is calculated from averaging the admittance with the surface area as

$$\begin{cases} \overline{aY} = 4\pi\int_0^\infty N(r)Y(r)r^2dr \text{ for sphere} \\ \overline{aY} = 2\pi\alpha\int_0^\infty N(r)Y(r)r^2dr \text{ for cylinder} \\ \overline{aY} = \alpha\beta\int_0^\infty N(r)Y(r)r^2dr \text{ for platelet} \end{cases} \quad (2.11)$$

where *N(r)* is the number density of particle radius *r*. In this work, we use the modified logarithm Gaussian distribution proposed by Meyers et al. [130] as eq. (2.12). The benefit of using Eq. (2.12) is that controlling the electrode design parameters (specific area *a*, volume fraction ε_s and mean particle radius) is straight forward.

$$N(r) = \frac{1}{r}\left[\frac{(a\lambda_a)^3 e^{-\left(\frac{\varphi}{4}\right)^2}}{(4\pi)9(\varepsilon_s\lambda_\varepsilon)^2\sqrt{\pi}\varphi}\right]\exp\left[-\left(\frac{\ln\left(\frac{ra\lambda_a}{3\varepsilon_s\lambda_\varepsilon}\right)}{\varphi}\right)^2\right]\exp\left[-\frac{5}{2}\ln\left(\frac{ra\lambda_a}{3\varepsilon_s\lambda_\varepsilon}\right)\right] \quad (2.12)$$

Here, φ the sharpness of distribution function can be used to decide the mean particle radius. λ_a and λ_ε are the adjusted constants for the morphology, which can be defined as

$$\lambda_a = \begin{cases} 1 & \text{for sphere} \\ \frac{2}{\alpha} & \text{for cylinder} \\ \frac{2\pi}{\alpha\beta} & \text{for platelet} \end{cases} \quad \text{and} \quad \lambda_\varepsilon = \begin{cases} 1 & \text{for sphere} \\ \frac{4}{3\alpha} & \text{for cylinder} \\ \frac{2\pi}{3\alpha\beta} & \text{for platelet} \end{cases} \quad (2.13)$$

From Eq. (2.12) and (2.13), we can make sure the specific area and the volume fraction of active material maintain constant when changing particle morphology

$$a = \int_0^\infty \mathrm{A}(r)N(r)dr \quad \text{and} \quad \varepsilon_s = \int_0^\infty V(r)N(r)dr \tag{2.14}$$

Here *A(r)* and *V(r)* are the surface area and volume of active material with particle radius *r*. One should notice that the microstructure constructed in Figure 2.1 is according to the particle size distribution defined from Eq. (2.12).

2.1.2 Delithiation/Lithiation and Side Reaction of Active Materials

The evaluation of particle electrochemical properties and SEI formation during delithiation/lithiation were based on the method developed by Rahimian *et al.*[105, 112] This method simulated the evolution of lithiation concentration inside the active particles and the side reaction under a certain flux of lithiation and delithiation. [151, 152] The mathematical formulation is briefly expressed as follows. By applying the average volume technique, Fick's second law can be simplified as Eq. (2.15) – (2.20) to predict the diffusion of lithium ion in the cathode (*p*) and anode (*n*)[105].

$$\frac{dx_{i,ave}}{dt} = \frac{-3J_i}{FR_s c_{i,\max}} \text{ for sphere} \tag{2.15}$$

$$\frac{dx_{i,ave}}{dt} = \frac{-2J_i}{FR_s c_{i,\max}} \text{ for cylinder} \tag{2.16}$$

$$\frac{dx_{i,ave}}{dt} = \frac{-J_i}{FR_s c_{i,\max}} \text{ for platelet} \tag{2.17}$$

$$x_{i,surf} - x_{i,ave} = \frac{-R_s J_i}{5FD_{s,i}c_{i,\max}} \text{ for sphere} \tag{2.18}$$

$$x_{i,surf} - x_{i,ave} = \frac{-R_s J_i}{4FD_{s,i}c_{i,\max}} \text{ for cylinder} \tag{2.19}$$

$$x_{i,surf} - x_{i,ave} = \frac{-R_s J_i}{3FD_{s,i}c_{i,\max}} \text{ for plate} \tag{2.20}$$

Here *i* denotes either anode (*n*) or cathode (*p*). The reaction current density J_p and J_n, side reaction current density J_s, and the applied current I_{app} follow the charge conservation (Eq. (2.21)). $x_{i,ave}$ and $x_{i,surf}$ are defined in Eq. (2.22).

$$J_p = \frac{I_{app}}{S_p} \text{ and } J_n = \frac{-I_{app}}{S_n} - J_s \tag{2.21}$$

$$x_{i,ave} = \frac{c_{i,ave}}{c_{i,\max}} \text{ and } x_{i,\text{surf}} = \frac{c_{i,surf}}{c_{i,\max}} \tag{2.22}$$

In the present paper, $x_{i,surf}$ also can be referred to the state of charge (SOC) of particles. J_s in Eq. (2.21) is the side reaction current density which can be calculated from Tafel kinetics as Eq. (2.23).

$$\begin{Bmatrix} J_s = i_{0f} \exp\left(\frac{-\alpha_{c,f} F}{RT}\eta_s\right), \text{Charge} \\ J_s = 0, \qquad\qquad \text{Discharge} \end{Bmatrix} \tag{2.23}$$

$$\eta_s = \phi_n - U_{ref} - \frac{I_{app}}{S_n} R_{film} \tag{2.24}$$

where R_{film} is the SEI resistance and can be calculated from Table. 2 for different morphologies of particles. The exchange current density for the side reaction $i_{0,f}$ is calculated from Eq. (2.25).

$$i_{o,f} = k_f c_e F \tag{2.25}$$

The formation of SEI thickness δ_{SEI} can be evaluated from the side reaction current as shown in Eq. (2.26).

$$\frac{d\delta_{SEI}}{dt} = \frac{-J_s M_f}{\rho_f F} \tag{2.26}$$

The Butler-Volmer equation was used to update the reaction current density J_i after each time step. The Butler-Volmer equation can be expressed as Eq. (2.27).

$$J_i = I_{i,0} \times \left[\exp\left(\frac{\alpha_{a,i} F}{RT} \eta_i \right) - \exp\left(\frac{-\alpha_{c,i} F}{RT} \eta_i \right) \right] \tag{2.27}$$

$I_{i,0}$ is the exchange current density which is a function of SOC $x_{i,surf}$ as shown in Eq. (2.5) . The over-potentials η_i for the interaction reaction for anode and cathode can be calculated from Eq. (28) and (29).

$$\eta_p = \phi_p - U_P \tag{2.28}$$

$$\eta_n = \phi_n - U_n \pm \frac{I_{app}}{S_n} R_{film} \begin{bmatrix} -\text{charge} \\ +\text{discharge} \end{bmatrix} \tag{2.29}$$

The loss of capacity are represented from the loss or gain of SOC $x_{i,surf}$, and $x_{i,surf}$ was updated after each charging process from Eq. (2.30)

$$x_{i,N,surf} = x_{i,N-1,surf} \pm \theta_{i,N-1} \begin{pmatrix} + \text{ cathode} \\ - \text{ anode} \end{pmatrix} \tag{2.30}$$

with N the number of steps; θ_i the loss of SOC which can be calculated from Eq. (2.31) – (2.33).

$$\theta_i = \frac{Q_s}{Q_{\max}} \tag{2.31}$$

$$Q_s = -\int_0^{t=\text{charge time}} \left(J_s S_n \right) dt \tag{2.32}$$

$$Q_{\max} = \int_0^{t=\text{charge time}} \left(I_{app} S_n \right) dt \tag{2.33}$$

In the active particle, the SOC ($x_{i,surf}$) during discharge/charge can be obtained from Eq. (2.15) – (2.20). The SOC dominates the value of $\partial U / \partial c_s$ slope and exchange current density I_0 in the impedance model as shown in Eq. (2.4) and (2.5), respectively. The most important part in the present model is calculating the growing of SEI thin layer as shown in Eq. (2.26). The thickness of the SEI thin layer generates additional resistance (Eq. (1)) and affects the impedance response.

Since the diffusion distance and specific capacity (mAh/g) varies with the active particle radius and morphology, the SOC and charging time of active particles inside an electrode is different. The SOC of particles affects the anode potential ϕ_n which has an

influence to the side reaction rate as shown in Eq. (2.24). The charging time also determined the SIE thickness as Eq. (2.26). Due to the variation of side reaction rate and charging time of active particles, the electrodes with different particle radius distribution should have different impedance response. By investigating the impedance response from different design of electrodes, we can (1) find an effective method to design an electrode which has less SEI resistance (2) study the trade-off between the SEI resistance, charge transfer resistance, and solid-phase diffusion resistance. It is important to note the effect of phase transformation, such as in $LiFePO_4$, and relevant dependence of solid-state transport on exposed surface facets and crystallographic orientation on the formation of SEI and the charge transfer characteristics are not included in the current version of the microstructure-aware impedance model. These important aspects will be discussed in a future study.

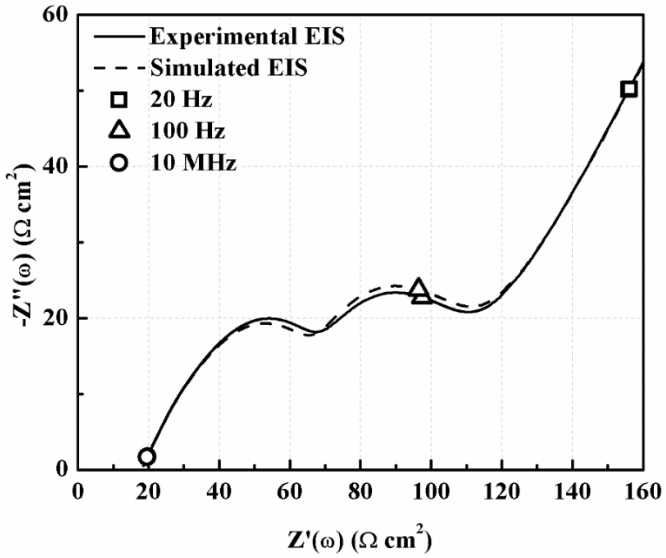

Figure 2.3 *The comparison between the experimental EIS and the simulated EIS from our model after the 10^{th} charge/discharge cycle (C/10 rate). Experimental data is adapted from Ref. [67]*

The comparison between our model and the experimental EIS is as shown in Figure 2.3.[137] The trend of simulated EIS shows good agreement with the experimental EIS. The error is mainly due to the selection of particle-size distribution. The comparison shows the ability of our model to study the degradation of anodes.

2.2 Results and Discussion

In order to study the SEI formation and the corresponding impedance response of the LIB anode, we used the microstructure-aware impedance model as mentioned in the previous section. The impedance study includes three stages. First, we calculated the SEI thickness δ_{SEI} and the SOC $x_{i,surf}$ for active particles with different particle-size distribution (0.3μm ~20μm) and morphology (spherical, cylindrical and platelet particles) inside the electrode microstructure during the charging/discharging process. The particle-size distribution (0.3μm ~20μm) selected in this study is based on the thickness of SEI film. Since the SOC of small particles reaches its maximum value faster than large particle under the same lithiation rate, therefore, the SEI thickness is significantly small for smaller particle size, e.g. below 0.3 μm. The importance of nanoscale size effect, e.g. in the range of $0.1 - 0.01$ μm, and corresponding influence on crystallographic orientation, columnar ordering and solid-phase transport have been shown in our recent work.[153] The specific influence of such morphological aspects on the SEI formation and impedance response will be considered in a future study. Second, the corresponding lithium concentration (e.g. SOC) and SEI thickness are used to calculate the admittance Y of an active particle from Eq. (2.1). Third, the admittance for active particles was integrated with the particle radius

r as Eq. (2.11) to get the impedance response for porous microstructure electrode with different electrode designs.

In this section, we study the porous electrode designed with different specific area (cm^{-1}), mean particle radius of active material, morphology of active material, and different volume fraction of the binder. The parameters used in the simulations are used according to previous researches for solid-phase diffusion, side reaction, and porous electrode EIS simulations.[105, 130, 144] One should notice that the influence of microstructure on the electrical and ionic conductivity was not considered in this study.

2.2.1 Effect of Active Material Morphological on SEI Formation and Impedance Response

During lithiation and delithiation process, all active materials were performed with the same current density J_i. The charge and discharge rates were set to 0.5 C (828 mA). The simulation for different microstructure designs were operated with 2000 cycles. The SEI thickness δ_{SEI}, exchange current density I_0, and $\partial U/\partial c_s$ was recorded after the end of charging process of each cycle. At the end of the charge process of each cycle (Charging time= 3600 sec), the EIS was calculated to observe the SEI resistance and the degradation of anodes. The active particles with different size and morphology were systematically studied in this section. The results show in the following section can help us to understand the impedance response for different electrode microstructures in the later sections.

Influence of spherical particle radius: Since the particle size varies in the electrode, the impedance for the active materials with different particle radius has been studied. The

impedance response for active materials, which calculated from Eq.(2.1), will later be used to calculate the impedance response for the porous electrode.

The SEI thicknesses calculated after the end of charging process of each cycle for different particle radius are shown in Figure 2.4(a). The SEI thickness decreases as particle radius increases when the radius is larger than 1 μm. This result can be explained by the relation between SOC and side reaction rate. Since the SOC increases slower in larger particles, as shown in Figure 2.4(b), the potentials of larger particles increase less than smaller particles after the same charge duration. Due to the low potential variation, larger particles have less side reaction current as shown in Eq. (2.23) and (2.24). On the opposite, when the radius is smaller than 1 μm, the SEI thickness decreases as the particle radius decreases. The small particles have opposite results because the SOC of small particles increases very fast, which causes the particles to reach their maximum SOC and stop the electrochemical reaction before the end of charge time (3600 sec). Therefore, the submicrometer particles have short side reaction time and thin SEI thickness.

The SOC, exchange current I_0 and $\partial U/\partial c_s$, with different particle radius after different cycles ,are shown in Figure 2.4(b) - (d) respectively. The value of exchange current I_0 and $\partial U/\partial c_s$ are dominated by the SOC of the particle. According to Eq.(2.15), larger particles have lower SOC after the same charge time. Additionally, the SOC decreases during cycling due to the capacity lost from the side reaction as shown in Figure 2.4(b). Therefore, as shown in Figure 2.4(c), the slope $\partial U/\partial c_s$ decreases as the number of cycles and particle size increase. For the exchange current density, since the formulation

of exchange current density I_0 is a second order equation which has the maximum value when SOC = 0.5, the exchange current density increases (decreases) with the increase of SOC when SOC < 0.5 (SOC > 0.5). Hence, the exchange current density of particles radius of 0.5 and 1 μm increase during cycling, and 2 μm particles have the largest exchange current density after 3600 sec of charge time as shown in Figure 2.4(d).

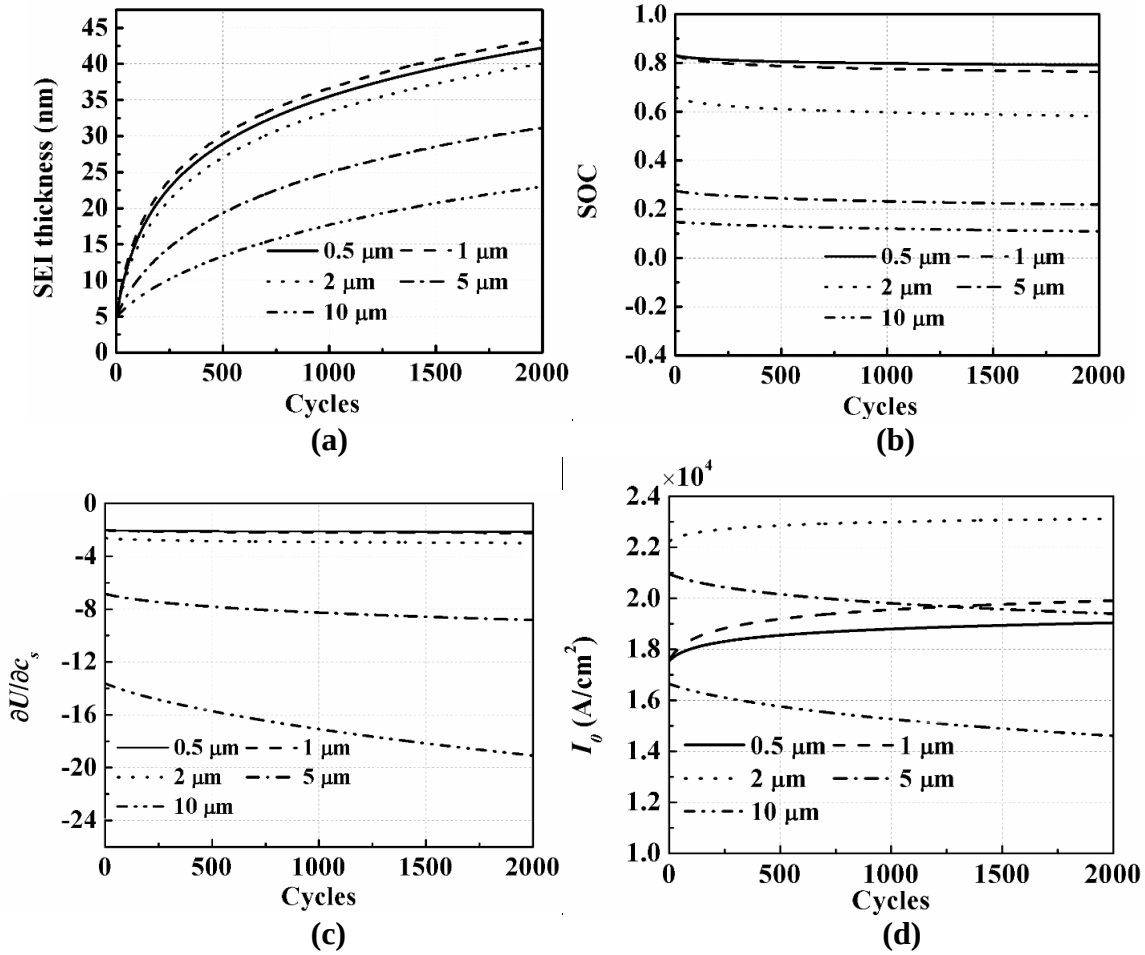

Figure 2.4. *(a) The SEI thickness, (b) SOC, (c)* $\partial U/\partial c_s$ *and (d) exchange current density of spherical particles with the radius of 0.5, 1, 2, 5 and 10 μm during the first 2000 discharge/charge cycles.*

From the result of SEI thickness, exchange current density I_0, and $\partial U/\partial c_s$, the impedance response for active particles with different radius can be evaluated. Fig. 5(a) shows the impedance response of 1μm active particles after 500, 1000 and 2000 cycles. The SEI resistance (first semicircle on the left) increases with cycling. The increase of SEI resistance is due to the growth of SEI thickness during cycling as shown in Figure 2.4(a).

Figure 2.5(b) shows that the impedance response varies with particle radius because of the difference in SEI thickness and SOC. As shown in the result, 10 μm particle has the smallest SEI resistance since it has the thinnest SEI thickness (Figure 2.4(a)). However, 10 μm particle has the largest charge transfer resistance because it has the lowest exchange current density I_0 as shown in Figure 2.4(d). In addition, 10 μm particle also has the largest solid-phase diffusion resistance, which is because (1) the radius of particles increases the diffusion distance of lithium ion (2) larger particles has smaller value of $\partial U/\partial c_s$ as shown in Figure 2.4(c). One should notice that the SEI resistance and the charge transfer resistance have no effects on the diffusion resistance because of the accepted nature of SEI and charge transfer resistance. [144]

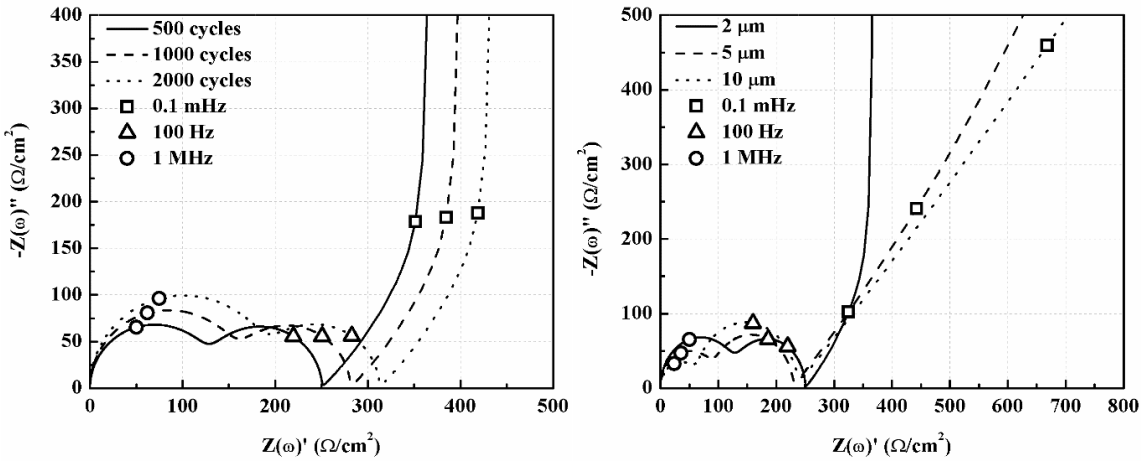

(a) **(b)**

Figure 2.5. *(a) Impedance response of a representative spherical active particle after 500, 1000 and 2000 discharge/charge cycles with 2 μm radius spherical active particles. (b)Impedance response of representative spherical active particles after 500 discharge/charge cycles with radius 2, 5 and 10 μm radius spherical active particles.*

Influence of particle morphology: The morphological effects was performed with spherical, cylindrical and platelet particles. The radius (thickness) of active particles in the microstructure varies from 0.5 μm to 20 μm. Each simulation was operated with 2000 cycles. According to Eq. (2.15) – (2.20), the SOC was influenced by the active material morphology and affected the SEI formation, exchange current density and the change of open circuit potential. The SEI thickness δ_{SEI}, exchange current density I_0 and $\partial U/\partial c_s$ was recorded after the end of charge process of each cycle. The results are represented in the following.

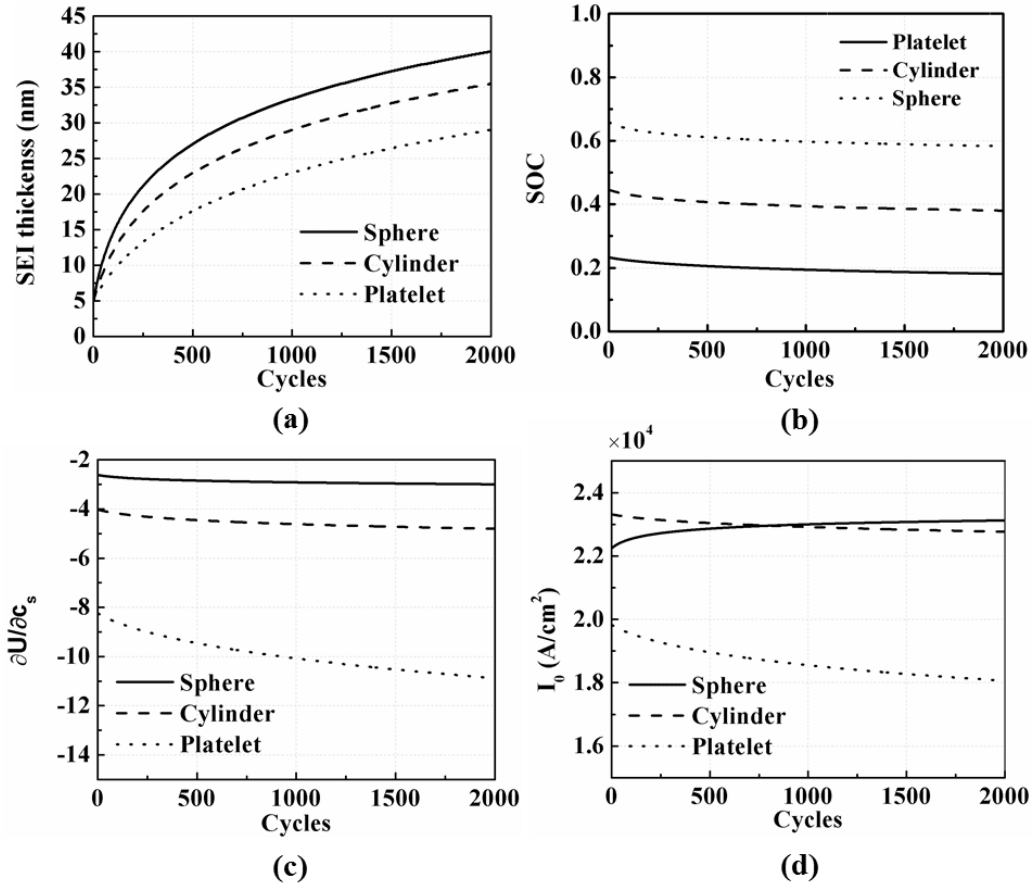

Figure 2.6. *The (a) SEI thickness, (b) SOC, (c)* $\partial U/\partial c_s$ *and (d) exchange current density of spherical, cylinder and platelet particles during the first 2000 discharge/charge cycles. The radius of spherical particles is 2 μm. The radius of cylinder particles is 2 μm and the aspect ratio is 1:5. The thickness of cylinder particles is 4 μm and the aspect ratio is 1:10:10.*

The SEI thickness growth with cycling number is shown in Figure 2.6(a). The spherical particles have the fastest side reaction rate, compared to the cylindrical and platelet particles. The reason is the same as the size effect on SEI thickness. The SOC of the spherical particle increases faster than cylindrical and platelet particles, according to Eq. (2.15) – (2.17), which causes higher side reaction rate and thicker SEI thickness. The exchange current $\partial U/\partial c_s$ and I_0 of different particle morphologies during cycling are

shown in Figure 2.6(c) and (d). Similar as the result of the size effect of spherical particles, the slope $\partial U/\partial c_s$ and exchange current density I_0 are dominated by the SOC. Due to the variation of SOC, the platelet particles have the smallest value of $\partial U/\partial c_s$ and the spherical has the largest $\partial U/\partial c_s$. Additionally, the exchange current density of spherical particles increases with the number of cycles (SOC > 0.5), but the exchange current density of cylinder and platelet particles decrease with the number of cycles (SOC < 0.5) as shown in Figure 2.6(d).

Figure 2.7 shows the impedance response varies with the particle morphologies after 500 cycles. The spherical particle has the largest SEI resistance while the platelet particle has the smallest SEI resistance, which is determined by the SEI thickness. The platelet particle has the largest charge transfer resistance while the cylindrical particle has the smallest charge transfer resistance due to the difference in exchange current I_0. The morphology effect on the diffusion resistance is attributed to the anisotropic of ion diffusion and the value of $\partial U/\partial c_s$. The anisotropic of large curvature particle (Ex. Platelet particles) increases the solid-phase diffusion resistance inside the particle.

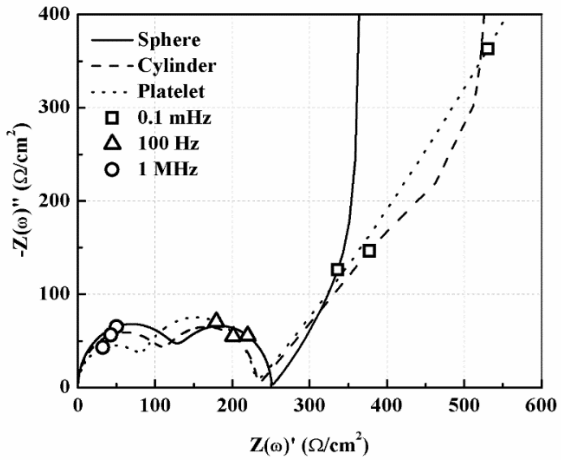

Figure 2.7. Impedance response of a representative spherical, cylinder, and platelet active particle during the first 500 discharge/charge cycles. The radius of spherical particles is 2 μm. The radius of cylinder particles is 2 μm and the aspect ratio is 1:5. The thickness of cylinder particles is 4 μm and the aspect ratio is 1:10:10.

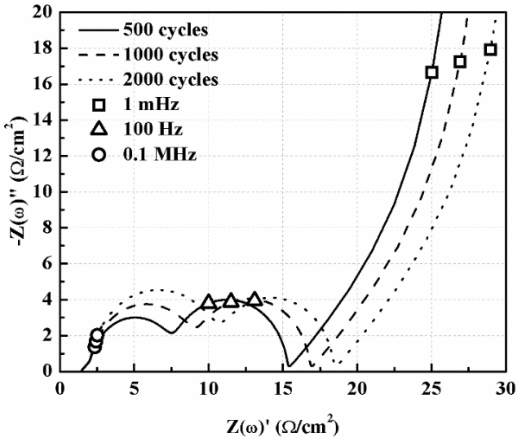

Figure 2.8. *Impedance response of electrode after 500, 1000 and 2000 cycles. The specific area, volume fraction and mean radius of the microstructure are 4000 cm^{-1}, 40% and 2.09 μm respectively.*

2.2.2 Effect of Electrode Microstructure on Impedance Response

In anodes, the particle-size distributions are different according to electrode microstructures. The particle-size distribution determined three design aspects of porous electrode, which are (1) the specific surface area (cm^{-1}), (2) the volume fraction of active

material and (3) the mean particle radius of the active material. As demonstrated above, the SEI thin layer, charge transfer resistance and diffusion resistance vary with the active particle size and morphology, which suggest strong dependence of the electrode microstructural variations (e.g. particle size distribution) on the impedance response. The impedance response of different porous electrodes after cycling is as shown in Figure 2.8. As expected, due the increase of SEI thickness, the SEI resistance increases during cycling

Influence of specific surface area: In order to keep the porosity and mean particle radius as a constant, the microstructure with larger surface area has a larger number of particles and smaller standard deviation as shown in Figure 2.9(a) and (b). From Figure 2.9(c) and (d), the impedance response shows that the microstructure with larger surface area has smaller resistance (SEI resistance, charge transfer resistance and solid-phase diffusion resistance) in the electrode. The result can be explained from Eq. (2.9) - (2.11) that the average admittance $\overline{aY_s}$ increase with the surface area in the microstructure. Figure 2.9(d) presents the increase of SEI resistance and charge transfer resistance during cycling. From the results, we can refer that the SEI thickness increases faster in the microstructure with small surface area. It is worth noticing that although the capacity loss increase with the (Brunauer-Emmew-Teler) BET surface area (m^2/g)[107], increasing the surface area has a positive effect on the resistance. ***Influence of active material volume fraction:*** Figure 2.10 shows the impedance response of the microstructures with different volume fraction of the active material. According to the plot of particle-size distribution and the microstructure (Figure 2.10(a) and (b)), it is found that the microstructure with a smaller volume fraction of active material has more number of particles and smaller standard

deviation. The electrode with a smaller volume fraction of active material has larger SEI resistance, but smaller charge transfer resistance and solid-phase diffusion resistance, as shown in Figure 2.10(c) and (d). The larger SEI resistance means larger capacity lost, which agrees well with the previous results that the microstructure with larger BET specific area has larger capacity lost [107]. The difference of the charge transfer resistance is attributed to that the average exchange current density I_0 is smaller in the electrode with a smaller volume fraction of active material. The smaller solid-phase diffusion resistance in the microstructure with smaller volume fraction of active material is mainly due to the lower average value of the slope $\partial U/\partial c_s$. Figure 2.10(d) shows the increase of SEI resistance and charge transfer resistance. Different from the influence of specific surface area, the influence of the volume fraction of active material to the SEI thickness increasing rate is not obvious.

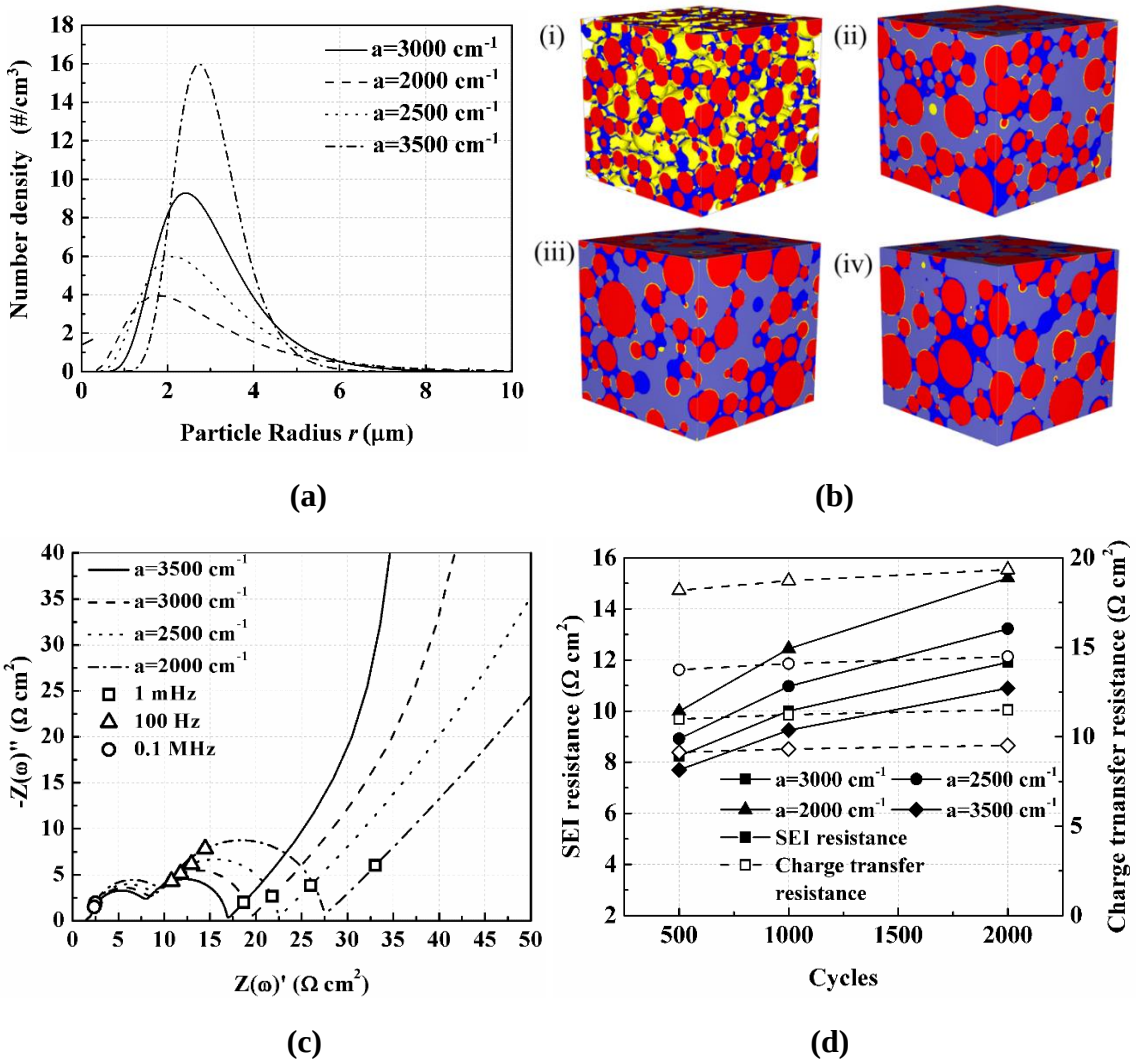

Figure 2.9. *The porous electrode impedance response with different specific surface area of active material. The volume fraction and mean particle radius of active material are 40% and 3 μm. (a) Particle-radius distribution with the specific area of 3500 cm^{-1}, 3000 cm^{-1}, 2500 cm^{-1} and 2000 cm^{-1}. (b) The microstructure for (i) a=3500 cm^{-1}(without electrolyte), (ii) a=3000 cm^{-1}, (iii) a=2500 cm^{-1}, (iv) a=2000 cm^{-1}. In the microstructure, the active material, binder, electrolyte and SEI layer are represented by the color of red, blue, purple and yellow respectively. (c) The porous electrode impedance response after 500 discharge/charge cycles. (d) The SEI resistance and charge transfer resistance after 500, 1000 and 2000 cycles.*

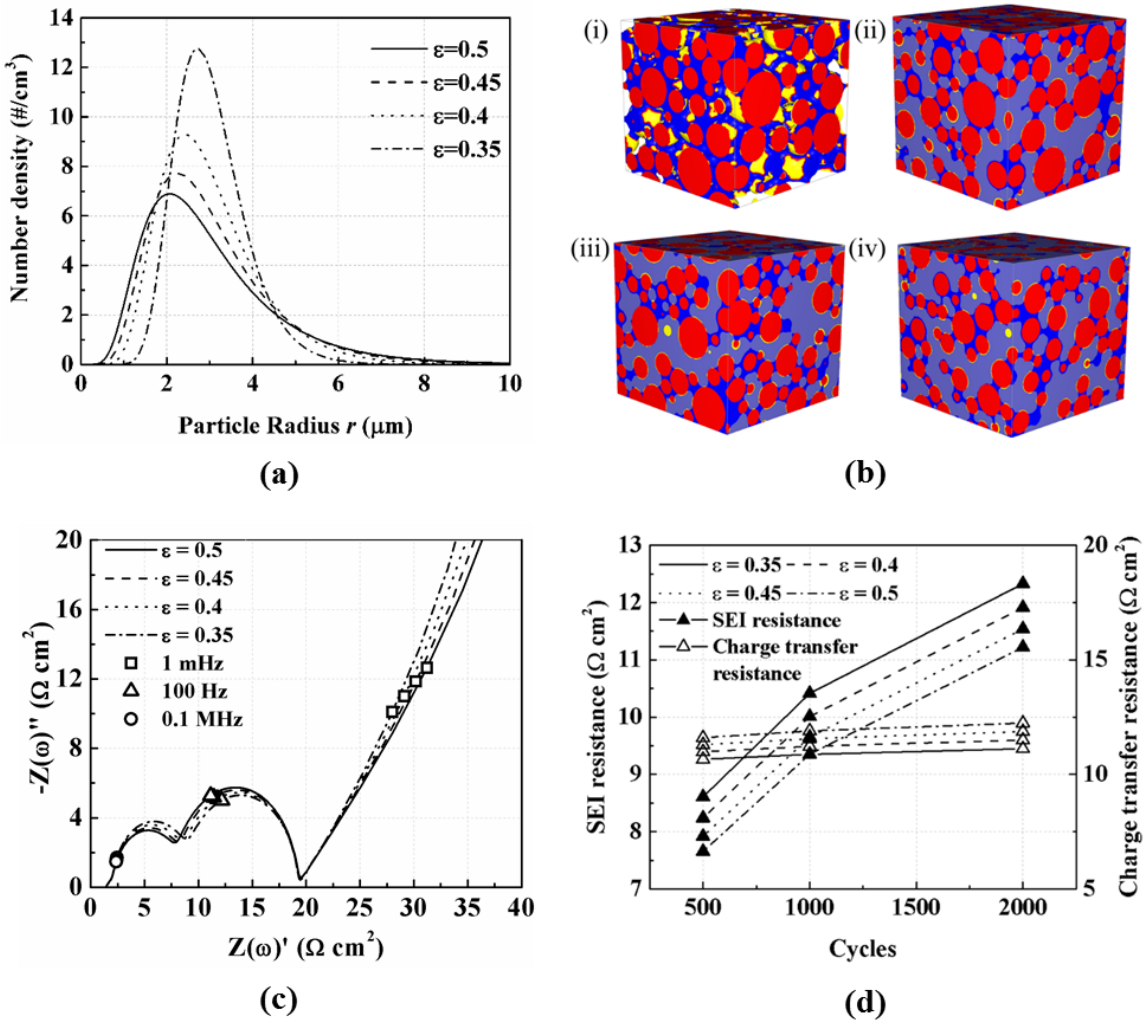

Figure 2.10. *The porous electrode impedance response with different volume fraction of active material. The specific area and mean particle radius of active material are 3000 cm^{-1} and 3 μm. (a) Particle-radius distribution with 50%, 45%, 40% and 35% volume fraction of active material. (b) The microstructure for (i) 50%(without electrolyte), (ii) 45% (iii) 40% and (iv) 35% of active material. In the microstructure, the active material, binder and electrolyte are represented by the color of red, blue and purple respectively. (c) The porous electrode impedance response after 500 discharge/charge cycles. (d) The SEI resistance and charge transfer resistance after 500, 1000 and 2000 cycles.*

Influence of mean particle size: In the following, we investigated the influence of mean particle radius of the particle-size distribution on the electrodes. In our study, we varied the sharpness φ in Eq. (2.12) to change mean particle radius. The porous electrodes with specific areas of 4000 cm^{-1} and 2000 cm^{-1}, and the sharpness of 1.0, 0.6 and 0.2 are discussed in this subsection. Figure 2.11 and Figure 2.12 show the effects of mean particle radius R_{mean} on the porous electrode impedance response with specific areas of 4000 cm^{-1} and 2000 cm^{-1}. From the particle-size distributions (Figure 2.11 (a) and Figure 2.12 (a)) and the microstructures (Figure 2.11 (b) and Figure 2.12 (b)), it can be found that the particle-size distributions in the electrode with 4000 cm^{-1} specific area have a larger standard deviation than that in the electrode with 2000 cm^{-1} specific area. In addition, in order to maintain the surface area while changing the mean particle radius, the range of R_{mean} we can change for a=4000 cm^{-1} is smaller than a=2000 cm^{-1}. As shown in Figure 2.11 (c) and (d), the SEI resistance and solid-phase diffusion resistance decrease with R_{mean} but the charge transfer resistance increase with the decrease of R_{mean} in the electrode with 4000 cm^{-1} specific surface area. On the opposite, the SEI resistance and charge transfer resistance increase with the decreasing of R_{mean} but the solid-phase diffusion resistance decreases with the R_{mean} in the electrode with 2000 cm^{-1} specific surface area (Figure 2.12 (c) and (d)).

The difference of SEI resistance with R_{mean} for the specific area of 4000 cm^{-1} and 2000 cm^{-1} is attributed to the particle-size distribution. For the particle-size distributions in Figure 2.11 (a) (a=4000 cm^{-1}), the particles with radius smaller than 1 μm (SEI thickness decrease with the decrease of radius) has more influence on the SEI resistance when we

averaged the impedance of active materials. On the contrary, for the particle-size distributions in Figure 2.12 (a) (a=2000 cm^{-1}), since most of the particles radius are larger than 1 μm (the range SEI thickness increase with the decrease of radius), the SEI resistance decreases with the increase of R_{mean}. Therefore, for the electrodes with large specific surface area, the electrode should choose smaller particles (smaller R_{mean}) for smaller SEI resistance.

As shown in Figure 2.11(c) and Figure 2.12(c), the charge transfer resistance increased with the decrease of R_{mean} for both specific surface areas of 2000 cm^{-1} and 4000 cm^{-1}. It means that the distribution with small R_{mean} has smaller average exchange current density I_0 than the one with large R_{mean}. The solid-phase diffusion resistance also depends on the R_{mean} of the distribution for both electrode microstructures. The solid-phase diffusion resistance increased with R_{mean} in both cases because the particle-size distributions with large R_{mean} have longer diffusion distance and smaller $\partial U/\partial c_s$ than the ones with small R_{mean}. The long diffusion distance and small $\partial U/\partial c_s$ for larger particles caused large diffusion resistance. In addition, Figure 2.11(d) and Figure 2.12(d) also show that the SEI resistance increasing speed is not changing with R_{mean}.

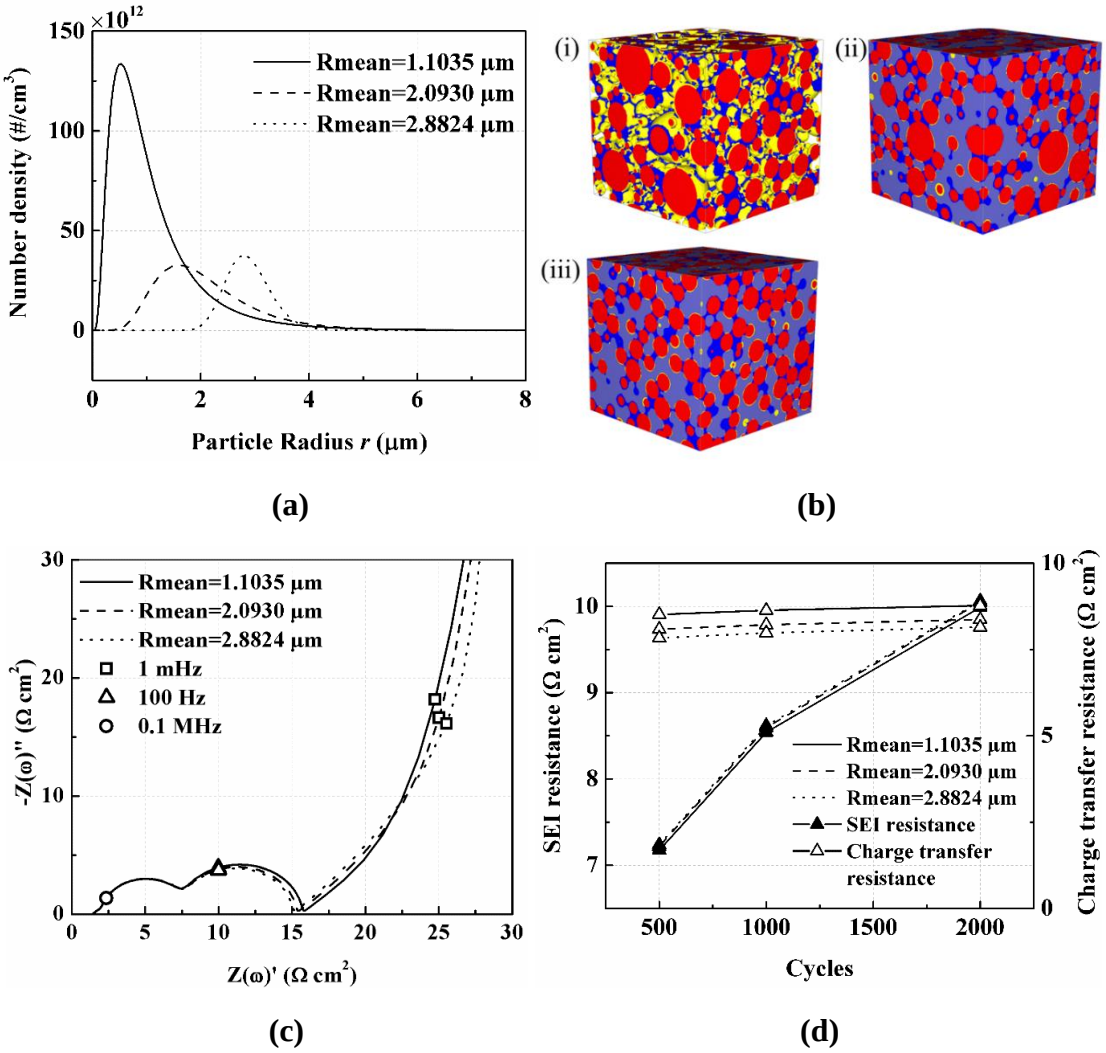

Figure 2.11. *The porous electrode impedance response with varying mean particle radius. The specific area and volume fraction of active material are 4000 cm^{-1} and 40%. (a) Particle-radius distribution of different mean particle radius. (b) The microstructure for (i) R_{mean}=2.8824(without electrolyte) (ii) R_{mean}=2.093 (iii) R_{mean}=1.1035. In the microstructure, the active material, binder and electrolyte are represented by the color of red, blue and purple respectively. (c) The porous electrode impedance response after 500 discharge/charge cycles. (d) The SEI resistance and charge transfer resistance after 500, 1000 and 2000 cycles.*

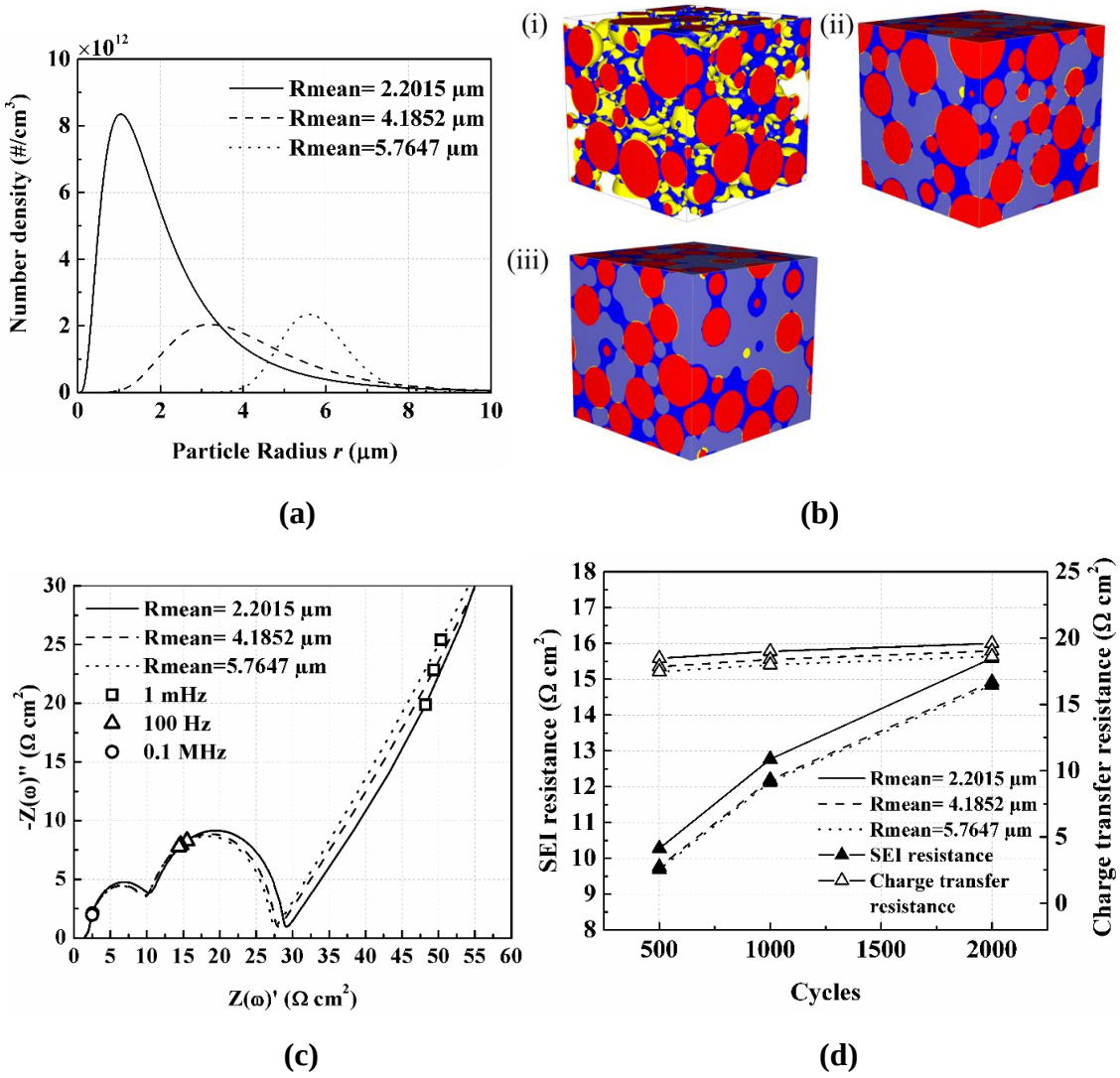

Figure 2.12. *The porous electrode impedance response with varying mean particle radius. The specific area and volume fraction of active material are 2000 cm^{-1} and 40%. (a) Particle-radius distribution of different mean particle radius. (b) The microstructure for (i) R_{mean}=5.7647(without electrolyte) (ii) R_{mean}=4.1852 (iii) R_{mean}=2.2015. In the microstructure, the active material, binder and electrolyte are represented by the color of red, blue and purple respectively. (c) The porous electrode impedance response after 500 discharge/charge cycles. (d) The SEI resistance and charge transfer resistance after 500, 1000 and 2000 cycles.*

Effect of active particle morphology: The porous electrode impedance response with a different morphology of active material is shown in Fig. 13. According to the particle-size distributions and microstructures (see, Figure 2.13(a) and (b)), it is found that spherical particles have more number of particles than the cylinder and platelet particles when the specific area is maintained at constant. As shown in Figure 2.13 (c) and (d), spherical particles have the largest SEI resistance and charge transfer resistance, while these particles have the smallest diffusion resistance. On the opposite, platelet particles have the smallest SEI resistance and charge transfer resistance, but the largest diffusion resistance. The electrode with spherical active material has the largest SEI resistance because the spherical particles have a thicker SEI thickness compared to the cylinder and platelet particles as shown in Figure 2.6(a). The result of charge transfer resistance shows that under the same charging time and process, the electrode with the platelet active material has the largest exchange current density. For the solid-phase diffusion resistance, because spherical particles have shorter diffusion distance than the cylinder and platelet particles due to the curvature of particle surface, the electrodes with spherical particles have the smallest diffusion resistance. In addition, the largest $\partial U/\partial c_s$ of spherical particles is also a reason why spherical particles have the smallest diffusion resistance. In addition, from Figure 2.13 (d), the SEI resistance increasing rate is faster for spherical particles than the cylinder and platelet particles.

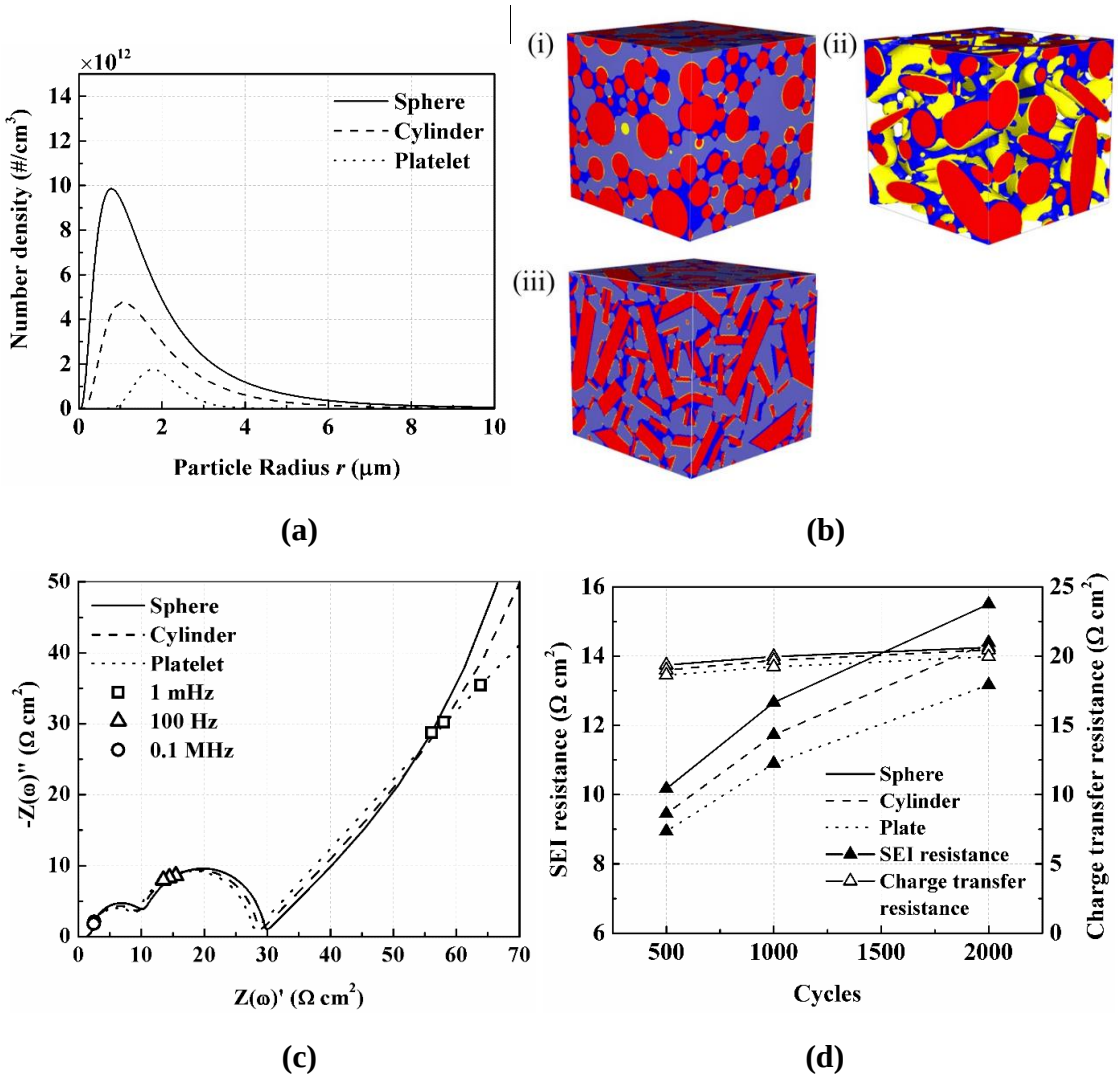

Figure 2.13. *The porous electrode impedance response with spherical, cylinder and platelet particles. The specific area and volume fraction of the active material of electrode is 2000 cm^{-1} and 47%. The aspect ratio of cylinder particles is 1:5. The aspect ratio of platelet particles is 1:10:10. (a) Particle-radius distribution for spherical, cylinder and platelet particles. (b) The microstructure for (i) Spherical (ii) Cylinder (without electrolyte) (iii) Platelet particles. In the microstructure, the active material, binder and electrolyte are represented by the color of red, blue and purple respectively. (c) The porous electrode impedance response after 500 discharge/charge cycles. (d) The SEI resistance and charge transfer resistance after 500, 1000 and 2000 cycles.*

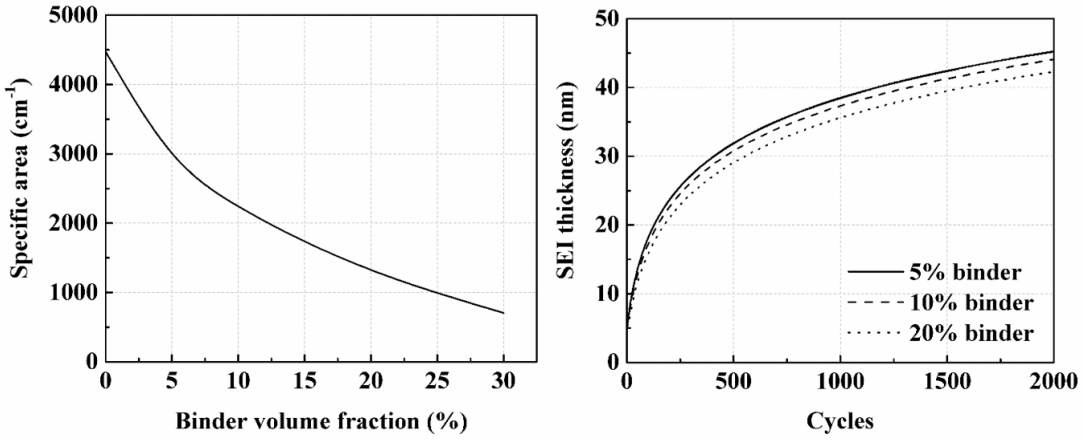

Figure 2.14. *(a) The specific surface area vs. the volume fraction of binder for the electrode with 2 µm spherical particles. (b) The SEI thickness with different volume fraction of binder during the first 2000 discharge/charge cycles for the electrode with 2 µm spherical particles.*

Effect of binder volume fraction: According to Eq. (2.9) - (2.11), we know that the impedance strongly depends on the specific surface area (cm^{-1}). In realistic electrodes, the volume fraction of binder influences the interface surface area between the electrolyte and active material as shown in Figure 2.14(a). Due to the decrease of surface area, under the same applied current, the current density (A/cm^2) will increase and affect the SEI formation as shown in Figure 2.14 (b). Figure 2.14 (b) shows that the SEI thickness grows faster in the electrode with a smaller volume fraction of the binder. The SEI thickness decreases as binder increases because the increase of current density (A/cm^2) decreases the charging time (i.e. the surface concentration reaches the maximum value faster). However, although the SEI grew faster for a low volume fraction of binder, the electrode with 5% of binder has the smallest SEI resistance as shown in Figure 2.15(a) and (b). It means the SEI resistance is dominated by the effective surface area between active

material and electrolyte. Besides the SEI resistance, the charge transfer resistance and diffusion resistance also increase with the volume fraction of binder due to the diminishing of effective surface area. In addition, the SEI resistance increased faster for the electrode with 20 % of the binder, as shown in Figure 2.15 (b), because the small effective surface area makes the SEI resistance grew faster than the one with the larger effective surface area.

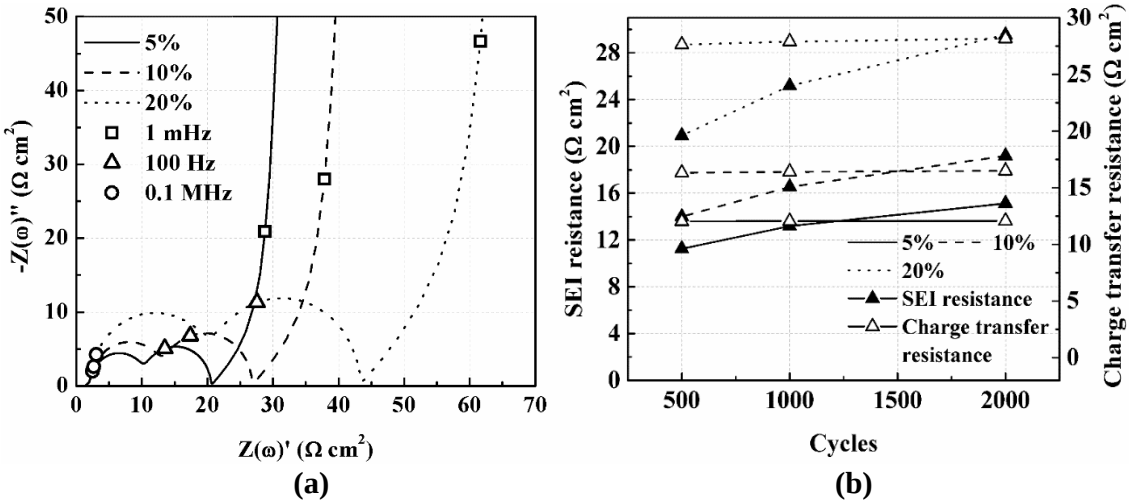

Figure 2.15. *(a) The porous electrode impedance response with different volume fraction of binder for spherical particles. The specific area, volume fraction and radius of active material are 4500 cm^{-1}, 30 % and 2 μm respectively. (b) The charge transfer resistance and SEI resistance after 500, 1000 and 2000 discharge/charge cycles.*

2.3 Conclusions

In this paper, the influence of electrode microstructural variability on the SEI formation and corresponding impedance response has been elucidated. In this regard, a microstructure-aware computational model has been presented which consists of physicochemical interactions pertinent to SEI formation in a typical LIB anode and elicits the influence thereof on the impedance characteristics. The impact of active particle

morphology, size distribution, binder and electrolyte volume fractions on the SEI thickness, SOC, and the underlying interdependencies of transport and interfacial resistances have been investigated in detail. This model enables a virtual diagnosis and characterization of the canonical mode of chemical degradation via prediction of the impedance spectra snapshots for intercalation electrodes.

Due to the variation of particle-size distribution, the impedance response changes with the active interfacial area, porosity, and mean particle size. The predictions suggest that the surface area change dominates the impedance response. Moreover, the trade-off between the SEI resistance and charge transfer resistance has been found to be of critically dependent on the variation of the mean size of active particles and electrolyte volume fraction. From morphological variability, the spherical active particles show the largest SEI and charge transfer resistances compared to the cylindrical and platelet active particles. However, the spherical particles exhibit the lowest solid-phase diffusion resistance. The volume fraction of binder has been found to affect the impedance response significantly. An increase of binder fraction decreases the interfacial active area, which in turn affects the reaction current density, charging time and the SEI growth rate and hence ultimately on the impedance response.

An important future development of this impedance model will include the effect of phase transformation material, such as in $LiFePO_4$, and concomitant dependence of solid-phase transport on crystallographic orientation. This will allow versatility of this microstructure-aware impedance model for a wide range of chemistry and materials choice.

CHAPTER III

DIFFUSION INDUCED DAMAGE AND IMPEDANCE RESPONSE IN LITHIUM-ION BATTERY ELECTRODES

Since the formation of microcracks in active particles affects lithium diffusion and hence the solid state transport and interfacial charge transport resistance, therefore, by studying the impact of fracture on the impedance response, we can predict the mechanical damage induced resistance evolution and the deleterious influence on the cell performance. In the electrochemical impedance spectra, the influence of chemical degradation, e.g. thin SEI layer formation, can be observed directly from the change in the Nyquist plot. The influence of fracture formation on the impedance response is, however, difficult to discern and extract. The microcracks affect the concentration distribution inside the active material, which in turn depends on the cycling and environmental conditions (e.g. temperature, charge/discharge rate) and active particle characteristics (e.g. morphology, size distribution, connectivity). The current mathematical model enables us to observe and quantify the effect of fracture formation and propagation on the impedance response by directly comparing the EIS spectra with and without the diffusion induced damage. Furthermore, the influence of mechanical degradation on the impedance response for different electrode microstructural characteristics and operational conditions can be probed.

---

*Reprinted with permission from "Diffusion Induced Damage and Impedance Response in Lithium-Ion Battery Electrodes" by C. -F. Chen, P. Barai and P. P. Mukherjee, 2014, JES, **161**, A2138, Copyright 2014, The Electrochemical Society.

In this study, we developed a coupled formalism which consists of a lattice spring based mechanical degradation model and a porous electrode theory based impedance model to quantify the impact of microcrack formation and propagation on the LIB electrode resistance change as shown in Figure 3.1. The lattice spring model was used to predict the location of cracks in the single particle. The diffusion equation has been solved to get the concentration distribution of lithium ions. The concentration gradient induced stress results in the formation, nucleation and propagation of cracks. In the end, by using the locations of fractures and lithium concentration, we can predict the impedance response with porous electrode EIS theory. The detailed methodology is presented in the following section.

3.1 Computational Methodology

3.1.1 Impedance Model

In the following section, we briefly express the single particle and porous electrode EIS model developed by Meyers *et al*. [130]. The values used in the calculation of impedance and the meaning of parameters in the equations are presented in nomenclature. In Figure 3.1(b), a representative impedance response is displayed. The semicircle on the left accounts for the charge transfer resistance. The larger diameter of semicircle corresponds to larger charge transfer resistance.

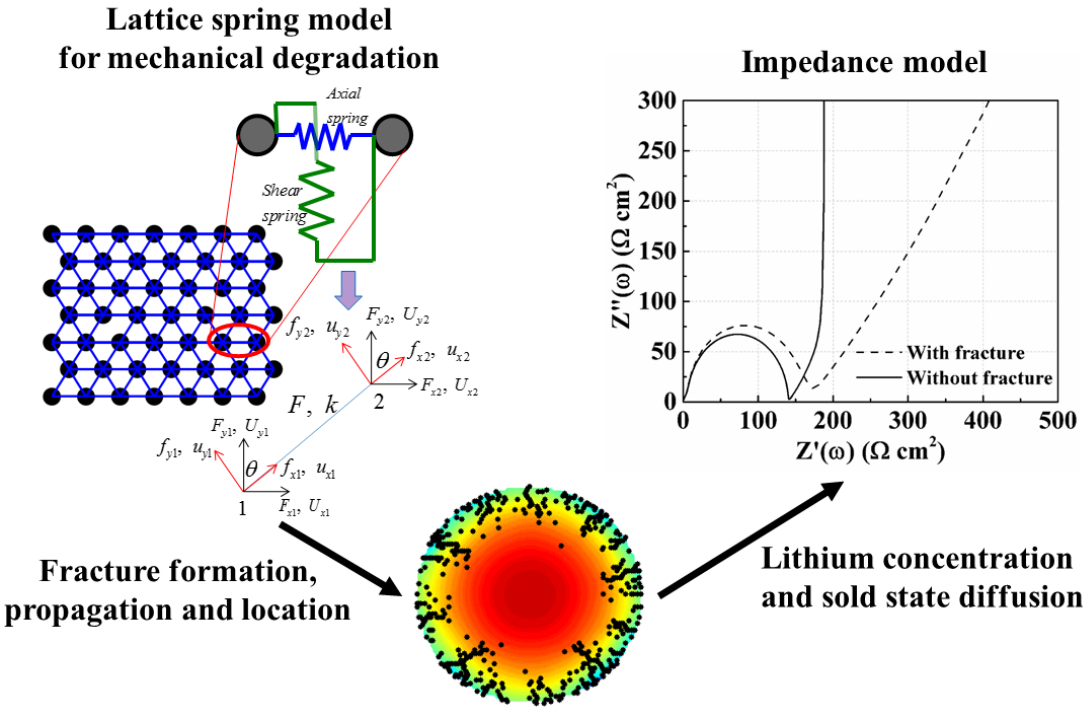

(a)

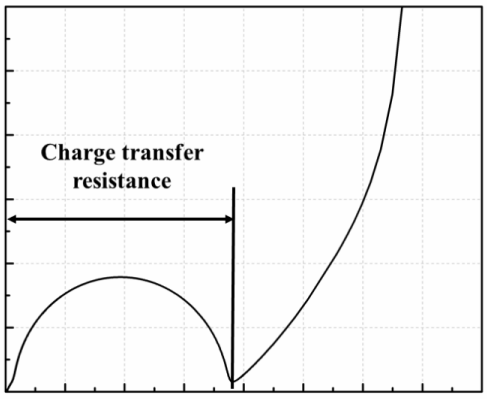

(b)

Figure 3.1. *(a) The schematic diagram of the coupling of lattice spring model and electrochemical impedance spectroscopy. (b) Sample of Electrochemical impedance spectroscopy. The semicircle accounts for the charge transfer resistance. The slope of the impedance tail accounts for the solid state diffusion resistance.*

The slope of the impedance tail corresponds to the solid phase diffusion resistance. The higher slope of this tail corresponds to smaller diffusion resistance and lower values of the slope signify enhanced diffusion resistance. In this study, we considered an electrode only model, specifically for a representative anode active particle. Therefore, all the parameters in the following impedance model refer to a typical graphite active material. In addition, since the influence of SEI has not been taken into consideration in this study, the impedance spectra will only include the charge transfer resistance (one semi-circle) and the diffusion resistance (impedance tail). It is important to note that as a first approximation, the influence of increased surface area due to the microcrack formation on the interfacial interaction is not taken into account. The exposure of the microcrack surfaces to the electrolyte and the resulting impact on the impedance response is left as a future exercise. The impedance for the analysis of diffusion induced damage is similar to the model described in section 2.1.1. The electrode impedance model, which only consider the spherical particle, is expressed as follows.

3.1.1.1 Single Particle Impedance Model

From the equivalent circuit, the EIS model for single particle can be expressed as follows. The admittance *Y* for a single particle can be expressed as eq. (3.1).

$$Y = \frac{1}{Z} = \frac{1}{\dfrac{R_{ct,1} + \dfrac{R_{part}}{Y_s}}{1 + j\omega C_{dl,1}\left(R_{ct,1} + \dfrac{R_{part}}{Y_s}\right)} + R_{film} + \dfrac{R_{ct,2}}{1 + j\omega R_{ct,2} C_{dl,2}}} + j\omega C_{film} \qquad (3.1)$$

where $R_{ct,1}$ and R_{part}/Y_s are the charge transfer and diffusion resistance between the solid phase and SEI layer which can be calculated from Eq. (3.2)– (3.3) when particle radius $r = R_s$.

$$R_{ct,1} = \frac{RT}{I_0(r)(\alpha_a + \alpha_c)F} \tag{3.2}$$

$$R_{part} = \left(-\frac{\partial U}{\partial c_s}\right)\frac{R_s}{FD_s} \tag{3.3}$$

with $\partial U/\partial c_s$ the change of open circuit potential which can be expressed as Eq.(3.4) [150]; I_0 the exchange current density which is a function of state of charge $x_{i,surf}$ as Eq. (3.5). The state of charge $x_{i,surf}$ is defined as the ratio between surface concentration and the maximum surface concentration $c_{surf}/c_{\max}$

$$\frac{\partial U}{\partial c_s} = -\frac{0.63562}{\left[\left(22.523x_{i,surf} - 3.653\right)^2 + 1\right]} - \frac{0.37}{\left[\left(28.348x_{i,surf} - 13.44\right)^2 + 1\right]} \\ -49.9789\,e^{\left(49.9789x_{i,surf} - 43.3789\right)} - 33.9111\,e^{-49.2036x_{i,surf}} - 106.6\,e^{-254.4x_{i,surf}} \tag{3.4}$$

$$I_{i,0} = k_i\left(c_{i,\max} - x_{i,surf}c_{i,\max}\right)^{0.5}\left(x_{i,surf}c_{i,\max}\right)^{0.5}c_e^{0.5} \tag{3.5}$$

The value of Y_s in Eq. (2.1) can be calculated from Eq. (2.6).

$$Y_s = \frac{R_s\sqrt{\frac{jw}{D_s}} - \tanh\left(R_s\sqrt{\frac{jw}{D_s}}\right)}{\tanh\left(R_s\sqrt{\frac{jw}{D_s}}\right)} \text{ for sphere} \tag{3.6}$$

The shift in the low frequency tail is due to the dual impact of fracture on the charge transfer resistance (radius of the semicircle) and the solid state diffusion resistance (slope of the tail). The increase in the charge transfer resistance is due to the influence of fracture on the surface concentration, which affects the exchange current density, I_0, as shown in eq. (3.5), and ultimately the value of $R_{ct,1}$. $R_{ct,1}$ is a major factor which decides the charge transfer resistance. The change in the slope of the low frequency tail is due to significant influence of fracture on the effective diffusivity D_s and $\partial U/\partial c_s$ in eq. (3.3). The value of $\partial U/\partial c_s$ is also affected by the surface concentration as shown in eq. (3.4). It is important to note that in our present simulation, we did not consider the loss of active material due to fracture. Therefore, the solid state resistance is a result of the change in local concentration gradient, surface concentration and effective solid state diffusivity.

3.1.1.2 Porous Electrode Impedance Model

By implementing the admittance *Y* calculated from Eq.(3.1), we can study the EIS for the porous electrode from the porous electrode EIS model. The impedance for the porous electrode *Z* can be expressed as

$$Z = \frac{L}{\kappa+\sigma}\left[1+\frac{2+\left(\frac{\sigma}{\kappa}+\frac{\kappa}{\sigma}\right)\cosh\upsilon}{\upsilon\sinh\upsilon}\right] \tag{3.7}$$

where

$$\frac{L}{\upsilon} = \left(\frac{\kappa\sigma}{\kappa+\sigma}\right)^{1/2}\left(\overline{aY}\right)^{-1/2} \tag{3.8}$$

The average of single particle admittance $\overline{aY}$ is calculated from averaging the admittance with the surface area as

$$\overline{aY_s} = 4\pi\int_0^\infty N(r)Y(r)r^2dr \tag{3.9}$$

where *N(r)* is the number density of particle radius *r*. In this work, we use the modified logarithm Gaussian distribution proposed by Meyers et al. [130] as Eq.(3.10). The benefit of using Eq. (3.10)is that controlling the electrode design parameters (specific area *a*, volume fraction ε_s and mean particle radius) is straight forward.

$$N(r) = \frac{1}{r}\left[\frac{(a)^3 e^{-\left(\frac{\varphi}{4}\right)^2}}{(4\pi)9(\varepsilon_s)^2\sqrt{\pi}\varphi}\right]\exp\left[-\left(\frac{\ln\left(\frac{ra}{3\varepsilon_s}\right)}{\varphi}\right)^2\right]\exp\left[-\frac{5}{2}\ln\left(\frac{ra}{3\varepsilon_s}\right)\right] \tag{3.10}$$

Here, φ the sharpness of distribution function can be used to decide the mean particle radius.

From Eq.(3.10), we can make sure

$$a = \int_0^\infty \mathrm{A}(r)N(r)dr \quad \text{and} \quad \varepsilon_s = \int_0^\infty V(r)N(r)dr \tag{3.11}$$

where *A(r)* and *V(r)* are the surface area and volume of active material with particle radius *r*.

3.1.2 Diffusion Induced Damage

The stochastic methodology of simulating the diffusion induced damage is briefly described below, which relies on the work by Barai and Mukherjee. [24] The model is based on a *random lattice spring* formalism coupled with solid state diffusion of lithium in active particles. This also included the analysis of the electrode performance and was able to predict the capacity loss due to fracture formation. The distribution of lithium ion concentration is calculated by solving the generalized diffusion equation, which can be derived from the Helmholtz free energy. [154, 155]

$$\frac{\partial c(\vec{r},t)}{\partial t} = \vec{\nabla}\cdot\left[\underset{\approx}{D}\cdot\vec{\nabla}c(\vec{r},t) + \frac{\delta V}{k_B T}c(\vec{r},t)\underset{\approx}{D}\cdot\vec{\nabla}c(\vec{r},t) - \frac{\delta V}{k_B T}c(\vec{r},t)\underset{\approx}{D}\cdot\vec{\nabla}\sigma_{kk}\right] \quad (3.12)$$

Here, $\vec{r}$ signifies the spatial coordinate, t is time, $c(\vec{r},t)$ is the space and time dependent concentration of Li ions, $\underset{\approx}{D}$ signifies the second order diffusion coefficient tensor, σ_{kk} is the hydrostatic stress, δ is a material dependent constant, k_B is the Boltzmann's constant, T signifies temperature and V is the atomic volume. Anisotropy in the diffusion coefficient can be incorporated in the $\underset{\approx}{D}$ tensor. In the current simulation, the effect of hydrostatic stress on the diffusion process has been neglected. Anisotropy in the diffusivity term has not been taken into consideration. Therefore, the $\underset{\approx}{D}$ tensor is a diagonal matrix with the scalar value of diffusion coefficient D_s. A circular cross section of the single particle has been taken into consideration to model the diffusion-induced stress and capture the fracture observed during operation. The governing differential

equation has been solved using finite volume method. Flux prescribed boundary condition at the outer surface of the electrode active particles has been taken into account. In Eq.(3.13), i is the applied current and S is the surface area of active particles in the electrode.

$$\frac{\partial c(\vec{r},t)}{\partial n} = \frac{i}{SF} \tag{3.13}$$

Based on random spring model (RSM), a technique has been implemented to estimate the initiation and accumulation of damage and fracture in the electrode material [156, 157]. A triangular mesh is considered in this study. The lattice network has a coordination number of six. The electrode material is assumed to display brittle fracture behavior. The breaking threshold energy of each spring $\left(E_t\right)$ is a uniformly distributed random parameter, where the mean value has been evaluated based on an energy equivalency scheme [158-160]. Coupling with Li diffusion, the resultant stress generation is incorporated through the Li concentration profile inside the electrode. The quasi-static equilibrium equation has been solved to determine the stress distribution inside the electrode.

$$\frac{\partial \sigma_{ij}}{\partial x_j} + F_i = \rho \ddot{\bar{u}}_i = 0 \tag{3.14}$$

with $u_i = \bar{u}_i$ on S_u and $\sigma_{ij} n_j = t_i = \bar{t}$ on S_t

Here, σ_{ij} is the stress tensor, F_i is the body force vector which is assumed to be zero for this particular problem $\left(F_i = 0\right)$, x_i signifies the spatial coordinates, $u_i\left(x_i\right)$ is the space dependent displacement vector, $\bar{u}_i$ is the prescribed displacement on the boundary, σ_{ij} is the stress tensor on the boundary, n_j is the outer normal direction on the domain boundary, t_i is the traction force, $\bar{t}_i$ is the prescribed traction force on the boundary, S_u is that portion of the boundary on which displacement prescribed boundary condition is specified and S_t is that portion of the boundary on which traction prescribed boundary condition is specified. Small strain small displacement analysis has been conducted here.

As mentioned earlier, spring type elements were used to discretize the above-mentioned equation. The springs display stiffness along both the axial and transverse direction. The local force vs. displacement relation for the spring is given as follows [161],

$$\begin{bmatrix} f_{x1} \\ f_{y1} \\ f_{x2} \\ f_{y2} \end{bmatrix} = \begin{bmatrix} k_n & 0 & -k_n & 0 \\ 0 & k_s & 0 & -k_s \\ -k_n & 0 & k_n & 0 \\ 0 & -k_s & 0 & k_s \end{bmatrix} \begin{bmatrix} u_{x1} \\ u_{y1} \\ u_{x2} \\ u_{y2} \end{bmatrix} \tag{3.15}$$

where $\vec{f}$ is the local force vector, $\vec{u}$ is the local displacement vector, k_n is the axial spring stiffness and k_s is the shear stiffness of each spring. Stress generated due to the diffusion of Li is incorporated as an axial displacement inside the spring. Diffusion induced displacement Δu^d and force $\vec{f}^d$ is defined as,

$$\Delta u^d = \Gamma \cdot \Delta c \cdot l \tag{3.16}$$

$$\vec{f}^{\,d} = \left[k_l\right] \cdot \Delta \vec{u}^{\,d} \tag{3.17}$$

Here, Γ signifies the volume expansion coefficient (with unit of m^3/mol) and Δc represents the local concentration gradient ($\Delta c = c(x,t) - c_{avg}(t)$, where $c_{avg}(t)$ represents the volume averaged concentration of the entire spherical particle), l is the length of the spring type element and $\left[k_l\right]$ is the local stiffness matrix. Fracture in each of the springs is defined in terms of an energy threshold criterion. Energy in each spring is calculated according to $\psi = \frac{1}{2}\vec{f} \times \vec{u}$. Here, $\vec{f}$ and $\vec{u}$ are the local force and displacement vectors for each of the springs. As the energy in a spring exceeds its breaking threshold $(\psi > \psi_t)$, it is irreversibly removed from the network. Fracture threshold for each of the springs (ψ_t) is obtained from a uniform random distribution around the mean fracture threshold. After one bond is broken, the lattice network is re-equilibrated before breaking subsequent bonds. The concentration distribution calculated from Eq. (3.12) was used to calculate the exchange current density I_0 and $\partial U/\partial c_s$ in Eq. (2.2) and (2.3) in order to evaluate the EIS. The temperature effects have been simulated by changing the temperature T in Eq. (3.12) . The diffusivity D_s also varies with temperature by following the Arrhenius relation as

$$D_s(T) = D_s \exp\left[\frac{E_a}{R}\left(\frac{1}{T} - \frac{1}{T_{ref}}\right)\right] \tag{3.18}$$

3.1.3 Impedance Response with Diffusion Induced Fracture

The diffusion induced fracture has a significant impact on the local lithium concentration in the active particle and the gradient between the particle center and interface, and the effective solid state diffusivity. Due to the change of solid state diffusivity, the lithium concentration distribution changes with the formation of fracture. In this study, the "charge transfer resistance" is only affected by the surface concentration (changes in the exchange current density I_0) and particle radius as shown in Eq.(3.2). If the particle size distribution is the same, the charge transfer resistance is only influenced by the surface concentration. However, the surface concentration is not only influenced by the microcracks but also influenced by the temperature, (dis)charge rate and particle-size distribution. Therefore, in order to minimize the variables, in this work, the impedance response with/without fracture has been studied. By comparing the impedance response with/without microcracks, the change in surface concentration becomes the primary influencing factor because of the diffusion induced stress and corresponding damage evolution. During the discharge process, the surface concentration is smaller for the particles with fracture than that in the case of without fracture because the microcracks locally block the diffusion pathway from the center to the interface, thereby leading to varying local concentration gradient. The reverse scenario is observed during charging where the surface concentration is larger for the particles with fracture compared to those without fracture. Change in the concentration gradient and effective solid state diffusivity ultimately affects the impedance response. The exchange current density I_0 and $\partial U/\partial c_s$ in Eq. (3.2) and (3.3) depends on the surface concentration of particles. The diffusivity

D_s is also affected by the fracture because the microcrack increases the diffusion path of lithium ion. Therefore, the calculation of effective diffusivity is necessary for proceeding forward. The effective diffusivity can be estimated from the ion concentration calculated in section 3.1.2.

$$\frac{D_{eff}}{D_s} = \frac{\left(c_{r=R} - c_{r=0}\right)_{\text{without fracture}}}{\left(c_{r=R} - c_{r=0}\right)_{\text{with fracture}}} \tag{3.19}$$

Eq. (3.19) is based on the idea that because the flux on the boundary of particle(r=R) is constant, the diffusivity is inversely proportional to the concentration gradient.

In addition to the influence of the transport property change, because the location of fracture formation is not uniform, the directional dependence as a function of angle θ is incorporated in Eq. (3.1), as shown in Figure 3.2 (a) and (c). Figure 3.2 (b) shows that the impedance response varies with location. In the location with more fractures, the EIS shows large charge transfer resistance and solid phase diffusion resistance. Then, because the fracture formation also changes with the particles radius as shown in Eq. (3.3), the EIS for single particles should be a function of particle radius and location θ as Eq. (3.20).

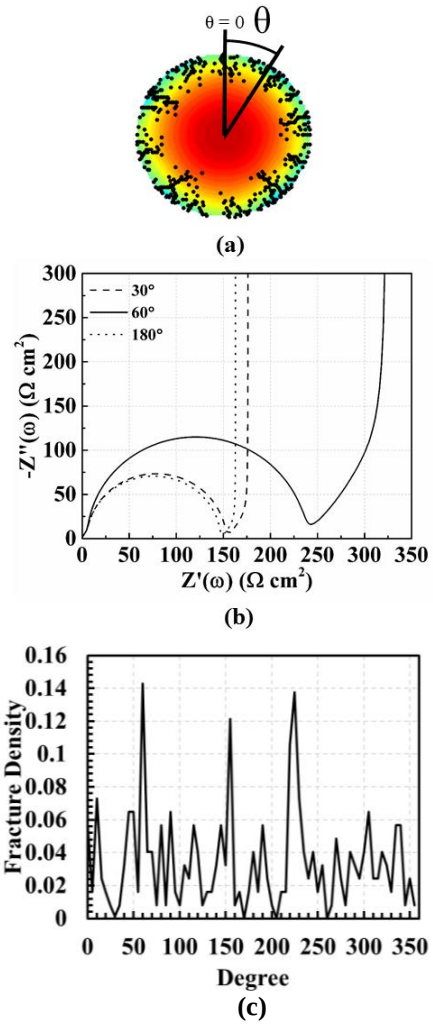

Figure 3.2. (*a) The fracture and concentration distribution plot observed in a single particle. (b) The impedance response at different location (angle) of particle (θ=30°, 60° and 180°) (c) The fracture density at different location (angle). The fracture density is the ratio between the broken nodes and the total number of nodes on the same azimuthal position.*

$$Z(R_s,\theta_N)=\frac{1}{Y(R_s,\theta_N)} \tag{3.20}$$

The average single particle admittance for a single particle of radius R_s is calculate by averaging the admittance at different azimuthal location as

$$\bar{Y}(R_s)=\frac{\sum_{1}^{N}Y_N(R_s,\theta_N)}{N} \tag{3.21}$$

where N is the Nth node on the surface, θ_N is the azimuthal location of the Nth node and Y_N is the admittance at the location of θ_N. After the average admittance for the discrete single particles is obtained, the porous structure EIS can be obtained by substituting Eq. (3.21) back into Eq.(3.7). The impedance model in this work builds on the model originally proposed by Newman and co-workers.[21] In their impedance model, there are two stages of calculation.[21] The first stage is the impedance of single particle and the formulation is as shown in Eq. (3.1). Since the model assumes that the properties of the particle are uniform, the admittance Y is calculated with 1-D simulation along the radial direction, and the admittance Y calculated in Eq. (3.1) is the admittance per unit surface area ($1/\Omega cm^2$) of the particles. The second stage is to calculate the impedance for the porous electrode from the admittance Y obtained from stage one. In the second stage, the single particle admittance Y obtained from the 1-D simulation (in stage 1) is integrated over the surface area of the particles in the porous electrode, as shown in Eq.(3.9), and incorporated in Eq. (3.7) to calculate the porous electrode impedance. In our current model, the diffusion induced stress and fracture is simulated in a circular cross-section.

Since isotropic solid state diffusion is considered, as a first step, the information from the circular cross-section is used for the averaged single particle impedance. The local variation in admittance Y ($1/\Omega cm^2$) is averaged as shown in Eq. (3.21). Thereafter, similar to the model by Newman and co-workers,[130] in the second stage, the averaged admittance Y was integrated over the surface area of spherical active particles to obtain the electrode impedance as shown in Eqs. (3.7) – (3.9).

It is important to note that the primary objective of this work is to investigate the effect of diffusion induced damage due to the formation of microcracks on the electrode impedance response. The influence of mechanical damage in the active particles manifests in the change of surface concentration and effective solid state diffusivity of lithium. For the same duration of (dis)charge, the surface concentration will be different in the case of with/without fracture. After a significant relaxation (resting) time following (dis)charge, although the concentration gradient inside the active particles will reduce depending on the particle size and morphology and the rate (high or low) of (dis)charge, same surface concentration for a representative active particle with and without fracture is quite a challenge to achieve. In the present simulations, the difference in the electrode impedance response with/without fracture is investigated after the same duration of charge/discharge in order to capture the influence of the surface concentration difference which further affects the $\partial U/\partial c_s$ slope, thereby reflecting on the charge transfer and diffusion resistance. Since the externally applied flux is constant, for the both the cases of with and without fracture, the bulk concentration is the same. Only the surface concentration varies

due to the mechanical degradation induced reduction in diffusivity. For a future study, a relaxation step following (dis)charge will be investigated.

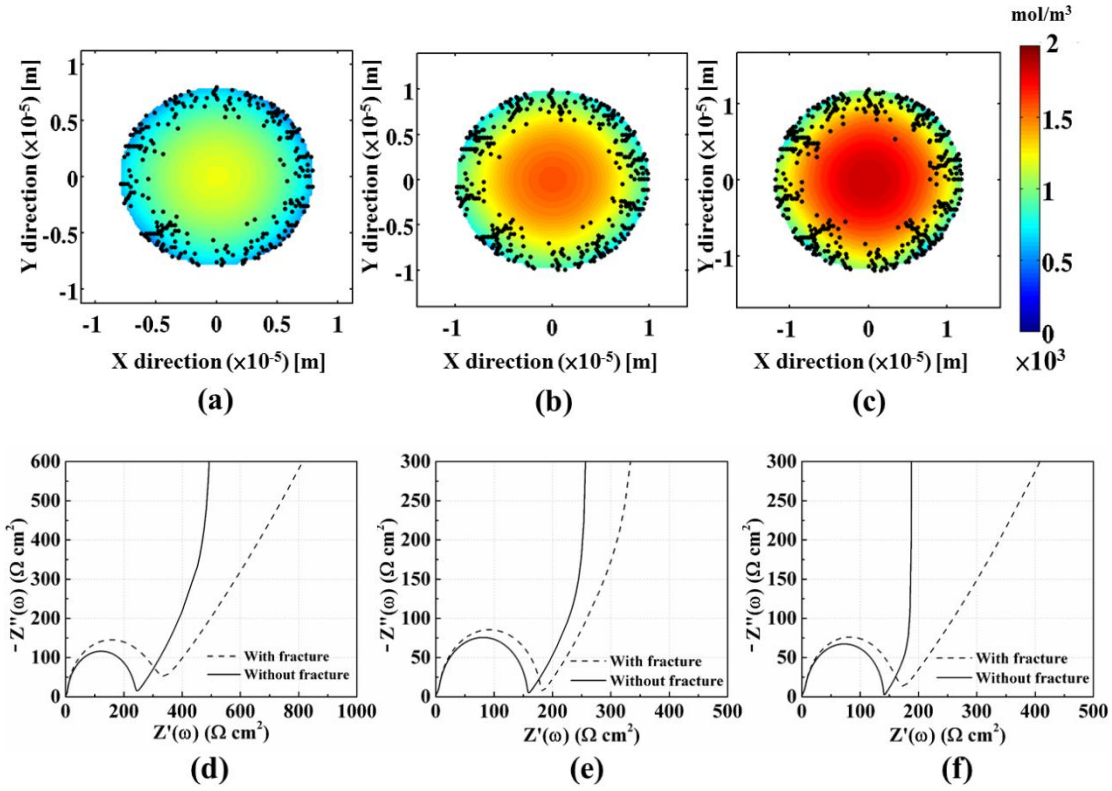

Figure 3.3. *(a – c) The fracture and concentration distribution of the particles with radius (a) 8 µm (b) 10 µm (c) 12 µm after charge for 1800 seconds under 2C at 25^{0}C. (d – f) Single particle impedance response for the particle radius of (d) 8 µm (e) 10 µm (f) 12 µm after 1800 second of discharge process under 2C discharge rate at T= 25^{0}C.*

3.2 Results and Discussion

In this section, we will present the mechanical degradation due to diffusion induced stress by comparing the impedance response of particles with and without fracture. The microstructural information (namely, particle size distribution, interfacial area) from the stochastically reconstructed electrodes is employed as input into the impedance model,

which includes the effect of particle size distribution. The concentration and stress field along with microcrack formation are solved in a discrete fashion for each particle size (e.g. 5 μm, 10 μm based on the particle size distribution input from the microstructure) and the corresponding lithium concentration (e.g. surface concentration) is fed back into the impedance model for the construction of the impedance response. In the diffusion induced damage simulation, we recorded the lithium concentration and fracture distribution after every 20 seconds. The current density has been maintained constant for different particle sizes. The concentration profile was used to calculate the desired properties, such as exchange current density and effective diffusivity, for EIS. For the single particle EIS, we inspect the influence of particle size on the fracture distribution and impedance response. The effect of microstructure, temperature, and charge/discharge rate on the porous electrode EIS were also discussed in the following section. It should be noted that, in this work, 1C (dis)charge rate corresponds to operation at 1.656A for one hour.

3.2.1 Single Particle Impedance Response

In this section, we present the concentration profile, fracture distribution, and the corresponding impedance response during charge/discharge as shown in Figure 3.3 and Figure 3.4. The fracture density along the radial direction which refers to the fracture profiles is shown in Figure 3.5.

3.2.1.1 Impedance Response during Discharge

The concentration and fracture profiles in the particles with radius 8 μm, 10 μm and 12 μm after discharge for 1800 seconds has been shown in Figure 3.3 (a) - (c). The fracture

density on the different radial position has also been shown in Figure 3.5 (a). The fracture density in Fig. 5 is defined as the ratio between the broken bonds and the total bonds at the same radial position. From the contour plots (Figure 3.3) and fracture density (Figure 3.5), it can be observed that larger particles experience enhanced microcrack formation with preferential fracture density on the particle surface. During the discharge process in an anode particle, lithium ions diffuse out of the particle from its outer surface. This local decrease in the lithium concentration around the peripheral region causes the material to shrink. However, the presence of excessive amount of lithium close to the center prevents it from attaining the desired compressed configuration, which gives rise to the formation of tensile stress around the periphery of the particle. This tensile stress leads to microcrack formation and propagation in the vicinity of the surface. As a result, higher fracture density is observed close to the particle surface in Figure 3.5 (a) during the discharge process. Formation of compressive stress around the center of the particle does not lead to significant damage evolution (see Figure 3.5 (a)). Larger particles exhibit increased crack formation due to the higher concentration gradient.

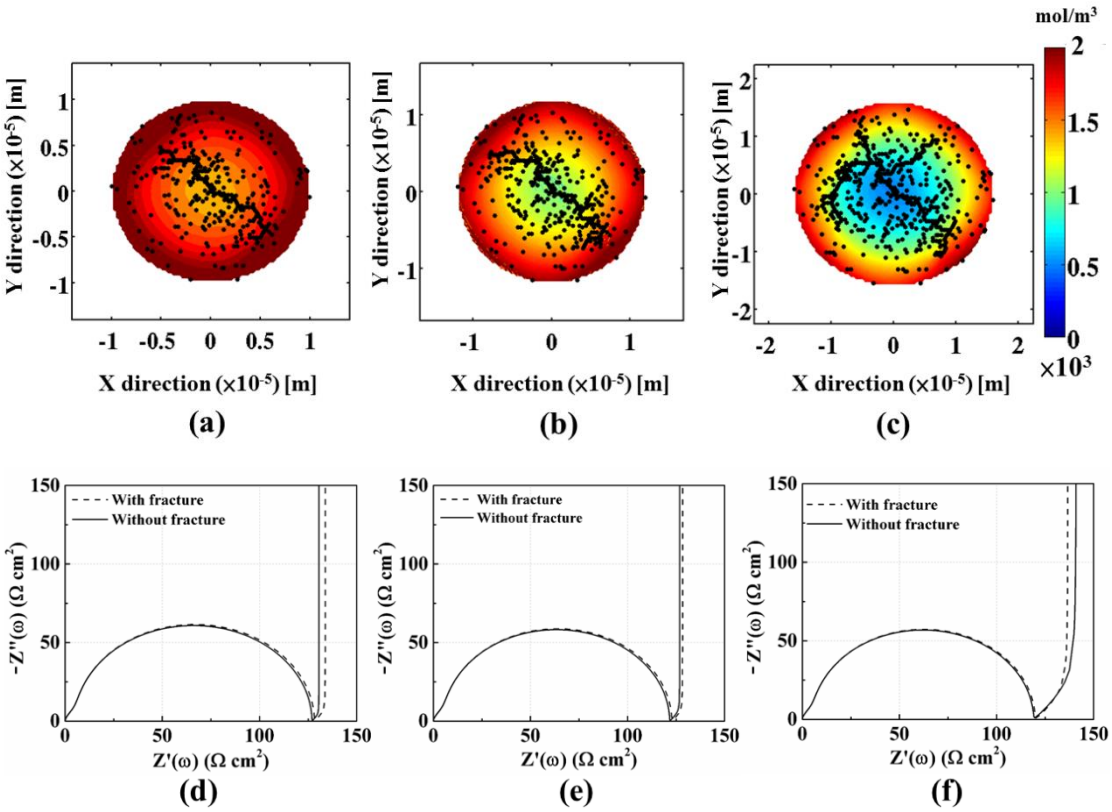

Figure 3.4. *(a – c) The fracture and concentration profile inside the particles with radius (a) 10 µm (b) 12 µm (c) 16 µm after charge for 3000 seconds under 2C charge rate at T= 25^{0}C. (d – f) Single particle impedance response for the particle radius of (d) 10 µm (e) 12 µm (f) 16 µm after 3000 second of charge under the rate of 2C at T= 25^{0}C.*

The single particle impedance response for the particle radius of 8 µm, 10 µm and 12 µm during the discharging process is shown in Figure 3.3 (d) - (f). From the results, mechanical degradation increases the charge transfer resistance because the formation of fractures decreases the surface concentration and exchange current I_0 in Eq. (3.5). The change of surface concentration is due to the lower effective diffusivity caused by the microcracks. In addition, during the discharging process, the fracture concentrated on the

surface of particles, as shown in Figure 3.5 (b), also change the surface concentration and impedance response drastically as shown in Figure 3.2.

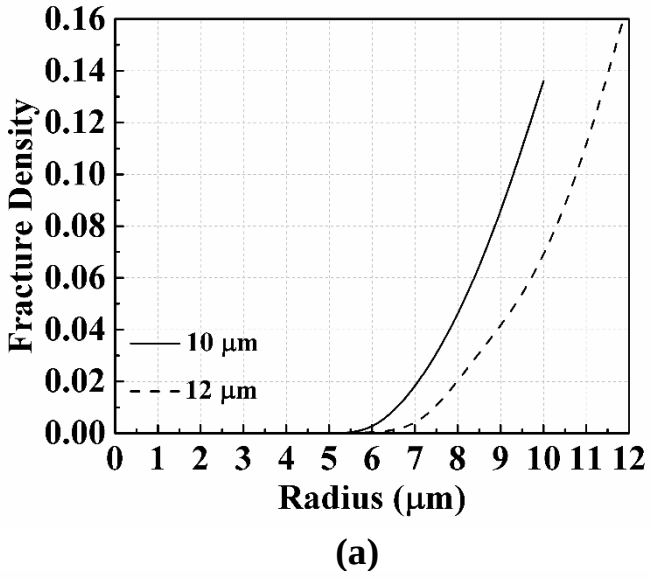

(a)

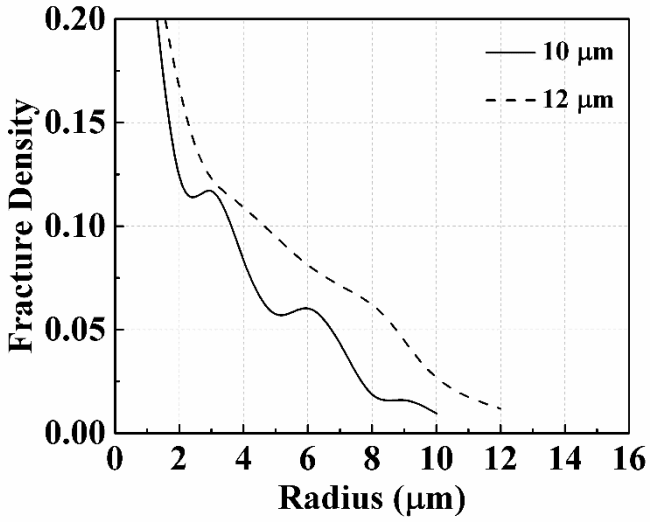

(b)

Figure 3.5. *The fracture density along the radial direction after (a) discharge for 1800 seconds (b) charge for 3000 seconds. The fracture density is the ratio between the broken bonds (black dots) and the total bonds at the same radial position.*

The fractures on the surface of particles caused the increase of average charge transfer resistance for a single particle. We should notice that although the fracture density and concentration gradient increases with particle size, the fracture has a larger influence on the solid phase diffusion resistance for the particles with radius 8 μm and 12 μm than the influence for the particle radius of 10 μm. This can be explained as (a) the surface concentration depletes faster in small particles than large particles, which also reflects in an increase in the charge transfer resistance; and (b) the surface concentration of the particle with fracture is less than the surface concentration of the one without fracture during the discharging process. If the surface concentration is low (for the small particle) (SOC < 0.2), the value of $\partial U/\partial c_s$ in Eq.(3.3), is quite sensitive to the change in surface concentration (due to fracture formation). Therefore, we see a larger difference for the particle radius of 8 μm than that for the 10 μm particle. For larger particles (> 10 μm), because the amount of fracture formation increases with the particle size as shown in Figure 3.3 (a) - (c), mechanical damage evolution lowers the surface concentration and effective diffusivity. Therefore, large particles have higher solid phase diffusion resistance and charge transfer resistance in the electrode.

3.2.1.2 Impedance Response during Charge

The concentration and fracture distribution in the particles with radius 10 μm, 12 μm and 16 μm are shown in Figure 3.4 (a) - (c). The fracture density along the radial position is as shown in Figure 3.5 (b). Similar to the discharge process, larger particle also exhibits higher microcrack formation during charge. However, most of the damage

concentrates around the center of the particle. During lithiation, influx of lithium ions creates compressive stress along the periphery of the particle. Tensile stress acts close to the center, which results in the evolution of higher mechanical damage. In charging process, the larger particles also have a larger concentration gradient and the microcracks increase the concentration gradient even further.

The single particle impedance response for the particle radius of 10 μm, 12 μm and 16 μm during charging process is as shown in Figure 3.4 (d) - (f). Compared to the discharging process, during charge mechanical degradation, the fracture has less influence to EIS because the fractures from inside the particles and has less influence on the surface concentration. Therefore, the charge transfer resistance of particles with the fracture is slightly larger than the one without fracture. The increase in charge transfer resistance is also due to the change in surface concentration, which influences the exchange current density I_0.

The difference in solid phase diffusion resistance is because of the value of $\partial U/\partial c_s$ and effective diffusivity. For the particle size of 12 μm and 16 μm, since the SOC is between 0.55 ~ 0.75, where $\left(-\partial U/\partial c_s\right)$ decreases with increasing SOC, the particles with fracture has a smaller value of $\left(-\partial U/\partial c_s\right)$ (lower diffusion resistance). However, the fracture decreased the effective diffusivity. According to Eq. (3.3), after the trade-off of between $\left(-\partial U/\partial c_s\right)$ and effective diffusivity, the effect of fracture to EIS decrease with particle size at the particle-size range of 12 μm~16 μm, and the fractures have a positive effect on the solid-phase diffusion resistance. For the particle radius of 10 μm, the particle

with fracture has higher diffusion resistance than the one without fracture because the value of $\left(-\partial U/\partial c_s\right)$ increase with the increase of SOC (SOC > 0.8). There is no trade-off between effective diffusivity and $\left(-\partial U/\partial c_s\right)$.

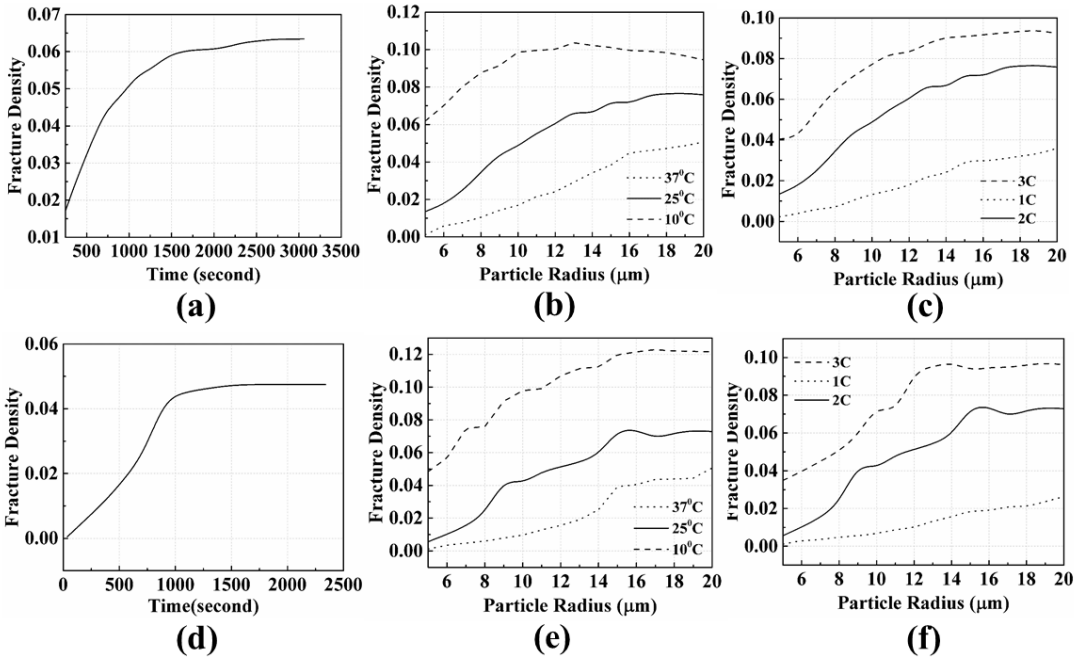

Figure 3.6. *Fracture evolution in a representative 12 μm spherical particle. (a) Time evolution of fracture density during 3200 seconds of discharge process; (b) Fracture density with different particle radius under different operating temperature after discharge for 1800 seconds; (c) Fracture density with different radius of particles under different C-rate after discharge for 1800 seconds (d) The time evolution of fracture density during 2400 seconds of charging process (e) The fracture density with different radius of particles under different temperature after charge for 3000 seconds (f) The fracture density with different radius of particles under different C-rate after charge for 3000 seconds. The fracture density is the ratio between the broken bonds (black dots) and the total number of bonds inside the particle.*

3.2.2 Electrode Microstructure and Impedance Response

In the following section, we will present the influence of temperature, discharge/charge rate and particle size distribution on the diffusion induced fracture and the corresponding impedance response. To study the evolution of damage and impedance spectra with time, temperature and discharge/charge rate, we used the microstructure with the particle size distribution provided in Eq. (3.10) with ε=0.35, a=2000 cm^{-1} and φ=0.2. The particle size distribution is as shown in Figure 3.9 (a). We implemented the single particle EIS to the porous electrode formulation in Eq. (3.7). The single particle EIS was calculated under different time, temperature and discharge/charge rate. For the study of particle-size distribution, we constructed the microstructures with a different volume fraction of particle but maintained the specific surface area and mean particle radius. In the following subsections, the expressions of concentration and microcrack distribution inside the particles of the porous electrode have been represented by single particle contour plots. With different conditions (time, temperature and discharge/charge rate), we can see the difference by comparing the single particle contour plots and link the difference to the impedance response.

3.2.2.1 Evolution of Fracture and Porous Electrode Impedance Response

The evolution of fracture and the change in concentration distribution during the discharge and charge processes are shown in Figure 3.7(a) - (d) and Figure 3.8(a) - (d) (a 12 μm particle inside the porous electrode). The time evolution of fracture density is shown in Figure 3.6(a) and (d) during discharge and charge, respectively. From the contour plots (see Figure 3.7) and fracture density (in Figure 3.6), the evolution of

microcrack formation reaches a plateau around 6% and 5% fracture density during discharge and charge as shown in Figure 3.6 (a) and (d), respectively. This is due to a rapid increase in the lithium concentration gradient during at first followed by saturation thereof. However, we can see the difference of concentration gradient and surface concentration between the particle with and without fracture. As mentioned before, mechanical degradation has a larger influence on the concentration distribution of larger particles. It means, although the fracture almost stops growing, the fracture still has an influence on the concentration profile.

In Figure 3.7 (e) and (f), the EIS shows the influence of fracture to the solid phase diffusion resistance and the charge transfer resistance during the discharging process. The increase in the influence of damage with time evolution is because the microcracks make the surface concentration decrease faster than the particle without fracture. The change in exchange current density I_0 and $\left(-\partial U/\partial c_s\right)$ due to the surface concentration reflects in the resultant impedance response. The exchange current density I_0 affect the value of $R_{ct,1}$ in Eq. (3.2) and $R_{ct,1}$ has the major effect to the charge transfer resistance. The value of $\left(-\partial U/\partial c_s\right)$ affect the value of R_{part}, and R_{part} has the major effect on the diffusion resistance. During the charging process, the effect of mechanical degradation also increases with the time evolution as shown in Figure 3.6(d), Figure 3.8(e) and (f), but the fracture has less influence compared to the discharging process. The difference is because most of the microcracks get concentrated in the center, which has less influence on the surface concentration.

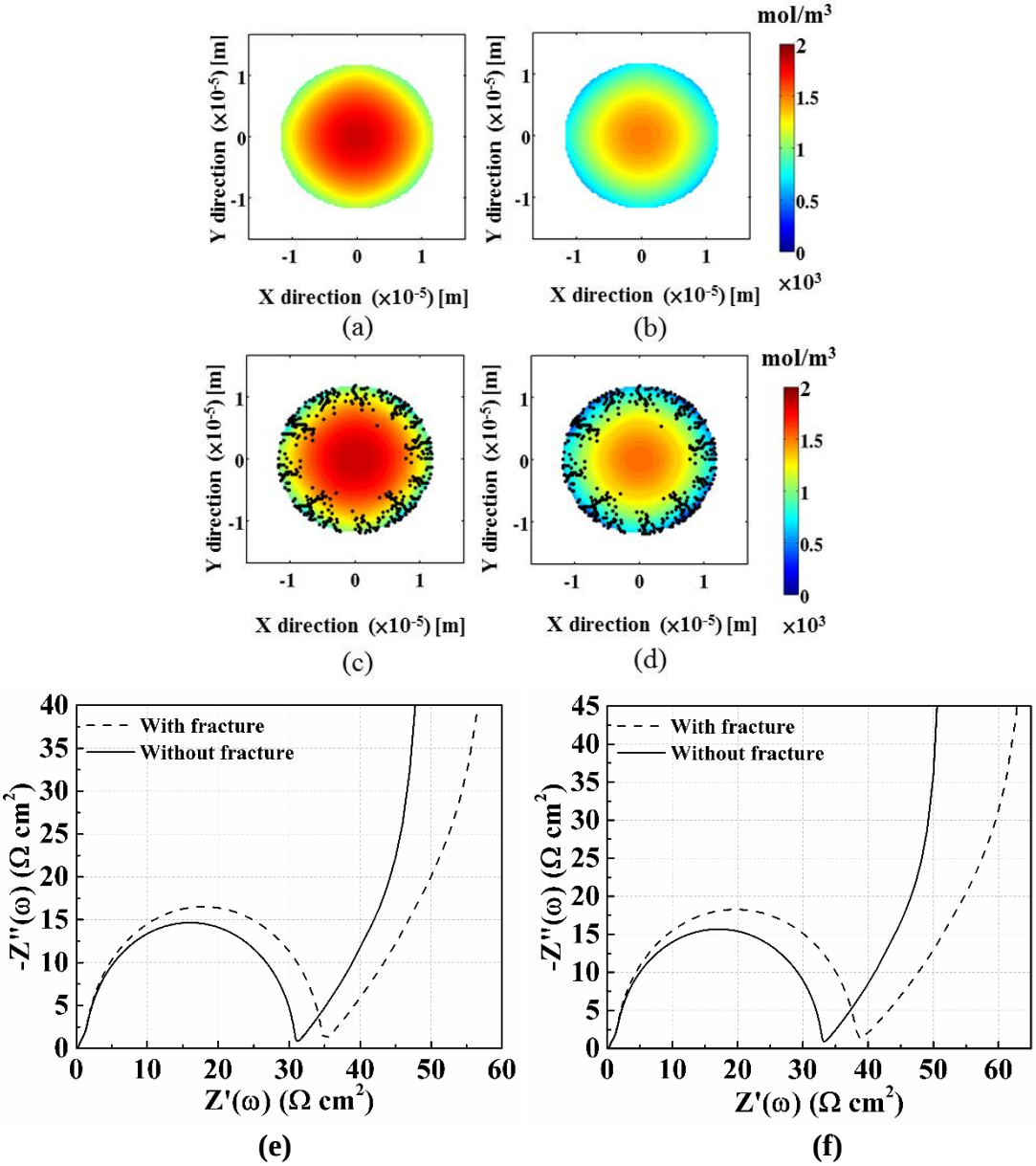

Figure 3.7. *(a – d) Contour plots after discharging for different amount of time in a particle with radius 12μm. After (a) discharge for 2200 seconds, without fracture. (b) discharge for 3000 seconds, without fracture. (c) discharge for 2200 seconds, with fracture. (d) discharge for 3000 seconds, with fracture. (e – f) The porous electrode impedance response after (e) discharge for 2200 seconds (f) discharge for 3000 seconds. The discharge rate is 2C and T= 25^{0}C.*

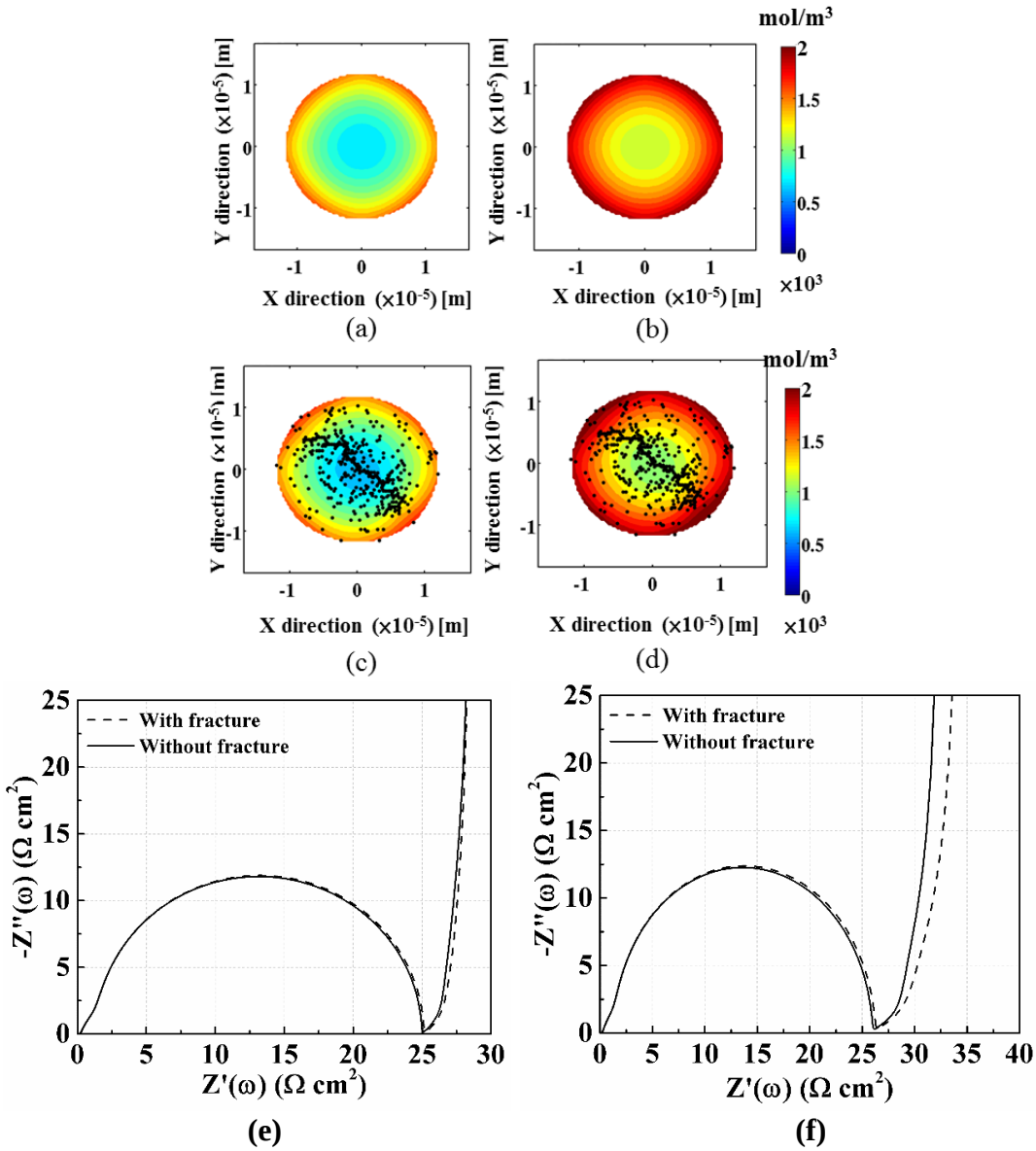

Figure 3.8. *(a – d) Contour plots after discharging for different amount of time in a particle with radius 12μm. After (a) charge for 2200 seconds, without fracture. (b) charge for 3000 seconds, without fracture. (c) charge for 2200 seconds, with fracture. (d) charge for 3000 seconds, with fracture. (e – f) The porous electrode impedance response after (e) charge for 2200 seconds (f) charge for 3000 seconds. The discharge rate is 2C and T= 25^{0}C.*

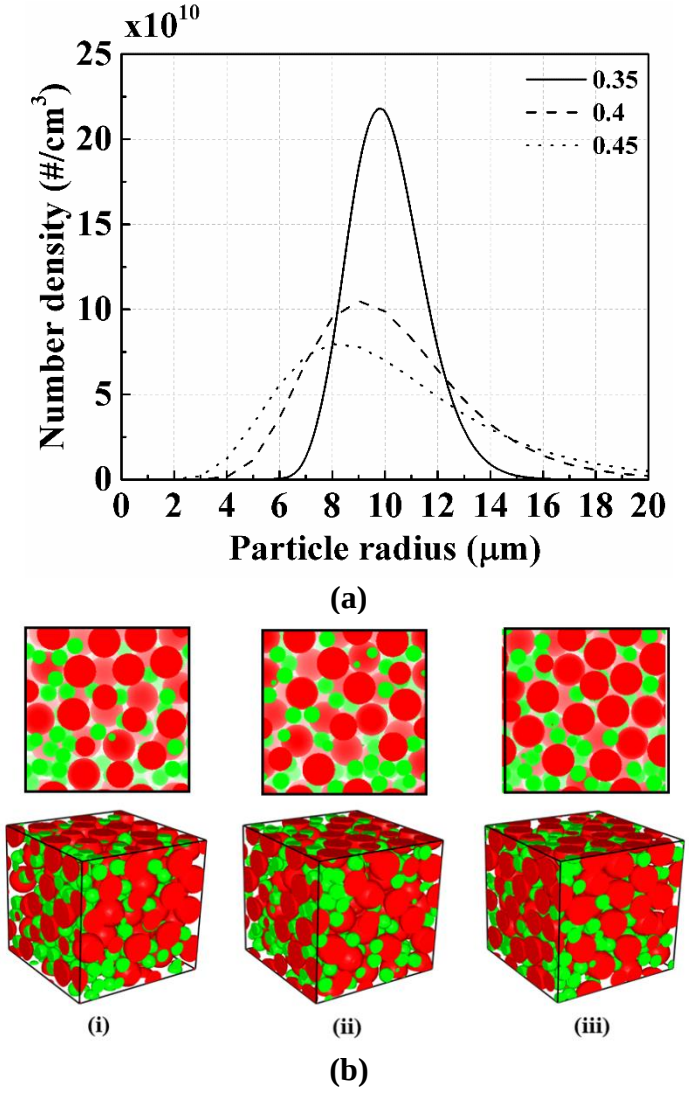

Figure 3.9. *(a) Particle size distribution with 35%, 40% and 45% of active material. The specific area is kept constant at a =2000 cm^{-1} and the mean particle radius is maintained at 10 μm. (b) The equivalent 3D and 2D microstructure plots of the particle-size distribution with (i) 35% (ii) 40% (iii) 45% volume fraction of active material. In the microstructure, Red: active material; Green: Graphite (carbon additives).*

While the fracture shows negligible influence after charge for 2200 seconds, the impact after charge for 3000 seconds, however, is quite evident. From the results, we can infer that the effect of damage evolution on the surface concentration has an obvious influence on the resistance after charge for 3000 seconds. Moreover, the local concentration

enhancement near the surface during charging is slower than the depletion rate during discharge. This causes fracture evolution during charging to be slower than that during the discharging process.

3.2.2.2 Effect of Particle Size Distribution

The influence of fracture changed with the particle size because of the rate of damage evolution and diffusion length. Since the particle size distribution change with the design of electrodes (porosity, active material surface area or mean particle radius), the influence of fracture to the electrodes with different particle-size distribution would also be different. The fracture density of different particle sizes under different temperature and rate conditions is presented for discharge in Figure 3.6 (b - c) and during charge in (e - f). From the fracture density, it is evident that the microcrack formation is enhanced for low temperature operation due to the lower solid state diffusivity of lithium, which results in an elevated local concentration gradient. Similarly, under high discharge/charge rate operation, higher local concentration gradient is the primary cause for the higher fracture density. In Figure 3.6 (b), (c), (e) and (f), reduced mechanical degradation for smaller particles can be attributed to smaller diffusion length resulting in reduced concentration gradients. Figure 3.9 (a) shows the different particle-size distribution, which makes the specific surface area (cm^{-1}) and mean particle radius constant but change the volume fraction of particles. The constant surface area maintained in all the microstructures ensures that the current density is the same for different particle size distribution under the same discharge/charge rate. The particle-size distribution shows that the standard deviation increases with the volume fraction of active material in order to maintain the

specific surface area at a constant value. Figure 3.9 (b) shows the corresponding microstructure for different particle-size distribution. This study of the microstructure is simulated under 2 C discharge/charge rate when T= 25℃.

The result of the porous electrode EIS under discharge condition has been shown in Figure 3.10 (a) - (c). From the result, the effect of fracture on the charge transfer resistance increases with the volume fraction of the active material. In other words, the high standard deviation in particle size distribution increases the influence of fracture. One possible reason is that electrodes with a higher volume fraction of active material contain more number of larger particles as compared to the electrodes with a low volume fraction of active material. Larger particles experience higher mechanical degradation, which leads to enhanced charge transfer resistance. For the solid phase diffusion resistance, mechanical degradation has the least influence on the diffusion resistance of the microstructure with 40 % volume fraction of active material. The result can be explained by the EIS of single particles, where the influence of fracture has the least effect when the particle size is 10 μm. After considering the effect of particle size according to its size distribution, there exists an optimal design for which the mechanical degradation has the least influence.

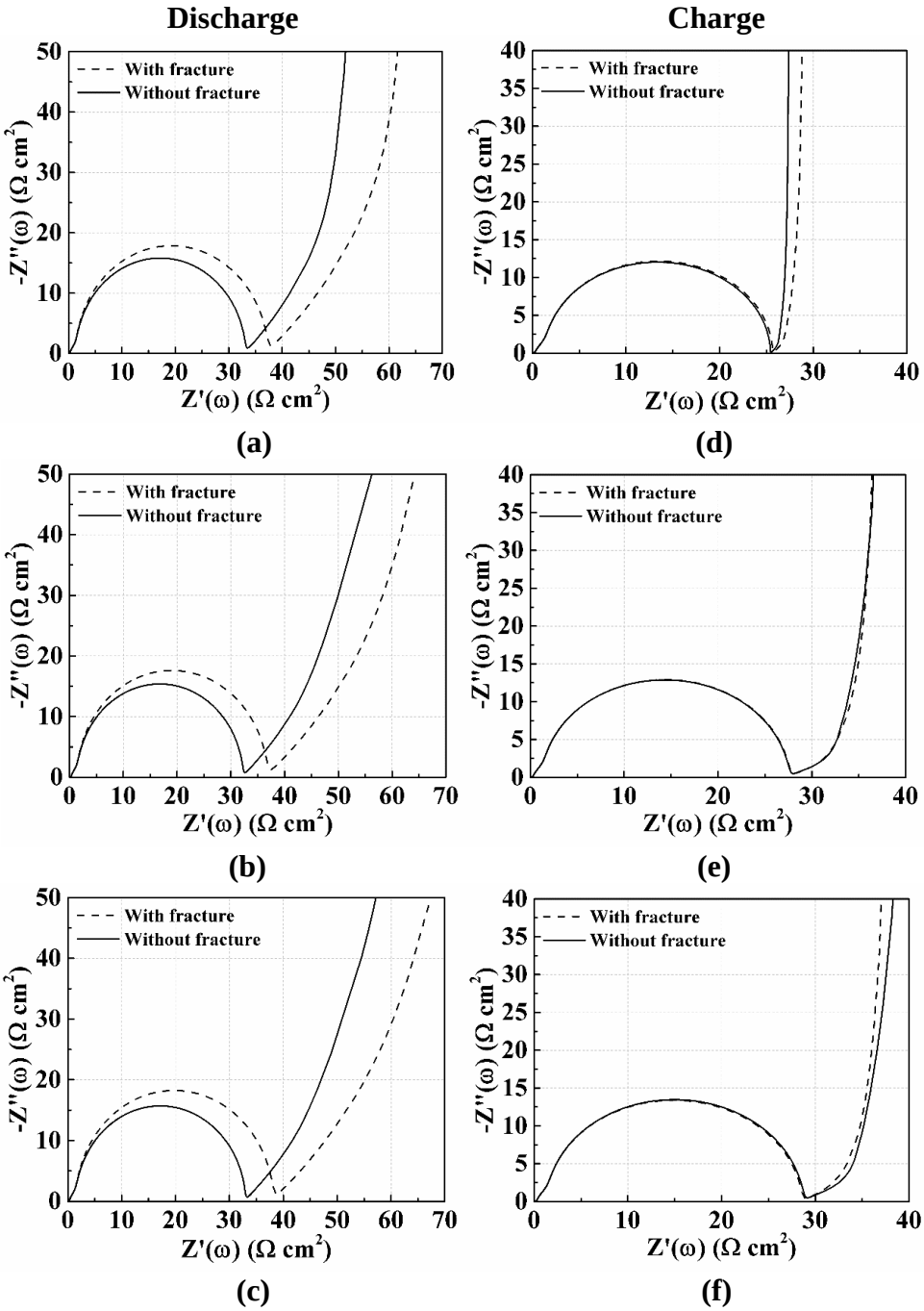

Figure 3.10. *(a - c) The impedance response after discharge for 2800 at the rate of 2C at T= 25^{0}C. The mean particle radius and specific area is 10 µm and 2000 cm^{-1}. The volume fraction of active material is (a) 35% (b) 40% and (c) 45%. (d – f) The impedance response after charge for 3000 seconds at the rate of 2C under T= 25^{0}C. The mean particle radius and specific area is 10 µm and 2000 cm^{-1}. The volume fraction of active material is (d) 35% (e) 40% and (f) 45%.*

The result of EIS during the charging process has been shown in Figure 3.10 (d) - (f). From the characteristic of the single particle EIS, the influence of damage strongly depends on the state of charge. After charge for 3000 seconds, the fracture has a positive effect on the solid phase diffusion resistance of the electrode with 45 % volume fraction of active material. On the other hand, the fracture almost has no influence for the electrode with 40 % volume fraction of active material, and has a negative effect to the electrode with 30 % volume fraction of active material. Unsurprisingly, similar to the single particle EIS, the fractures almost have no influence on the charge transfer resistance due to the position of the microcracks.

According to the results, although increasing the volume fraction of active material can increase the energy density (capacity) of the electrode, increasing the volume fraction of the active material also increases the influence of fracture to the charge transfer resistance. Rise in resistance decreases the power ability of electrodes. Moreover, the possible optimal design of electrodes with respect to the solid phase diffusion resistance has also become an important aspect of improving the maximum power of the battery.

3.2.2.3 Effect of Operating Temperature

According to recent work by An *et al*., the operating temperature has a significant influence on the formation of microcracks.[162] Figure 3.11 (a) - (c) and Figure 3.12 (a) - (c) show the concentration and fracture distribution in a single particle under different operating temperatures during discharging and charging process. The fracture density under different temperature has also been shown in Figure 3.6 (b) and (e). The

concentration profile shows that the effective diffusivity is low at lower temperatures. The low effective diffusivity causes high concentration gradient, low (discharge) /high (charge) surface concentration and high (discharge) /low (charge) center concentration. The diffusivity is mainly affected by the temperature and microcracks. Even without fracture, the solid state diffusion is low at low temperatures, which increase the concentration gradient between the surface and center of particles. The high concentration gradient under low temperature operation enhances the formation of fractures. With the larger fracture density in the particles, as shown in Figure 3.6 (b) and (e), the mechanical degradation further decreases the effective diffusivity. This cascading effect causes the formation of fracture to have a larger influence on the concentration distribution. The different levels of damage formation also reflect on the porous electrode impedance response. The impedance response of electrodes operating at different temperatures during the discharging process is as shown in Figure 3.11 (d) - (f). The influence of fracture to the solid phase diffusion resistance increases with the decrease of temperature because of the rise in fracture density.

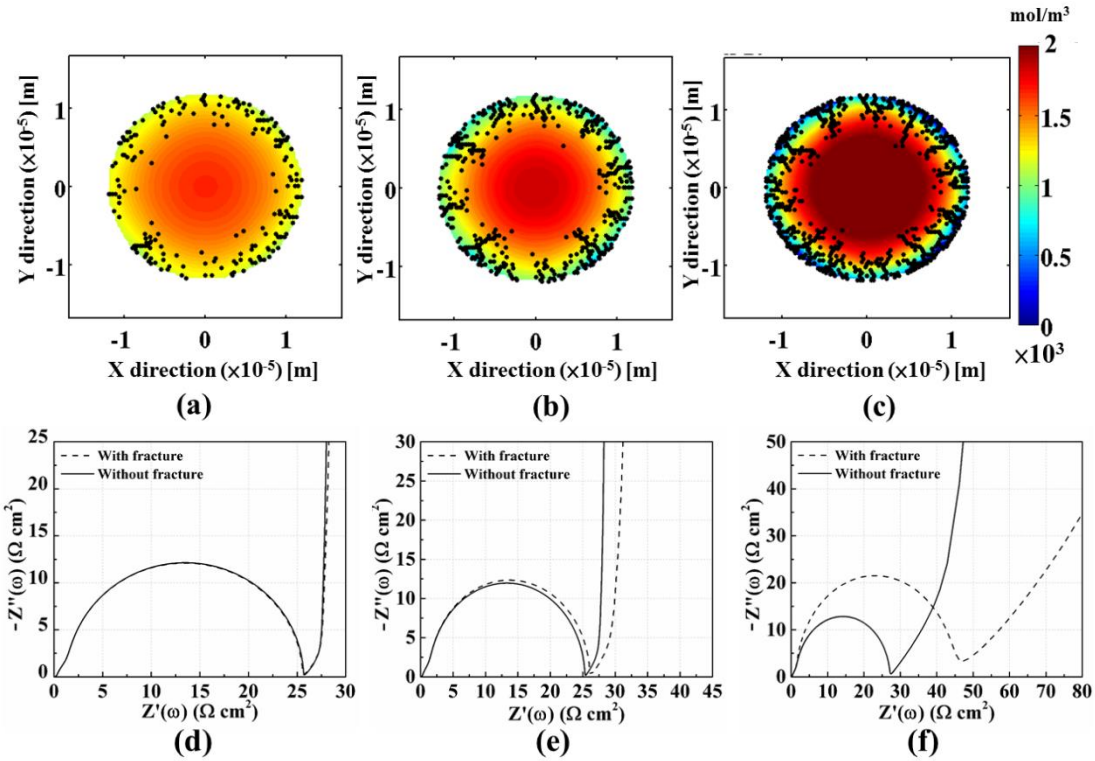

Figure 3.11. *(a – c) The fracture and concentration distribution of the particles with different temperature at (a) 37^0C (b) 25^0C (c) 10^0C under 2C discharge rate after discharge for 1800 second. The particle size is 12 μm. (d – f) The impedance response after discharge for 1800 seconds with 2C discharge rate at (d) 37^0C (e) 25^0C (f) 10^0C.*

The large fracture density makes the electrodes operating under low temperature to have a larger influence from the degradation. From Figure 3.11 (f), the fractures show much larger influence on the charge transfer resistance and solid phase diffusion resistance when T= 25℃. The increase of charge transfer resistance reflects the drop of surface concentration, which causes the decrease of exchange current density I_0. The large fracture density and reduced effective diffusivity increase the influence of damage on the solid phase diffusion resistance. When T= 37℃, the cracks almost have no influence to the EIS. It is because the fracture density is small and the distribution of damage is more scattered in nature, which makes the mechanical degradation have less effect on the concentration

and diffusivity. During the charging process, the influence of temperature to the fracture and EIS can be observed from Figure 3.12 (d) - (f). Similar to the discharging process, the increase of the fracture density also reflects on the EIS response, where the mechanical degradation has higher influence under low temperature. When T= 10℃, the fracture shows much larger effect than the other two temperatures. Besides the reason of the large fracture density, the low diffusion rate under low temperature makes the diffusion of ion even more difficult under the presence of fractures. The difficulty of ion transport enhances the effect of fracture on the resistance. We should also note that during the charging process, the fracture in the particle under low temperature can reach the surface of particles, which means it can have a larger influence of the surface concentration. This is also a reason why the damage has a much larger influence at T= 25℃ during the charging process. Similarly, when T= 37℃, the fractures almost have no influence to the EIS because of the reduced microcrack generation under high temperature operating condition. In general, the performances of LIBs decrease with temperature [163] because of the lower ion transport speed in the electrolyte and ion diffusion speed in the active material. From the porous electrode EIS discussed in this section, increased resistance due to the fracture may decrease the performance more than the one without the influence of fracture, especially the power ability of electrodes.

3.2.2.4 Effect of Charge/Discharge Rate

Figure 3.13(a) - (c) and Figure 3.14(a) - (c) shows the concentration and fracture distribution in a single particle under different discharging and charging rate. The fracture density under different discharge/charge rate is shown in Figure 3.6(c) and (f). From the

contour plots and fracture density, it is clear that under high discharge/charge rate, the particles have a higher concentration gradient. Under operation at different C-rate, because of the difference in concentration gradient inside the active particles, the fracture density is different after the same amount of discharge/charge time.

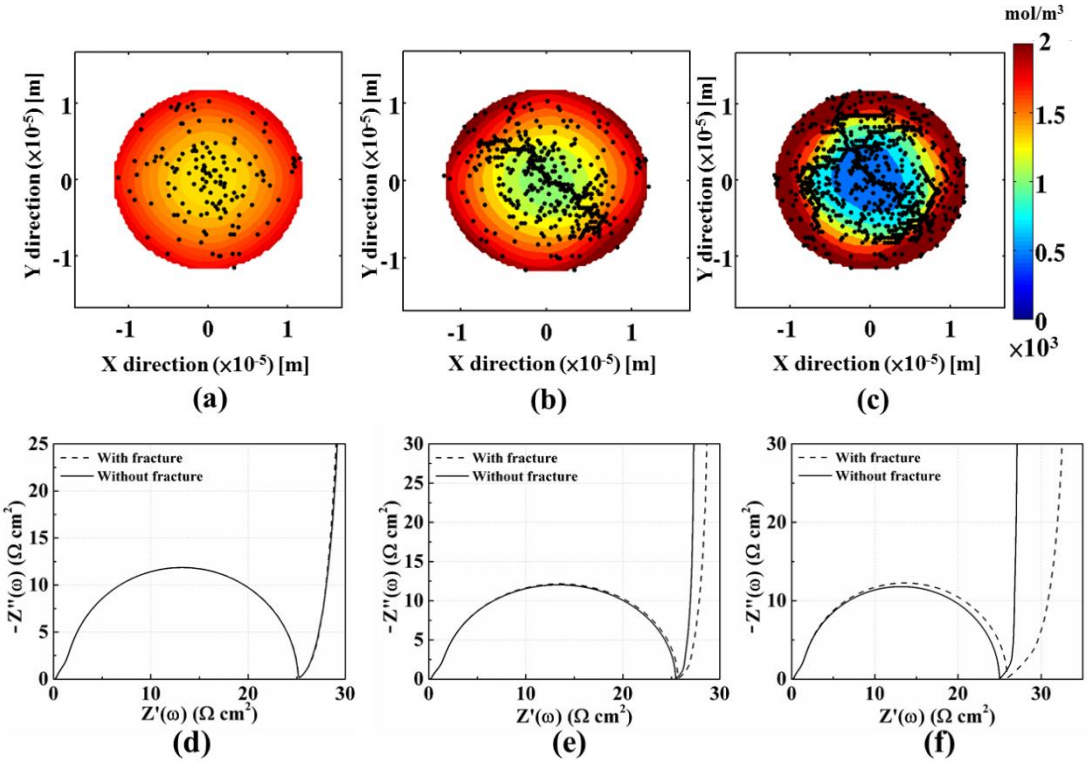

Figure 3.12. *(a – c) The fracture and concentration distribution of the particles with different temperature at (a) 37^0C (b) 25^0C (c) 10^0C under 2C charge rate after charge for 3000 seconds. The particle size is 12 μm. (d – f) The impedance response after charge for 3000 seconds with 2C charge rate at (d) 37^0C (e) 25^0C (f) 10^0C.*

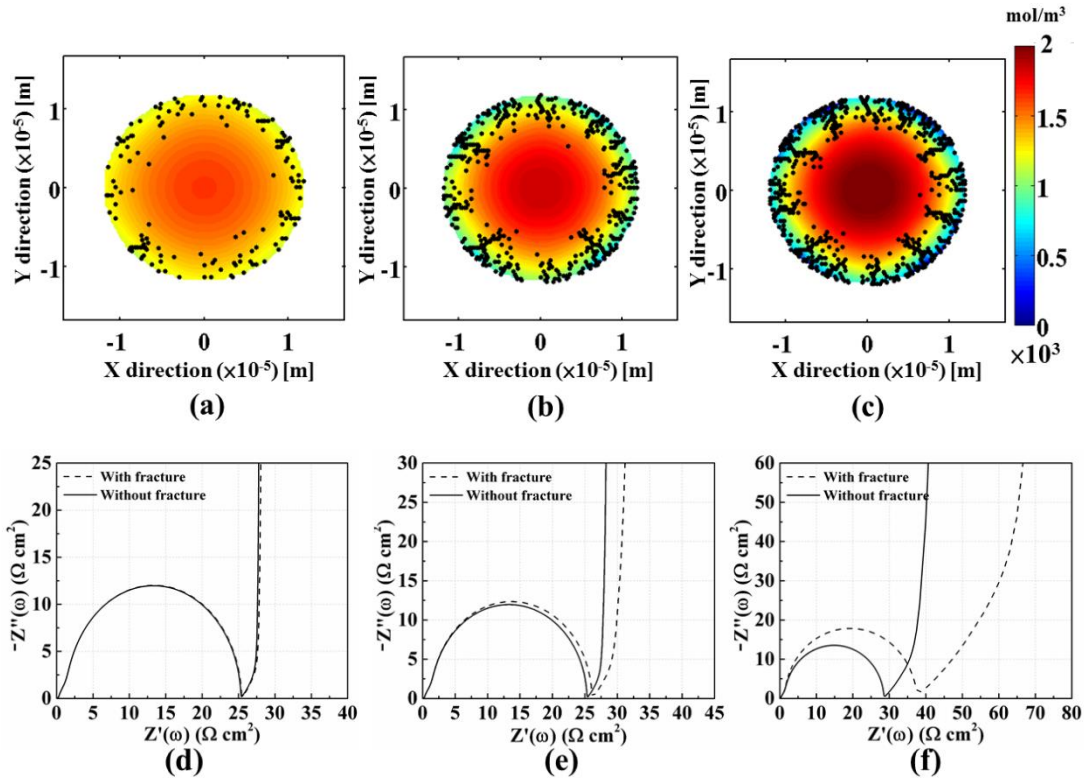

Figure 3.13*. (a – c) The fracture and concentration distribution of the particles with different discharge rate (a) 1C (b) 2C (c) 3C after discharge for 1800 seconds at T= 25^{0}C. The particle size is 12 μm. (d – f) The impedance response after discharge for 1800 seconds with (d) 1C (e) 2C (f) 3C rate of discharge at T= 25^{0}C.*

With a high rate of delithiation and lithiation, the concentration gradient inside the particles is high due to the high current density on the surface. The high concentration gradient enhances the formation of fracture. On the other hand, reduced damage formation is observed under low discharge/charge rate because of the lower concentration gradient. The microcracks make the ion even harder to transport between center and surface, which enhances the drop (discharge) /accumulation (charge) of surface concentration.

Figure 3.13(d) - (f) shows the influence of fracture on the porous electrode EIS. The influence of fracture is higher in the electrode which discharge at the high rate because of

the fracture density and ion depletion speed is high compared to 2C and 1C discharge rate. The difference in charge transfer resistance shows the increase in microcrack formation and the depletion of surface concentration under high C-rate. From the change of solid phase diffusion resistance, we can see the influence from the effective diffusivity and the value of $\left(-\partial U/\partial c_s\right)$, which has been affected by the fracture and surface concentration respectively. At 1C discharge rate, the fractures almost have no influence on the EIS, which can be explained from the contour plot of concentration and microcrack distribution. The damage in the particle discharged under 1C is more diffused and the fracture density bonds are small compared to higher discharge rate. Similarly, during the charging process, the fracture has less influence to the EIS under low charge rate as shown in Figure 3.14 (d) - (f). Under high discharge/charge rate, the influence of degradation is much larger than that at low C-rate. The reason is similar to the influence of temperature. During discharging process, the high fracture density and high depletion/accumulation speed of ion on the surface of the particle, under high C-rate operations, increases the influence of mechanical degradation.

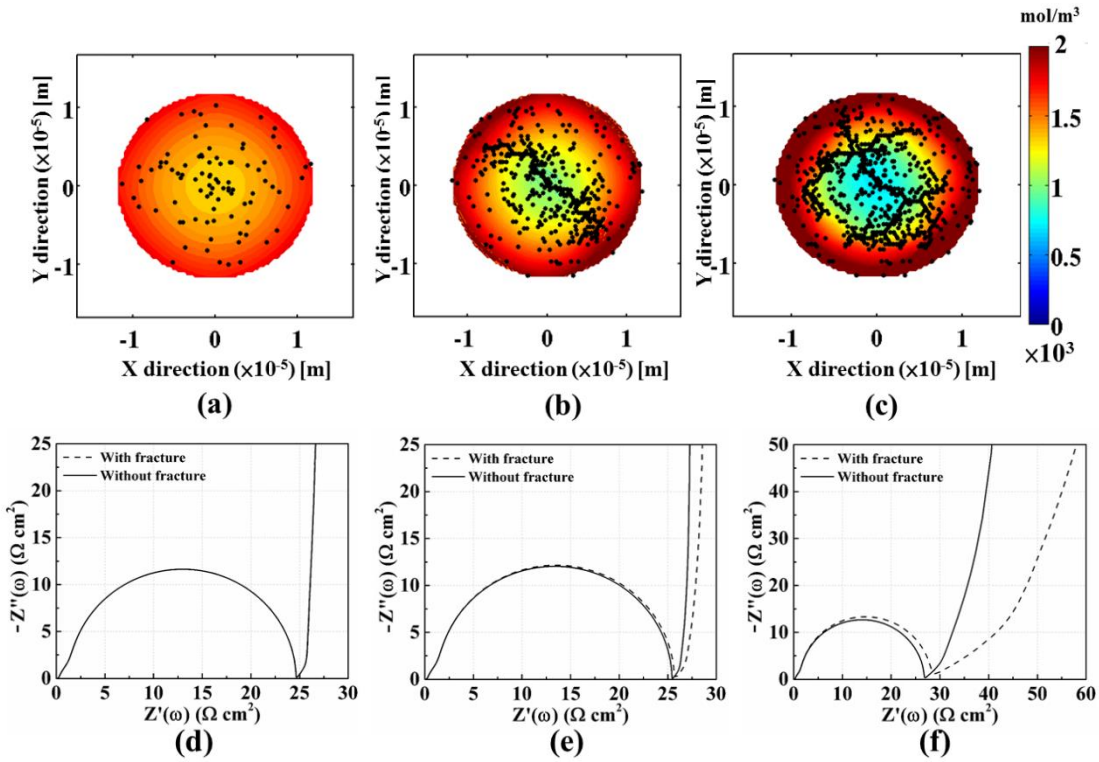

Figure 3.14. *(a – c) The fracture and concentration distribution of the particles with different charge rate (a) 1C (b) 2C (c) 3C after charge for 3000 seconds at T= 25^{0}C. The particle size is 12 μm. (d – f) The impedance response after charge for 3000 seconds with (d) 1C (e) 2C (f) 3C charge rate at T= 25^{0}C.*

According to Figure 3.14 (d) - (f), the C-rate has less influence on the charge transfer resistance during charging process because of the position of the crack, where most of the damage is concentrated at the center of the particles. In other words, since mechanical degradation during the charging process has less influence on the surface concentration, it has less influence on the exchange current density I_0 as well. However, during the high charging rate (3C), since the crack can reach the surface of the particles, it may increase the influence on the surface concentration. The effect of the surface concentration makes the fracture have larger and obvious influence on the charge transfer resistance.

Charge/discharge under high C-rate increases the capacity loss because of the limitation of lithium ion transport in the electrolyte and diffusion in the active material. From the results, it is evident that the existence of fracture further increases the diffusion resistance inside the electrode, which may cause more capacity loss. With the consideration of both temperature and C-rate, Figure 3.15 shows the plots of charge transfer resistance under different C-rate and temperature after 1800 second of the discharging process. From the results, it can be concluded that the damage has a higher influence on the charge transfer resistance when operating under low temperature and high C-rate. This concept of phase map can be useful in the mechano-electrochemical design of LIB electrodes.

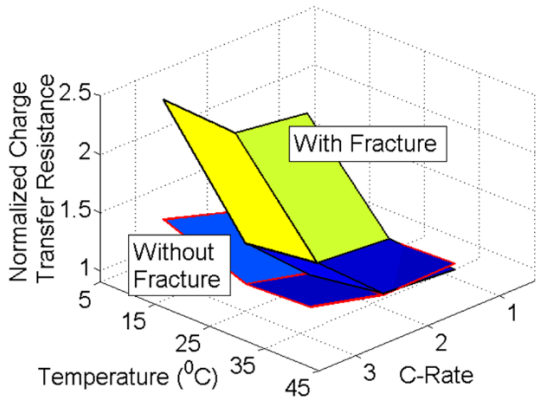

Figure 3.15. *The plots of normalized charge transfer resistance under different temperature (10^0C - 37^0C) and discharge rate (1C - 3C) after discharge for 1800 seconds.*

3.3 Conclusions

By coupling the lattice spring based damage model with the impedance model, the impact of mechanical degradation on the electrode impedance response has been investigated. Specifically, the effect of fracture formation and propagation due to diffusion induced stress on the charge transfer and solid phase diffusion resistance in the LIB electrode particle has been illustrated. Furthermore, the influence of active particle size distribution, operating temperature and discharge/charge rate on the impedance behavior has been discussed.

The results suggest a significant difference in the impedance behavior due to the variation of the damage evolution pattern for different operational conditions. During the delithiation process, more cracks develop close to the periphery of the particle. During lithiation, due to the tensile force acting at the center, more microcracks in the interior of the particle are observed. The cracks at the peripheral region affect the surface concentration significantly more than those locate near the center of the active particle. Subsequently, the microcracks have a larger influence on the impedance response during delithiation than in the lithiation process. It has also been observed that fracture formation around the particle center has less effect on the surface concentration and solid phase diffusion resistance. The influence of electrode microstructure on the impedance response has been demonstrated in terms of the active particle volume fraction and particle size distribution. The charge transfer resistance is primarily affected due to the change in active material volume fraction. The effective diffusivity and solid state transport properties for

an active particle with fracture can be estimated from the slope of the long tail of the impedance curve, which is left as a future exercise.

For the operating conditions taken into consideration, the porous electrode impedance response suggests that the diffusion induced damage has a larger influence on the resistance under low temperature and high discharge/charge rate operation. The higher concentration gradient, observed at both low temperature and high C-rate conditions, is the main reason behind the formation of enhanced mechanical degradation. In this study, we showed that the impact of diffusion induced damage on the impedance response is an important aspect and needs to be considered, especially at high charge/discharge rates and low temperatures. By controlling the operating conditions and the electrode microstructure design, the deleterious impact of mechanical damage on the electrode performance may be ameliorated, which will be considered in a future study.

CHAPTER IV

SCALING RELATIONS FOR INTERCALATION INDUCED DAMAGE IN ELECTRODES

Scaling analysis and reduced order models are often used to reduce the complexity of governing equations in simulation and generalize material properties, which can reduce the computational cost. The scaling analysis has been used to reduce the complexity of the governing equations of vanadium redox flow batteries [164] and generalize the expression of the transport properties of $LiPF_6$-based electrolytes [69]. The reduced order models of the lithium-ion battery also have been introduced to alleviate the computational cost [165-167]. For the damage evolution in materials, scaling analysis has been used to interpret and better understand damage evolution in brittle [168] and ductile [169] materials. To simulate microcrack formation using lattice-based models, the continuum media were described as a set of elastic bonds with randomly distributed failure threshold [125]. Even though fracture surfaces for different brittle materials are never smooth, a universality in the roughness exponent exists [127, 170]. Qualitative estimation of the universal fracture surface roughness exponent can be conducted using lattice-based models [128].

---

*Reprinted with permission from "Scaling Relations for Intercalation Induced Damage in Electrodes" by C. -F. Chen, P. Barai, K.Smith, and P. P. Mukherjee, 2016, Electrochimica Acta, **204**, 31, Copyright 2015, Elsevier.

To the best of our knowledge, no scaling methodology for damage evolution in LIB electrodes has been established. Because the formation of microcracks inside the active particle is affected by the strain energy, which is induced by the lithium diffusion and is proportional to the concentration gradient inside the active particle, the correlation between concentration gradient, cumulative strain energy (CSE), and microcrack formation is worth studying. Moreover, although the microcrack formation has been successfully predicted from our previous work [24], the computational expense is still an obstacle we need to overcome. Reduced order models obtained from data-driven scaling analysis of diffusion induced damage can significantly decrease the computational cost.

In this study, systematic simulations have been implemented by using the diffusion induced damage model developed by Barai and Mukherjee [24] to probe the concentration distribution, CSE, and microcrack formation during the single discharge process and drive cycles. Because the microcrack formation is strongly dependent on temperature [171], delithiation/lithiation rate, and particle size [23, 172], these operating conditions are chosen for our numerical simulation experiments. According to the simulation results from the single discharge process, the relations between (i) CSE and concentration gradient and (ii) CSE and microcrack formation can be found as a function of particle size and operating condition (*i.e.,* temperature and C-rate) by using the data-driven scaling method (see Figure 4.1 (a)). The relations can reduce the complexity of the diffusion induced damage model developed by Barai and Mukherjee [24]. The relations are further implemented in the electrochemical model of lithium-ion batteries to study the influence of mechanical damage on the cell performance. In addition, the scaling laws, developed using constant

current discharge numerical simulation experiments, are validated versus the higher order model for drive cycle charge/discharge profiles representing a more complex operating condition. From the investigation of damage evolution during the drive cycle, we observe that besides delithiation/lithiation rate, temperature, and particle size, the drive pattern also has an influence on the microcrack formation.

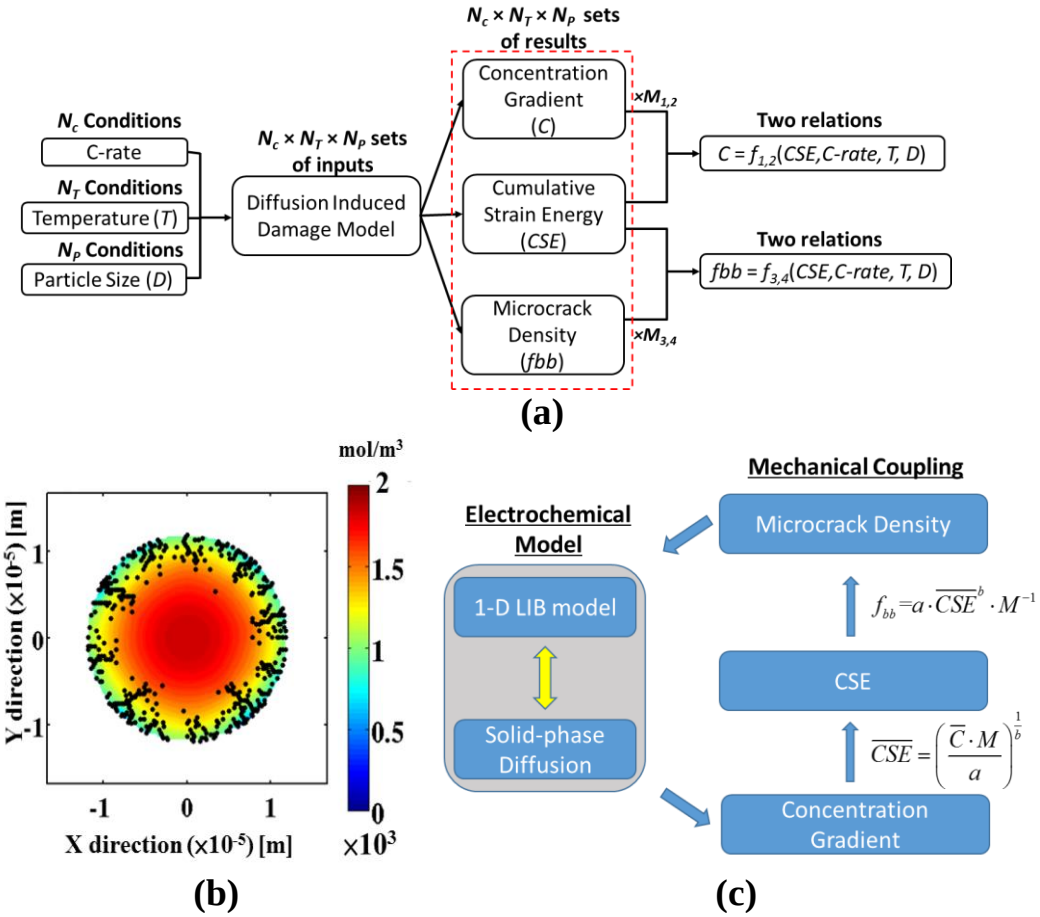

Figure 4.1. *(a) The schematic diagram of data-driven approach toward reduced order relations. With the scaling factor M, the massive number of results can be reduced to four relations. (b) Example of microcrack formation inside a representative active particle, which includes the microcrack and concentration distribution. (c) Schematic diagram for the electrochemical-mechanical coupled model.*

4.1 Method and Theory

4.1.1 Diffusion Induced Damage

The lithium diffusion inside the active particle induces the displacement of atoms and causes the accumulation of strain energy inside the material. When the strain energy stored in the material exceeds its fracture threshold, the microcracks form. The externally applied diffusion induced load is a function of the concentration gradient. Therefore, the CSE, which is the total energy released due to the evolution of the microcrack, is also proportional to the concentration gradient inside the active particle. Since the formation of microcracks hinders the diffusion of lithium inside the active particle, the effective solid phase diffusivity decreases with the increase of microcrack density (f_{bb}). The decrease of effective solid phase diffusivity further increases the concentration gradient inside the active particle. The increase of concentration gradient leads to additional strain energy that forms more microcracks. The cascade process causes the microcrack propagation and capacity fade of the cell. According to the mechanism of microcrack formation, it is worth finding the relation between (i) concentration gradient and CSE and (ii) CSE and microcrack density. Moreover, because the microcrack formation is affected by the C-rate (reaction current density), temperature T, and particle size D [23], the relations between concentration gradient, CSE, and microcrack should also be a function of C-rate, temperature, and particle size. In this study, we used a stochastic methodology of simulate the diffusion induced damage developed by Barai and Mukherjee [24] to probe the concentration gradient, cumulative strain energy, and microcrack density during the delithiation process of active particles. The detail of this model is described in section

3.1.2. Figure 4.1 (b) shows an example of simulation results from the diffusion induced damage model. Concentration and microcrack distribution are shown in the representative active particle. The microcrack density can be approximately defined as the ratio between the broken bonds (black dots) and the total number of springs inside the particle. As shown in Figure 4.1 (b), during the delithiation process, the microcrack forms on the surface of the particle due to the large concentration gradient. The parameters used in the diffusion induced damage model are listed in Table 4.1.

Table 4.1. List of parameters used to solve the diffusion induced damage model (see Ref. [24]).

Name	Units	Value
Expansion coefficient (Γ)	m^3/mol	1.14×10^{-6}
Diffusion coefficient ($\underset{\sim}{D}$)	m^2/s	3.9×10^{-14}
Anode particle surface area (S)	m^2	0.7824
Axial direction spring stiffness	kN/m	88.1717
Shear direction spring stiffness	kN/m	11.6688

4.1.2 Dimensionless Parameters

In order to better correlate the relation between CSE, concentration gradient, and microcrack density, the dimensionless radius $\overline{R}$, temperature $\overline{T}$, cumulative strain energy $\overline{CSE}$, and concentration gradient $\overline{C}$ are introduced as follows

$$\overline{R} = \frac{R}{R_{ref}},\ R_{ref} = 12.5\ \mu\text{m} \tag{4.1}$$

$$\bar{T} = \left(\frac{T}{T_g} - 1 \right), \; T_g = 238 \; K \tag{4.2}$$

$$\overline{CSE} = \frac{CSE}{E_{threshold}}, \; E_{threshold} = 2 \; \mathrm{J/m^2} \tag{4.3}$$

$$\bar{C} = \frac{C_{avg} - C_{surf}}{C_{\max}}, \; C_{\max} = 31833 \; \mathrm{mol/m^3} \tag{4.4}$$

where T_g is the glass transition temperature of the binder, $E_{threshold}$ is the mean fracture threshold energy, C_{avg} is the average bulk concentration in the particle, C_{max} is the maximum bulk concentration one particle can store, and C_{surf} is the average surface concentration in the particle. As mentioned, the relations between CSE, concentration gradient, and microcrack density strongly depend on temperature, C-rate, and particle size. Therefore, one possibility for the relations between CSE, concentration gradient, and microcrack can be assumed as Eqs. (4.5) and (4.6). The microcrack density in Eq. (4.5) is defined as the ratio between the broken springs and the total number of springs inside the lattice network.

$$\bar{C} \text{ and } Microcrack \; Density = a \cdot \overline{CSE}^{b} \cdot M^{-1} \tag{4.5}$$

where M is the scaling factor, which is based on the temperature, particle radius, and C-rate.

$$M = \bar{T}^{c} \cdot \bar{R}^{d} \cdot \left(\text{C-rate} \right)^{e} \tag{4.6}$$

The schematic diagram of finding the relation between CSE, concentration gradient, and microcrack density (Eq. (4.5)) is as shown in Figure 4.1 (a). With the diffusion induced damage model described in the previous subsection, one set of operating conditions (*i.e.*, *the* combination of C-rate, temperature, and particle size) can have one set of results, which includes CSE, concentration gradient, and microcrack density. By conducting a

systematic study of variable possible operating conditions (see Table 4.2.), we can get a map of operating conditions and results. By tuning the scaling factor M (Eq. (4.6)), the massive sets of results can converge to four relations, which can be expressed by Eqs. (4.5) and (4.6). The four relations are the relation between CSE and concentration gradient when (i) $T > 0°C$ (f_1) and (ii) $T \leq 0°C$ (f_2) and the relation between CSE and microcrack density when (iii) $T > 0°C$ (f_3) and (iv) $T \leq 0°C$ (f_4).

Table 4.2. Combinatorial matrix of operating and drive cycle conditions.

	Factor	**Conditions**
Single Delithiation	Temperature	[-10, -5, 0, 10, 20, 30] °C
	C-rate	[1, 2, 3, 4, 5] C
	Particle Diameter	[5.5, 6, 8.5, 12.5] μm
	(Total: 120 sets of operating conditions)	
Drive Cycles	Temperature	[-10, 0, 20] °C
	Particle Diameter	[6, 8.5, 12.5] μm
	Drive Pattern	[HEV, PHEV, BEV]
	(Total: 27 sets of drive cycle conditions)	

4.2 Results and Discussion

4.2.1 Scaling Analysis of Delithiation Process

In this section, we present the correlation between CSE, concentration gradient, and microcrack density during a single delithiation process under different operating conditions with varied particle size. A series of simulations, which used the high order diffusion induced damage model, were implemented to tune the parameters in Eqs. (4.5) and (4.6). The simulated operating conditions and particle sizes are listed in Table 4.2. The 1C delithiation rate corresponds to operation at 1.656 A (i = 2.11 A/m^2). The concentration distribution, CSE, and number of microcracks were recorded whenever the

microcrack formed. In the single delithiation process, the applied current is maintained constant. Under the same applied current, the delithiation process was stopped when the surface concentration reached zero. In this study, we considered an electrode-only model, specifically for a representative anode active particle. Therefore, all the parameters in the following diffusion induced damage model refer to a typical graphite active material.

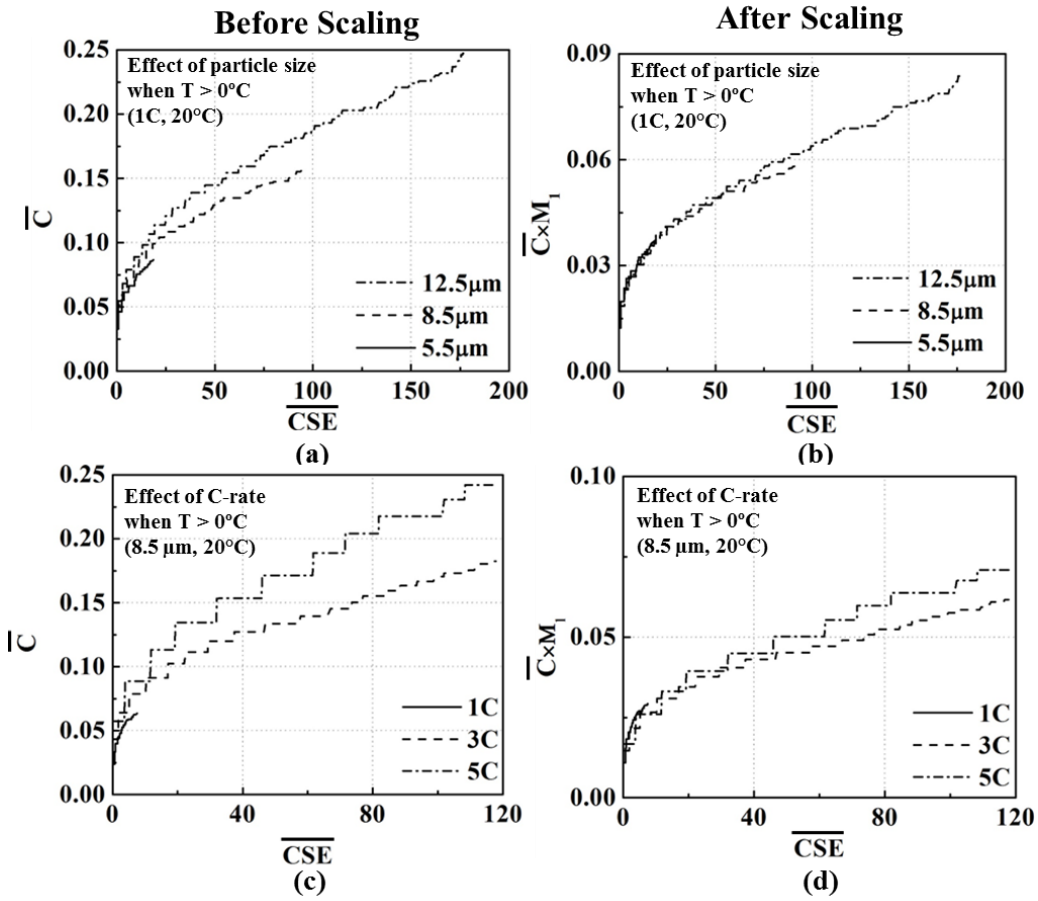

Figure 4.2. *Relation between cumulative strain energy and concentration gradient for (a) different particle sizes at 1 C-rate and 20°C before multiplying by the scaling factor; (b) different particle sizes at 1 C-rate and 20°C after multiplying by the scaling factor; (c) different C-rates at 20°C before multiplying by the scaling factor with the particle diameter of 8.5 µm; and (d) different C-rates at 20°C after multiplying by the scaling factor with the particle diameter of 8.5 µm.*

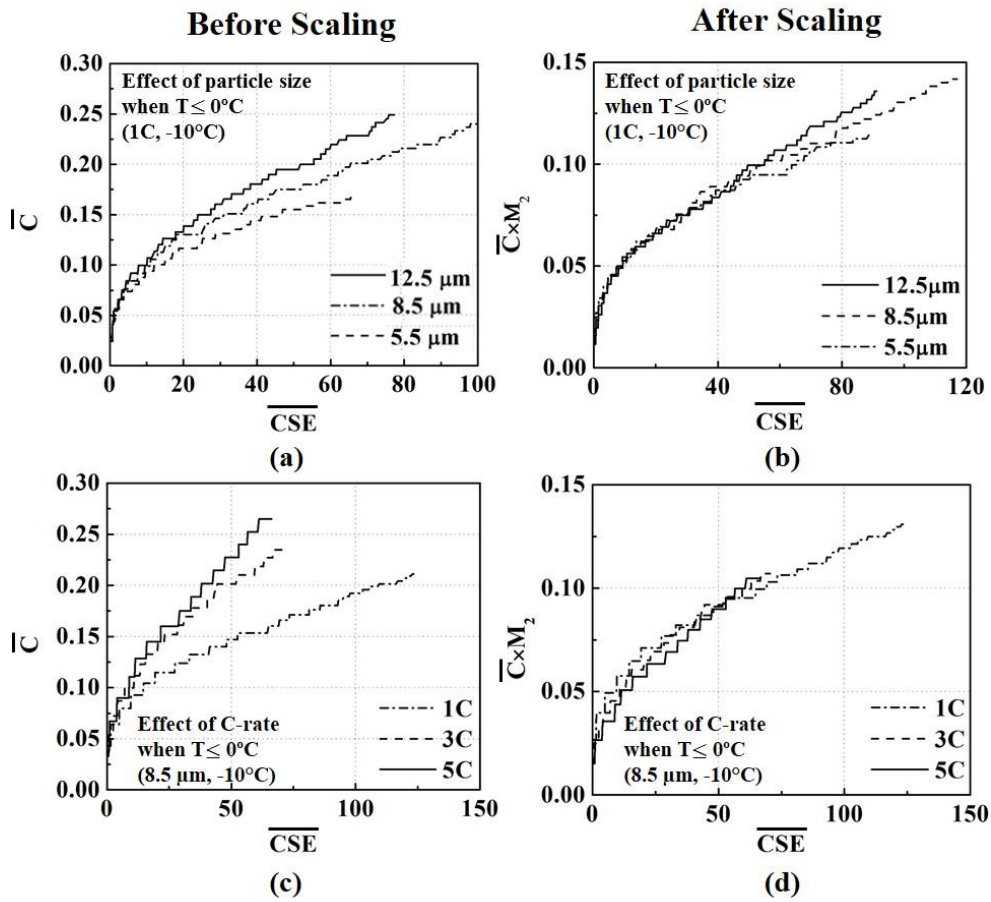

Figure 4.3. *Relation between cumulative strain energy and concentration gradient for (a) different particle sizes at 1 C-rate and -10°C before multiplying by the scaling factor; (b) different particle sizes at 1 C-rate and -10°C after multiplying by the scaling factor; (c) different C-rates at -10°C before multiplying by the scaling factor with the particle diameter of 8.5 µm; and (d) different C-rates at -10°C after multiplying by the scaling factor with the particle diameter of 8.5 µm.*

4.2.1.1 Cumulative Strain Energy and Concentration Gradient

As mentioned in the previous section, due to the imbalance between the delithiation rate and solid phase diffusion rate, there is a concentration gradient inside the active particle that generates strain energy inside the active material. The CSE is calculated by summing the strain energy released due to the microcrack formation inside the active

particle. The relation between CSE and concentration gradient can be affected by the temperature, C-rate, and particle size.

Figure 4.2 (a) and Figure 4.3 (a) show the influence of particle size on the relation between CSE and concentration gradient when T = 20°C and -10°C. The 5.5 μm particle has a lower maximum CSE because it has less microcrack formation compared to larger particles. From the results, we can observe that, with the same CSE, the concentration gradient increases with the particle size. The reason is because the length for lithium to diffuse from the center to the surface is longer in larger particles. The larger concentration gradient leads to faster lithium depletion at the particle surface [153]. Figure 4.2 (c) and Figure 4.3 (c) show the influence of delithiation rate (*i.e.,* C-rate) on the relation between CSE and concentration gradient when T = 20°C and -10°C. Similarly, we can observe that the concentration gradient increases with the C-rate, which is due to the high lithium depletion rate on the surface of particles under high C-rate. Figure 4.4 presents the effect of temperature. From the results, under the same CSE, the concentration gradient increases with a decrease in operating temperature. The influence of temperature is mainly on the solid phase diffusivity. According to Eq. (3.18), the solid phase diffusivity decreases with temperature. The decrease of diffusivity further hinders the diffusion of lithium from center to surface and hence increases the concentration gradient.

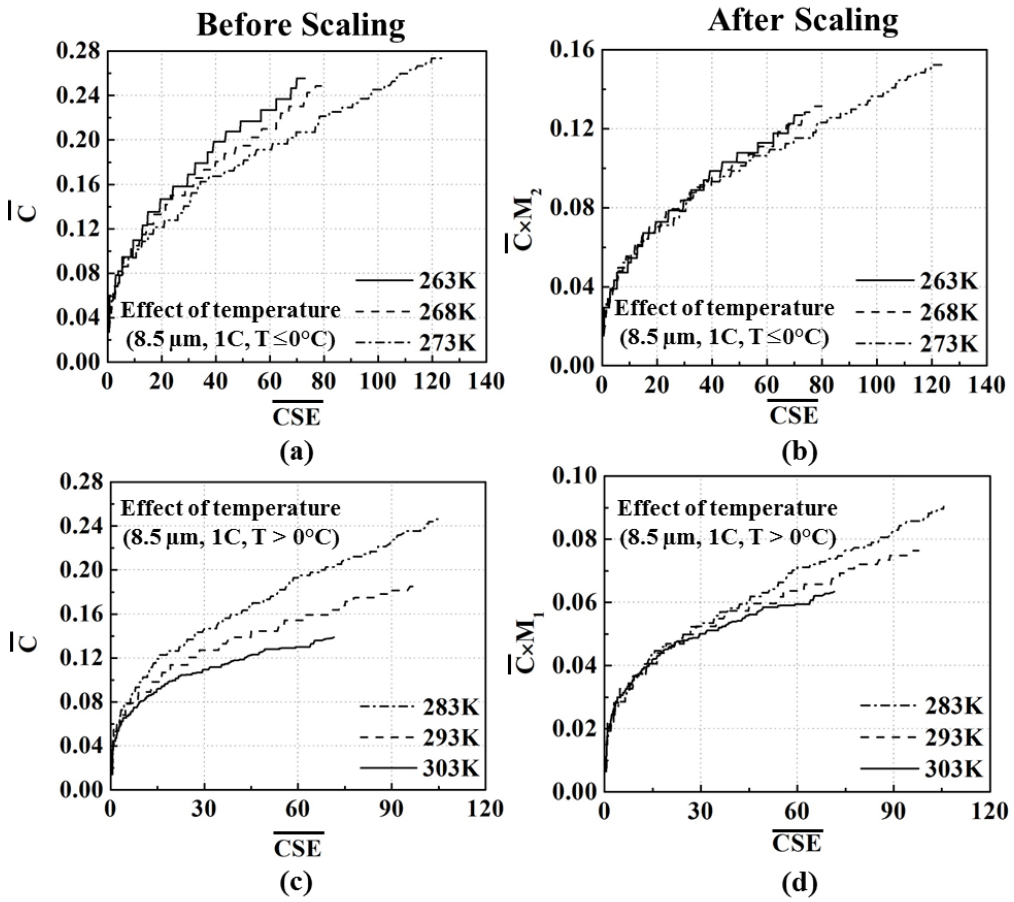

Figure 4.4. *Relation between cumulative strain energy and concentration gradient for different operation temperatures at 1 C-rate with the particle diameter of 8.5 µm. (a) T ≤ 0°C, before multiplying by the scaling factor. (b) T ≤ 0°C, after multiplying by the scaling factor. (c) T > 0°C, before multiplying by the scaling factor. (d) T > 0°C, after multiplying by the scaling factor.*

With this systematic study, we found that if we multiply the concentration gradient with a scaling factor *M*, the data converge as shown in Figure 4.2, Figure 4.3, and Figure 4.4. The scaling factor *M* for the relation of CSE and concentration gradient under different temperatures, C-rates, and particle sizes are listed in Table 4. Figure 4.2 (b) and (d) suggests that the data from different particle sizes and C-rates converge after multiplying a scaling factor M_1 to the concentration gradient when T= 20°C. Similarly,

under subzero temperature, the data converge after multiplying a scaling factor M_2 to the concentration gradient as shown in Figure 4.3 (b) and (d). The effect of temperature also can be generalized by the scaling factor as suggested in Figure 4.4 (b) and (d). It is worth noting that the scaling factor is different when $T > 0$°C and $T < 0$°C as shown in Table 4.3. From the scaling factor, we can infer the contribution of C-rate, temperature, and particle size to the relation between CSE and concentration gradient from the order of C-rate, temperature, and particle size. The higher the order, the larger the influence. Because the variation of solid phase diffusivity (dD_s/dT) is higher when $T > 0$°C (M_1) compared to $T \leq 0$°C (M_2), according to Eq. (3.18), the temperature has a larger influence on concentration gradient when $T > 0$°C (M_1) compared to $T \leq 0$°C (M_2). Similarly, due to the low solid phase diffusivity, the variation of the C-rate has a larger influence on the concentration gradient when $T \leq 0$°C (M_2) compared to $T > 0$°C (M_1).

Table 4.3. *Scaling constructs in Eq. (4.5)**.***

Relation	*a*	b	*M*
$\overline{CSE}$ and $\overline{C}$ (T > 0°C)	0.0061	0.465	$M_1 = \left[\frac{C\text{-}Rate \times \overline{R}}{\overline{T}^2}\right]^{-0.28}$
$\overline{CSE}$ and $\overline{C}$ (T ≤ 0°C)	0.0072	0.275	$M_2 = \left[\frac{C\text{-}Rate \times \overline{R}}{\overline{T}}\right]^{-0.28}$
$\overline{CSE}$ and *Microcrack Density* (T >0°C)	0.0015	0.657	$M_3 = \left[\frac{C\text{-}Rate \times \overline{R}}{\overline{T}^2}\right]^{0.14}$
$\overline{CSE}$ and *Microcrack Density* (T ≤ 0°C)	0.0016	0.8443	$M_4 = \left[\frac{C\text{-}Rate^2 \times \overline{R}}{\overline{T}}\right]^{0.14}$

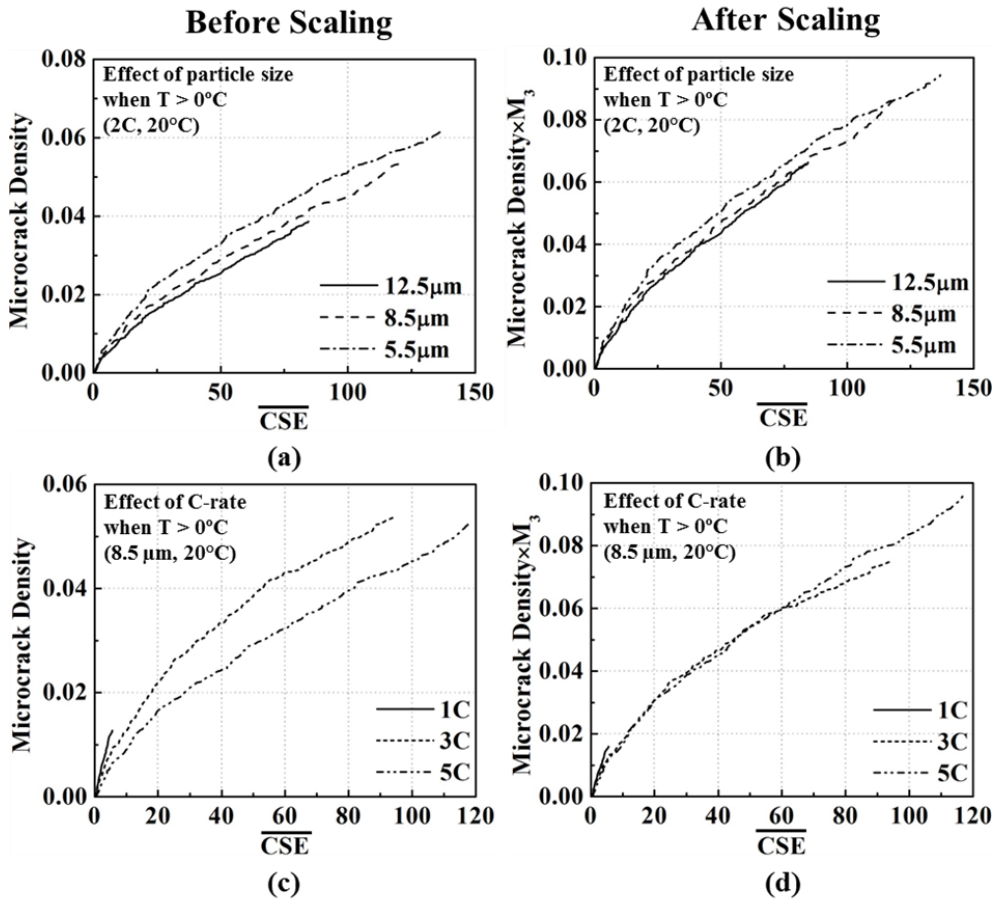

Figure 4.5. *Relation between cumulative strain energy and microcrack density for (a) different particle sizes at 2 C-rate and 20ºC before multiplying by the scaling factor; (b) different particle sizes at 2 C-rate and 20ºC after multiplying by the scaling factor; (c) different C-rates at 20ºC before multiplying by the scaling factor with the particle diameter of 8.5 μm; and (d) different C-rates at 20ºC after multiplying by the scaling factor with the particle diameter of 8.5 μm.*

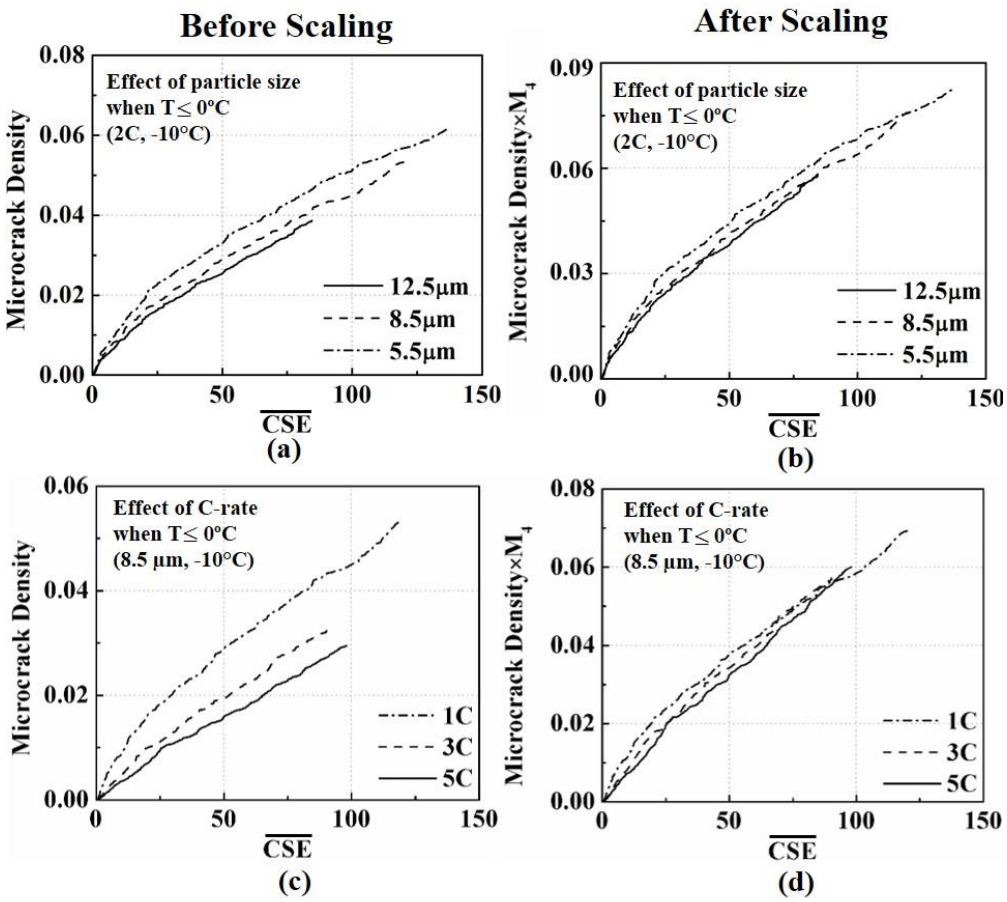

Figure 4.6. *Relation between cumulative strain energy and microcrack density for (a) different particle sizes at 1 C-rate and -10°C before multiplying by the scaling factor; (b) different particle sizes at 1 C-rate and -10°C after multiplying by the scaling factor; (c) different C-rates at -10°C before multiplying by the scaling factor with the particle diameter of 8.5 μm; and (d) different C-rates at -10°C after multiplying by the scaling factor with the particle diameter of 8.5 μm.*

4.2.1.2 Cumulative Strain Energy and Microcrack Density

From the mechanism of microcrack formation, when the strain energy exceeds the threshold energy, the microcrack will form. Therefore, the microcrack inside the active particle should be proportional to the CSE. In this subsection, we present the relation between CSE and microcrack density with the same approach of finding the relation

between CSE and concentration gradient. Figure 4.5 (a) and Figure 4.6 (a) show the effect of particle size on the relation between CSE and microcrack density under different temperature. In Figure 4.5 (a), we can see that the particle size of 12.5 μm has the smallest maximum microcrack density compared to the other two particle sizes. This is because the long diffusion distance for lithium and the resultant high concentration gradient decrease the discharge time (*i.e.*, the discharge stops when the surface concentration reaches zero). Moreover, the microcrack density decreases with the increase of particle size when the CSE is the same. This result can be explained from the perspective of the concentration gradient and the distribution of strain energy. As mentioned in the previous section, the bonds break when the strain energy exceeds the threshold energy. In other words, if the strain energy is below the threshold energy, the bond will sustain. CSE is defined as the summation of energy released due to the rupture of the connecting bonds. The cumulative strain energy can be written as,

$$CSE = \frac{1}{2}\sum_{e=1}^{n_{bb}} \vec{f}_e \cdot \vec{u}_e \approx \frac{1}{2} k_a \cdot \Omega \cdot (\Delta c) \cdot l \cdot u_a \cdot n_{bb} \tag{4.7}$$

where n_{bb} is the total number of broken bonds, and $\vec{f}_e$ and $\vec{u}_e$ signify the force and displacement in each of the broken bonds, respectively. Also, k_a, Ω, l and u_a denote axial stiffness, partial molar volume, length of each element, and axial displacement, respectively. These four parameters and variables can be approximated to remain almost constant. The last variable Δc signifies the concentration gradient, which differs based

on particle size, operating condition, and ambient temperature. Let's denote the cumulative strain energy for a large particle as CSE_l and for a small particle as CSE_s.

$$CSE_l = \frac{1}{2} k_a \cdot \Omega \cdot (\Delta c)_l \cdot l \cdot u_a \cdot n_l \text{ and } CSE_s = \frac{1}{2} k_a \cdot \Omega \cdot (\Delta c)_s \cdot l \cdot u_a \cdot n_s \quad (4.8)$$

Here, $(\Delta c)_l$ and $(\Delta c)_s$ correspond to the concentration gradient for large and small particles, respectively. Similarly, n_l and n_s signify the number of broken bonds for the larger and the smaller particles, respectively. For this particular case, where cumulative strain energy released from the larger and smaller particle is same, we can write $CSE_l = CSE_s$, comparing it with the previous equation, $(\Delta c)_l \cdot n_l = (\Delta c)_s \cdot n_s$. Concentration gradient in a larger particle is greater in magnitude than the concentration gradient for a small particle, which implies that $(\Delta c)_l > (\Delta c)_s$. As a result, $n_l < n_s$, which implies that for a constant value of CSE, microcrack density in the larger particle is less than the microcrack density within the smaller particle. Figure 4.5 (c) and Figure 4.6 (c) show the influence of C-rate on the relation between CSE and microcrack density when T = 20°C and -10°C. Similar to Figure 4.5 (a) and Figure 4.6 (a), under the same CSE, the microcrack density decreases with the increase of the C-rate, which is similar to the case for different particle size. During discharge under a high C-rate, due to the larger concentration gradient, smaller microcrack density will be observed under the constraint of constant CSE. Therefore, the particle discharge under high C-rate has less microcrack density compared to the one discharge under low C-rate. Figure 4.7 (a) and (c) shows the

influence of temperature on the relation between CSE and microcrack density. The results suggest that the microcrack density decreases with decreasing temperature under the same CSE, which can also be explained by the variation in the concentration gradient. The concentration gradient in the particle operating at low temperature is much higher than the one operating at high temperature. As a result, under constant cumulative strain energy, particles operating at low temperature will have smaller microcrack density as compared to active particles at higher ambient temperature conditions.

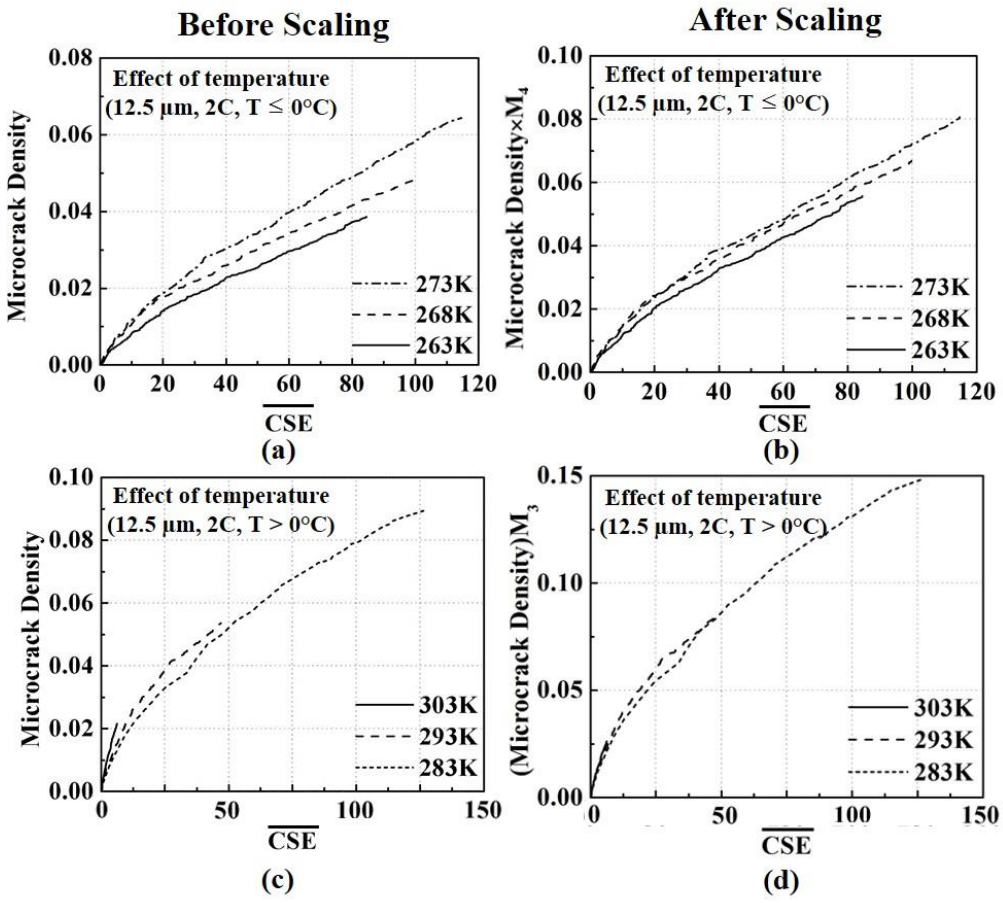

Figure 4.7. *Relation between cumulative strain energy and concentration gradient for different operation temperatures at 2 C-rate with the particle diameter of 12.5 µm. (a) T ≤ 0°C, before multiplying by the scaling factor. (b) T ≤ 0°C, after multiplying by the scaling factor. (c) T > 0°C, before multiplying by the scaling factor. (d) T > 0°C, after multiplying by the scaling factor.*

Similar to the relation between CSE and concentration gradient, the data converges when multiplying the microcrack density with a scaling factor *M*, as shown in Figure 4.5, Figure 4.6, and Figure 4.7. The scaling factors for the relations between CSE and microcrack density are listed in Table 4.3. In Figure 4.5 and Figure 4.6, the effects of C-rate and particle size can be generalized by using scaling factor M_3 and M_4 when T = 20°C and 0°C respectively. For the influence of temperature, the data also converges after multiplying the scaling factor by the microcrack density as shown in Figure 4.7. This scaling result is similar to the relationship between CSE and the concentration gradient. The scaling factor varies with the temperature and can be used to infer which factor has a higher influence on damage. Since the variation of solid phase diffusivity (dD_s/dT) is higher when T > 0°C (M_3) compared to $T \leq$ 0°C (M_4) according to Eq. (3.18), the temperature has a larger influence on concentration gradient when T > 0°C (M_3) compared to $T \leq$ 0°C (M_4). When $T \leq$ 0°C, the effect of temperature decreases, but different from the relation between CSE and concentration, the influence of C-rate was not enhanced by the low temperature. Moreover, by comparing the order in the scaling factor for the relation between CSE/concentration gradient (0.14) and CSE/microcrack density (0.28), we can observe that the temperature, C-rate, and particle size have a higher impact on the relation of CSE/microcrack density than the relation of CSE/concentration.

With the introduction of the scaling factor, we can find the parameters in Eq. (4.5) by fitting the data obtained from the simulations as shown in Figure 4.8. The data in

Figure 4.8 is from the simulation conditions listed in Table 4.2. From the curve fitting, the suggested parameters for Eq. (4.5) are listed in Table 4.3.

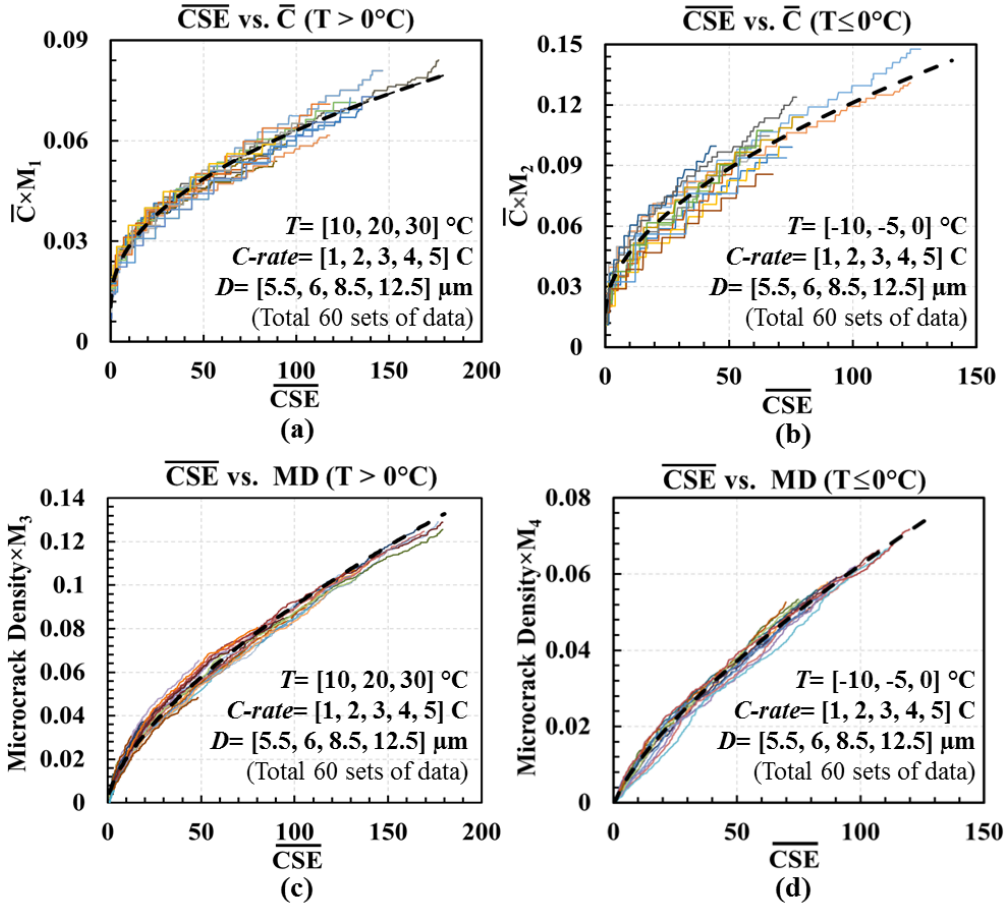

Figure 4.8. *The fitting result for (a) relation between cumulative strain energy and concentration gradient when T > 0°C; (b) relation between cumulative strain energy and concentration gradient when T ≤ 0°C; (c) relation between cumulative strain energy and microcrack density when T > 0°C; and (d) relation between cumulative strain energy and microcrack density when T ≤ 0°C. The dashed line shows the fitting result.*

4.2.2 Scaling Analysis of Drive Cycle

In addition to the scaling study for the single delithiation process, the microcrack formation during the drive cycle is also discussed in this paper. One should note that because the C-rate is not constant during the drive cycle, the pattern for the relation

between CSE and the concentration gradient is irregular. Therefore, the relation between CSE and the concentration gradient is not discussed in this subsection. This subsection considers drive cycles for three different electric-drive vehicle applications: plug-in hybrid electric vehicle (PHEV), hybrid electric vehicle (HEV), and battery electric vehicle (BEV). The three were simulated using the high order diffusion induced damage model [24]. The scaling equations obtained from the previous section (see Eq. (4.5) and Table 4.3) have been used to reproduce the relation between CSE and microcrack density for drive cycle.

Figure 4.9 shows the pattern of C-rate during different drive cycles. The average discharge rate, average charge rate, discharge fraction, and charge fraction are shown in Table 4.4. The HEV drive cycle has a higher discharge/charge rate compared to PHEV and BEV drive cycles. However, because the fraction of the discharge/charge period of the HEV drive cycle is nearly 50%/50%, the average C-rate is lower than the PHEV and BEV drive cycles.

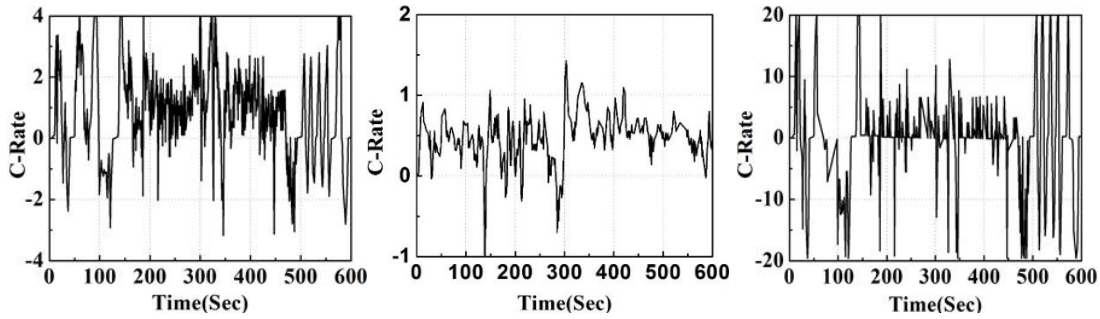

Figure 4.9. *(a) Variation of C-rate over time for the PHEV drive cycle. (b) Variation of C-rate over time for the BEV drive cycle. (c) Variation of C-rate over time for the HEV drive cycle.*

Table 4.4. *Statistical data of drive cycle.*

Drive Cycle	***Average Discharge Rate***	***Average Charge Rate***	***Discharge Fraction***	***Charge Fraction***
HEV	2.66 C	2.04 C	44.5%	55.5%
PHEV	1.46 C	1.03 C	75.8%	24.2%
BEV	0.496 C	0.305 C	88%	12%

Figure 4.10, Figure 4.11, and Figure 4.12 present the influence of temperature and particle size on the microcrack formation for PHEV, BEV, and HEV drive cycles, respectively. The time evolution of the concentration gradient varies frequently due to the variable C-rate of the different drive cycles. For the PHEV drive cycle shown in Figure 4.10 (a) and (d), because the variation of C-rate is large, we can see a large fluctuation of the concentration gradient. In contrast, the smaller C-rate variation during the BEV drive cycle causes less fluctuation of concentration gradient compared to the PHEV drive cycle as shown in Figure 4.11 (a) and (d). For the HEV drive cycles, we can see large fluctuations of the concentration gradient as shown in Figure 4.12 (a) and (d). The difference in the concentration gradient of the different drive cycles greatly affects the average microcrack density. The small concentration gradients of the BEV drive cycle (Figure 4.11 (a) and (d)) results in microcrack density about 10 times smaller than the other two drive cycles.

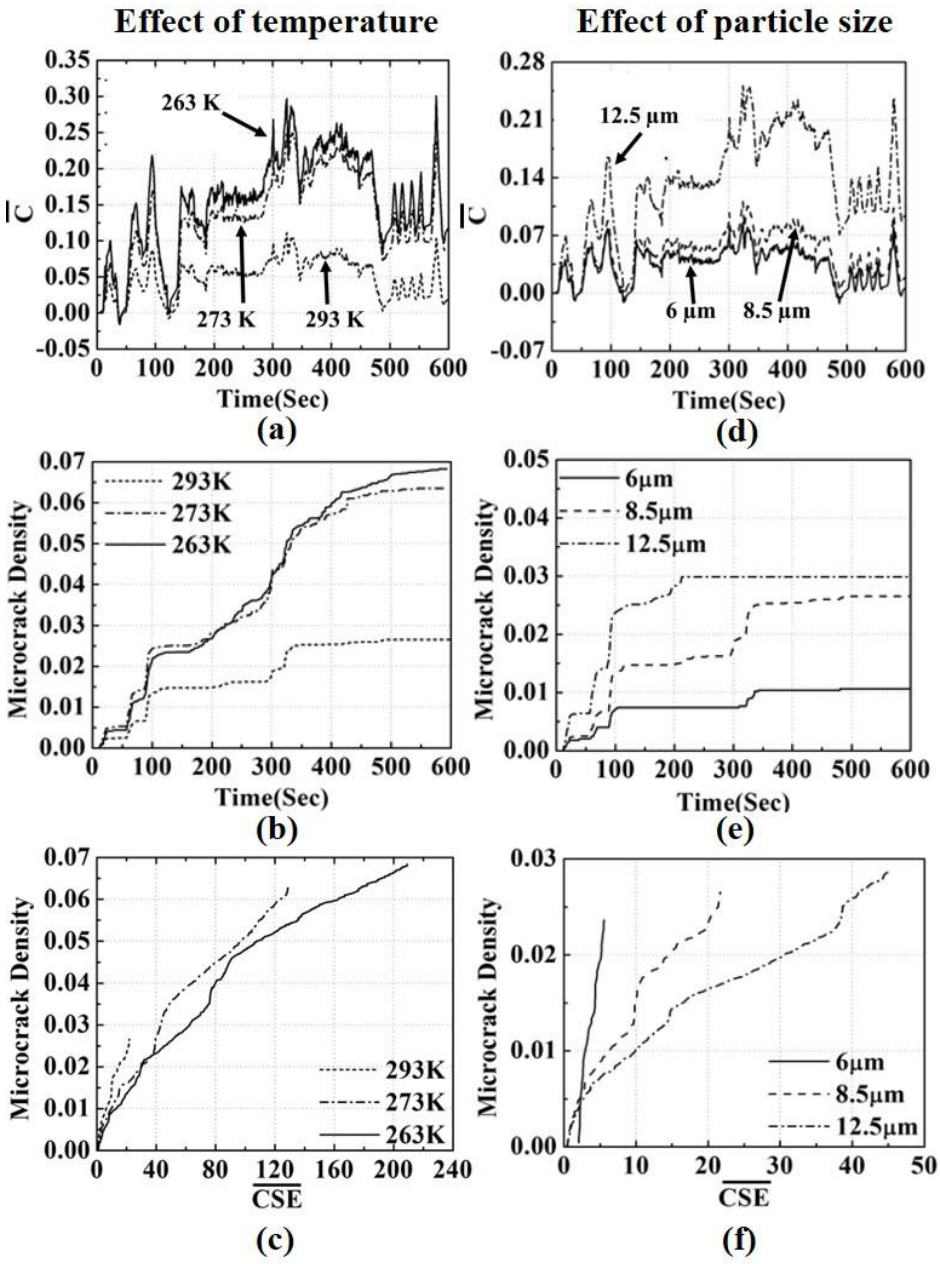

Figure 4.10. *(a–c) The influence of temperature on the PHEV drive cycle with particle diameter of 8.5 µm. (a) The time evolution of the concentration gradient. (b) The time evolution of microcrack density. (c) The relation between microcrack density and CSE. (d–f) The influence of particle size on the PHEV drive cycle at T = 20°C. (d) The time evolution of the concentration gradient. (e) The time evolution of microcrack density. (f) The relation between microcrack density and CSE.*

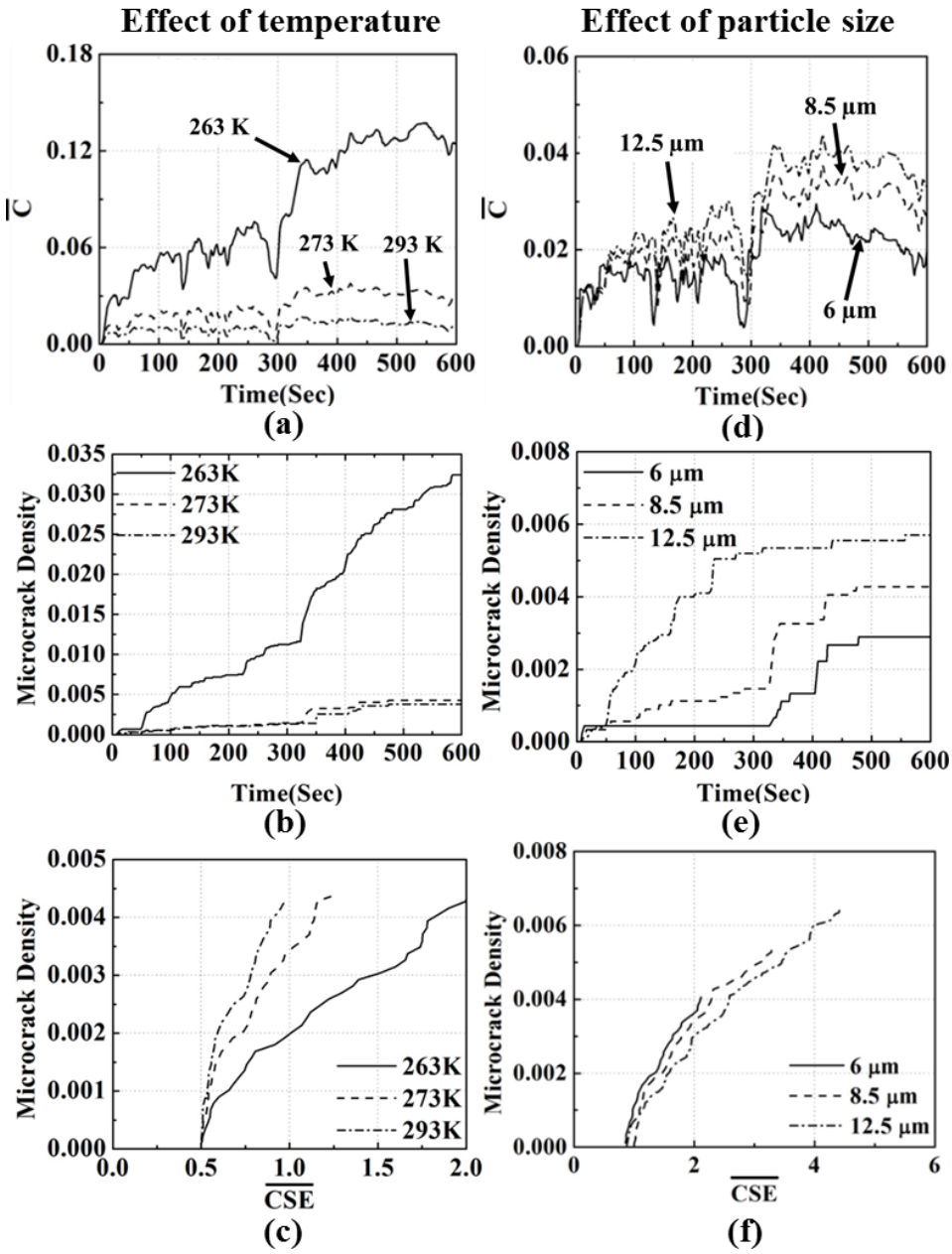

Figure 4.11. *(a–c) The influence of temperature on the BEV drive cycle with particle diameter of 8.5 µm. (a) The time evolution of the concentration gradient. (b) The time evolution of microcrack density. (c) The relation between microcrack density and CSE. (d–f) The influence of particle size on the BEV drive cycle at T = 20°C. (d) The time evolution of the concentration gradient. (e) The time evolution of microcrack density. (f) The relation between microcrack density and CSE.*

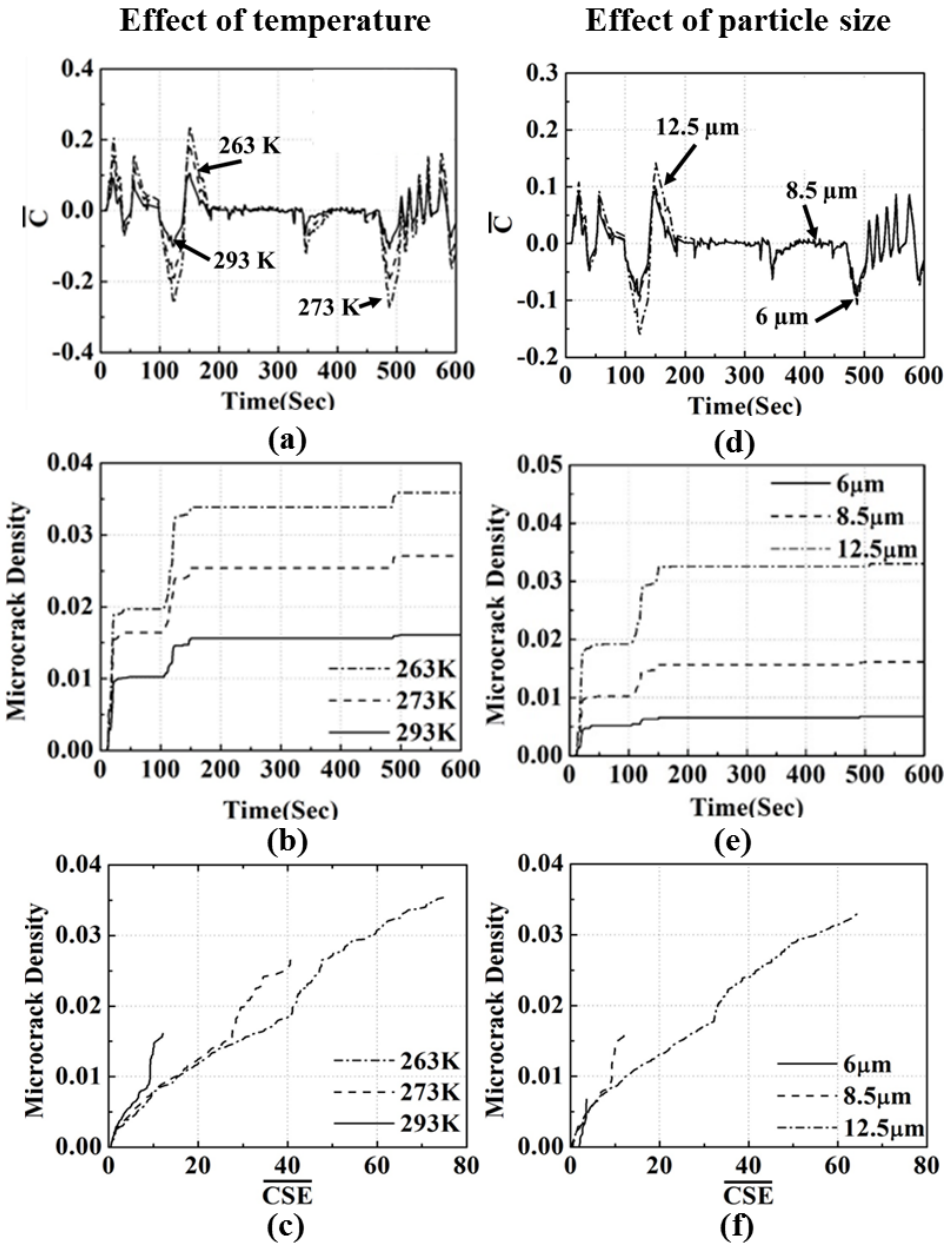

Figure 4.12. *(a–c) The influence of temperature on the HEV drive cycle with particle diameter of 8.5 µm. (a) The time evolution of the concentration gradient. (b) The time evolution of microcrack density. (c) The relation between microcrack density and CSE. (d–f) The influence of particle size on the HEV drive cycle at T = 20°C. (d) The time evolution of the concentration gradient. (The results of particle size 6 µm and 8.5 µm almost overlap). (e) The time evolution of microcrack density. (f) The relation between microcrack density and CSE.*

For the PHEV drive cycle, Figure 4.10 (a) shows that the concentration gradient increases with the decrease of temperature. This is due to the temperature-dependent characteristic of diffusivity as shown in Eq.(3.18). Since the concentration gradient is high under low operating temperature, the particle has a higher microcrack density than operating under higher temperature as shown in Figure 4.10 (b). The relation between CSE and microcrack density shown in Figure 4.10 (c) is similar to the single delithiation process, in which low temperature has a lower microcrack density under the same value of CSE. This is caused by the difference in concentration gradient as explained in the previous section. Figure 4.10 (d) shows the time evolution of the concentration gradient in different particle sizes during the PHEV drive cycle. The results suggest that the concentration gradient increases with the particle size. The variation of concentration gradient is due to the change in diffusion length when the particle size is different. The change of concentration gradient affects the microcrack density as shown in Figure 4.10 (e). Figure 4.10 (f) presents the relation between CSE and microcrack density for different particle sizes, with similar trends as the single delithiation process. The microcrack density decreases with the increased particle size under the same CSE. By comparing the time evolution of the concentration gradient in Figure 4.10 (a) and (d), and the time evolution of microcrack density in Figure 4.10 (b) and (e), we discover the difference in microcrack density is mainly due to the peak concentration gradient, observable as step changes in microcrack density in Figure 4.10 (e), at the approximate times of t = 50, 100, and 300 seconds. One should note that since the concentration gradient is large in the 12.5 μm particle, the sudden increase of microcrack density shifts from t = 300 seconds to 200

seconds. At these times, due to the large peak in the concentration gradient, the microcrack density has a significant increase. Moreover, it is worth noting that, although there is a large fluctuation after 500 seconds, the microcrack density does not increase. This is because the concentration gradient during ~300 to 500 seconds saturates the microcrack density, and the lower concentration gradient after 500 seconds has no potential to form new microcracks. This phenomenon is even obvious when the particle size is 12.5 μm and T = 20°C, that the microcrack density saturated after 200 seconds.

Figure 4.11 shows the effects of temperature and particle size on the microcrack formation for the BEV drive cycle. Similar to the PHEV drive cycle, the concentration gradient increases with the decrease of temperature and the increase of particle size, as shown in Figure 4.11 (a) and (d). The relation between CSE and microcrack density shown in Figure 4.11 (c) and (f) also has the same trend as the singe delithiation process and PHEV drive cycle. Similarly, we can also observe a sudden increase of microcrack density in the 6 μm and 8.5 μm particle when t = 300 seconds due to the large impulse of the concentration gradient. The phenomenon is less obvious because of the low concentration gradient. The microcrack density only has a significant increase when T = -10°C.

Figure 4.12 shows the effects of temperature and particle size on the microcrack formation for the charge sustaining HEV drive cycle. The trend of time evolution in the concentration gradient, time evolution of microcrack density, and the CSE/microcrack density relations show the same trend as for the PHEV and BEV drive cycles. However, the influence of temperature and particle size on the concentration gradient is

insignificant as shown in Figure 4.12 (a) and (d), which is because of the discharge/charge period fraction during the drive cycles. The nearly 50%/50% period fraction alleviates the influence of diffusion length and solid phase diffusivity on the concentration gradient. Due to the insignificant variation of the concentration gradient, the microcrack formation during the HEV drive cycle is mainly caused by the sudden pulse of concentration gradient at the beginning of the drive cycle and t = 100 seconds. It is worth noting that although the HEV drive cycle was operating under the highest discharge/charge rate, due to the nearly 50%/50% charge/discharge period fraction, the HEV drive cycle has less mechanical damage compared to the PHEV drive cycle.

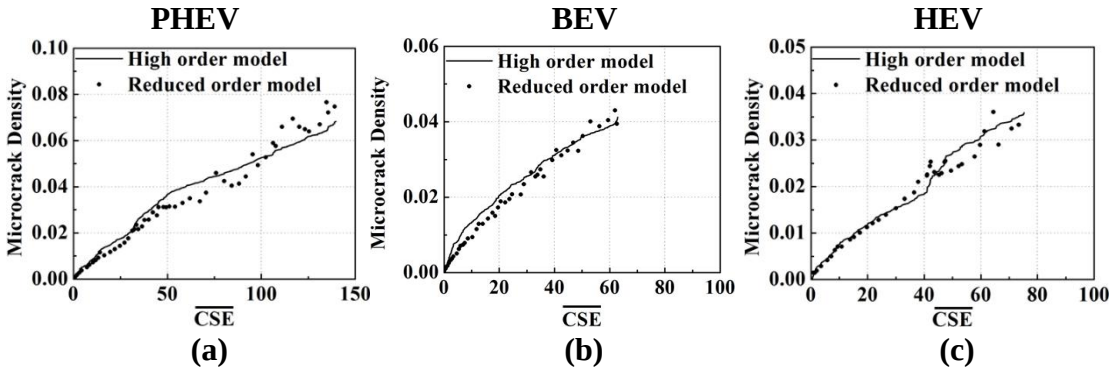

Figure 4.13. *Comparison of the relation between microcrack density and CSE between high order diffusion induced damage model and reduced order relation in Eq. (4.5). (a) PHEV drive cycle with 8.5 μm particle under -10°C. (b) BEV drive cycle with 8.5 μm particle under -10°C. (c) HEV drive cycle with 8.5 μm particle under -10°C.*

Figure 4.13 shows the reproduction of the relation between CSE and microcrack density by using the scaling laws found in the previous section. The relation is as shown in Eq. (4.5) and Table 4.3. During the drive cycle operation, whenever the microcrack formed, the corresponding cumulative strain energy and C-rate were recorded. For

reproduction, the recorded C-rate was used to calculate the scaling factor *M* (see Table 4.3). With the scaling factor and CSE, we can evaluate the microcrack density from Eq. (4.5). When calculating the scaling factor, because not every C-rate in the drive cycle has contributed to the microcrack formation according to the results shown in Figure 4.10, Figure 4.11 and Figure 4.12, we averaged the C-rate every five time steps of microcrack formation and used the average C-rate to calculate the scaling factor. In general, the scaling law (reduced order model) in Eq. (4.5) reasonably captures the microcrack growth trend. The fitting equation shows good agreement with the results of the BEV drive cycle. However, we still can see fluctuations in the reproduction of the PHEV and HEV drive cycle data, because (i) it is hard to pick the exact average C-rate, which has contributed to microcrack formation, and (ii) the formation location of microcracks is different during delithiation and lithiation processes.[23]

4.3 Conclusions

The influence of temperature, particle size, and delithiation rate on the damage evolution in an active particle of LIB electrodes has been investigated using a high order diffusion induced damage model. The evolution of microcrack formation was quantified both for a single delithiation process and for several drive cycles with highly variable C-rate profiles.

From the single delithiation simulations, the temperature, particle size, and C-rate show significant influence on the relation between (i) CSE and concentration gradient and (ii) CSE and microcrack density. For the relation between CSE and concentration

gradient, the results suggest that, under the same value of CSE, the concentration gradient increases with (i) decrease of temperature, (ii) increase of particle size, and (iii) increase of C-rate. In contrast, for the relation between CSE and microcrack density, the microcrack density increases with (i) increase of temperature, (ii) decrease of particle size, and (iii) decrease of C-rate under the same value of CSE. According to the results, we introduced a scaling factor *M*, which can collapse the data from different operating conditions. Scaling law expressions for the relationships between CSE, concentration gradient, and microcrack density were found by fitting data from the high order diffusion induced damage model. From the data-drive scaling process, different temperature conditions (T > 0°C or $T \leq$ 0°C) suggested different scaling factors *M*, which means that the contribution of operation factors (*i.e.*, temperature, particle size, and C-rate) varied with the temperature. The reduced-order equations were coupled with the electrochemical model to study the influence of mechanical damage on cell performance. According to the results, the capacity fade is larger when the microcrack density is higher. Further, the capacity fade is directly proportional to the size of the electrode active particles and discharging rates. Another important observation is that the microcrack density is higher in the region near the separator as compared to the region near the current collector since the current density is higher near the separator.

In addition to the observation of the single delithiation process, we also investigated the damage evolution during the drive cycle. Three kinds of drive cycles (HEV, PHEV, and BEV) were tested in this study. The results quantified the microcrack formation dependence on temperature, particle size, and C-rate. Since PHEV and HEV applications

operate under a higher C-rate than the BEV application, the model predicts those applications will experience higher microcrack density. During the drive cycle, the microcrack was saturated after operation over time. After saturation, new microcracks can only form when the average concentration gradient exceeds its previous peak value. In addition, the scaling law expression for the relation between CSE and microcrack density found from the single delithiation process has successfully predicted the damage evolution during different drive cycles. This result validates our proposed approach for reduced order modeling of mechanical damage evolution in LIB active material particles.

CHAPTER V

ELECTRODE MICROSTRUCTURE EFFECT ON THE THERMAL BEHAVIOR OF THE LITHIUM-ION BATTERY

In this section, to study the influence virtual microstructure on the thermal behavior of LIBs, a microstructure-aware electrochemical-thermal coupled model (METCM) has been proposed, which links the virtual electrode microstructure with electrochemical reaction and heat generation. The advantage of using this mathematical approach is that it can separately observe different heat source (i.e. joule heating, reversible heating, and reaction heating) at a different state of charge (SOC) and position of the electrode. Unlike the experimental approach, which only total heat generation and cell temperature can be detected and calculated. In this paper, with the reconstructed virtual microstructure, the influence of electrode microstructure on the thermal behavior and the energy density of cell has been studied and discussed. The thermal behavior of cell was analyzed by observing the time and spatial distribution of different heating source (i.e. joule heating, reversible heating, and reaction heating). From the results, we found out that there exists a trade-off between desired capacity and safety temperature limit. In addition, the microstructure dependent thermal behavior provides an insight of using electrode microstructure to control the cell temperature to maintain the safety of cell without using external control mechanism.

5.1 Simulation Methodology

To increase the capacity of the cell, one common approach is increasing the amount of active material inside the electrode. Figure 5.1 (a) shows the charge of cathode microstructure when the vol. % of active material increase (the wt. % of active material, carbon additive, and binder was maintained at 90:5:5). Accompany with the increasing amount of active material, the porosity decrease (volume of the electrode was maintained constant) and the electrochemical interfacial area (active material/electrolyte) increase. Following with the porosity decrease, the tortuosity increase inside the electrode. If the anode capacity is fixed, the increase in the amount of active material of cathode also changes the Negative/Positive electrode loading ratio of the cell. The change of N/P loading ratio affects the range of open-circuit potential of the anode, if cathode has a smaller capacity than the anode. The change of microstructure properties can further affect the thermal behavior of electrode. As shown in Figure 5.1 (a), the decrease of porosity and increase of tortuosity can enlarge the polarization of Li^+ concentration and electrolyte potential, and increase the internal resistance. The increase of internal resistance enhances the joule heating inside the cell. The variation of the interfacial area changes the overpotential for electrochemical reaction and varies the reaction heating. The difference in N/P loading ratio changes the OCP range of anode, which affects the reversible heating. To capture the interaction between microstructure change and the thermal behavior of the cell, a Microstructure-aware Electrochemical-Thermal Coupled Model (METCM) has been developed. The detail description of the model, calculation of different heat sources, and reconstruction of the microstructure are presented in the following section.

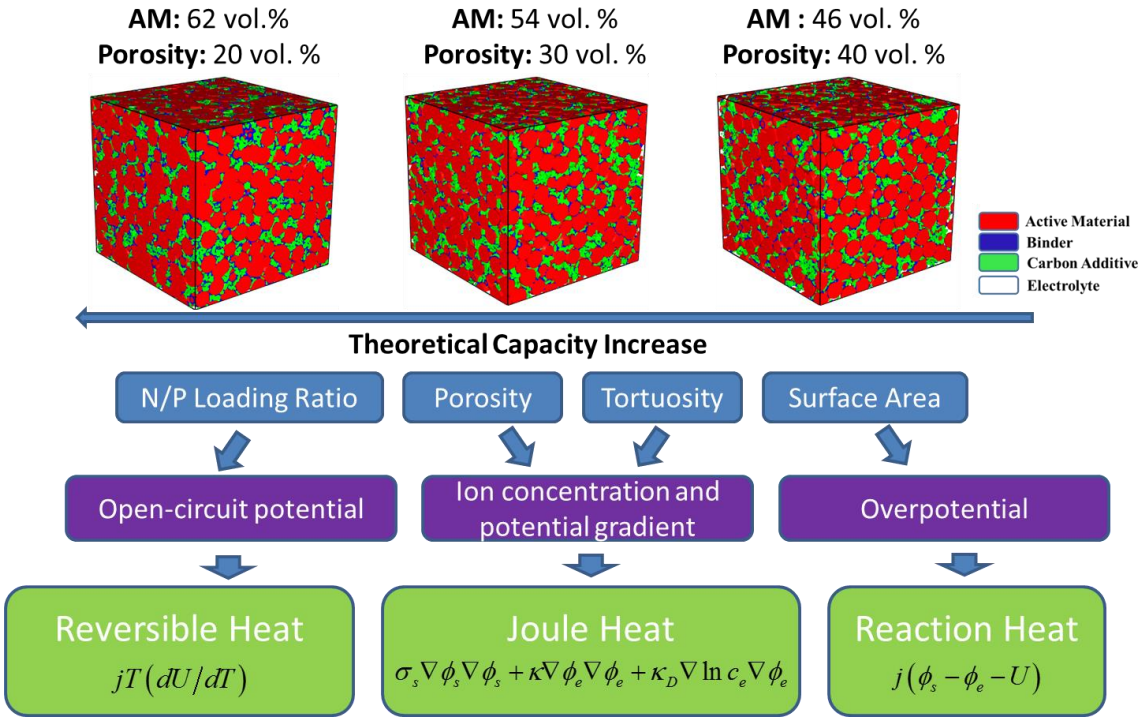

(a)

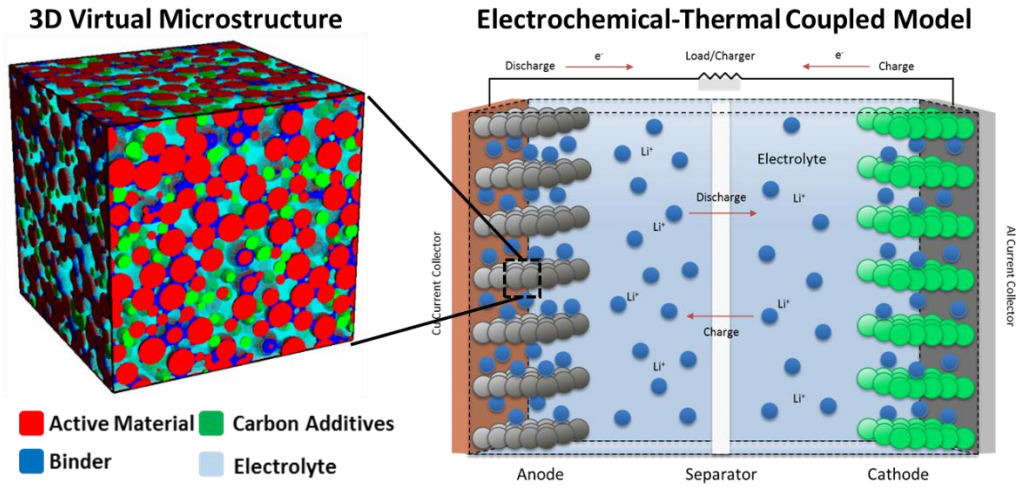

(b)

Figure 5.1. *(a) Interaction between microstructure and heat generation. The wt. % of active material, carbon additive, and binder is 90:5:5. (b) Schematic diagram of microstructure-aware electrochemical-thermal coupled (MAETC) model.*

5.1.1 Electrochemical-Thermal Coupled Model

The macro-homogenous lithium ion battery model has been reported in the literature by several authors [75-77, 84]. The foundation of the model is the porous electrode theory given by Newman [74] wherein the electrodes are considered as two-phase structures consisting of solid active material and liquid electrolyte. The separator is sandwiched in between the anode and the cathode and allows for the diffusion of lithium ions while hindering electron transport through the electrolyte. The model accounts for the intercalation kinetics, mass conservation in the solid and electrolyte phase and charge conservation in the solid and electrolyte phase. The governing equations and corresponding boundary conditions are elaborated below. The transport and thermodynamic properties involved are generally dependent on concentration and temperature. The functional relationships for ionic diffusivity, conductivity and thermodynamic factor have been taken from [173]. Effective properties are used wherever porous media approximations are involved in accounting for porosity and tortuosity of the electrodes.

5.1.1.1 Lithium Intercalation Kinetics

Butler-Volmer kinetics is used to describe the lithium intercalation reaction at both the anode and cathode, which gives us the following relation for the reaction current density.

$$i = i_0 \left[\exp\left(\frac{\alpha_a F}{RT} \eta \right) - \exp\left(-\frac{\alpha_c F}{RT} \eta \right) \right] \tag{5.1}$$

$$\eta = \phi_s - \phi_e - U(\theta, T) \tag{5.2}$$

$$i_0 = k(T) c_{se}^{\alpha_c} c_e^{\alpha_a} \left(c_{s,\max} - c_{se} \right)^{\alpha_a} \tag{5.3}$$

Here, i is the reaction current density, i_0 is the exchange current density , α_a, α_c are the anodic and cathodic transfer coefficients of the electrode reaction respectively , F is Faraday's constant, T is temperature, R is the universal gas constant and η is the overpotential given by Eq. 2. It is a function of the solid phase potential ϕ_s , electrolyte potential ϕ_e and the open circuit potential (OCP) of the electrode denoted by U which is a function of both state of charge θ and temperature. The functional relationships of OCP for graphite and NMC are readily available in literature and have been taken from [93, 174] and is expressed in Eq. (5.4) and (5.5) respectively . The exchange current density i_0 is a function of temperature dependent rate constant k and lithium concentration in both solid c_{se} and electrolyte phase c_e .

$$\begin{aligned} U_a = {} & 0.1493 + 0.8493\exp\left(-61.79\theta\right) + 0.3824\exp\left(-665.8\theta\right) - \exp\left(-39.42\theta - 41.92\right) - \\ & 0.03131\arctan\left(25.59\theta - 4.099\right) - 0.009434\arctan\left(32.49\theta - 15.74\right) \quad \left(0 \le \theta \le 1\right) \end{aligned} \tag{5.4}$$

$$U_c = -10.72\theta^4 + 23.88\theta^3 - 16.77\theta^2 + 2.595\theta + 4.563 \quad \left(0.3 \le \theta \le 1\right) \tag{5.5}$$

5.1.1.2 Mass Conservation in Solid Phase

Active material particles are considered to have spherical geometry and Fickian diffusion is used for solving lithium transport inside the particles.

$$\frac{\partial c_s}{\partial t} = \frac{1}{r^2} \frac{\partial}{\partial r} \left(D_s r^2 \frac{\partial c_s}{\partial r} \right) \tag{5.6}$$

with the boundary condition of

$$\left.\frac{\partial c_s}{\partial r}\right|_{r=0} = 0, \left.\frac{\partial c_s}{\partial r}\right|_{r=R_s} = -\frac{i}{D_s F} \tag{5.7}$$

Here c_s is the concentration of lithium atoms in the solid phase, D_s is the solid phase diffusion coefficient and i is the reaction current density on the particle surface. The boundary conditions (BC) correspond to zero flux at sphere center due to symmetry and reaction current density dependent flux at the surface.

5.1.1.3 Mass Conservation in Electrolyte Phase

Diffusion of lithium ions inside the electrolyte is also modeled using Fick's law with D_e^{eff} giving the effective diffusion rate of lithium ions in the electrolyte phase. The volumetric source term in the equation represents the production/destruction of lithium ions in the electrolyte due to the reaction current. t_+ is the transference number of lithium ions and represents the fraction of current carried by the lithium ions, usually taken to be a constant. The relation between volumetric current density j and reaction current density i at the particle surface is given by Eq. 6. Here, a_s is the electrode active area per unit volume.

$$\epsilon \frac{\partial c_e}{\partial t} = \nabla.\left(D_e^{eff} \nabla c_e\right) + \frac{1-t_+}{F} j \tag{5.8}$$

$$j = a_s i \tag{5.9}$$

The boundary condition is expressed as the following.

$$\left.\frac{\partial c_e}{\partial x}\right|_{x=0,L_a+L_s+L_c} = 0, D_e^{eff}\left.\frac{\partial c_e}{\partial x}\right|_{x=L_a-\epsilon,x=L_a+L_s-\epsilon}^{x=L_a+\epsilon,x=L_a+L_s+\epsilon} = 0 \tag{5.10}$$

The electrode-current collector interface bounds the cell, as such, the flux of lithium ions at this boundary should be zero. The BC at the interior electrode-separator interface represents the continuity of the flux at this interface.

5.1.1.4 Charge Conservation in the Solid Phase

Electric potential in the solid phase ϕ_s can be determined using Ohm's law. At the electrode-current collector interface, the current flux BC is prescribed. Here, I is the total current coursing through the cell and A is the electrode-current collector interface area. The separator hinders electronic current flow, as such, the flux of electronic current is zero at the electrode-separator interface.

$$\nabla\cdot\left(\sigma_s^{eff}\nabla\phi_s\right) - j = 0 \tag{5.11}$$

with the boundary condition of

$$\sigma_s^{eff}\left.\frac{\partial\phi_s}{\partial x}\right|_{x=0,L_a+L_s+L_c} = -\frac{I}{A}, \sigma_s^{eff}\left.\frac{\partial\phi_s}{\partial x}\right|_{x=L_a,L_a+L_s} = 0 \tag{5.12}$$

5.1.1.5 Charge Conservation in the Electrolyte Phase

Charge motion in the electrolyte phase is driven by gradients of electrolyte potential ϕ_e and ionic concentration c_e . The total ionic current has contribution from two components, the first term represents the migration current due to Ohm's law while the

second term represents the diffusional current arising from differences in concentration of ions throughout the length of the cell. The diffusional conductivity κ_D is related to ionic conductivity κ and is given by Eq. (5.14).

$$\nabla \cdot \left(\kappa^{eff} \nabla \phi_e \right) + \nabla \cdot \left(\kappa_D^{eff} \nabla \ln c_e \right) + j = 0 \tag{5.13}$$

$$\kappa_D^{eff} = \frac{2RT\kappa^{eff}}{F}\left(t_+ - 1\right)\left(1 + \frac{d \ln f_{\pm}}{d \ln c_e}\right) \tag{5.14}$$

with the boundary condition of

$$\left.\frac{\partial \phi_e}{\partial x}\right|_{x=0, x=L_a+L_s+L_c} = 0, \kappa^{eff} \nabla \phi_e + \kappa_D^{eff} \nabla \ln c_e \Big|_{x=L_a-\epsilon, x=L_a+L_s-\epsilon}^{x=L_a+\epsilon, x=L_a+L_s+\epsilon} = 0 \tag{5.15}$$

The BCs represent zero flux at the electrode-current collector interface and continuity of flux at the electrode separator interface. As the above equation is an elliptic equation, we impose a dirichlet BC $\phi_e\big|_{x=L_a+L_s+L_c} = 0$ at the cathode-current collector interface for solution purposes.

5.1.1.6 Energy Conservation in Complete Cell

Energy conservation in the cell can be described using a lumped thermal model owing to low Biot number characteristics of an 18650 cell under natural convection conditions. The heat generation rate $\dot{Q}$ comprises of irreversible heat, reversible heat and joule heat. Joule heating arises because of three different factors: electronic resistance, ionic resistance and concentration overpotential. The total rate is calculated by integrating

the source terms over the entire length of the cell and multiplying with the electrode area A. The resulting equation can be solved for temporal evolution of temperature.

$$mC_p \frac{dT}{dt} = \dot{Q} + hA_S \left(T - T_\infty\right) \tag{5.16}$$

$$\dot{Q} = A \int_0^{L_a+L_s+L_c} \left(\begin{array}{l} \left(j(\phi_s - \phi_e - U\right) + j\left(T \frac{dU}{dT} \right) + \\ \sigma_s^{eff} \nabla \phi_s \cdot \nabla \phi_s + \kappa^{eff} \nabla \phi_e \cdot \nabla \phi_e + \kappa_D^{eff} \nabla \ln c_e \cdot \phi_e \end{array} \right) dx \tag{5.17}$$

Finite volume discretization is used for the governing equations with five unknowns at each cell cebter: $c_s, c_e, \phi_s, \phi_e, T$. Source term linearization using Taylor series expansion is done to take care of the non-linear Butler Volmer equation. The value of *dU/dT* used in (5.17) is given by Eq. (5.18) and (5.19).[174, 175]

$$\frac{dU_a}{dT} = -58.294\theta^6 + 189.93\theta^5 - 240.40\theta^4 + 144.32\theta^3 - 38.87\theta^2 + 2.8642\theta + 0.1079 \tag{5.18}$$

$$\frac{dU_c}{dT} = -190.34\theta^6 + 733.46\theta^5 - 1172.6\theta^4 + 995.88\theta^3 - 474.04\theta^2 + 119.72\theta - 12.457 \tag{5.19}$$

5.1.2 Reconstruction of Microstructure and Evaluation of Charge Transport Properties

The virtual 3D microstructure was reconstructed according to the composition of the active material, carbon additive, and binder. The active material, which is used to store lithium, and carbon additives, which is used to boost electrical conductivity, is reconstructed with the stochastic method. [45, 176-178] The spherical particles of active material (D = 10 μm) were randomly distributed with the desired vol. %. The particles are prohibited from overlapping when the vol. % of active material is smaller than 50 vol. %. The carbon additives are assumed as platelet particles (D = 4 μm, thickness = 0.8 μm) and

also randomly distributed inside the control volume. The carbon additives were prohibited from overlapping with active materials, but allowed to overlap with each other. The binder was randomly added to a structure in the shape of a concave meniscus in locations where material surfaces get close together. In cathode, the wt. % of active material ($Li(Ni_{1/3}Mn_{1/3}Co_{1/3})O_2$), carbon additive (Graphite), and binder (PVDF/C) is maintained at 90:5:5. In the anode, wt. % of active material and the binder is maintained at 90:5, and there is no carbon additives. Figure 5.1 (a) shows the representative cathode electrode microstructure with different loading of active material. The electrical conductivity is calculated according to material properties expressed in Table 5.1. The transport properties of electrode (i.e. tortuosity, and electrical conductivity) and the corresponding capacity in the 18650 configurations are shown in Table 5.2.

The tortuosity and effective electrical conductivity are used as input of Eq. (5.8), (5.11), (5.13), and (5.14) in the electrochemical-thermal coupled model. One should notice that, in this study, we focus on the influence of cathode microstructure on the thermal behavior of the cell. Therefore, the anode microstructure is fixed in all the simulations.

Table 5.1. *Material properties of cathode and anode system*

Parameter		Particle diameter (μm)	Bulk conductivity ($S\ m^{-1}$)	Mass density ($g\ cm^{-3}$)
Cathode	$Li(Ni_{1/3}Mn_{1/3}Co_{1/3})O_2$	10[a]	0.00106[49]	4.8[49]
	Graphite	4[a]	16700[45]	1.95[45]
	PVDF/C	–	760[49]	1.86[a]
Anode	Graphite	10[a]	16700[45]	1.95[45]
	PVDF/C	–	760[49]	1.86[a]

[a] assumed value

Table 5.2. *Variation of microstructure properties with porosity and the corresponding theoretical capacity in 18650 cell configuration.*

	Cathode						Anode
	Porosity						
	0.15	0.2	0.25	0.3	0.35	0.4	0.25
vol. % of NMC	66.39	62.49	58.58	54.68	50.77	46.87	70.52
vol. % of additive	9.08	8.54	8.01	7.47	6.94	6.40	0
vol. % of binder	9.51	8.95	8.39	7.83	7.27	6.71	4.43
σ^{eff}	96.938	54.09	36.13	25.47	7.02	6.45	5900
Tortuosity	7.194	4.064	3.190	2.687	2.138	1.945	3.2
Capacity (Ah)	2.631	2.476	2.321	2.166	2.012	1.945	2.713

5.2 Results and Discussion

5.2.1 Microstructure-aware Electrochemical-Thermal Coupled Model

In the conventional porous electrode theory, the tortuosity was calculated from Bruggeman ideal relation as Eq. (5.20).

$$\tau = \varepsilon^{-0.5} \tag{5.20}$$

However, the Bruggeman ideal relation is based on the assumption that the particles are spherical and uniform distributed.[50] Since in the electrode of LIBs include amorphous active particles and binder, the Bruggeman ideal relation is not sufficient to represent the tortuosity of the virtual porous microstructure.[58] Figure 5.2 (a) shows the comparison of the tortuosity calculated from 3D reconstructed virtual microstructure and the one calculated from Bruggeman ideal relation. From the result, the tortuosity calculated from virtual microstructure is higher than the Bruggeman ideal relation, which is mainly due to the amorphous shape of binder and overlap of particles. The difference in tortuosity increase with the decrease of porosity The difference in tortuosity affects the simulation of discharge profile, heat generation, and temperature evolution as shown in Figure 5.2

(b), (c), and (d) respectively. The increase of tortuosity enlarges the internal resistance, which increases the voltage drop, joule heating rate, and temperature increase. It is worth noticing that, the difference in tortuosity only has a significant effect on joule heating rate, and the influence on the reaction and reversible heating rate is almost negligible.

5.2.2 Influence of Microstructure on the Thermal Behavior of LIBs

As mentioned in the previous section, increase the amount of active material is a common way to increase the capacity of the cell. However, the additional amount of active material can vary the microstructure, and change the thermal behavior of LIBs. The variation of thermal behavior may cause overheating of the cell, especially during the high current discharge process. To maintain the cell temperature below a safety limit (< 85 °C), the cell should stop before full discharge, which causes capacity lost. In addition, since the microstructure can affect the thermal behavior of the cell, it exists an electrode design window, which can keep the temperature below the safety limit. The trade-off between capacity and safety concern along with the safety design window will be further presented in the following section.

Figure 5.3 shows the influence of microstructure on the cell capacity, energy density, power ability, and time evolution of temperature. Figure 5.3 (a) presents the reconstructed 3D virtual microstructure with different loading of active material.

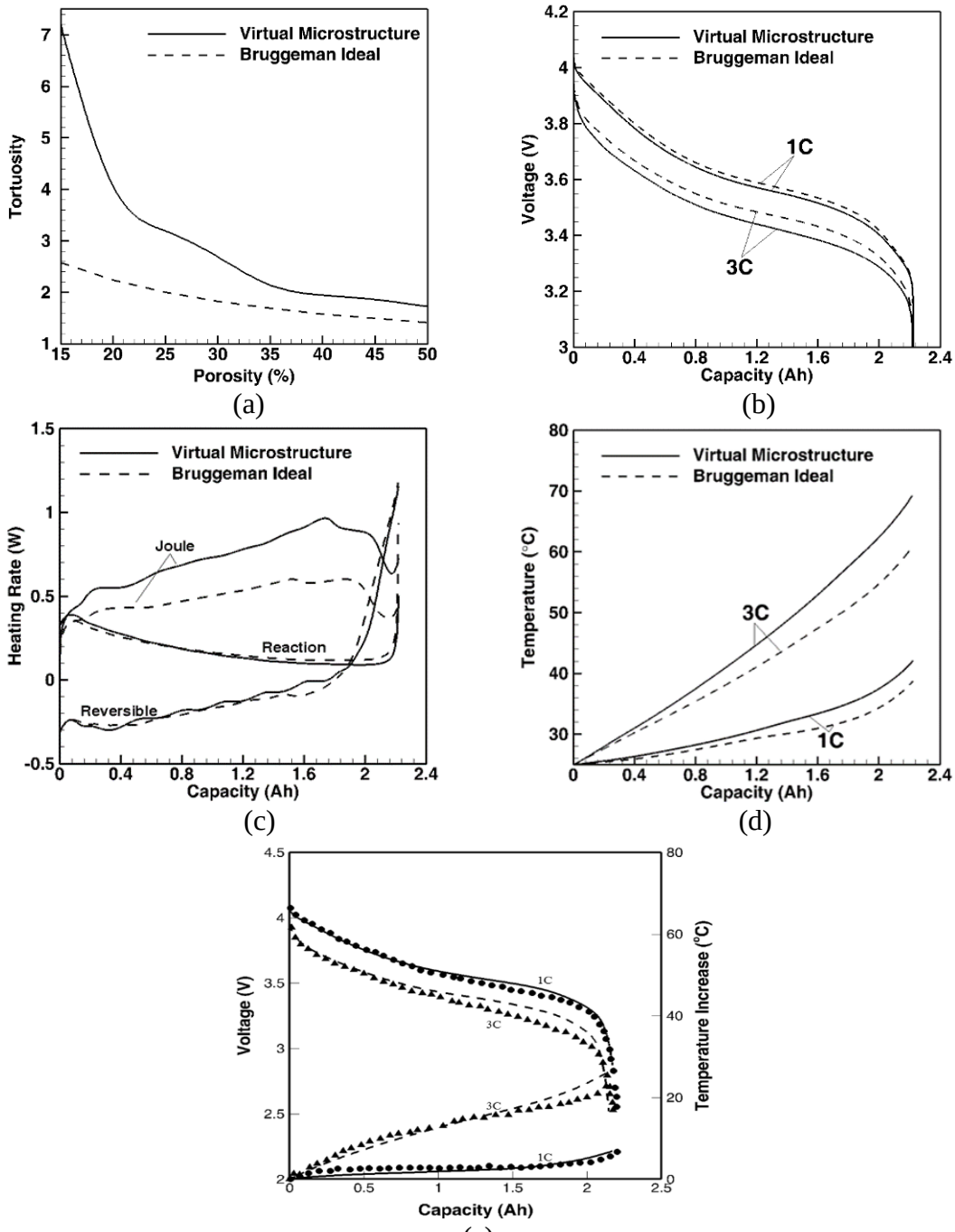

Figure 5.2*.Comparison of (a) tortuosity (b) voltage (c) heat generation (d) temperature evolution between Bruggeman ideal and microstructure-aware electrochemical-thermal coupled model. (e) Validation of microstructure-aware electrochemical-thermal coupled model. The porosity of cathode and anode is 0.25. The simulation temperature is 25°C.*

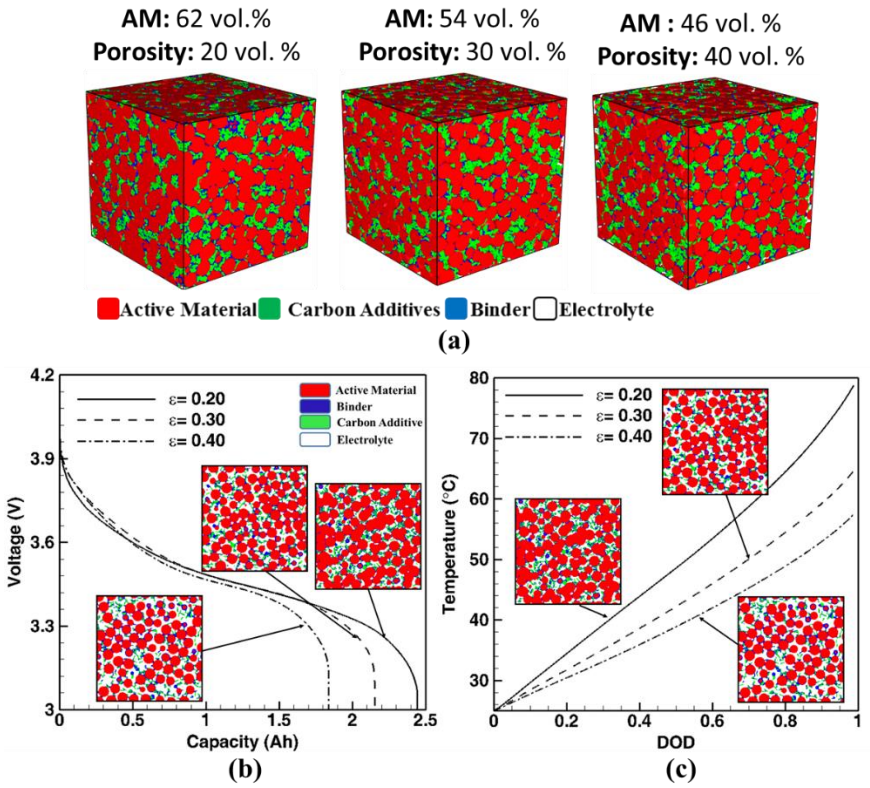

Figure 5.3*. (a) Corresponding microstructure with different vol% of active material. (b) Influence of microstructure on the cell performance and the corresponding cross section of microstructure when I = 6A and T = 25°C. (c) Influence of microstructure on the temperature evolution and the corresponding cross section of microstructure when I = 6A and T = 25°C.*

Since the wt. % of active material, carbon additive, and binder are maintained as 90:5:5, the amount of binder and carbon additives increase with the amount of active material. With the increase of active material, the porosity of electrode decrease, which results in the increase of tortuosity as shown in Figure 5.2 (a). Figure 5.3 (b) shows the improvement of capacity when the amount of active material is increased. The corresponding 2D reconstructed virtual microstructures are also included in Figure 5.3 (b).

The time evolution of temperature is shown in Figure 5.3 (c). As shown in Figure 5.3 (c), the temperature increase faster in the cell with low porosity cathode.

The difference in the temperature evolution is affected by different heat sources (i.e. joule heat, reaction heat, and reversible heat). As mentioned in the previous section, the variation of microstructure changes the porosity, tortuosity, interfacial area, and OCP range, which results in different heating rate as shown in Figure 5.2 and Figure 5.3. Figure 5.4 and Figure 5.5 show the time evolution and spatial distribution of different sources of heating rate respectively. In Figure 5.4 (a), the low porosity cathode shows the highest joule heating rate. The high joule heating rate is because the low porosity and high tortuosity porous electrode result in high internal resistance. This high internal resistance increases the polarization of Li^+ concentration and electrolyte potential. According to Eq. (5.17), high concentration and potential gradient cause high joule heating rate. Figure 5.5 (a – c) shows a more detail comparison of heating rate in the cell with different porosity of cathode. From the results, the different in the joule heating rate is mainly contributed by the region of the cathode where is close to the separator. Since the porosity of the anode is fixed, the change of joule heating rate in anode is not obvious, besides the end of discharge. This result suggests that the concentration and potential gradient in the region near cathode/electrolyte interface is the main reason causes large joule heating rate in the cell with low porosity cathode. It is also worth noticing that, in the end of discharge, the joule heating rate and the heating region in the anode become smaller in the cell with low porosity cathode. This is because the high temperature in the cell with low porosity cathode increases the ionic conductivity and diffusivity, which decrease the concentration

and potential gradient in the anode. The change of heating region in the cathode is also because of the temperature increase during the discharge process. The increase of temperature decrease the polarization in the middle of discharge, but when the concentration further decreases in cathode, the internal resistance, and polarization increase again.

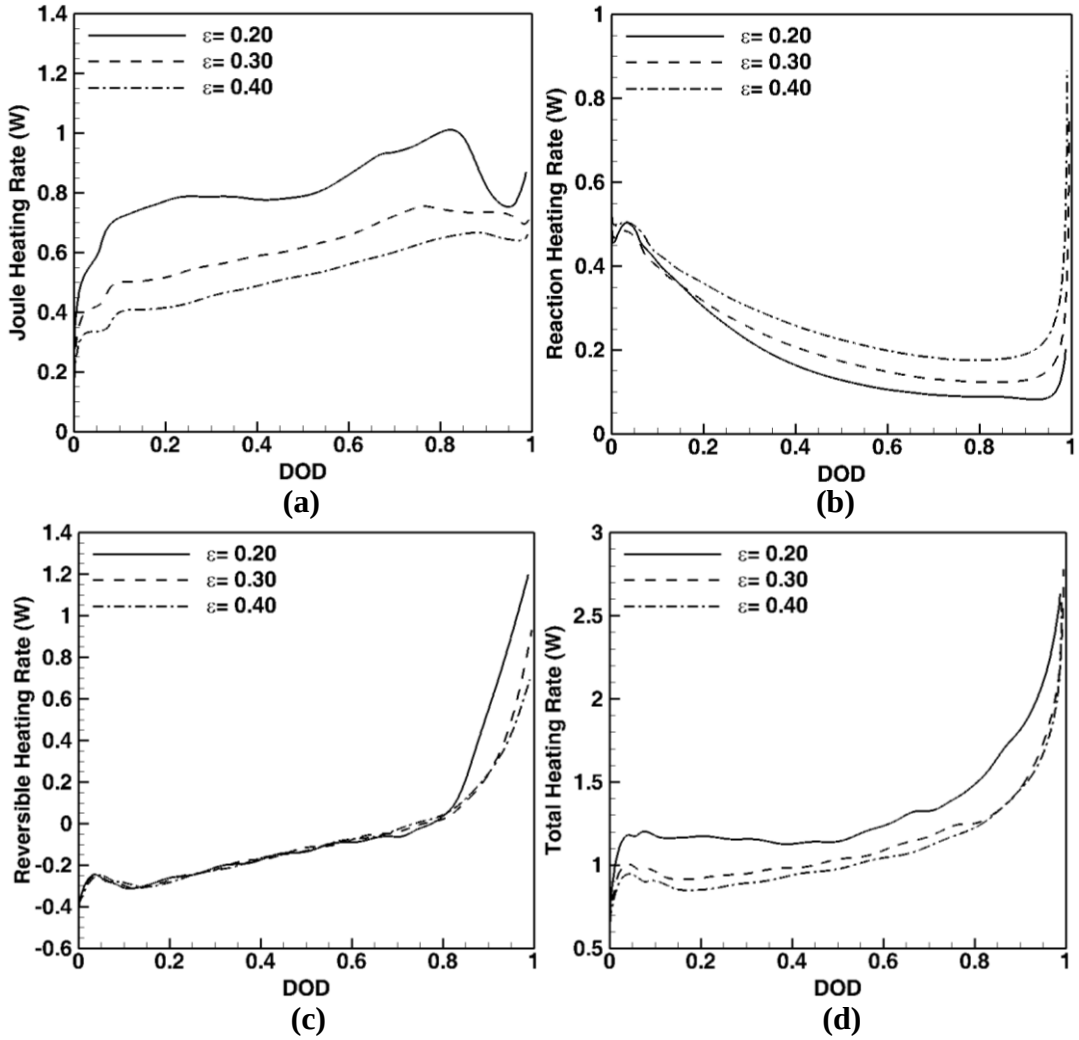

Figure 5.4.*The microstructure effect on the (a) Joule heating rate (b) Reaction heating rate (c) Reversible heating rate (d) Total heating rate when discharge with I = 6A and T = 25°C.*

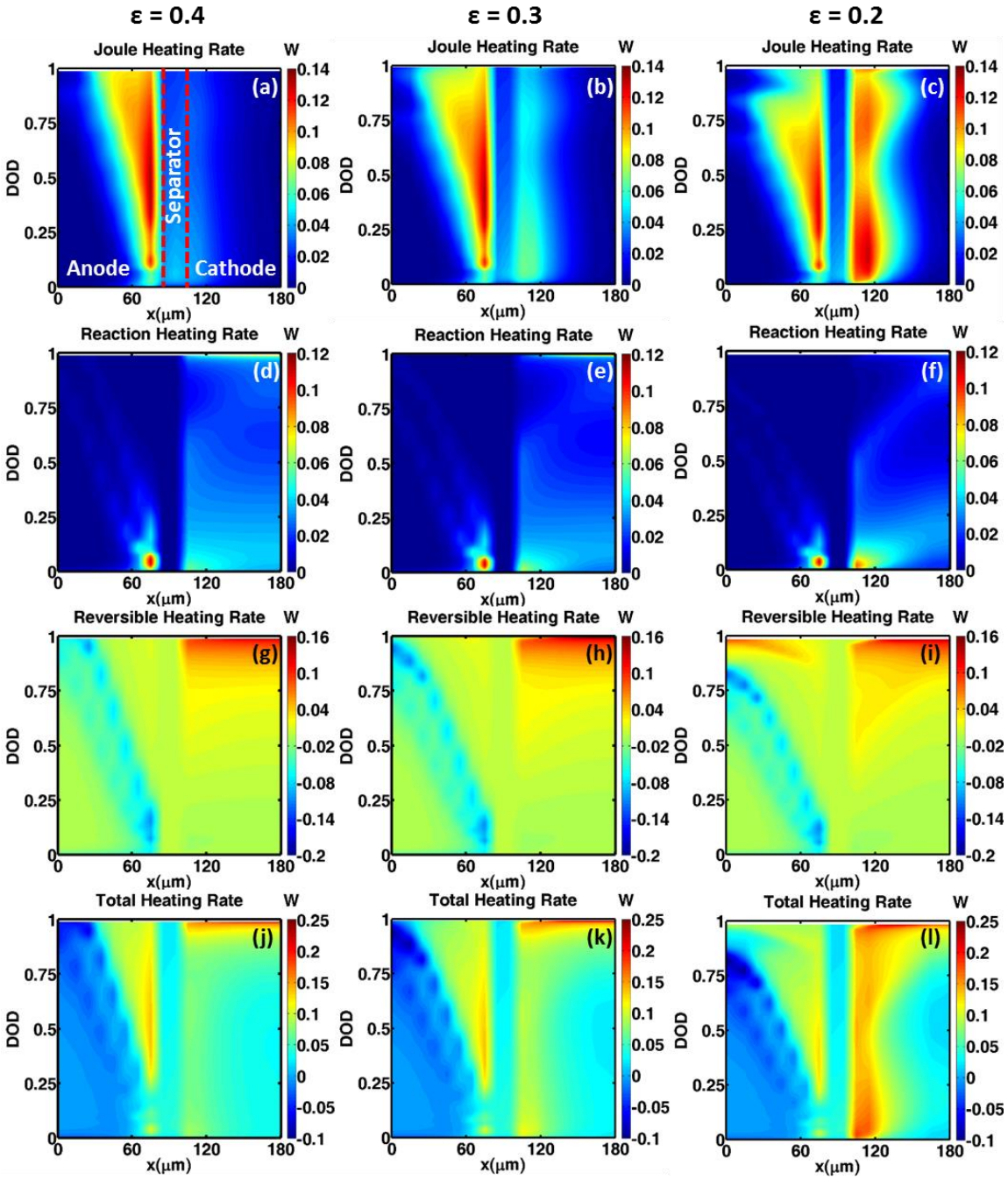

Figure 5.5.*The influence of microstructure on the spatial and time distribution of heating rate when I = 6A and T = 25°C. (a – c) Joule heating rate. (d – f) Reaction heating rate. (g – i) Reversible heating rate. (j – l) Total heating rate.*

Figure 5.4 (b) shows the time evolution of reaction heating rate. Opposite to the joule heating rate, the cell with low porosity cathode has the least reaction heating rate during the discharging process. The difference of reaction heating rate is mainly due to the difference in the interfacial area. When the amount of active material increase, although the porosity decrease, the interfacial area is enlarged. The enlargement of interfacial area decreases the overpotential when the output current is the same. According to Eq. (5.17), the decrease of overpotential lowers the reaction heating rate. From the spatial distribution of reaction heating rate shown in Figure 5.5 (d – f), we can observe that the reaction heating rate in cathode decrease with the porosity of cathode. The anode has compared less reaction heating rate is because the exchange current density is higher in the anode, which can result in lower overpotential in the anode. The distribution of reaction heating rate shown in Figure 5.5 (d – f) is highly dependent on the spatial distribution of reaction current density j. In the beginning of discharge, the reaction heating rate is concentrated in the region near the separator, which is because the peak of electrochemical reaction current density j is in the region near the separator. In addition, during the discharging process, the distribution of reaction heating rate is more uniform in the cell with high porosity cathode. This is because the distribution of the electrochemical reaction current density j is more uniform in the cell with high porosity cathode. The difference in the reaction current density j distribution is affected by the internal resistance inside the cathode. The peak of reaction heating rate in the anode is also because of the distribution of the electrochemical reaction current j.

For the reversible heating rate, the heating rate is negligible when the DOD = 0 – 0.8 (see Figure 5.4 (c)), besides the end of discharge. In the end of discharge (DOD > 0.8), the cell with low porosity cathode has higher reversible heating rate compare to higher porosity cathode. Figure 5.5 (g – i) shows the spatial distribution of reversible heating rate. As shown in the distribution, different from joule heating and reaction heating, the main difference of reversible heating is in the anode. The difference of reversible heating in the cathode is almost negligible. For the cell with 20% porosity cathode, there is high reversible heating in the end of discharge. The difference of reversible heating in the anode in the end of discharge is mainly due to the usage of anode SOC during the discharging process. When the amount of active material in cathode increase, since the capacity of anode is fixed, the N/P loading ratio changed. For the cell with 40% porosity cathode, the SOC range of anode during the discharging process is 0.95 – 0.4. For the cell with 20% porosity cathode, the SOC range of anode during the discharging process is 0.95 – 0.2. According to Eq. (5.18), the value of dU/dT is negative (heat depletion) when SOC = 1 – 0.3, and the value of dU/dT is positive (heat generation) when SOC < 0.3. Since the SOC range of anode in the cell with 20% porosity cathode can achieve the reversible heating region (SOC < 0.3), there is reversible heating in the end of discharge. It is also worth noticing the region where the reversible heating rate is negative (heat consuming). The heat consuming region is more close to the current collector, which is because the SOC is lower in the region near the anode/separator interface during the discharging process.

Figure 5.4 (d) and Figure 5.5 (j – l) shows the time evolution and spatial distribution of total heating rate. As shown in Figure 5.4 (d), the total heating rate increase with the

decrease of porosity, which explains the faster temperature increase in the cell with low porosity cathode (see Figure 5.3 (c)). Between the porosity of 30% and 40%, the difference of total heating rate mainly happens when DOD = 0 – 0.8. In the end of discharge, due to the compensation between reversible heating and reaction heating, the difference of total heating rate is almost the same. From the spatial distribution of heating rate (see Figure 5.5 (j – l)), in the cathode, the heating rate is large near the cathode/separator interface and at the end of discharge. In anode, the difference of total heating rate is mainly contributed by the variation of reversible heating due to the N/P ratio.

5.2.3 Trade-off between Temperature Control and Cell Capacity

According to the results present in the previous section, increase the amount of active material in the cathode can increase the capacity of the cell. However, the increase of capacity accompanied with the rise of cell temperature. Since the heat generation is also affected by the discharge rate and ambient temperature, it is worth studying the influence of microstructure on the thermal behavior under different operation condition. Figure 5.6 presents the max temperature and capacity obtained from the cell with different a porosity of cathode (i.e. different amount of active material) during the discharging process with different discharge current. Figure 5.6 (a) and (c) shows max temperature and capacity when the cell operates under 25°C. Figure 5.6 (b) and (d) shows max temperature and capacity when the cell operates under 40°C. In Figure 5.6 (a) and (b), according to the max temperature, it can separate into three regions. (i) The *Unsafe* region refers to T >80°C, which the temperature has the risk of thermal runaway. (ii) The region of *Potential*

Risk refers to 80°C >*T* >60°C, which the temperature has the potential risk of thermal runaway if a sudden input of heat source add to the cell, such as external short.

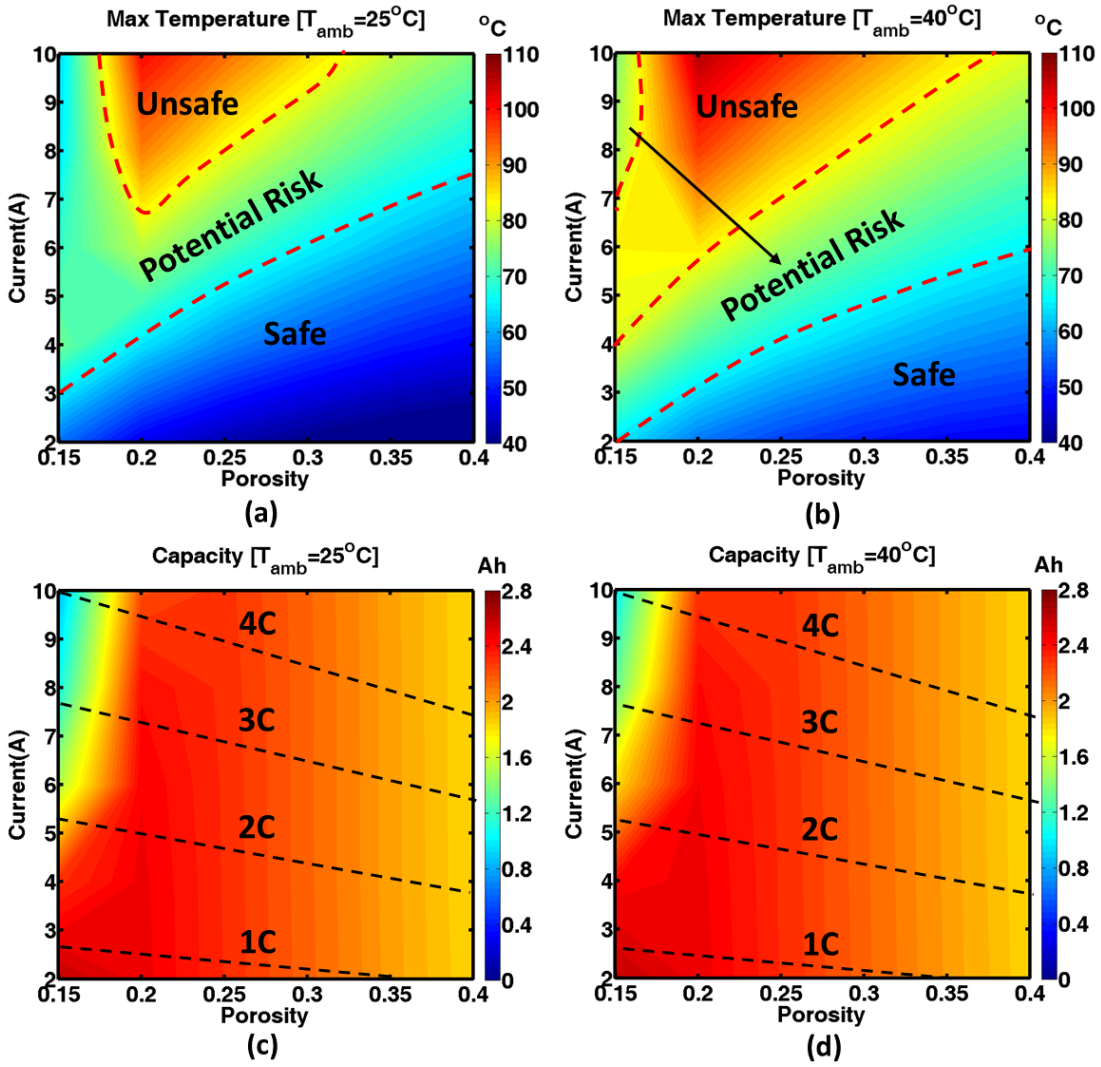

Figure 5.6. *The influence of discharge current and microstructure on the max temperature obtained in the end of discharge when (a) T_{amb} = 25°C (b) T_{amb} = 40°C. The influence of discharge current and microstructure on the cell capacity obtained in the end of discharge when (a) T_{amb} = 25°C (b) T_{amb} = 40°C.*

(iii) The *Safe* region refers to $T < 60°C$, which the temperature is comparable safe to the other two regions. From Figure 5.6 (a), when the discharge current is below 7A, the max temperature rise with the decrease of porosity ($\varepsilon = 0.15 – 0.4$). When the cathode porosity is between 0.18 – 0.32, the cell has the risk to reach *unsafe* temperature when the discharge current is higher than 7A. The lower max temperature for the cell with cathode porosity of $\varepsilon = 0.15 – 0.18$ is due to the self-shutdown of the cell. Under high discharge rate, because of large internal resistance of low porosity electrode, the cell shuts down before it fully discharge. Figure 5.6 (c) expresses the capacity lost due to the self-shut down for low porosity cathode. Under high discharge current ($I > 5A$), there is significant capacity loss for low porosity electrode compare to the capacity obtain under low discharge current. Due to the self-shutdown, although the heating rate is large, the decrease of time for temperature rise decrease the max temperature we get from low porosity cathode. From Figure 5.6 (b), we can observe that the *unsafe* region becomes larger when the cell operates under high ambient temperature. Beside the cathode porosity of 40%, the cell with another porosity of cathode has the risk to reach the *unsafe* temperature and the tolerated discharge current decrease with cathode porosity. Similar to Figure 5.6 (a), for the cathode porosity of 15%, if the discharge current is larger than 7A, the induced self-shutdown limits the max temperature below the 80°C. The self-shutdown under T_{amb}=40°C also can be observed from the capacity contour plot shown in Figure 5.6 (d). It is worth noticing that the capacity loss happened at higher discharge current and lower porosity cathode when T_{amb}=40°C compare to T_{amb}=25°C. This is because the increase of ambient temperature enlarges the ionic conductivity and diffusivity, and hence decreases the internal resistance.

The decrease of internal resistance shrinks the range of discharge current and porosity, which can trigger the self-shutdown. However, the shrink of range also decreases the safety operation range, which controlled by the self-shutdown.

From Figure 5.6, we can conclude that the max temperature varies with electrode porosity and discharge current. To limit the temperature of the cell, there are two ways. One way is external shut down, which shut down the battery when it reaches the temperature limit with external control or mechanism.

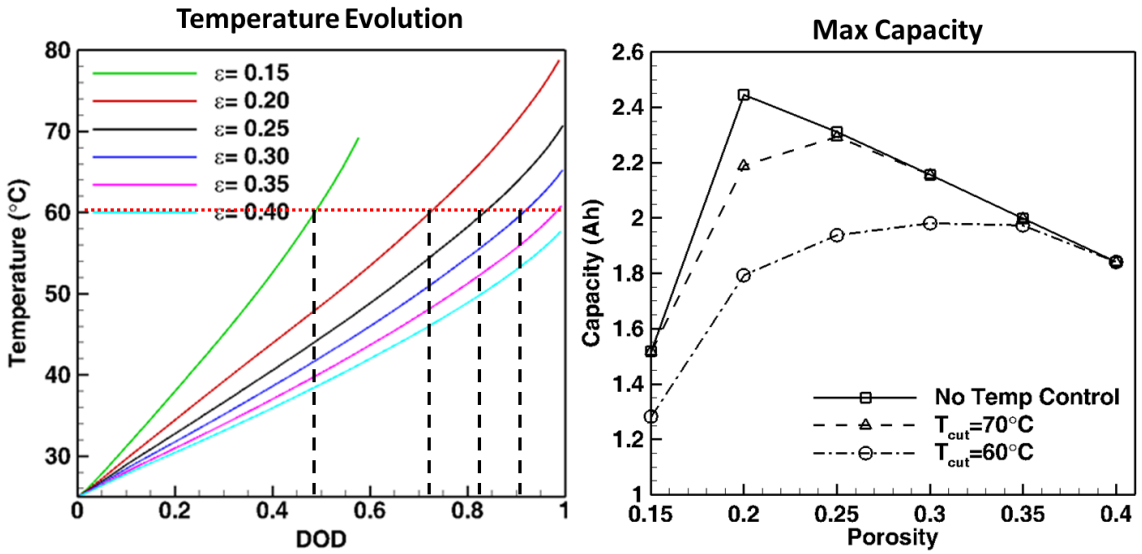

(a) (b)

Figure 5.7.*(a) To limit the cell temperature at certain temperature, the cell should cut-off at different DOD, which sacrifices the capacity of cell. (b) The capacity can obtain with different cut-off temperature. The temperature evolution and max temperature is referring to the cell discharge with I = 6A and T_{amb}=25°C.*

However, with the shutdown mechanism, the cells are forced to stop before it fully discharge as shown in Figure 5.7 (a). Figure 5.7 (a) shows an example if we want to limit the temperature below 60°C. Figure 5.7 (b) presents the obtained capacity if the

temperature is limited to 60°C and 70°C. If there is no temperature control, the cell with cathode porosity of 20% has the highest capacity when the discharge current is 6A. The decrease of capacity for the cathode porosity of 15% is due to the self-shutdown. When the temperature is limited to 70°C, the cell with cathode porosity of 20% no longer can provide the max capacity, but the cell with cathode porosity of 25% provides the max capacity. If we further limit the temperature at 60°C, the cathode porosity, which can provide the max temperature, shift to 35%. Another way to control the cell temperature is by controlling microstructure. From Figure 5.6 (a) and (b), by controlling the porosity (i.e. amount of active material), the max temperature can be controlled. To keep the max temperature away from the *unsafe* region shown in Figure 5.6 (a) and (b), we can choose to simply increase the porosity or decrease the porosity until the self-shutdown happen. Figure 5.8 (a) and (b) shows the window of microstructure design when the discharge current is 8A. In Figure 5.8 (a), if the desired temperature limit is 80°C, the cell should with the cathode porosity larger than 26% or smaller 18%. Similarly, if the desired temperature limit is 70°C, the cell should with the cathode porosity larger than 36% or smaller 16%. The lower the desired temperature-limit the less choice for the microstructure design. Similar to the external control, when the microstructure is designed to control the temperature, there is some compensation in cell capacity. The corresponding capacity the designed electrode microstructure can obtain is also shown in Figure 5.8 (a). From the comparison, the choice increase porosity (*i.e.* decrease the amount of active material) can result in a higher capacity of cell. Figure 5.8 (b) shows the microstructure

control when the cell operates at T_{amb} = 40°C. Due to the higher max temperature, the design window of the microstructure is smaller than the cell operate at T_{amb} = 25°C.

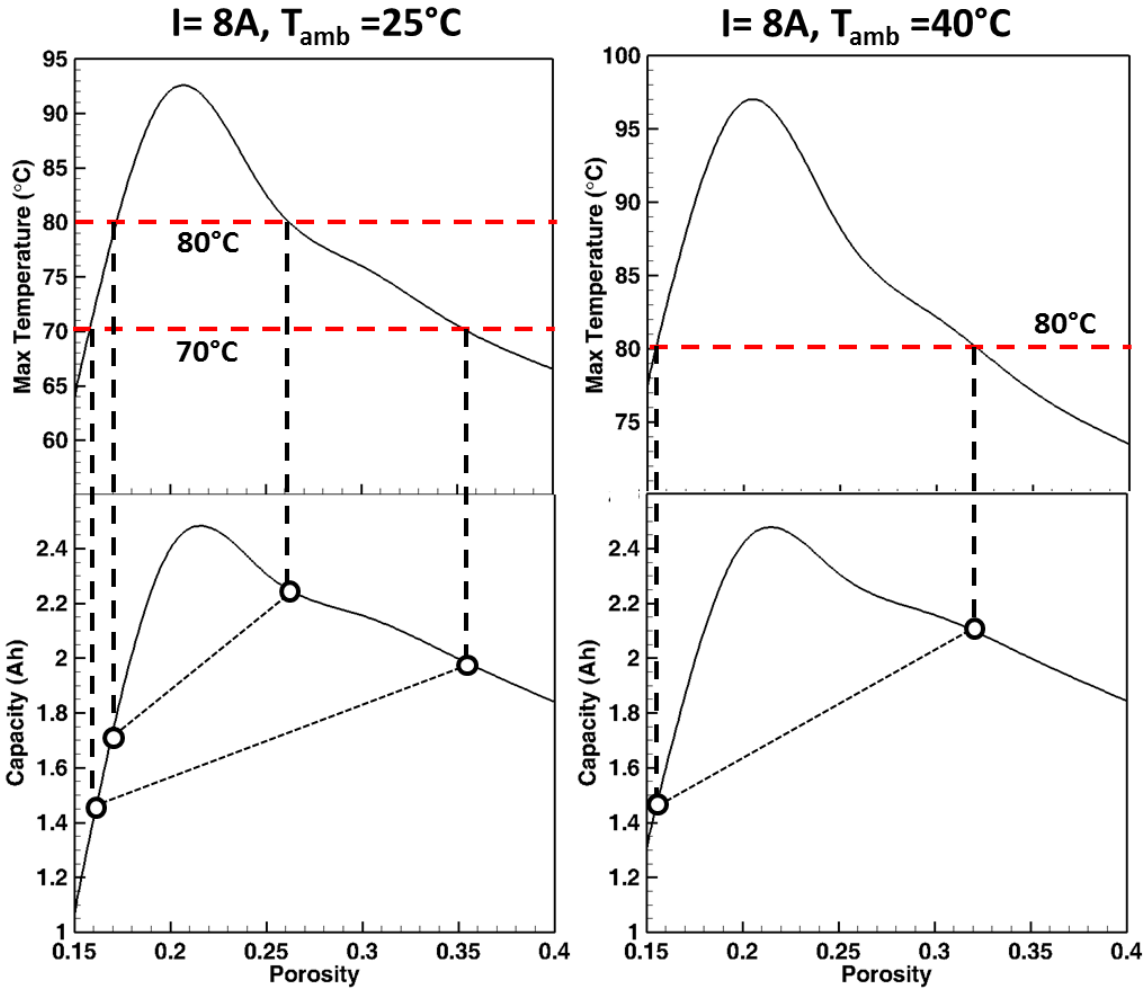

Figure 5.8.*(a) The microstructure design window and the corresponding capacity when I= 8A and T_{amb}=25°C. (b) The microstructure design window and the corresponding capacity when I= 8A and T_{amb}=40°C.*

From the results, it seems that to control the temperature with microstructure, increase porosity is a better choice since it can have a higher capacity. However, this is only true if the high discharge current is *"intentional"*. There are lots of conditions, which the high current is *"not intentional"*, such as the failure of the control system and external short. In this condition, decrease the porosity, which can have self-shutdown is a better choice for some certain conditions. As shown in Figure 5.6 (a), in the discharge current range of 0A – 10A, both low porosity electrode (ε = 0.15 – 0.18) and high porosity electrode (ε = 0.32 – 0.4) keep the max temperature below 80°C. However, under low discharge current, which may be the *normal* operation current, low porosity electrode (ε = 0.15 – 0.18) has higher capacity due to the larger amount of active material. Therefore, the low porosity electrodes (ε = 0.15 – 0.18) have the advantage of (i) high capacity under low discharge current (ii) self-shutdown mechanism to prevent the temperature rise to thermal runaway. For larger ambient temperature, such as T_{amb} = 40°C, even with the self-shutdown mechanism, the cell still unsafe in the discharge current range between 4A to 7A. In this condition, the electrode porosity may need to decrease further to keep the max temperature below the safety limit. In general, according to the operation condition of the cell and the microstructure dependent thermal behavior, there exist an optimize microstructure design to keep the safety of cell.

5.3 Conclusions

In this paper, the influence of electrode microstructure on the thermal behavior of lithium-ion batteries has been elucidated. In this regard, a microstructure-aware electrochemical-thermal model has been proposed, which adopted the reconstruction of

the 3D virtual microstructure. This model can better capture the transport property (i.e. tortuosity) compare to the Bruggeman ideal relation. The impact of cathode microstructure on the cell temperature has detailed addressed and analyzed by studying the time evolution and spatial distribution of different heat sources (i.e joule heating, reversible heating, and reaction heating). During the discharging process, the influence of cathode microstructure on the joule heating and reaction heating is mainly observed in the cathode, and the influence of microstructure on the reversible heating is mainly observed in the anode. The difference in the total heating rate is mainly observed near the cathode/separator interface and at the end of discharge.

From the study of the microstructure dependent thermal behavior, the trade-off between cell capacity and temperature control has been addressed and discussed. Although increase the amount of active material can boost the cell capacity, it also raises the cell temperature and increases the risk of thermal runaway. To control the temperature below the safety limit, parts of the capacity of the cell are sacrificed. In addition, the study of the microstructure dependent thermal behavior provides the insight of using electrode microstructure to control the cell temperature. Increasing electrode porosity can decrease the cell temperature due to the low heating rate. Besides increasing electrode porosity, the self-shutdown mechanism also can limit the cell temperature if the electrode porosity is low enough, especially discharge with high current. In summary, the study of microstructure dependent thermal behavior provides a direction to improve the safety of battery without additional external control mechanism.

CHAPTER VI

MICROSTRUCTURE EFFECT ON THE IMPEDANCE RESPONSE OF LITHIUM-SULFUR BATTERY CATHODE

In this study, with the frameworks from previous EIS study of lithium-ion batteries, we develop a microstructure-aware impedance model, which takes the electrochemical reactions, lithium polysulfide precipitation, and microstructure evolution into account. The advantage mathematical approach of impedance analysis is that it can directly connect the electrochemical reactions and microstructure properties to the impedance response. Unlike the experimental approach, which can only interpret the impedance response with a series of resistor-capacitor (RC) circuit. The resistor-capacitor (RC) circuit fitting method does not have the ability to identify the source of resistance or capacitance. In this study, the microstructure and impedance evolution during the discharging process has been detailing addressed and discussed. The influence of microstructure change has been studied from transport properties, interfacial area, pore size change, and path blockage. From the proposed microstructure-aware impedance model, the impedance evolution during the discharging process has been discussed based on the change of active species concentration and microstructure. In addition, according to the study of impedance evolution during the discharging process, a possible strategy of carbon substrate (i.e. without any solid sulfur and precipitation) microstructure selection has been proposed and analyzed from the impedance response. This microstructure-aware computational model

prediction provides a virtual diagnosis of impedance response and insights of determining the cathode of lithium-sulfur batteries.

6.1 Simulation Methodology

The schematic diagram of our microstructure-aware impedance model is as shown in Figure 6.1 (a). First, microstructures with desired mean pore size, porosity, and volume fraction of precipitation/loaded solid sulfur were reconstructed. From the 3D virtual microstructure, the microstructure properties (i.e. porosity, tortuosity, and active interfacial area) can be obtained. The microstructure properties were used as inputs for the electrochemical model to predict species concentration (i.e. S_8, S_8^{2-}, S_6^{2-}, S_4^{2-}, S_2^{2-}, S^{2-}, Li^+, and A^-) variation during the discharge process. With the calculated species concentration and microstructure properties, the impedance response of the porous electrode of Li-S battery can be predicted.

6.1.1 Species Concentration Variation during Discharge

During the discharging process of lithium-sulfur batteries, the species evolution can be divided into several steps. First, the solid phase sulfur ($S_{8(s)}$) loaded in the cathode is dissolved into the electrolyte and become $S_{8(l)}$. The $S_{8(l)}$ is reduced to lower order sulfide ions by taking electrochemical reactions (reactions [2] – [6]) on the interface between solid phases (i.e. carbon substrate, precipitation, undissolved solid sulfur) and electrolyte.

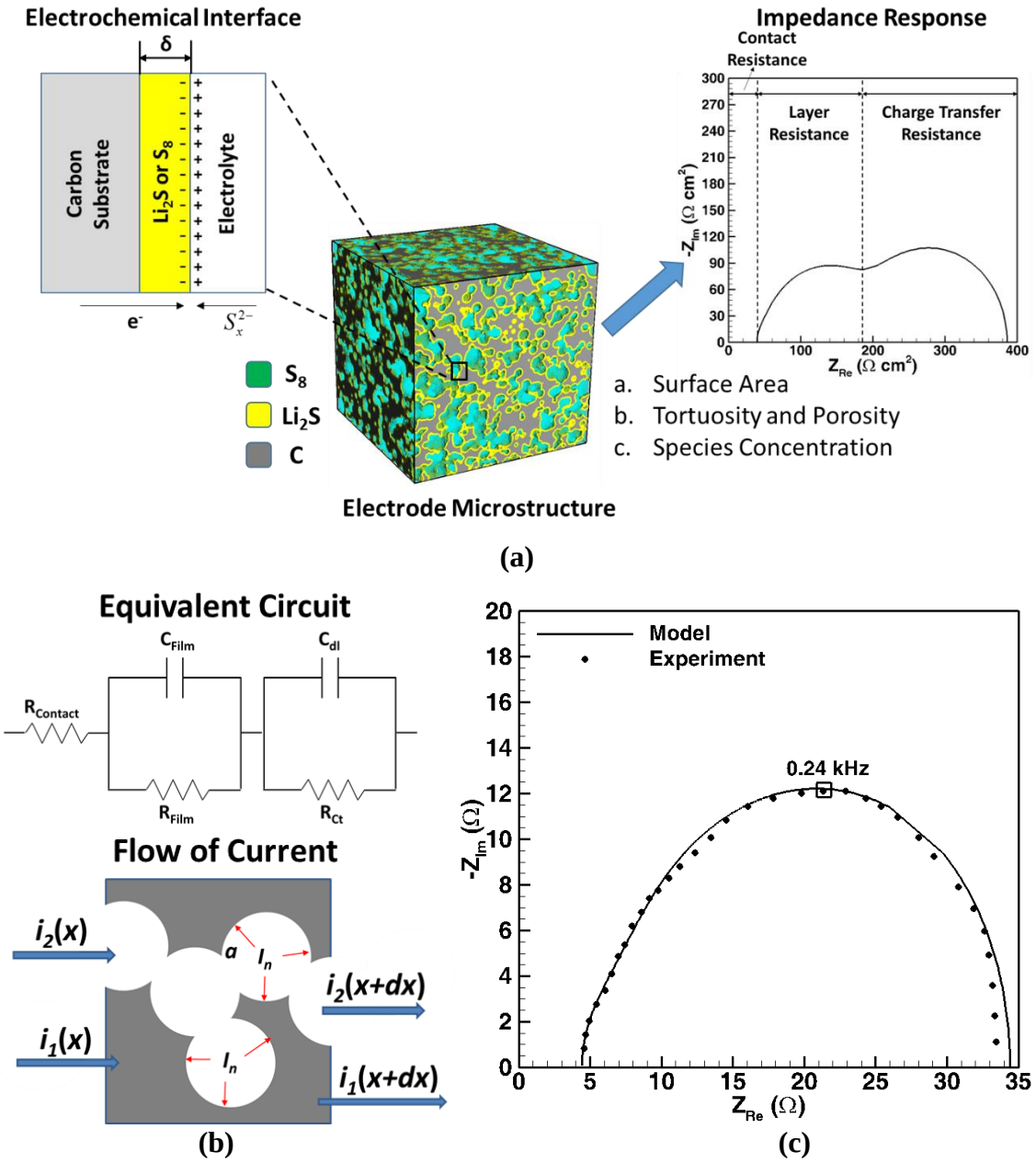

Figure 6.1. *(a) Schematic diagram of microstructure-aware impedance model for lithium-sulfur battery (b) Equivalent circuit of the interface and the schematic diagram showing the differential flow of current in the cathode of Li-S battery (c) Validation of microstructure-aware impedance model with experiment [148].*

[1] $Li^+ + e^- \underset{c}{\overset{d}{\rightleftharpoons}} Li$

[2] $\frac{1}{2} S_{8(l)} + e^- \underset{c}{\overset{d}{\rightleftharpoons}} \frac{1}{2} S_8^{2-}$

[3] $\frac{3}{2} S_8^{2-} + e^- \underset{c}{\overset{d}{\rightleftharpoons}} 2S_6^{2-}$

[4] $S_6^{2-} + e^- \underset{c}{\overset{d}{\rightleftharpoons}} \frac{3}{2} S_4^{2-}$

[5] $\frac{1}{2} S_4^{2-} + e^- \underset{c}{\overset{d}{\rightleftharpoons}} S_2^{2-}$

[6] $\frac{1}{2} S_2^{2-} + e^- \underset{c}{\overset{d}{\rightleftharpoons}} S^{2-}$

Besides the electrochemical reactions, the sulfide ions and reaction with lithium ions and form lithium polysulfide Li_2S_x (reaction [7] – [10]), which can precipitate on the carbon substrate. In this study, only the precipitation of Li_2S is considered.

[7] $2Li^+ + S_8^{2-} \rightleftharpoons Li_2S_{8(s)}$

[8] $2Li^+ + S_4^{2-} \rightleftharpoons Li_2S_{4(s)}$

[9] $2Li^+ + S_2^{2-} \rightleftharpoons Li_2S_{2(s)}$

[10] $2Li^+ + S^{2-} \rightleftharpoons Li_2S_{(s)}$

To obtain the species evolution during the discharge process, this paper used the model developed in our previous study. For the multispecies electrolyte system of Li-S batteries, the mass conservation can be described as

$$\frac{\partial \varepsilon C_i}{\partial t} = r_i - R_i \tag{6.1}$$

where ε is the porosity, and C_i is the concentration of species i (i = S_8, S_8^{2-}, S_6^{2-}, S_4^{2-}, S_2^{2-}, S^{2-}, Li^+, and A^-). A^- is the anion of lithium salt used in the electrolyte. r_i is the mass

production/consumption due to the electrochemical reactions, which can be calculated from reaction current density i_j.

$$r_i = -a\sum_j \frac{s_{i,j} i_j}{n_j F} \tag{6.2}$$

where a is the specific active interfacial area, n_j is the number of electrons participate in the reaction j, and $s_{i,j}$ is the stoichiometric coefficient of species i participated in reaction j (see

Table ***6.1***).

Table 6.1. *Stoichiometric coefficients,* $s_{i,j}$

	Species, *i*						
Reaction, *j*	Li^+	$S_{8(l)}$	S_8^{2-}	S_6^{2-}	S_4^{2-}	S_2^{2-}	S^{2-}
1	-1	0	0	0	0	0	0
2	0	-1/2	1/2	0	0	0	0
3	0	0	-3/2	2	0	0	0
4	0	0	0	-1	3/2	0	0
5	0	0	0	0	-1/2	1	0
6	0	0	0	0	0	-1/2	1

Table 6.2. *Properties for Electrochemical Reaction*

Reaction, *j*	$i_{0,jref}$[a] **(A/m^2)**
1	0.394
2	9.86×10^{-3}
3	9.5×10^{-5}
4	9.5×10^{-5}
5	9.85×10^{-7}
6	9.85×10^{-10}

[a] Assumed parameters.

Table 6.3. *Transport properties and reference concentrations*

Species, *i*	z_i	D_i^a **(m²/s)**	$C_{i,ref}$*[179]* **(mol/m³)**
Li^+	+1	1×10^{-11}	1001.04
$S_{8(l)}$	0	1×10^{-10}	19[a]
S_8^{2-}	-2	6×10^{-11}	0.178
S_6^{2-}	-2	6×10^{-11}	0.324
S_4^{2-}	-2	1×10^{-11}	0.02
S_2^{2-}	-2	1×10^{-11}	5.229×10^{-7}
S^{2-}	-2	1×10^{-11}	8.267×10^{-10}
A^-	-1	4×10^{-11}	1000.0

[a] Assumed parameters.

The reaction current density i_j can be calculated by the Butler-Volmer for multispecies as shown in Eq. (6.3).[179, 180] The parameters used for Eq. (6.3) is given in Table ***6.2*** and Table 6.3.

$$i_j = i_{0,\mathrm{j}ref}\left\{\prod_i\left(\frac{C_i}{C_{i,ref}}\right)^{s_{ij}}\exp\left(\frac{\alpha_{a,j}F}{RT}\eta_j\right)-\prod_i\left(\frac{C_i}{C_{i,ref}}\right)^{-s_{ij}}\exp\left(-\frac{\alpha_{\mathrm{c},j}F}{RT}\eta_j\right)\right\} \qquad (6.3)$$

where the overpotential η_j is defined as

$$\eta_j = \phi_s - \phi_e - U_{j,ref} \qquad (6.4)$$

The summation of reaction current should equation to the apply current as

$$I_{app} = \sum_j i_j \cdot S \tag{6.5}$$

where S is the interfacial area between electrolyte and solid phase.

Table 6.4. *Parameters for precipitation/dissolution reactions.*

Parameter		Value[a]
K_{Li_2S}	Solubility of Li_2S (mol^3m^{-9})	1000
$K_{S_{8(s)}}$	Solubility of $S_{8(l)}$ ($mol\ m^{-3}$)	19
$k_{S_{8(s)}}$	Rate constant of $S_{8(l)}$ (s^{-1})	1.0
S_0	Surface area of solid phase (m^2)	5.51×10^{-2}
V_{Li_2S}	Molar volume of Li_2S (m^3/mol)	2.768×10^{-5}
V_0	Reference volume of Li_2S (m^3)	7.87×10^{-8}

[a] Assumed parameters.

R_i in Eq. (6.1) denotes the production/consumption of species i due to the dissolution/precipitation. The parameters for Ri calculation is given in Table 6.4.

The consumption of species i due to the precipitation is obtained from the film growing rate of precipitation calculated from the Kinetic Monte Carlo (KMC) simulation.

$$\frac{d\delta_{Film}}{dt} = 1.04\times10^{-6}\frac{VS_0}{V_0 S}\left(C_{S^{2-}} \cdot C_{Li^+}^2 - K_{Li_2S}\right) \tag{6.6}$$

where V_0 and S_0 are the reference volume of Li_2S and the reference surface area of solid phase respectively, and K_{Li_2S} is the solubility of Li_2S. The volume of Li_2S (V) and the surface area of solid phase (S) are obtained from virtual 3D microstructure. The precipitation thickness δ_{Film} was referring to a certain virtual 3D reconstructed

microstructure and the corresponding volume fraction of precipitation ε_{Li_2S}. With the change of precipitation volume fraction, the consumption of S^{2-} and Li^+ can be calculated from

$$R_i = \frac{\partial \varepsilon_k}{\partial t} \frac{\gamma_{i,k}}{V_k} \tag{6.7}$$

where V_k is the molar volume of Li_2S or $S_{8(l)}$ and $\gamma_{i,k}$ is the number of moles of S^{2-} and Li^+ in Li_2S ($\gamma_{S^{2-},Li_2S} = 1, \gamma_{Li^+,Li_2S} = 2,$).

The production of $S_{8(l)}$ due to the dissolution of loaded solid sulfur $S_{8(s)}$ is calculated from Eq. (6.8).

$$R_{S_{8(l)}} = k_{S_{8(s)}} \varepsilon_{S_{8(s)}} \left(C_{S_{8(l)}} - K_{S_{8(s)}} \right) \tag{6.8}$$

where $k_{S_{8(s)}}$ is the rate constant and $K_{S_{8(s)}}$ is the solubility of $S_{8(l)}$. To accommodate the $S_{8(s)}$ dissolution, the change of the volume fraction of $S_{8(s)}$ can be calculated from Eq. (6.7), and the microstructure was changed accordingly. One should notice that since the discharge rate is set to C/20 in this study, the species transport has been ignored in Eq. (6.1). The specific active interfacial area *a* is obtained from the reconstructed virtual 3D microstructure. The result of species concentration is used as input of impedance model. The detail of impedance model and reconstruction of 3D virtual microstructure will be presented in the following section.

6.1.2 Impedance Response of Porous Electrode

In this paper, the electrochemical interface can be described as Figure 6.1 (a). This model assumes that the loaded solid sulfur $S_{8(s)}$ or precipitation of Li_2S can be treated as a homogeneous layer throughout the porous electrode with certain thickness δ. The electrochemical reactions take place at the interface between electrolyte and precipitation (or $S_{8(s)}$). For electrochemical reaction to happen, the electrons should pass the additional layer. The equivalent circuit for charge transport through the interface can be described as Figure 6.1 (b). $R_{contact}$ is the contact resistance between carbon substrate and precipitation (or $S_{8(s)}$). R_{Film} is the resistance due to the low conductivity of precipitation (or $S_{8(s)}$) and C_{Film} is the film capacitance. The film resistance and capacitance can be calculated by

$$R_{Film} = \rho_{Film} \cdot \delta_{Film} \text{ and } C_{Film} = \frac{\varepsilon_{Film}}{\delta_{Film}} \tag{6.9}$$

where ρ_{Film} is the film resistivity and ε_{Film} is the film permittivity. C_{dl} is the capacitance due to the double layer near the interface. R_{ct} is the charge transfer resistance contributed by the electrochemical reaction. The charge transfer resistance can be derived from the Butler-Volmer equation for multispecies as shown in Eq. (6.3).[179, 180] To calculate the impedance response under equilibrium potential, the reference open-circuit potential $U_{j,ref}$ should change to equilibrium open-circuit potential $U_{j,\mathrm{eq}}$ by

$$U_{j,\mathrm{eq}} = U_{j,ref} - \frac{RT}{n_j F} \sum_i s_{i,j} \ln\left[\frac{C_i}{C_{i,ref}}\right] \tag{6.10}$$

With Eq.(6.10), the Butler-Volmer equation can be rewrote to

$$i_j = i_{0,ref}\left(\frac{C_{a,i}}{C_{a,i,ref}}\right)^{\alpha_a \cdot s_{a,i,j}}\left(\frac{C_{c,i}}{C_{c,i,ref}}\right)^{-\alpha_c \cdot s_{c,i,j}}\left\{\exp\left(\frac{\alpha_{a,j}F}{RT}\eta_{j,\mathrm{eq}}\right)-\exp\left(-\frac{\alpha_{a,j}F}{RT}\eta_{j,\mathrm{eq}}\right)\right\} \quad (6.11)$$

where the subscript *a* and *c* corresponding to anodic species and cathodic species respectively and the overpotential $\eta_{j,eq}$ is given by

$$\eta_{j,eq} = \phi_s - \phi_e - U_{j,\mathrm{eq}} \quad (6.12)$$

The charge transfer resistance can be calculated by linearizing the Butler-Volmer equation (Eq. (6.11))[181] with the ignorance of Warburg impedance (since there is no solid phase diffusion inside the cathode of Li-S battery and the resistance of the diffusion layer has been neglected in this study). The expression of charge transfer resistance under equilibrium potential can be finalized as

$$R_{ct}^{-1} = \frac{\Delta E}{\Delta I} = \sum_j i_{0,\mathrm{j}ref}\left(\frac{C_{a,i,j}}{C_{a,i,\mathrm{j}ref}}\right)^{\alpha_a \cdot s_{a,i,j}}\left(\frac{C_{c,i,j}}{C_{c,i,\mathrm{j}ref}}\right)^{-\alpha_c \cdot s_{c,i,j}}\frac{F(\alpha_{a,j}+\alpha_{\mathrm{c},j})}{RT} \quad (6.13)$$

From Eq. (6.13), the total charge transfer resistance is the summation of all the kinetic resistance take place in the cathode (reaction [2]–[6]). The values used in this study for charge transfer resistance is listed in

Table ***6.2*** and Table 6.3.With all the components, the impedance response of the equivalent circuit can be calculated by

$$Z_{\text{interface}} = R_{contact} + \frac{R_{ct}}{1 + j\omega R_{ct} C_{dl}} + \frac{R_{Film}}{1 + j\omega R_{Film} C_{Film}} \tag{6.14}$$

Eq. (6.14) can be treated the impedance on the electrochemical interface.

By implementing the method developed Meyers and Newman et al. [130] the impedance response for the porous electrode can be derived with the using of interfacial impedance *Z*. Figure 6.1 (b) shows the schematic diagram of the differential flow inside the porous electrode. i_1 and i_2 are the current contributed by electron and ion respectively. The summation of i_1 and i_2 should equation to the total current *I*. From Ohm's law, the potential gradient of solid phase and electrolyte phase can be calculated from

$$\begin{aligned} \frac{\partial \phi_s}{\partial x} &= -\frac{I - i_2}{\sigma^{eff}} \\ \frac{\partial \phi_e}{\partial x} &= -\frac{i_2}{\kappa^{eff}} \end{aligned} \tag{6.15}$$

where σ^{eff} is the effective electronic conductivity and κ^{eff} is the effective ionic conductivity. The effective charge transport properties are calculated by the Bruggeman relation.

$$\Phi^{eff} = \Phi \frac{\varepsilon}{\tau} \tag{6.16}$$

where τ is the tortuosity which is calculated from the 3D virtual microstructure. The ionic conductivity κ is obtained from Eq. (6.17) and the species concentration calculated from the electrochemical model.

$$\kappa^{eff} = \sum_i \frac{z_i^2 D_i^{eff}}{RT} F^2 C_i \tag{6.17}$$

With the charge conservation, the gradient of ionic current can be expressed as

$$\frac{\partial i_2}{\partial x} = aI_n = \overline{aY}\left(\phi_s - \phi_e\right), \text{ where } Y = Z^{-1} \text{ and } I_n = \sum_j i_j \tag{6.18}$$

By solving Eq. (6.15) and (6.18) with the boundary condition of

$$\begin{aligned} &i_2 = I \text{ at } x = 0 \text{ (seperator/electrode interface)} \\ &i_2 = 0 \text{ at } x = L \text{ (current collector)} \end{aligned} \tag{6.19}$$

The impedance response of porous electrode can be expressed as

$$Z_{electrode} = \frac{L}{\kappa^{eff} + \sigma^{eff}}\left[1 + \frac{2 + \left(\frac{\sigma^{eff}}{\kappa^{eff}} + \frac{\kappa^{eff}}{\sigma^{eff}}\right)\cosh\nu}{\nu\cosh\nu}\right], \nu = L\left(\frac{\kappa^{eff}\sigma^{eff}}{\kappa^{eff} + \sigma^{eff}}\right)^{-0.5}\left(\overline{aY}\right)^{0.5} \tag{6.20}$$

The parameters need to evaluate the impedance response are listed in Table 6.5. The Nyquist plot showed in Figure 6.1 (a) shows an example of impedance response of the microstructure-aware impedance model. The impedance response can be distributed to three parts. The semi-circle at the low frequency region (semi-circle on the right) corresponding to the charge transfer resistance. The semi-circle at the medium frequency region (semi-circle on the left) is contributed by the layer resistance. The shift of impedance response at the high frequency region is referring to the contact resistance between the precipitation (solid sulfur) layer and carbon substrate.

Table 6.5. *Properties for the calculation of impedance response*

Parameters		**Value**
L	Electrode thickness (μm)	60
R	Gas constant	8.3143
ε_{Film}	Layer permittivity (F cm^{-1})	30.989×10^{-13}
ρ_{Film}	Layer resistivity (Ω cm)	7×10^{6}
σ^{eff}	Effective electrical conductivity (S/cm)	1

6.1.3 Reconstruction of Microstructure and Evaluation of Charge Transport Properties

The virtual 3D microstructure was reconstructed according to the SEM image of the experimental cathode framework and the amount of solid sulfur/lithium polysulfide precipitation and porous carbon substrate. The carbon substrate, which is used to store solid sulfur and to provide pathways for ionic transport, is reconstructed with the stochastic method.[45, 176-178] The spherical pores are randomly distributed within the carbon substrate with desired porosity. The pore size distribution can be varied with different cathode design. The spherical pores are allowed to overlap with one another. In this study, solid sulfur and lithium polysulfide precipitation are assumed as a uniform film between electrolyte and carbon substrate. The thickness of film changes with the amount remaining solid sulfur and lithium polysulfide precipitation. Figure 6.2 (a) shows the corresponding microstructure with different volume fraction of precipitation.

Effective electrochemical properties are calculated by solving the concentration gradient inside the microstructure. It is worth mentioning that the diffusion mechanism is dependent on the Knudsen number, which is characterized by the pore size relative to the mean free path of the diffusing ions. In the case of porous lithium sulfur cathode, the

Knudsen number is very small (Kn<<1), which means that the pore diameters are large compared to the mean free path length of the diffusing ions. Thus, bulk diffusion modeling can be utilized. The diffusion is governed by Laplace's equation

$$-\Delta c_i = 0 \,, i = \mathrm{x}, \mathrm{y}, \mathrm{z} \tag{6.21}$$

with the boundary condition of

$$c(0) = c_{left} \quad \text{and } c(L) = c_{right} \tag{6.22}$$

where c is the Li^+ ion concentration. The effective diffusivity can be calculated from Eqns. (6.21) and (6.22). [60]

$$\frac{D}{D_i^{eff}} = \frac{\left(c_R - c_L\right)/L}{\int\int \nabla c(x) dadi / AL} \tag{6.23}$$

where L is the length of modeling domain (control volume), A is the surface area of simulation box of direction i flux ,and D_κ^{eff} is the effective diffusivity in direction i. The tortuosity can then be determined via Bruggeman relation[51, 77]

$$D_i^{eff} = D\frac{\varepsilon}{\tau} \tag{6.24}$$

where D is the intrinsic diffusivity of a substance in a gas, ε is the porosity (*i.e.* volume fraction of pore space) of the microstructure and τ is the tortuosity of the microstructure.

The comparison between the EIS obtain from the microstructure-aware impedance model and experimental result is as shown in Figure 6.1.[148] The simulation result shows good agreement with the experimental EIS.

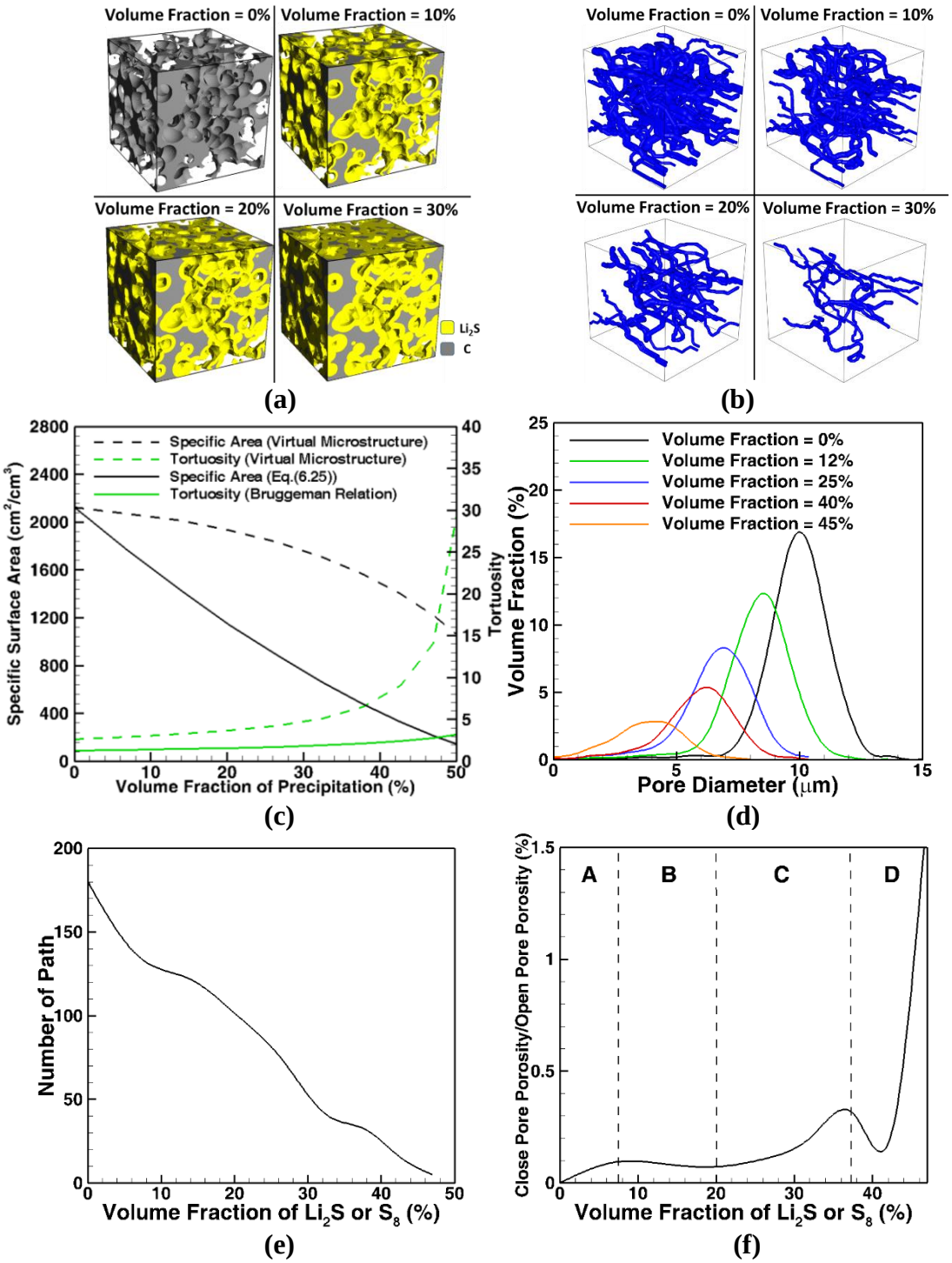

Figure 6.2*.(a) Corresponding microstructure with different volume fractions of S_8 loading or precipitation. (b) The particle transport path in the microstructure (c) Comparison between theoretical value and the value obtained from 3D virtual microstructure. (d) Pore size distribution (e) Number of Path and mean path length (f) Fraction of closed pores.*

6.2 Results and Discussion

6.2.1 Validation of Microstructures with S_8 Loading and Precipitation

As mentioned in the previous section, due to the precipitation or solid sulfur loading, the microstructure of sulfur electrode varies according to the volume fraction of precipitation (solid sulfur). The variation of microstructure properties with different volume fraction of precipitation (solid sulfur) is presented in this section. In this section, the initial porosity (i.e. porosity of carbon substrate) is fixed at 60%. The representative microstructure with different volume fraction of precipitation (solid sulfur) is as shown in Figure 6.2 (a). As shown in Figure 6.2 (a), the thickness of the layer between carbon substrate and electrolyte changes with the increase of volume fraction of precipitation (solid sulfur). With the presence of precipitation (solid sulfur), the microstructure properties, such as porosity, tortuosity, and electrochemical interfacial area vary accordingly as shown in Figure 6.2 (c). Figure 6.2 (c) also shows the comparison between the values calculated from 3D virtual microstructure and theoretical calculation. For the interfacial area, lots of previous research used the relation of [179]

$$a = a_0 \left(\frac{\varepsilon}{\varepsilon_{initial}} \right)^{1.5} \tag{6.25}$$

where a_0 is the interfacial area without loading sulfur and precipitation.

However, from Figure 6.2 (c), Eq. (6.25) under the estimate surface area. Similarly, the Bruggeman ideal relation suggested that the tortuosity can be calculated from Eq. (6.26).

$$\tau = \varepsilon^{-0.5} \tag{6.26}$$

However, since the distribution of pores is not uniform within the electrode and the pores can be closed by the precipitation, the tortuosity inside the electrode microstructure is larger than the tortuosity calculated by Bruggeman ideal relation (see Figure 6.2 (c)). The variation of pore size distribution is as shown in Figure 6.2 (d). From Figure 6.2 (d), when the volume fraction of precipitation (solid sulfur) increases, the mean pore size decrease because of the increase of layer thickness. The diminution of pore size could increase the species transport path length and disconnect between pores, which can increase the internal resistance or electrode isolation. Figure 6.2 (b) and (e) show the particle transport path inside the microstructure with different volume fraction of precipitation (solid sulfur). Figure 6.2 (b) represents the transport path for the particles with the diameter range of 10 μm – 2 μm. Figure 6.2 (e) shows the the number of transport path for the particles larger than 0.8 μm. When the precipitation (solid sulfur) increase, the increase of layer thickness closes the path for ionic transport in the electrolyte. Following with path close, the number of transport path decrease. Since the number of path decrease, the particle or ion are forced to detour and cause the increase the transport path.

The increase of transport path length and the decrease of path number can hinder the species transport inside the electrode microstructure. Figure 6.2 (f) shows the fraction between open pores porosity and close pores porosity. Close pores referring to the pores, which do not connect with other pores at one certain direction (x-, y-, or z-direction). By averaging fraction between open and close pores at x, y, and z plane, we can obtain the result shown in Figure 6.2 (f). From Figure 6.2 (f), we can divide the results into four regions. At region A, the fraction increases since the precipitation (solid sulfur) close a

portion pores (~0.1%). After region A, the fraction starts to decrease at region B (vol. % = 8 – 20%), which means there is no more close pores and the closed pores at region A become smaller and smaller. Then, the fraction starts to increase again at region C because there are more and more closed pores appear. In the end at region D, between vol. % = 38 – 40% the fraction decrease due to the shrink of closed pore diameter. When the volume fraction larger than 40%, large amount of pores is closed by the precipitation (solid sulfur). The close of pores can result in the increase of transport path and the possible reason to cause the electrode insolation, which can result in capacity loss.

6.2.2 Microstructure–aware Impedance Model

The proposed microstructure-aware impedance model can be used to observe the impedance response of sulfur cathode at different depth of discharge (DOD). In the sulfur cathode, the impedance response is mainly affected by (i) interfacial area (ii) ionic conductivity (iii) charge transfer resistance (iv) layer (Li_2S and S_8) thickness. The influence of these four factors is shown in Figure 6.3. The influence of interfacial area is shown in Figure 6.3 (a). From Figure 6.3 (a), the radius of both semi-circle increase with the decrease of the interfacial electrochemical area. Besides the radius of the semi-circle, the impedance response also shifts to the right when the interfacial area decreases, which means the decrease of contact resistance.

From the results, we can refer that the decrease of interfacial area enlarges all the resistance (i.e. charge transfer resistance, film resistance, and contact resistance) in the sulfur cathode. The influence of ionic conductivity on the impedance response is similar

to the interfacial area as shown in Figure 6.3 (b). However, the ionic conductivity has less influence on the radius of semi-circles. The ionic conductivity has pronounced effect on the radius of semi-circle only when the value of ionic conductivity is low. In other words, when the ionic conductivity is high, the influence of ionic conductivity is mainly on the high frequency resistance and causes the shift of Nyquist plot.

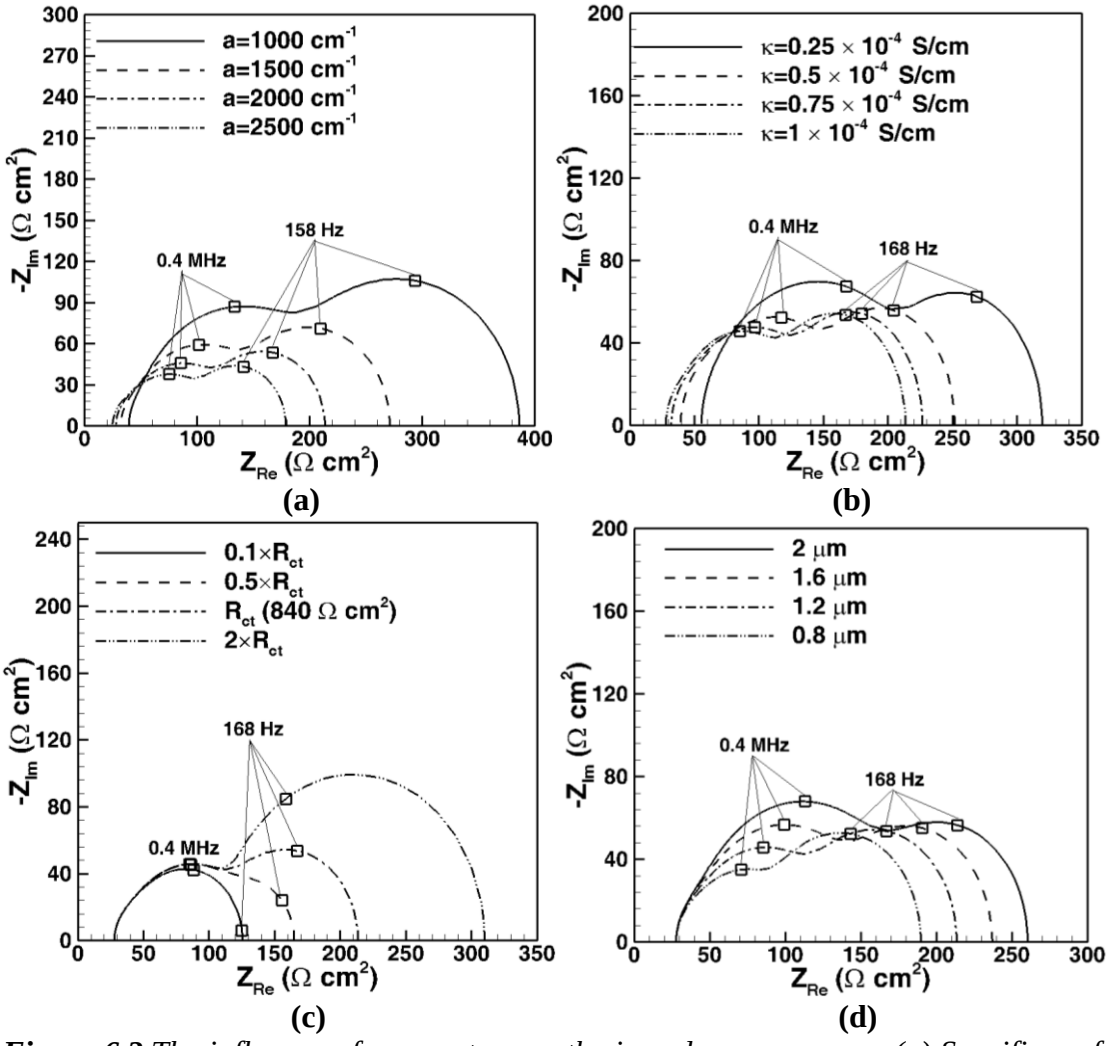

Figure 6.3.*The influence of parameters on the impedance response. (a) Specific surface area (b) Ionic conductivity (c) Charge transfer resistance (d) Layer thickness.*

Figure 6.3 (c) shows the influence charge transfer resistance on the impedance response. The charge transfer resistance is dominated by exchange current density $i_{0,jref}$, and species concentration $C_{i,j}$ according to Eq. (6.13). The variation of charge transfer resistance mainly changes the radius of the semi-circle at the low frequency region (semi-circle on the right), where the radius of left semi-circle remaining the same. Figure 6.3 (d) shows the influence of layer thickness on the impedance response. Opposite to the influence of charge transfer resistance, the variation of layer thickness only changes the radius of semi-circle at the high frequency region (semi-circle on the right). The parametric study on the impedance response can help us to interpret the variation of impedance response during discharge and the impact of microstructure on the impedance response presented in the following sections.

6.2.3 Impedance and Microstructure Evolution during the Discharge Process

With the microstructure-aware impedance model, the impedance evolution during the discharge process can be observed and discussed. The species concentration, which is used to evaluate the charge transfer resistance is calculated from the electrochemical model by discharging the cell under C/20. For the cathode microstructure, the initial loading volume fraction of solid sulfur is 20%. The porosity of carbon substrate is 60%. The representative microstructure can refer to the microstructures showed in *Figure 6.2* (a).

Figure 6.4 (a) shows the time evolution of microstructure during the discharging process. The representative of discharge curve and corresponding DOD is shown in Figure

6.4 (c). At the beginning of discharge, with the presence of loaded solid sulfur, the porosity is 40% and the corresponding layer thickness is ~1.2 μm. At stage one of discharging process (t = 0 – 3 hours), the solid sulfur dissolves into the electrolyte, which decreases the porosity and decreases the layer thickness. The decrease of porosity lowers the tortuosity and enlarges the interfacial electrochemical area. When the solid sulfur full dissolved, there is no film cover on the carbon substrate (thickness = 0 μm) and the microstructure reaches its maximum porosity and interfacial area during the discharging process. After five hours of discharge, the discharge curve reaches its second plateau and the precipitation starts to affect the microstructure. During discharging, the precipitation becomes more and more which causes the decrease of porosity and interfacial area following with the increase of tortuosity and layer thickness. To the end of discharge, the layer thickness can reach ~2 μm and the porosity drops below 25%, which results in large tortuosity and low interfacial area. The variation of pore size distribution is shown in Figure 6.4 (d). When the DOD changes from 0.1 (green) to 0.2 (red), the mean pore size and the fraction of pores increase, which is due to the dissolve of solid sulfur and the decrease of layer thickness.

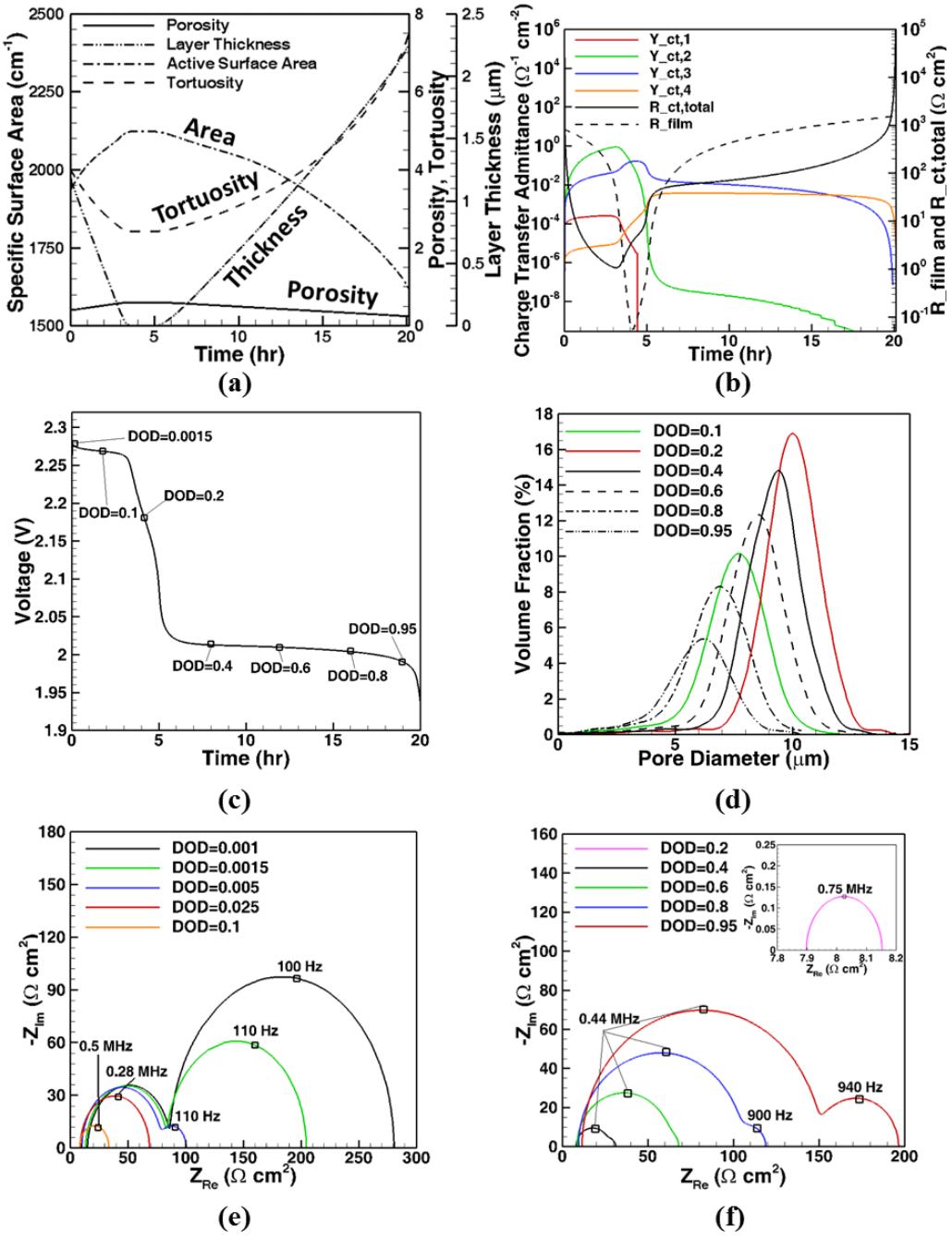

Figure 6.4.*Time evolution of properties and impedance response during the discharging process with C/20. (a) Porosity, tortuosity, active surface area, and layer thickness. (b) Charge transfer admittances of each reaction, total charge transfer resistance, and film (layer) resistance. (c) The corresponding DOD during the discharge process. (d) Pore size distribution. (e) Impedance response at DOD=0.001 – DOD=0.1 (f) Impedance response at DOD=0.2 – DOD=0.95.*

In the rest of discharging process (black), since the increase of precipitation and layer thickness, the mean pore size and volume fraction of pores decrease. The decrease of mean porosity further increases tortuosity for the species transport.

Figure 6.4 (b) shows the time evolution of resistance (admittance) during the discharging process. According to Eq.(6.13), the charge transfer resistance is contributed by the kinetic admittance of electrochemical reactions (reaction [2]–[6]). Study the kinetic admittances of each electrochemical reaction can help us to understand the evolution of charge transfer resistance during the discharging process. Y_{ct_1} to Y_{ct_4} referring to reaction [2] to [5] respectively. Since the concentration of S^{2-} is extremely low, which is because of the large reaction rate between Li^+ and S^{2-}, the admittance for reaction [6] is almost 0. At stage one (t = 0 – 3 hours), both charge transfer resistance and film resistance decrease. The decrease of film resistance is because of the decrease of layer thickness (see Figure 6.4 (a)). The decrease of charge transfer resistance is because of the increase of kinetic admittance of all reactions, especially by reaction [3], due to the large increase species concentration from the electrochemical reactions. At stage two (t = 3 – 5 hours), where the sulfur fully dissolved, the consuming of $S_{8(l)}$, S_8^{2-}, and S_6^{2-} causes the sudden decrease of the kinetic admittance of reaction [2] and [3] and total charge transfer resistance. In addition, the reactions [4] and [5] start to play an important role in the charge transfer resistance. At the third state (t > 5hours), the charge transfer resistance and layer resistance increase with time. The increase of layer resistance is because of the increase of layer thickness of precipitation. The charge transfer resistance is mainly contributed by

reaction [4] and [5]. Since S_6^{2-}, S_4^{2-} and S_2^{2-} keep been consuming by the electrochemical reaction, the kinetic admittance of reaction [4] and [5] keep decreasing, and hence causes the increase of charge transfer resistance. At the end of discharging process, the species concentrations become really low, which causes very low kinetic admittance (<1 $\Omega^{-1}cm^{-2}$). The low kinetic admittance then results in large charge transfer resistance.

By implementing the calculated charge transfer resistance and microstructure properties, such as interfacial area, porosity, tortuosity, and layer thickness, to the microstructure-aware impedance model, the impedance evolution during the discharging process can be predicted. The predicted impedance response at different DOD is as shown in Figure 6.4 (e) and (f). Figure 4 (e) shows the impedance response at the beginning of discharge (DOD = 0.001 – 0.1). When the discharge start, the charge transfer resistance (semi-circle on the right) start to decrease very fast (DOD= 0.001 – 0.005) due to the rapid increase in the species concentration. After DOD = 0.005, the charge transfer resistance becomes very small compared to layer resistance, and there is only one semi-circle in the impedance response. At this stage (DOD= 0.005 – 0.1), the impedance response is dominated by the layer resistance and the resistance decreases with time because of the decrease of the layer thickness of solid sulfur (see Figure 6.4 (a)). When the DOD ~0.2, since the solid sulfur is fully and the precipitation still not obvious, the impedance response is only contributed by the charge transfer resistance, which is very small (because of the large species concentration). When DOD > 0.2, the layer thickness of precipitation start to increase (see Figure 6.4 (a)) and the charge transfer resistance also starts to increase

(see Figure 6.4 (b)) again because of the consuming of species by the electrochemical reactions.

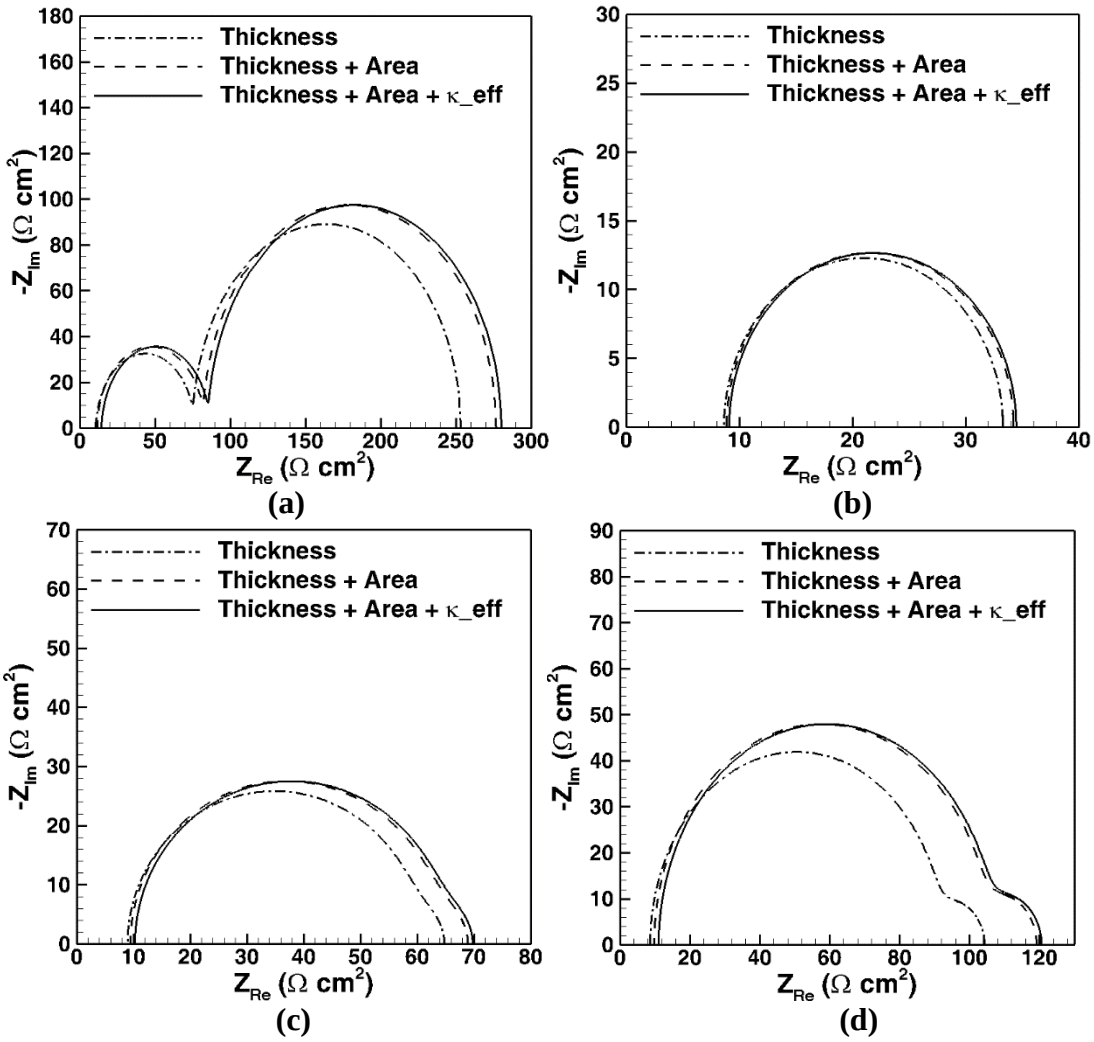

Figure 6.5.*The influence of microstructure on the impedance response during the discharge process by comparing the microstructure properties between carbon substrate and corresponding properties at (a) DOD = 0.001 (b) DOD = 0.1 (c) DOD = 0.6 (d) DOD = 0.8.*

As shown in Figure 6.3, the microstructure properties have an influence on the impedance response. Besides the layer thickness, which directly affect the radius of the semi-circle on the left, it is hard to distinguish the influence of interfacial area and ionic

conductivity since both factors can increase the radius of semi-circles and shift the Nyquist plot as shown in Figure 6.3 (b) and (c). Figure 6.5 shows the comparison of impedance response between the microstructure properties of carbon substrate and the one with precipitation or solid sulfur. At different DOD, three cases have been studied. The first case, the impedance only accounts for the layer thickness. The interfacial area and porosity/tortuosity, which affect the ionic conductivity, are maintained the same as the carbon substrate. The second case, the impedance response accounts for the layer thickness and interfacial area. The porosity/tortuosity are maintained the same as the carbon substrate. The third case, the impedance response accounts for the layer thickness, interfacial area, and porosity/tortuosity. The properties used in these three cases are list in Table 6.6. In all the cases, the charge transfer resistance corresponding to the resistance at the certain DOD.

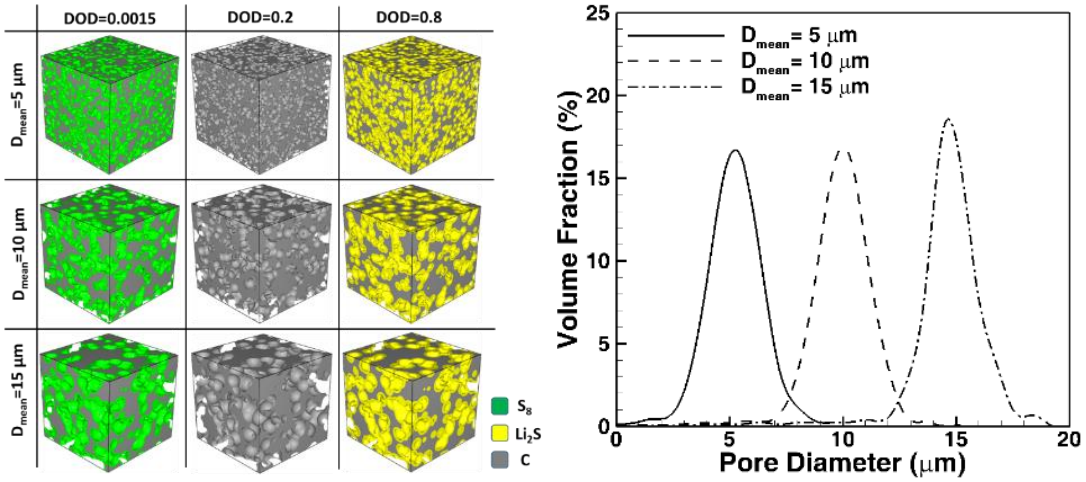

(a) **(b)**

Figure 6.6.*(a) The representative microstructure with different mean pore size at different DOD. (b) Pore size distribution of carbon substrate.*

Table 6.6. *Microstructure Properties for impedance comparision*

		Thickness (μm)	Specific Area (cm^{-1})	Tortuosity	Porosity
DOD=0.001	**case I**	**1.168[a]**	2122.421[b]	2.61[b]	60.0[b]
	case II	**1.168[a]**	**1939.763[a]**	2.61[b]	60.0[b]
	case III	**1.168[a]**	**1939.763[a]**	**3.65[a]**	**40.1[a]**
DOD=0.1	**case I**	**0.445[a]**	2122.421[b]	2.61[b]	60.0[b]
	case II	**0.445[a]**	**2062.217[a]**	2.61[b]	60.0[b]
	case III	**0.445[a]**	**2062.217[a]**	**2.96[a]**	**52.2[a]**
DOD=0.6	**case I**	**0.924[a]**	2122.421[b]	2.61[b]	60.0[b]
	case II	**0.924[a]**	**1992.962[a]**	**2.61[b]**	**60.0[b]**
	case III	**0.924[a]**	**1992.962[a]**	3.39[a]	44.0[a]
DOD=0.8	**case I**	**1.510[a]**	2122.421[b]	2.61[b]	60.0[b]
	case II	**1.510[a]**	**1854.701[b]**	2.61[b]	60.0[b]
	case III	**1.510[a]**	**1854.701[b]**	**4.13[a]**	**34.7[a]**

[a]Property at certain DOD
[b]Property of carbon substrate
Case I: Thickness; Case II: Thickness + Specific area; CaseIII: Thickness + Spedific area + κ^{eff}

The results of the comparison (see Figure 6.5) suggest that the interfacial area has a larger influence on the impedance response compare to the porosity/tortuosity at different DOD. This is because the ionic conductivity is high during the discharging process due to the large species concentration (see Eq. (6.17)). The ionic conductivity has less impact on the impedance response when the value is high. Therefore, although the porosity and tortuosity change effective ionic conductivity, but it has limite influence on the impedance due to the high species concentration. In addition, when DOD = 0.001 and 0.8, the interfacial area has a larger influence on the impedance response compare to DOD =0.1 and 0.6. The difference is because the interfacial area at DOD = 0.001 and 0.8 are much lower than the carbon substrate.

6.2.4 Influence of Pore Size on Microstructure Evolution and Impedance Response

With the conclusion of the previous section, which the interfacial area dominates the impedance response, it is worth studying the influence initial microstructure (i.e. microstructure of carbon substrate) on the microstructure evolution and impedance response during the discharging process. In this study, we change the electrochemical interfacial area by changing the pose size distribution. With the same standard deviation, the smaller the mean pore size can result in a larger interfacial area. Figure 6.6 (a) shows the representative microstructure of different mean pore diameter and Figure 6.6 (b) shows the corresponding pore size distribution. The microstructure at DOD = 0.0015 and DOD = 0.8 also presented in Figure 6.6 (a).

Figure 6.7 shows the microstructure evolution during the discharging process. As expected, the interfacial surface area increase with the decrease of mean pore size as shown in Figure 6.7 (a). The interfacial surface area is larger for small mean pores size microstructure for the whole discharge process. The time evolution of layer thickness at different microstructure is presented in Figure 6.7 (b), where the microstructure with small pore size has thinner layer thickness. The difference in layer thickness is mainly due to the difference in surface area. With the same volume fraction of precipitation (solid sulfur), the large surface area can have thinner layer thickness. During the discharging process, the pore size does not have significant effect on the porosity as shown in Figure 6.7 (c). However, under the same porosity, small mean pore size microstructure has larger tortuosity compare to the other two cases (see Figure 6.7 (d)).

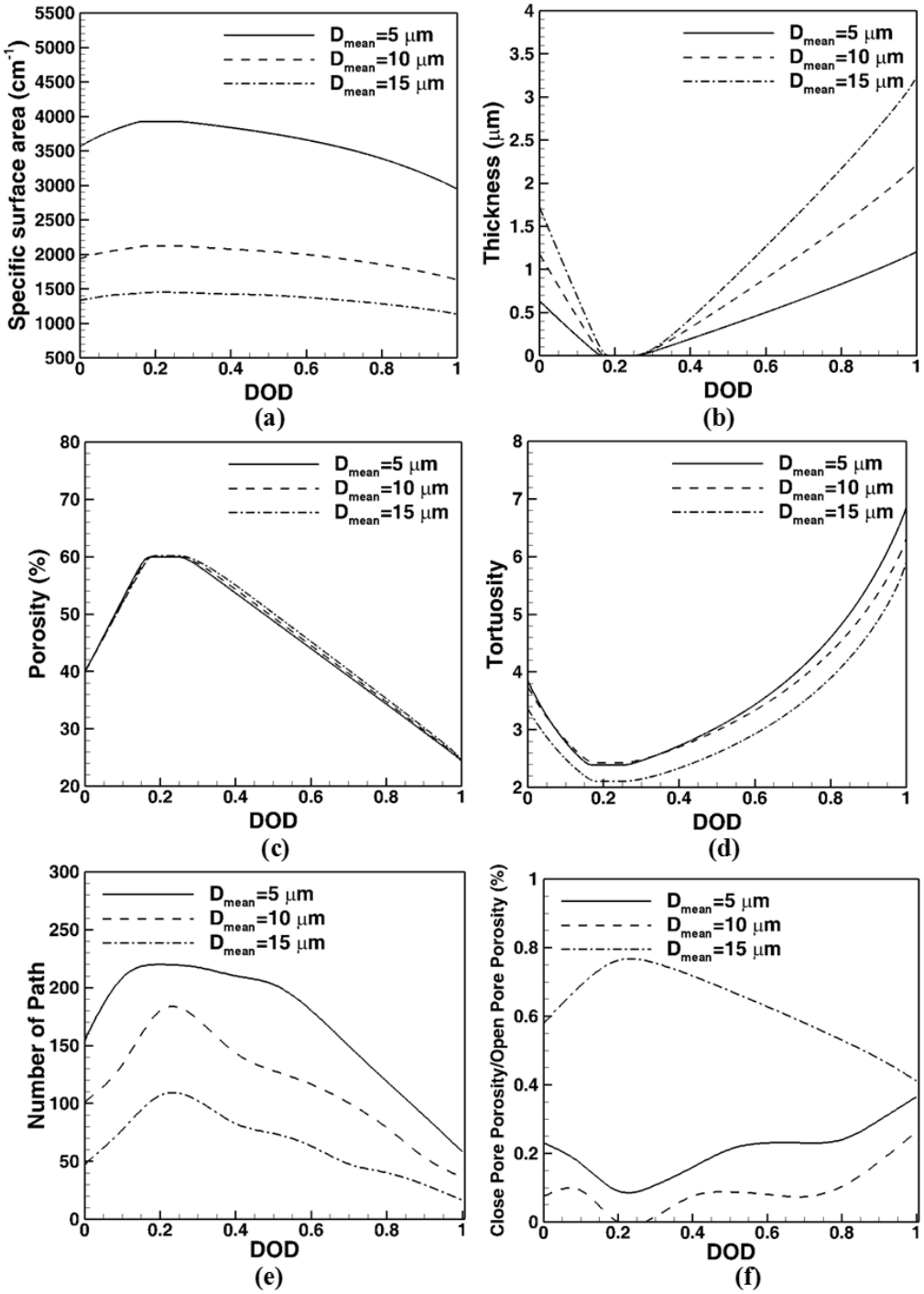

Figure 6.7. *Variation of microstructure properties of different initial mean pore size at different DOD. (a) Specific active surface area (b) Thickness (c) Porosity (d) Tortuosity (e) Number of transport path (c) Fraction of closed pores.*

This is because the transport path for species is more tortuous when the pore size is small. Similar to the previous section, the influence of pore size on the number of transport path and the closure of pores are also studied as shown in Figure 6.7 (e) and (f). Different from the transport length, which reflects as tortuosity, the number of path increase with the decrease of pore size. This result suggests that small pore size has a better interconnection between pores, but it results in longer transport length. In Figure 6.7 (f), the fraction between open pores and close pores is higher for the microstructure with a mean pore diameter of 5 μm than the microstructure with a mean pore diameter of 10 μm. This means the tunnels of the transport path for the small pore microstructure is narrow which can easily block by precipitation (solid sulfur). It is worth noticing that, when the mean pore diameter is 15 μm, the fraction is higher than the other two cases. This is because when the pore size is too large, the microstructure has poor pore interconnection, which forms closed pore even when there is no precipitation (solid sulfur). However, the decrease of fractions with the increase of precipitation (solid sulfur) means that there is no new closed pore during the discharging process since the transport path is wider enough due to the large pore size. The decrease of the fraction is mainly because of the diameter decrease.

Since the microstructure properties have an influence on the species concentration during the discharging process (see Eq. (6.1) and (6.2)), the microstructure properties can vary the charge transfer resistance and hence the impedance response. Figure 6.8 shows the kinetic admittance of each electrochemical reaction, total charge transfer resistance, and layer resistance during the discharging process.

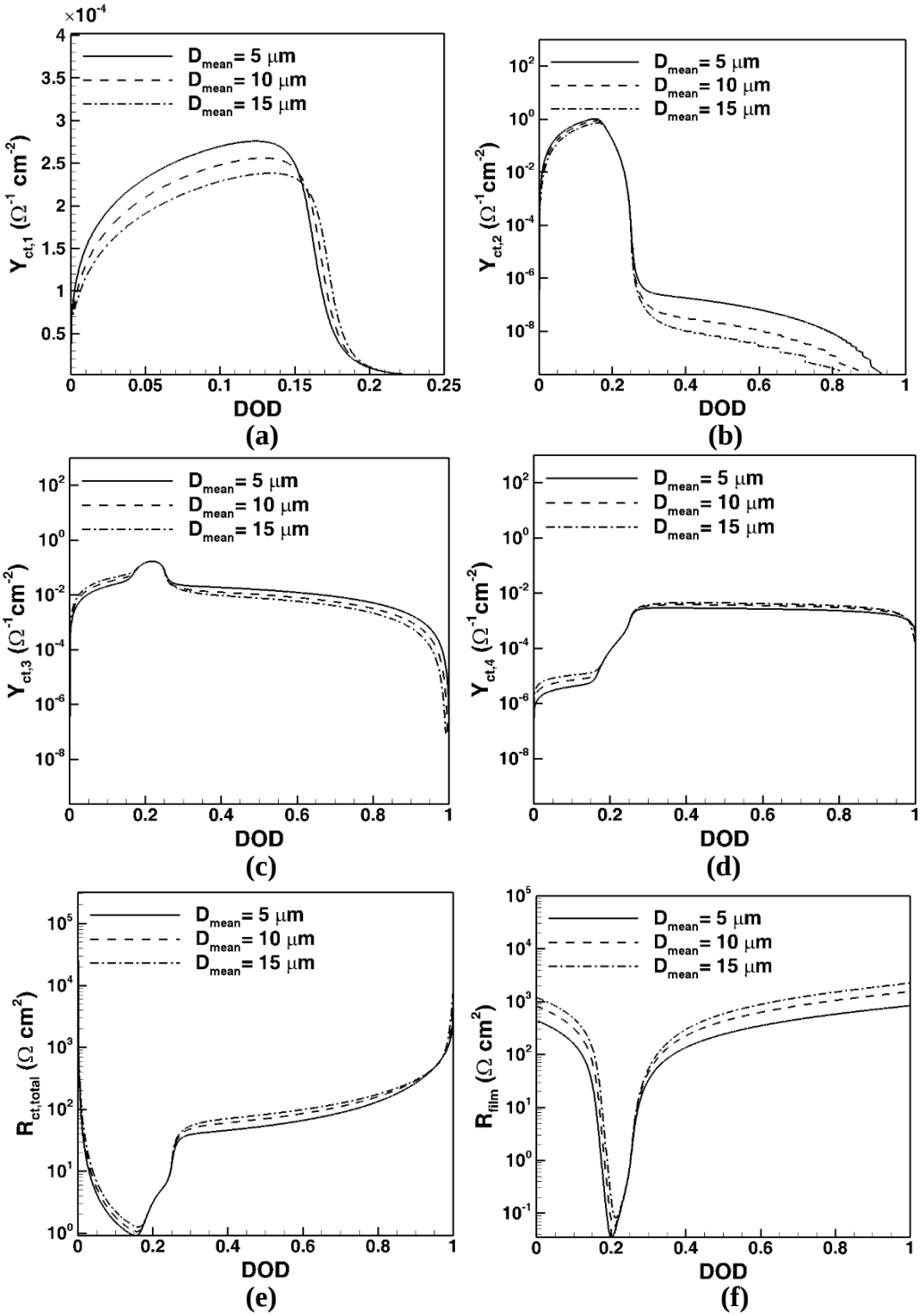

Figure 6.8.*The microstructure effect (different mean pore size) on the charge transfer resistance. (a) $Y_{ct,1}$ (b) $Y_{ct,2}$ (c) $Y_{ct,3}$ (d) $Y_{ct,4}$ (e) $R_{ct,total}$ (f) R_{film}*

Figure 6.8 (a) – (d) present the kinetic admittance for reaction [2] – [5] respectively. From the results, at the beginning of discharge (DOD = 0 – 0.2), where the solid sulfur have not dissolved totally. Small mean pore size microstructure has better admittance for reaction [2] and [3] but worse for reaction [4] and [5]. When precipitation starts to take into place, small mean pore size microstructure has better admittance for reaction [3] and [4] but worse for reaction [5]. With the consideration of all the kinetic admittance, the charge transfer resistance is lower in the microstructure with small pore size compare to the other two cases as shown in Figure 6.8 (e). For the layer thickness, the microstructure with small pore size also has smaller layer resistance due to the thinner layer thickness.

Figure 6.9 shows the impedance response of different microstructure at different DOD. During the whole discharging process, the microstructure with small pore size has the smallest charge transfer resistance (semi-circle on the right), layer resistance (semi-circle on the left), and contact resistance. These resistances are all affected by the interfacial area as shown in Figure 6.7 (a), which large interfacial area of small pore size microstructure lower the impedance of the electrode. Besides interfacial area, according to the variation of layer thickness (see Figure 6.7 (b)) and charge transfer resistance at the interface (see Figure 6.8 (e)), small mean pore size microstructure also should have smaller layer resistance and charge transfer resistance on the interface. The combining influence of interfacial area, layer thickness, and charge transfer resistance result in the impedance response shown in Figure 6.9. At DOD = 0.0015, the radius of the two semi-circles is close when the pore size is large. This is because large pore size microstructure has less kinetic admittance and larger layer thickness compare to the other two case.

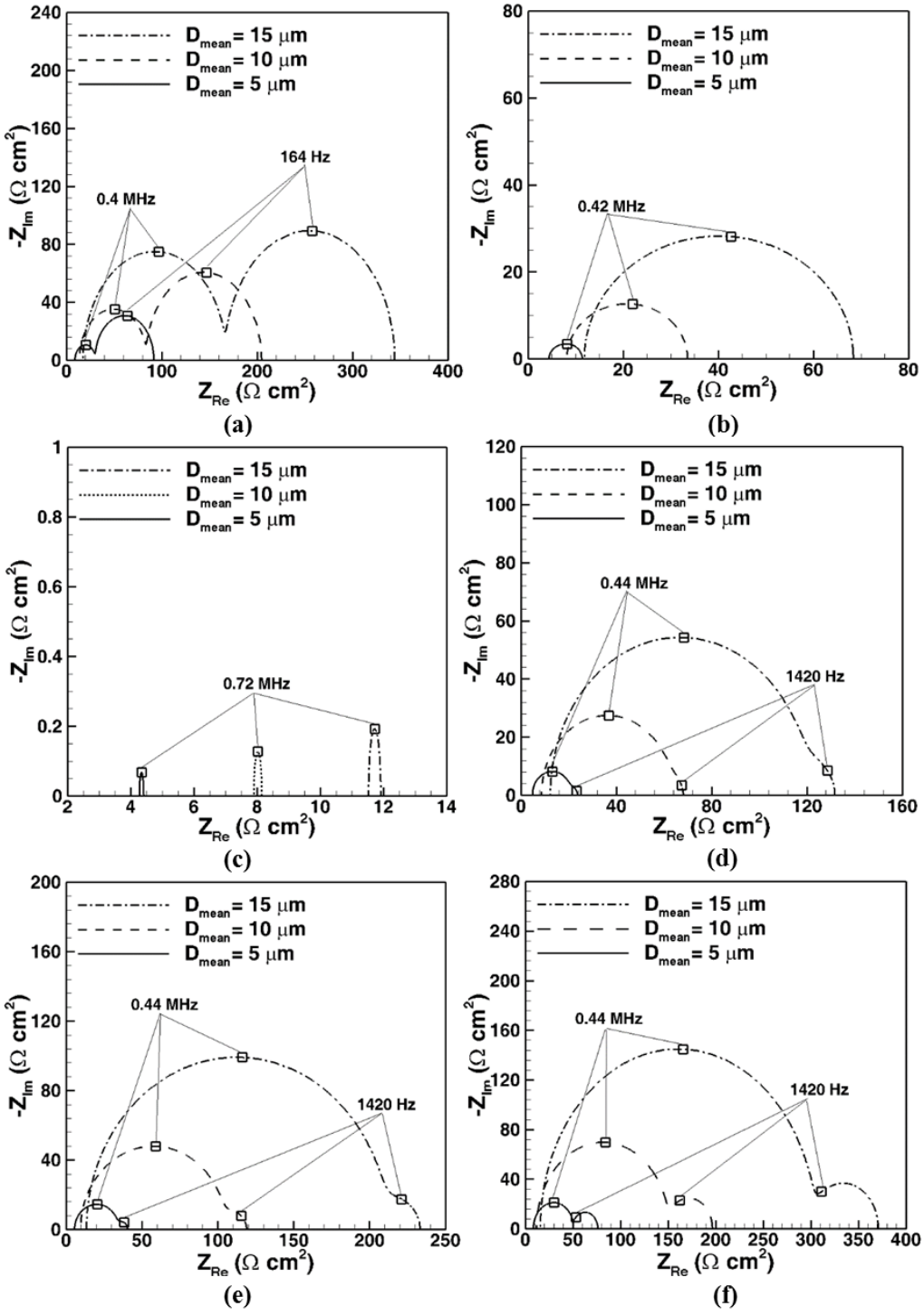

Figure 6.9. *The microstructure effect (different mean pore size) on the impedance response at (a) DOD=0.0015 (b) DOD =0.1 (c) DOD =0.2 (d) DOD =0.6 (e) DOD =0.8 (f) DOD =0.95*

On the other hand, since the small pore size microstructure has larger kinetic admittance and smaller layer thickness, the radius of the two semi-circles has a larger difference. For DOD = 0.1 , the different in impedance response is because of the different in interfacial area and layer thickness according to the DOD dependent study shown in Figure 6.4 (e). In the contrary, the difference of impedance response when DOD = 0.2 is mainly because of the interfacial area and charge transfer resistance, since there is no loaded sulfur or precipitation. Similar to the impedance response at DOD = 0.0015, due to the larger charge transfer resistance, the semi-circle representative the charge transfer resistance is more obvious in the microstructure with larger pore size compare the small pore microstructure.

6.3 Conclusions

In this paper, the microstructure evolution during the discharging process and the influence of electrode microstructure variability on the corresponding impedance response has been elucidated. In this regard, a microstructure-aware impedance model has been proposed for lithium-sulfur batteries, which accounts from lithium polysulfide precipitation and solid sulfur loading thereof on the impedance characteristics. The impact of lithium polysulfide precipitation (or sulfur loading) on the transport properties (i.e. porosity and tortuosity), transport path, interfacial electrochemical area, pore size distribution, and pore closure has been detail addressed and discussed. With the impact of microstructure variation, the corresponding impedance response is predicted by the microstructure-aware impedance model during the discharging process within different carbon substrate microstructure. The prediction of impedance response enables a virtual

diagnosis and characterization of the discharging process of the lithium-sulfur battery. Moreover, this model provides a direction of electrode microstructure synthesis, which can minimize the internal resistance.

Due to the difference of pore size distribution inside the carbon substrate microstructure, the microstructure properties, and the corresponding impedance response changes accordingly. In the microstructure with mean pore size, the results suggest that decrease the mean pore diameter can increase the electrochemical interfacial area, increase the number of transport path, and decrease the layer thickness. However, in the point of view of pore closure, there is an optimize pore size. When the pore size is too large, the poor pore interconnection could cause pore isolation, even there is no precipitation or sulfur loading. In the other hand, if the pore size is too small, the narrow transport path can easily block by the precipitation (solid sulfur) and result in pore closure. For the impedance response, from the comparison between the impedance responses from different microstructure properties, the results suggest that the interfacial area is the dominated factor of impedance response. The results of impedance prediction from different carbon substrate microstructure also show that increase the interfacial area by decreasing the mean pore size can have smaller internal resistance during the whole discharging process.

CHAPTER VII

CONCLUSION AND FUTURE WORK

Due to the increased requirement of energy storage system, significant efforts are focusing on predicting and extending the life, performance, and safety of energy storage system. In this thesis, the impact of electrode microstructure on the degradation, performance, and safety of energy storage has been investigated. The conclusion of the observations is expressed in this section.

7.1 Conclusions

From the chemical degradation (*i.e.* SEI formation), the influence of electrode microstructural variability on the SEI formation and corresponding impedance response has been elucidated. In this regard, a microstructure-aware computational model has been presented which consists of physicochemical interactions pertinent to SEI formation in a typical LIB anode and elicits the influence thereof on the impedance characteristics. The impact of active particle morphology, size distribution, binder and electrolyte volume fractions on the SEI thickness, SOC, and the underlying interdependencies of transport and interfacial resistances have been investigated in detail. This model enables a virtual diagnosis and characterization of the canonical mode of chemical degradation via prediction of the impedance spectra snapshots for intercalation electrodes. Due to the variation of particle-size distribution, the impedance response changes with the active interfacial area, porosity, and mean particle size. The predictions suggest that the surface area change dominates the impedance response. Moreover, the trade-off between the SEI

resistance and charge transfer resistance has been found to be of critically dependent on the variation of the mean size of active particles and electrolyte volume fraction. From morphological variability, the spherical active particles show the largest SEI and charge transfer resistances compared to the cylindrical and platelet active particles. However, the spherical particles exhibit the lowest solid-phase diffusion resistance. The volume fraction of binder has been found to affect the impedance response significantly. An increase of binder fraction decreases the interfacial active area, which in turn affects the reaction current density, charging time and the SEI growth rate and hence ultimately on the impedance response.

For the mechanical degradation, by coupling the lattice spring based damage model with the impedance model, the impact of mechanical degradation on the electrode impedance response has been investigated. Specifically, the effect of fracture formation and propagation due to diffusion induced stress on the charge transfer and solid phase diffusion resistance in the LIB electrode particle has been illustrated. Furthermore, the influence of active particle size distribution, operating temperature and discharge/charge rate on the impedance behavior has been discussed. The results suggest a significant difference in the impedance behavior due to the variation in the damage evolution pattern for different operational conditions. During the delithiation process, more cracks develop close to the periphery of the particle. During lithiation, due to the tensile force acting at the center, more microcracks in the interior of the particle are observed. The cracks at the peripheral region affect the surface concentration significantly more than those located close to the center of the active particle. Subsequently, the microcracks have a larger

influence on the impedance response during delithiation than in the lithiation process. It has also been observed that fracture formation around the particle center has less effect on the surface concentration and solid phase diffusion resistance. The influence of electrode microstructure on the impedance response has been demonstrated in terms of the active particle volume fraction and particle size distribution. The charge transfer resistance is primarily affected due to the change in active material volume fraction. The effective diffusivity and solid state transport properties for an active particle with fracture can be estimated from the slope of the long tail of the impedance curve, which is left as a future exercise. For the operating conditions taken into consideration, the porous electrode impedance response suggests that the diffusion induced damage has a larger influence on the resistance under low temperature and high discharge/charge rate operation. The higher concentration gradient, observed at both low temperature and high C-rate conditions, is the main reason behind the formation of enhanced mechanical degradation. In this study, we showed that the impact of diffusion induced damage on the impedance response is an important aspect and needs to be considered, especially at high charge/discharge rates and low temperatures. By controlling the operating conditions and the electrode microstructure design, the deleterious impact of mechanical damage on the electrode performance may be ameliorated, which will be considered in a future study.

As mentioned in the mechanical degradation study, the microcrack formation is affected by the temperature, particle size, and the delithiation rate. From the single delithiation simulations, the temperature, particle size, and C-rate show significant influence on the relation between (i) CSE and concentration gradient and (ii) CSE and

microcrack density. For the relation between CSE and concentration gradient, the results suggest that, under the same value of CSE, the concentration gradient increases with (i) decrease of temperature, (ii) increase of particle size, and (iii) increase of C-rate. In contrast, for the relation between CSE and microcrack density, the microcrack density increases with (i) increase of temperature, (ii) decrease of particle size, and (iii) decrease of C-rate under the same value of CSE. According to the results, we introduced a scaling factor *M*, which can collapse the data from different operating conditions. Scaling law expressions for the relationships between CSE, concentration gradient, and microcrack density were found by fitting data from the high order diffusion induced damage model. From the data-drive scaling process, different temperature conditions ($T > 0°C$ or $T \leq 0°C$) suggested different scaling factors *M*, which means that the contribution of operation factors (*i.e.*, temperature, particle size, and C-rate) varied with the temperature. The reduced-order equations were coupled with the electrochemical model to study the influence of mechanical damage on cell performance. According to the results, the capacity fade is larger when the microcrack density is higher. Further, the capacity fade is directly proportional to the size of the electrode active particles and discharging rates. Another important observation is that the microcrack density is higher in the region near the separator as compared to the region near the current collector since the current density is higher near the separator. In addition to the observation of the single delithiation process, we also investigated the damage evolution during the drive cycle. Three kinds of drive cycles (HEV, PHEV, and BEV) were tested in this study. The results quantified the microcrack formation dependence on temperature, particle size, and C-rate. Since

PHEV and HEV applications operate under a higher C-rate than the BEV application, the model predicts those applications will experience higher microcrack density. During the drive cycle, the microcrack was saturated after operation over time. After saturation, new microcracks can only form when the average concentration gradient exceeds its previous peak value. In addition, the scaling law expression for the relation between CSE and microcrack density found from the single delithiation process has successfully predicted the damage evolution during different drive cycles. This result validates our proposed approach for reduced order modeling of mechanical damage evolution in LIB active material particles.

The influence of electrode microstructure on the thermal behavior of lithium-ion batteries has been elucidated in this thesis. In this regard, a microstructure-aware electrochemical-thermal model has been proposed, which adopted the reconstruction of the 3D virtual microstructure. This model can better capture the transport property (i.e. tortuosity) compare to the Bruggeman ideal relation. The impact of cathode microstructure on the cell temperature has detailed addressed and analyzed by studying the time evolution and spatial distribution of different heat sources (i.e joule heating, reversible heating, and reaction heating). During the discharging process, the influence of cathode microstructure on the joule heating and reaction heating is mainly observed in the cathode, and the influence of microstructure on the reversible heating is mainly observed in the anode. The difference in the total heating rate is mainly observed near the cathode/separator interface and at the end of discharge. From the study of the microstructure dependent thermal behavior, the trade-off between cell capacity and temperature control has been addressed

and discussed. Although increase the amount of active material can boost the cell capacity, it also raises the cell temperature and increases the risk of thermal runaway. To control the temperature below the safety limit, parts of the capacity of the cell are sacrificed. In addition, the study of the microstructure dependent thermal behavior provides the insight of using electrode microstructure to control the cell temperature. Increasing electrode porosity can decrease the cell temperature due to the low heating rate. Besides increasing electrode porosity, the self-shutdown mechanism also can limit the cell temperature if the electrode porosity is low enough, especially discharge with high current. In summary, the study of microstructure dependent thermal behavior provides a direction to improve the safety of battery without additional external control mechanism.

Besides the LIBs, the microstructure evolutions during the discharging process and the influence of electrode microstructure variability on the corresponding impedance response have been elucidated for Li-S battery. In this regard, a microstructure-aware impedance model has been proposed for lithium-sulfur batteries, which accounts from lithium polysulfide precipitation and solid sulfur loading thereof on the impedance characteristics. The impact of lithium polysulfide precipitation (or sulfur loading) on the transport properties (i.e. porosity and tortuosity), transport path, interfacial electrochemical area, pore size distribution, and pore closure has been detail addressed and discussed. With the impact of microstructure variation, the corresponding impedance response is predicted by the microstructure-aware impedance model during the discharging process within different carbon substrate microstructure. The prediction of impedance response enables a virtual diagnosis and characterization of the discharging

process of the lithium-sulfur battery. Moreover, this model provides a direction of electrode microstructure synthesis, which can minimize the internal resistance. Due to the difference of pore size distribution inside the carbon substrate microstructure, the microstructure properties, and the corresponding impedance response changes accordingly. In the microstructure with mean pore size, the results suggest that decrease the mean pore diameter can increase the electrochemical interfacial area, increase the number of transport path, and decrease the layer thickness. However, in the point of view of pore closure, there is an optimize pore size. When the pore size is too large, the poor pore interconnection could cause pore isolation, even there is no precipitation or sulfur loading. In the other hand, if the pore size is too small, the narrow transport path can easily block by the precipitation (solid sulfur) and result in pore closure. For the impedance response, from the comparison between the impedance responses from different microstructure properties, the results suggest that the interfacial area is the dominated factor of impedance response. The results of impedance prediction from different carbon substrate microstructure also show that increase the interfacial area by decreasing the mean pore size can have smaller internal resistance during the whole discharging process.

7.2 Future Work

Almost all the works presented in this thesis can be extended to solve problems that are more complex. In the studies of the interaction between microstructure and degradation of LIBs (Chapter I – Chapter III), the simulations were based on the assumption that the electrolyte has no influence on the degradation phenomena, such as the non-uniform distribution of lithium ion concentration. However, due to the non-

uniform concentration distribution of lithium ion, the SEI or microcrack formation should change with the position of the electrode. The local variation of SEI and microcrack formation can further affect the predicted impedance response. The non-uniform distribution of SEI and microcrack formation should be more obvious when the C-rate is high or the temperature is low, due to the large polarization of lithium ion concentration. In the present model, since the lithium ion concentration was considered as uniform distribution, the SEI thickness, and microcrack density is the same if the particle radius is the same. To observe to the local chemical and mechanical degradation and its influence on the impedance response, a higher dimension (two-dimensional or three-dimensional) of simulation is required.

For the study of SEI formation, the SEI layer is simply considered as a single conduct phase, which the SEI is treated as a film resistance when calculated the impedance response. In the real SEI structure, it includes different species, such as Li_2CO_3, LiF and an amorphous polymer layer. The film resistance comes from the transport of lithium ion through these species. The assumed value of SEI layer resistance may deviate from the resistance of the realistic SEI structure, and hence affect the predicted impedance response. To obtain a more realistic film resistance, the reconstruction of SEI layer structure is required. According to the experimental observation, the SEI structure can be reconstructed with a similar method of electrode microstructure reconstruction. With the reconstructed virtual SEI structure, the resistance for the positive charge transport resistance can be evaluated and implemented to the impedance model to obtain a more accurate prediction of impedance response. Besides the evaluation of film resistance, this

thesis used a compared simpler version of SEI formation, which did not solve the reduction of electrolyte and the diffusion of species through the SEI layer. Although the adopted SEI formation method shows good potential in predicting the capacity loss and SEI formation according to previous studies, this method losses the flexibility to solve more complex problems. To study more complex problems, such as the influence of electrolyte reduction on the impedance response, the impedance model should incorporate with an SEI formation model, which includes the detailed chemistry of SEI formation.

For the study of microcrack formation, the simulation based on the assumption that the electrolyte cannot flow into the microcrack, which connected to the surface of the particle. However, this is not strictly true in the realistic scenario. If the microcrack connects to the surface of the particle, the electrolyte can easily fill the microcrack crack with electrolyte and create new electrolyte/active material interface for electrochemical reaction or SEI formation. This can significantly vary the lithium concentration distribution and the microcrack propagation inside the active particle. The change of interfacial area, microcrack propagation, and lithium concentration distribution inside the active particle can further change the prediction of impedance response. To better capture the influence of mechanical degradation on the impedance response, the impedance model should incorporate the flow of electrolyte within the microcrack region, and take the increase interfacial area and surface concentration of the entire interface into account.

As shown in this thesis, the mechanical and chemical degradation was studied separately. According to the mechanism of SEI formation, the SEI thickness growing rate is highly dependent on the solid phase potential. Since the solid phase potential of the

anode is affected by the open-circuit potential, which is a function of surface concentration, the solid phase potential can be dominated by the surface concentration. With the presence of microcrack formation, the microcracks hinder the transport of lithium inside the active particle, and hence the surface concentration. Therefore, the microcrack formation could affect the SEI formation during cycling. In this study, the side reaction of SEI formation will be combined with the diffusion induced damage model mentioned in section 3.1.2. The interaction between SEI and microcrack will be discussed under different C-rate and temperature.

For the study of microstructure dependent thermal behavior, the porosity of electrode is assumed uniform inside the electrode microstructure. However, in the realistic electrode, the porosity varies inside the electrode. The non-uniform distribution of porosity can cause local heat generation, which the heating rate is not just concentrated near the separator. Different distribution of porosity inside the electrode can change the temperature increase inside the cell. To study the influence of porosity distribution, the porosity can be assigned differently along the electrode in the 1D performance model. The model can even extend to direct use 2D or 3D virtual electrode microstructure to study the local heat generation inside the electrode. Besides the non-uniform distribution of porosity, the model in this thesis ignored the heat transfer inside the cell, which considered the whole 18650 cell has uniform temperature distribution. Since the heat conductivity of the separator and electrode is different, the temperature distribution can vary inside the cell. In addition, since the conductivity of the active material, binder, and electrolyte is different, the effective heat conductivity of the electrode changes with the composition of

electrode. It is worth studying in the future to include the heat transfer inside the cell to study the influence the composition of microstructure on the thermal behavior of the cell, especially on the heat depletion during the discharging and charging process.

Finally, the study of Li-S battery assumed that the precipitation and loaded solid sulfur is uniformly coated on the surface of carbon substrate. The resistance contributed by the layer is treated as a conducting layer similar to the SEI layer. In the realistic case, the solid sulfur cannot coat uniformly on the surface of the carbon substrate, and the precipitation can growth heterogeneously. The variation of interfacial situation can affect the impedance response. By incorporating the impedance model with heterogeneous precipitation/dissolution, the predicted impedance response can be more close to real Li-S electrode. In addition, similar to the SEI study in this thesis, the value of layer resistance of precipitation is an assumed value. To better capture the contribution of layer resistance on the impedance response, the structure of precipitation layer and loaded sulfur layer should be studied. The effective or equivalent resistance of precipitation layer and the loaded sulfur layer can be calculated by solving the electron and ion transport through the layer with virtual reconstructed structure.

REFERENCES

1. R. Wagner, N. Preschitschek, S. Passerini, J. Leker, and M. Winter, "*Current Research Trends and Prospects Among the Various Materials and Designs Used in Lithium-Based Batteries*," *Journal of Applied Electrochemistry*, 2013, 43, 481-496.

2. M. S. Whittingham, "*Lithium Batteries and Cathode Materials*," *Chemical Reviews*, 2004, 104, 4271-4302.

3. B. L. Ellis, K. T. Lee, and L. F. Nazar, "*Positive Electrode Materials for Li-Ion and Li-Batteries†*," *Chemistry of Materials*, 2010, 22, 691-714.

4. J. M. Tarascon and M. Armand, "*Issues and Challenges Facing Rechargeable Lithium Batteries*," *Nature*, 2001, 414, 359-367.

5. E. Yoo, J. Kim, E. Hosono, H.-s. Zhou, T. Kudo, and I. Honma, "*Large Reversible Li Storage of Graphene Nanosheet Families for Use in Rechargeable Lithium Ion Batteries*," *Nano Letters*, 2008, 8, 2277-2282.

6. Y.-N. Xu, S.-Y. Chung, J. T. Bloking, Y.-M. Chiang, and W. Y. Ching, "*Electronic Structure and Electrical Conductivity of Undoped LiFePO4*," *Electrochemical and Solid-State Letters*, 2004, 7, A131-A134.

7. K. Mizushima, P. C. Jones, P. J. Wiseman, and J. B. Goodenough, "*LixCoO2 (0<x<-1): A New Cathode Material for Batteries of High Energy Density*," *Materials Research Bulletin*, 1980, 15, 783-789.

8. E. Plichta, S. Slane, M. Uchiyama, M. Salomon, D. Chua, W. B. Ebner, *et al.*, "*An Improved Li / Li x CoO2 Rechargeable Cell*," *Journal of The Electrochemical Society*, 1989, 136, 1865-1869.

9. J. N. Reimers and J. R. Dahn, "*Electrochemical and In Situ X-Ray Diffraction Studies of Lithium Intercalation in Li x CoO2*," *Journal of The Electrochemical Society*, 1992, 139, 2091-2097.

10. R. J. Gummow, M. M. Thackeray, W. I. F. David, and S. Hull, "*Structure and Electrochemistry of Lithium Cobalt Oxide Synthesised at 400°C*," *Materials Research Bulletin*, 1992, 27, 327-337.

11. K. M. Shaju, G. V. Subba Rao, and B. V. R. Chowdari, "*Performance of Layered Li(Ni1/3Co1/3Mn1/3)O2 as Cathode for Li-Ion Batteries*," *Electrochimica Acta*, 2002, 48, 145-151.

12. J.-M. Kim and H.-T. Chung, "*Role of Transition Metals in Layered Li[Ni,Co,Mn]O2 Under Electrochemical Operation*," *Electrochimica Acta*, 2004, 49, 3573-3580.

13. Y. Kim, H. S. Kim, and S. W. Martin, "*Synthesis and Electrochemical Characteristics of Al2O3-Coated LiNi1/3Co1/3Mn1/3O2 Cathode Materials for Lithium Ion Batteries*," *Electrochimica Acta,* 2006, 52, 1316-1322.

14. H. S. Kim, Y. Kim, S. I. Kim, and S. W. Martin, "*Enhanced Electrochemical Properties of LiNi1/3Co1/3Mn1/3O2 Cathode Material by Coating with LiAlO2 Nanoparticles*," *Journal of Power Sources,* 2006, 161, 623-627.

15. N. N. Sinha and N. Munichandraiah, "*Synthesis and Characterization of Carbon-Coated LiNi1/3Co1/3Mn1/3O2 in a Single Step by an Inverse Microemulsion Route*," *ACS Applied Materials & Interfaces,* 2009, 1, 1241-1249.

16. C. Ban, Z. li, Z. Wu, M. J. Kirkham, L. Chen, Y. S. Jung, *et al.*, "*Extremely Durable High-Rate Capability of a LiNi0.4Mn0.4Co0.2O2 Cathode Enabled with Single-Walled Carbon Nanotubes*," *Advanced Energy Materials,* 2011, 1, 58-62.

17. F. Hao and D. Fang, "*Diffusion-Induced Stresses of Spherical Core-Shell Electrodes in Lithium-Ion Batteries: The Effects of the Shell and Surface/Interface Stress*," *Journal of The Electrochemical Society,* 2013, 160, A595-A600.

18. S. Kalnaus, K. Rhodes, and C. Daniel, "*A Study of Lithium Ion Intercalation Induced Fracture of Silicon Particles Used as Anode Material in Li-Ion Battery*," *Journal of Power Sources,* 2011, 196, 8116-8124.

19. M. D. Levi and D. Aurbach, "*The Mechanism of Lithium Intercalation in Graphite Film Electrodes in Aprotic Media .1. High Resolution Slow Scan Rate Cyclic Voltammetric Studies and Modeling*," *Journal of Electroanalytical Chemistry,* 1997, 421, 79-88.

20. M. D. Levi, E. A. Levi, and D. Aurbach, "*The Mechanism of Lithium Intercalation in Graphite Film Electrodes in Aprotic Media .2. Potentiostatic Intermittent Titration and In Situ XRD Studies of the Solid-State Ionic Diffusion*," *Journal of Electroanalytical Chemistry,* 1997, 421, 89-97.

21. D. Aurbach, "The Role of Surface Films on Electrodes in Li-ion Batteries," in *Advances in Lithium-Ion Batteries,* W. A. v. Schalkwijk and B. Scrosati, Eds., ed New York: Academic/Plenem Publishers, 2002, p. 7.

22. J. W. Jiang and J. R. Dahn, "*Effects of Solvents and Salts on the Thermal Stability of LiC6*," *Electrochimica Acta,* 2004, 49, 4599-4604.

23. C.-F. Chen, P. Barai, and P. P. Mukherjee, "*Diffusion Induced Damage and Impedance Response in Lithium-Ion Battery Electrodes*," *Journal of The Electrochemical Society,* 2014, 161, A2138-A2152.

24. P. Barai and P. P. Mukherjee, "*Stochastic Analysis of Diffusion Induced Damage in Lithium-Ion Battery Electrodes*," *Journal of the Electrochemical Society,* 2013, 160, A955-A967.

25. D. Marmorstein, T. H. Yu, K. A. Striebel, F. R. McLarnon, J. Hou, and E. J. Cairns, "*Electrochemical Performance of Lithium/Sulfur Cells with Three Different Polymer Electrolytes*," *Journal of Power Sources,* 2000, 89, 219-226.

26. J. Sun, Y. Huang, W. Wang, Z. Yu, A. Wang, and K. Yuan, "*Application of Gelatin as A Binder For the Sulfur Cathode in Lithium–Sulfur Batteries*," *Electrochimica Acta,* 2008, 53, 7084-7088.

27. J. Shim, K. A. Striebel, and E. J. Cairns, "*The Lithium/Sulfur Rechargeable Cell - Effects of Electrode Composition and Solvent on Cell Performance*," *Journal of the Electrochemical Society,* 2002, 149, A1321-A1325.

28. C. Barchasz, J. C. Lepretre, F. Alloin, and S. Patoux, "*New Insights Into the Limiting Parameters of The Li/S Rechargeable Cell*," *Journal of Power Sources,* 2012, 199, 322-330.

29. Y. V. Mikhaylik and J. R. Akridge, "*Polysulfide Shuttle Study in the Li/S Battery System*," *Journal of the Electrochemical Society,* 2004, 151, A1969-A1976.

30. J. H. Shin, S. S. Jung, K. W. Kim, H. J. Ahn, and J. H. Ahn, "*Preparation and Characterization of Plasticized Polymer Electrolytes Based on The Pvdf-Hfp Copolymer for Lithium/Sulfur Battery*," *Journal of Materials Science: Materials in Electronics,* 2002, 13, 727-733.

31. Y. M. Lee, N.-S. Choi, J. H. Park, and J.-K. Park, "*Electrochemical Performance of Lithium/Sulfur Batteries with Protected Li Anodes*," *Journal of Power Sources,* 2003, 119–121, 964-972.

32. S.-E. Cheon, K.-S. Ko, J.-H. Cho, S.-W. Kim, E.-Y. Chin, and H.-T. Kim, "*Rechargeable Lithium Sulfur Battery: II. Rate Capability and Cycle Characteristics*," *Journal of The Electrochemical Society,* 2003, 150, A800-A805.

33. D.-R. Chang, S.-H. Lee, S.-W. Kim, and H.-T. Kim, "*Binary Electrolyte Based on Tetra(Ethylene Glycol) Dimethyl Ether and 1,3-Dioxolane for Lithium–Sulfur Battery*," *Journal of Power Sources,* 2002, 112, 452-460.

34. J. Wang, S. Y. Chew, Z. W. Zhao, S. Ashraf, D. Wexler, J. Chen, *et al.*, "*Sulfur–Mesoporous Carbon Composites in Conjunction with A Novel Ionic Liquid Electrolyte for Lithium Rechargeable Batteries*," *Carbon,* 2008, 46, 229-235.

35. B. H. Jeon, J. H. Yeon, and I. J. Chung, "*Preparation and Electrical Properties of Lithium–Sulfur-Composite Polymer Batteries*," *Journal of Materials Processing Technology*, 2003, 143–144, 93-97.

36. M. V. Merritt and D. T. Sawyer, "*Electrochemical Reduction of Elemental Sulfur in Aprotic Solvents. Formation of A Stable S8- Species*," *Inorganic Chemistry*, 1970, 9, 211-215.

37. H. Yamin, A. Gorenshtein, J. Penciner, Y. Sternberg, and E. Peled, "*Lithium Sulfur Battery: Oxidation/Reduction Mechanisms of Polysulfides in THF Solutions*," *Journal of The Electrochemical Society*, 1988, 135, 1045-1048.

38. S.-E. Cheon, K.-S. Ko, J.-H. Cho, S.-W. Kim, E.-Y. Chin, and H.-T. Kim, "*Rechargeable Lithium Sulfur Battery: I. Structural Change of Sulfur Cathode During Discharge and Charge*," *Journal of The Electrochemical Society*, 2003, 150, A796-A799.

39. C. D. Liang, N. J. Dudney, and J. Y. Howe, "*Hierarchically Structured Sulfur/Carbon Nanocomposite Material for High-Energy Lithium Battery*," *Chemistry of Materials*, 2009, 21, 4724-4730.

40. B. Zhang, X. Qin, G. R. Li, and X. P. Gao, "*Enhancement of Long Stability of Sulfur Cathode by Encapsulating Sulfur Into Micropores of Carbon Spheres*," *Energy & Environmental Science*, 2010, 3, 1531-1537.

41. J. J. Chen, Q. Zhang, Y. N. Shi, L. L. Qin, Y. Cao, M. S. Zheng, *et al.*, "*A Hierarchical Architecture S/Mwcnt Nanomicrosphere with Large Pores for Lithium Sulfur Batteries*," *Physical Chemistry Chemical Physics*, 2012, 14, 5376-5382.

42. M. M. Rao, X. Y. Song, H. G. Liao, and E. J. Cairns, "*Carbon Nanofiber-Sulfur Composite Cathode Materials with Different Binders for Secondary Li/S Cells*," *Electrochimica Acta*, 2012, 65, 228-233.

43. D. X. Wang, A. P. Fu, H. L. Li, Y. Q. Wang, P. Z. Guo, J. Q. Liu, *et al.*, "*Mesoporous Carbon Spheres with Controlled Porosity for High-Performance Lithium-Sulfur Batteries*," *Journal of Power Sources*, 2015, 285, 469-477.

44. H. Zheng, J. Li, X. Song, G. Liu, and V. S. Battaglia, "*A Comprehensive Understanding of Electrode Thickness Effects on the Electrochemical Performances of Li-Ion Battery Cathodes*," *Electrochimica Acta*, 2012, 71, 258-265.

45. Y. H. Chen, C. W. Wang, X. Zhang, and A. M. Sastry, "*Porous Cathode Optimization for Lithium Cells: Ionic and Electronic Conductivity, Capacity, and Selection Of Materials*," *Journal of Power Sources*, 2010, 195, 2851-2862.

46. X. Xiang, X. Li, and W. Li, "*Preparation and Characterization of Size-Uniform Li[Li0.131ni0.304mn0.565]O2 Particles as Cathode Materials for High Energy Lithium Ion Battery*," *Journal of Power Sources,* 2013, 230, 89-95.

47. N. H. Kwon, "*The Effect of Carbon Morphology on The LiCoO2 Cathode of Lithium Ion Batteries*," *Solid State Sciences,* 2013, 21, 59-65.

48. G. Liu, H. Zheng, X. Song, and V. S. Battaglia, "*Particles and Polymer Binder Interaction: A Controlling Factor in Lithium-Ion Electrode Performance*," *Journal of the Electrochemical Society,* 2012, 159, A214-A221.

49. Y. H. Chen, C. W. Wang, G. Liu, X. Y. Song, V. S. Battaglia, and A. M. Sastry, "*Selection of Conductive Additives in Li-Ion Battery Cathodes - A Numerical Study*," *Journal of the Electrochemical Society,* 2007, 154, A978-A986.

50. D. W. Chung, M. Ebner, D. R. Ely, V. Wood, and R. E. Garcia, "*Validity of the Bruggeman Relation For Porous Electrodes*," *Modelling and Simulation in Materials Science and Engineering,* 2013, 21,

51. I. V. Thorat, D. E. Stephenson, N. A. Zacharias, K. Zaghib, J. N. Harb, and D. R. Wheeler, "*Quantifying Tortuosity in Porous Li-Ion Battery Materials*," *Journal of Power Sources,* 2009, 188, 592-600.

52. S. J. Cooper, D. S. Eastwood, J. Gelb, G. Damblanc, D. J. L. Brett, R. S. Bradley, *et al.*, "*Image Based Modelling of Microstructural Heterogeneity in LiFePO4 Electrodes for Li-Ion Batteries*," *Journal of Power Sources,* 2014, 247, 1033-1039.

53. D. Kehrwald, P. R. Shearing, N. P. Brandon, P. K. Sinha, and S. J. Harris, "*Local Tortuosity Inhomogeneities in a Lithium Battery Composite Electrode*," *Journal of the Electrochemical Society,* 2011, 158, A1393-A1399.

54. C. J. Bae, C. K. Erdonmez, J. W. Halloran, and Y. M. Chiang, "*Design of Battery Electrodes with Dual-Scale Porosity to Minimize Tortuosity and Maximize Performance*," *Advanced Materials,* 2013, 25, 1254-1258.

55. M. Ebner, D. W. Chung, R. E. Garcia, and V. Wood, "*Tortuosity Anisotropy in Lithium-Ion Battery Electrodes*," *Advanced Energy Materials,* 2014, 4,

56. H. Zheng, L. Tan, G. Liu, X. Song, and V. S. Battaglia, "*Calendering Effects on the Physical and Electrochemical Properties Of Li[Ni1/3Mn1/3Co1/3]O2 Cathode*," *Journal of Power Sources,* 2012, 208, 52-57.

57. B. Vijayaraghavan, D. R. Ely, Y. M. Chiang, R. Garcia-Garcia, and R. E. Garcia, "*An Analytical Method to Determine Tortuosity in Rechargeable Battery Electrodes*," *Journal of the Electrochemical Society,* 2012, 159, A548-A552.

58. M. Ebner, D.-W. Chung, R. E. García, and V. Wood, "*Tortuosity Anisotropy in Lithium-Ion Battery Electrodes*," *Advanced Energy Materials,* 2013, n/a-n/a.

59. W. Wu and F. M. Jiang, "*Simulated Annealing Reconstruction and Characterization of a LiCoO2 Lithium-Ion Battery Cathode*," *Chinese Science Bulletin,* 2013, 58, 4692-4695.

60. A. Gupta, J. H. Seo, X. C. Zhang, W. B. Du, A. M. Sastry, and W. Shyy, "*Effective Transport Properties of LiMn2O4 Electrode via Particle-Scale Modeling*," *Journal of the Electrochemical Society,* 2011, 158, A487-A497.

61. D. E. Stephenson, B. C. Walker, C. B. Skelton, E. P. Gorzkowski, D. J. Rowenhorst, and D. R. Wheeler, "*Modeling 3D Microstructure and Ion Transport in Porous Li-Ion Battery Electrodes*," *Journal of The Electrochemical Society,* 2011, 158, A781-A789.

62. P. R. Shearing, L. E. Howard, P. S. Jorgensen, N. P. Brandon, and S. J. Harris, "*Characterization of the 3-Dimensional Microstructure of a Graphite Negative Electrode from a Li-Ion Battery*," *Electrochemistry Communications,* 2010, 12, 374-377.

63. Y. Ji, Y. C. Zhang, and C. Y. Wang, "*Li-Ion Cell Operation at Low Temperatures*," *Journal of the Electrochemical Society,* 2013, 160, A636-A649.

64. S. E. Cheon, K. S. Ko, J. H. Cho, S. W. Kim, E. Y. Chin, and H. T. Kim, "*Rechargeable Lithium Sulfur Battery - I. Structural Change of Sulfur Cathode During Discharge and Charge*," *Journal of the Electrochemical Society,* 2003, 150, A796-A799.

65. S. E. Cheon, K. S. Ko, J. H. Cho, S. W. Kim, E. Y. Chin, and H. T. Kim, "*Rechargeable Lithium Sulfur Battery - Ii. Rate Capability and Cycle Characteristics*," *Journal of the Electrochemical Society,* 2003, 150, A800-A805.

66. J. Christensen and J. Newman, "*A Mathematical Model for the Lithium-Ion Negative Electrode Solid Electrolyte Interphase*," *Journal of the Electrochemical Society,* 2004, 151, A1977-A1988.

67. M. F. Hasan, C. F. Chen, C. E. Shaffer, and P. P. Mukherjee, "*Analysis of the Implications of Rapid Charging on Lithium-Ion Battery Performance*," *Journal of the Electrochemical Society,* 2015, 162, A1382-A1395.

68. C. Y. Wang, G. S. Zhang, S. H. Ge, T. Xu, Y. Ji, X. G. Yang, *et al.*, "*Lithium-Ion Battery Structure that Self-Heats at Low Temperatures*," *Nature,* 2016, 529, 515-+.

69. L. O. Valoen and J. N. Reimers, "*Transport properties of LiPF6-based Li-ion battery electrolytes*," *Journal of the Electrochemical Society,* 2005, 152, A882-A891.

70. M. C. Smart and B. V. Ratnakumar, "*Effects of Electrolyte Composition on Lithium Plating in Lithium-Ion Cells*," *Journal of the Electrochemical Society,* 2011, 158, A379-A389.

71. R. Spotnitz and J. Franklin, "*Abuse Behavior of High-Power, Lithium-Ion Cells*," *Journal of Power Sources,* 2003, 113, 81-100.

72. C. Arbizzani, G. Gabrielli, and M. Mastragostino, "*Thermal Stability and Flammability of Electrolytes for Lithium-Ion Batteries*," *Journal of Power Sources,* 2011, 196, 4801-4805.

73. J. S. Newman and C. W. Tobias, "*Theoretical Analysis of Current Distribution in Porous Electrodes*," *Journal of the Electrochemical Society,* 1962, 109, 1183-1191.

74. J. Newman and W. Tiedemann, "*Porous-Electrode Theory with Battery Applications*," *AIChE Journal,* 1975, 21, 25-41.

75. M. Doyle, T. F. Fuller, and J. Newman, "*Modeling of Galvanostatic Charge and Discharge of the Lithium/Polymer/Insertion Cell*," *Journal of the Electrochemical Society,* 1993, 140, 1526-1533.

76. T. F. Fuller, M. Doyle, and J. Newman, "*Simulation and Optimization of the Dual Lithium Ion Insertion Cell*," *Journal of the Electrochemical Society,* 1994, 141, 1-10.

77. M. Doyle, J. Newman, A. S. Gozdz, C. N. Schmutz, and J. M. Tarascon, "*Comparison of modeling predictions with experimental data from plastic lithium ion cells*," *Journal of the Electrochemical Society,* 1996, 143, 1890-1903.

78. C. R. Pals and J. Newman, "*Thermal Modeling of The Lithium/Polymer Battery I. Discharge Behavior of A Single Cell*," *Journal of the Electrochemical Society,* 1995, 142, 3274-3281.

79. C. R. Pals and J. Newman, "*Thermal Modeling of the Lithium/Polymer Battery II. Temperature Profiles in A Cell Stack*," *Journal of the Electrochemical Society,* 1995, 142, 3282-3288.

80. M. W. Verbrugge, "*Three-Dimensionai Temperature and Current Distribution in A Battery Module*," *AIChE Journal,* 1995, 41, 1550-1562.

81. C. Wang, W. Gu, and B. Liaw, "*Micro-Macroscopic Coupled Modeling of Batteries and Fuel Cells I. Model Development*," *Journal of the Electrochemical Society,* 1998, 145, 3407-3417.

82. G. G. Botte, B. A. Johnson, and R. E. White, "*Influence of Some Design Variables on the Thermal Behavior of a Lithium-Ion Cell*," *Journal of the Electrochemical Society,* 1999, 146, 914-923.

83. W. Gu and C. Wang, "*Thermal-Electrochemical Modeling of Battery Systems*," *Journal of The Electrochemical Society,* 2000, 147, 2910-2922.

84. W. Gu and C.-Y. Wang, "*Thermal and Electrochemical Coupled Modeling of a Lithium-Ion Cell*," *Proc.-Electrochem. Soc,* 2000, 99, 748-762.

85. L. Song and J. W. Evans, "*Electrochemical-Thermal Model of Lithium Polymer Batteries*," *Journal of the Electrochemical Society,* 2000, 147, 2086-2095.

86. V. Srinivasan and C. Wang, "*Analysis of Electrochemical and Thermal Behavior of Li-Ion Cells*," *Journal of The Electrochemical Society,* 2003, 150, A98-A106.

87. K. E. Thomas and J. Newman, "*Thermal Modeling of Porous Insertion Electrodes*," *Journal of the Electrochemical Society,* 2003, 150, A176-A192.

88. K. Smith and C.-Y. Wang, "*Power and Thermal Characterization of A Lithium-Ion Battery Pack for Hybrid-Electric Vehicles*," *Journal of power sources,* 2006, 160, 662-673.

89. W. Fang, O. J. Kwon, and C. Y. Wang, "*Electrochemical–Thermal Modeling of Automotive Li-Ion Batteries and Experimental Validation Using a Three-Electrode Cell*," *International journal of energy research,* 2010, 34, 107-115.

90. R. E. Gerver and J. P. Meyers, "*Three-Dimensional Modeling of Electrochemical Performance and Heat Generation of Lithium-Ion Batteries in Tabbed Planar Configurations*," *Journal of the Electrochemical Society,* 2011, 158, A835-A843.

91. G.-H. Kim, K. Smith, K.-J. Lee, S. Santhanagopalan, and A. Pesaran, "*Multi-Domain Modeling of Lithium-Ion Batteries Encompassing Multi-Physics in Varied Length Scales*," *Journal of The Electrochemical Society,* 2011, 158, A955-A969.

92. X. Zhang, "*Thermal Analysis of a Cylindrical Lithium-Ion Battery*," *Electrochimica Acta,* 2011, 56, 1246-1255.

93. Y. Ji, Y. Zhang, and C.-Y. Wang, "*Li-Ion Cell Operation at Low Temperatures*," *Journal of The Electrochemical Society,* 2013, 160, A636-A649.

94. E. Prada, D. Di Domenico, Y. Creff, J. Bernard, V. Sauvant-Moynot, and F. Huet, "*A Simplified Electrochemical and Thermal Aging Model of LiFePO4-Graphite Li-ion Batteries: Power and Capacity Fade Simulations*," *Journal of the Electrochemical Society,* 2013, 160, A616-A628.

95. E. Peled, "*The Electrochemical Behavior of Alkali and Alkaline Earth Metals in Nonaqueous Battery Systems—The Solid Electrolyte Interphase Model*," *Journal of The Electrochemical Society,* 1979, 126, 2047-2051.

96. D. Aurbach, B. Markovsky, A. Shechter, Y. Ein-Eli, and H. Cohen, "*A Comparative Study of Synthetic Graphite and Li Electrodes in Electrolyte Solutions Based on Ethylene Carbonate-Dimethyl Carbonate Mixtures*," *Journal of The Electrochemical Society,* 1996, 143, 3809-3820.

97. J. O. Besenhard, M. Winter, J. Yang, and W. Biberacher, "*Filming Mechanism of Lithium-Carbon Anodes in Organic And Inorganic Electrolytes*," *Journal of Power Sources,* 1995, 54, 228-231.

98. K. Zaghib, G. Nadeau, and K. Kinoshita, "*Effect of Graphite Particle Size on Irreversible Capacity Loss*," *Journal of The Electrochemical Society,* 2000, 147, 2110-2115.

99. S. Q. Shi, P. Lu, Z. Y. Liu, Y. Qi, L. G. Hector, H. Li, *et al.*, "*Direct Calculation of Li-Ion Transport in the Solid Electrolyte Interphase*," *Journal of the American Chemical Society,* 2012, 134, 15476-15487.

100. R. Fong, U. Vonsacken, and J. R. Dahn, "*Studies of Lithium Intercalation into Carbons Using Nonaqueous Electrochemical-Cells*," *Journal of the Electrochemical Society,* 1990, 137, 2009-2013.

101. R. Kanno, Y. Kawamoto, Y. Takeda, S. Ohashi, N. Imanishi, and O. Yamamoto, "*Carbon-Fiber as a Negative Electrode in Lithium Secondary Cells*," *Journal of the Electrochemical Society,* 1992, 139, 3397-3404.

102. C. Lenain, L. Aymard, F. Salver-Disma, J. B. Leriche, Y. Chabre, and J. M. Tarascon, "*Electrochemical Properties of AB(5)-type Hydride-Forming Compounds Prepared by Mechanical Alloying*," *Solid State Ionics,* 1997, 104, 237-248.

103. P. Lu, C. Li, E. W. Schneider, and S. J. Harris, "*Chemistry, Impedance, and Morphology Evolution in Solid Electrolyte Interphase Films during Formation in Lithium Ion Batteries*," *Journal of Physical Chemistry C,* 2014, 118, 896-903.

104. T. Zheng, A. S. Gozdz, and G. G. Amatucci, "*Reactivity of the Solid Electrolyte Interface on Carbon Electrodes at Elevated Temperatures*," *Journal of The Electrochemical Society,* 1999, 146, 4014-4018.

105. S. K. Rahimian, S. C. Rayman, and R. E. White, "*Maximizing the Life of a Lithium-Ion Cell by Optimization of Charging Rates*," *Journal of the Electrochemical Society,* 2010, 157, A1302-A1308.

106. P. Verma, P. Maire, and P. Novák, "*A Review of the Features and Analyses of the Solid Electrolyte Interphase in Li-Ion Batteries*," *Electrochimica Acta,* 2010, 55, 6332-6341.

107. M. Winter, P. Novák, and A. Monnier, "*Graphites for Lithium-Ion Cells: The Correlation of the First-Cycle Charge Loss with the Brunauer-Emmett-Teller Surface Area*," *Journal of The Electrochemical Society,* 1998, 145, 428-436.

108. J. Deng, G. J. Wagner, and R. P. Muller, "*Phase Field Modeling of Solid Electrolyte Interface Formation in Lithium Ion Batteries*," *Journal of The Electrochemical Society,* 2013, 160, A487-A496.

109. H. J. Ploehn, P. Ramadass, and R. E. White, "*Solvent Diffusion Model for Aging of Lithium-Ion Battery Cells*," *Journal of The Electrochemical Society,* 2004, 151, A456-A462.

110. A. M. Colclasure and R. J. Kee, "*Thermodynamically Consistent Modeling of Elementary Electrochemistry in Lithium-Ion Batteries*," *Electrochimica Acta,* 2010, 55, 8960-8973.

111. A. M. Colclasure, K. A. Smith, and R. J. Kee, "*Modeling Detailed Chemistry and Transport for Solid-Electrolyte-Interface (SEI) Films in Li–Ion Batteries*," *Electrochimica Acta,* 2011, 58, 33-43.

112. S. K. Rahimian, S. Rayman, and R. E. White, "*Optimal Charge Rates for a Lithium Ion Cell*," *Journal of Power Sources,* 2011, 196, 10297-10304.

113. P. Arora, R. E. White, and M. Doyle, "*Capacity Fade Mechanisms and Side Reactions in Lithium-Ion Batteries*," *Journal of the Electrochemical Society,* 1998, 145, 3647-3667.

114. S. J. Harris, R. D. Deshpande, Y. Qi, I. Dutta, and Y.-T. Cheng, "*Mesopores Inside Electrode Particles Can Change the Li-Ion Transport Mechanism and Diffusion-Induced Stress*," *Journal of Materials Research,* 2010, 25, 1433 - 1440.

115. F. Joho, B. Rykart, A. Blome, P. Novak, H. Wilhelm, and M. E. Spahr, "*Relation Between Surface Properties, Pore Structure and First Cycle Charge Loss of*

Graphite as Negative Electrode in Lithium-Ion Batteries," *Journal of Power Sources,* 2001, 97 - 98, 78 - 82.

116. J. Lemaitre and J. L. Chaboche, *Mechanics of Solid Materials*: Cambridge University Press, 1990.

117. K. Zhao, M. Pharr, J. J. Vlassak, and Z. Suo, "*Fracture of Electrodes in Lithium-Ion Batteries Caused by Fast Charging*," *Journal of Applied Physics,* 2010, 108, 073517.

118. W. H. Woodford, Y.-M. Chiang, and W. C. Carter, "*"Electrochemical Shock" of Intercalation Electrodes: A Fracture Mechanics Analysis*," *Journal of The Electrochemical Society,* 2010, 157, A1052 - A1059.

119. R. Grantab and V. B. Shenoy, "*Location - and Orientation - Dependent Crack Propagation in Cylindrical Graphite Electrode Particles*," *Journal of The Electrochemical Society,* 2011, 158, A948 - A954.

120. B. J. Dimitrijevic, K. E. Aifantis, and K. Hackl, "*The Influence of Particle Size and Spacing on The Fragmentation of Nanocomposite Anodes for Li Batteries*," *Journal of Power Sources,* 2012, 206, 343 - 348.

121. Y.-T. Cheng and M. W. Verbrugee, "*The Influence of Surface Mechanics on Diffusion Induced Stresses within Spherical Nanoparticles*," *Journal of Applied Physics,* 2008, 104, 083521.

122. C. K. Chan, H. Peng, G. Liu, K. McIlwrath, X. F. Zhang, R. A. Huggins, *et al.*, "*High-Performance Lithium Battery Anodes using Silicon Nanowires*," *Nature Nanotechnology,* 2008, 3, 31 - 35.

123. Y.-T. Cheng and M. W. Verbrugee, "*Diffusion-Induced Stress, Interfacial Charge Transfer, and Criteria for Avoiding Crack Initiation of Electrode Particles.*," *Journal of The Electrochemical Society,* 2010, 157, A508 - A516.

124. S. Golmon, K. Maute, and M. L. Dunn, "*Numerical Modeling of Electrochemical–Mechanical Interactions in Lithium Polymer Batteries*," *Computers and Structures,* 2009, 87, 1567 - 1579.

125. L. Dearcangelis, S. Redner, and H. J. Herrmann, "*A Random Fuse Model for Breaking Processes*," *Journal De Physique Lettres,* 1985, 46, L585-L590.

126. S. Zapperi, P. K. V. V. Nukala, and S. Simunovic, "*Crack Avalanches in the Three-Dimensional Random Fuse Model*," *Physica a-Statistical Mechanics and Its Applications,* 2005, 357, 129-133.

127. J. Krim and J. O. Indekeu, "*Roughness Exponents - a Paradox Resolved*," *Physical Review E,* 1993, 48, 1576-1578.

128. P. K. V. V. Nukala, S. Zapperi, M. J. Alava, and S. Simunovic, "*Anomalous Roughness of Fracture Surfaces in 2D Fuse Models*," *International Journal of Fracture,* 2008, 154, 119-130.

129. E. Barsoukov, S. H. Ryu, and H. Lee, "*A Novel Impedance Spectrometer Based on Carrier Function Laplace-Transform of the Response to Arbitrary Excitation*," *Journal of Electroanalytical Chemistry,* 2002, 536, 109-122.

130. J. P. Meyers, M. Doyle, R. M. Darling, and J. Newman, "*The Impedance Response of A Porous Electrode Composed of Intercalation Particles*," *Journal of the Electrochemical Society,* 2000, 147, 2930-2940.

131. W. Gao, N. Singh, L. Song, Z. Liu, A. L. M. Reddy, L. Ci, *et al.*, "*Direct Laser Writing of Micro-Supercapacitors on Hydrated Graphite Oxide Films*," *Nat Nano,* 2011, 6, 496-500.

132. A. Zaban and D. Aurbach, "*Impedance Spectroscopy of Lithium and Nickel Electrodes in Propylene Carbonate Solutions of Different Lithium Salts a Comparative Study*," *Journal of Power Sources,* 1995, 54, 289-295.

133. J. Fan and P. S. Fedkiw, "*Composite Electrolytes Prepared from Fumed Silica, Polyethylene Oxide Oligomers, and Lithium Salk*," *Journal of the Electrochemical Society,* 1997, 144, 399-408.

134. R. Koksbang, I. I. Olsen, P. E. Tonder, N. Knudsen, and D. Fauteux, "*Polymer Electrolyte Lithium Batteries Rechargeability and Positive Electrode Degradation - an Ac Impedance Study*," *Journal of Applied Electrochemistry,* 1991, 21, 301-307.

135. F. Capuano, F. Croce, and B. Scrosati, "*Composite Polymer Electrolytes*," *Journal of the Electrochemical Society,* 1991, 138, 1918-1922.

136. G. Pistoia, A. Antonini, R. Rosati, and C. Bellitto, "*Effect of Partial Ga3+ Aubstitution for Mn3+ in LiMn2O4 on its Behaviour as a Cathode for Li Cells*," *Journal of Electroanalytical Chemistry,* 1996, 410, 115-118.

137. A. Lewandowski, B. Kurc, I. Stepniak, and A. Swiderska-Mocek, "*Properties of Li-Graphite and LiFePO4 Eectrodes in LiPF6–Sulfolane Electrolyte*," *Electrochimica Acta,* 2011, 56, 5972-5978.

138. E. Barsoukov, J. H. Kim, D. H. Kim, K. S. Hwang, C. O. Yoon, and H. Lee, "*Parametric Analysis Using Impedance Spectroscopy: Relationship Between*

Material Properties and Battery Performance," *Journal of New Materials for Electrochemical Systems*, 2000, 3, 301-308.

139. M. Jun, K. Smith, and P. Graf, "*State-Space Representation of Li-Ion Battery Porous Electrode Impedance Model with Balanced Model Reduction*," *Journal of Power Sources,* 2015, 273, 1226-1236.

140. J. Song and M. Z. Bazant, "*Effects of Nanoparticle Geometry and Size Distribution on Diffusion Impedance of Battery Electrodes*," *Journal of The Electrochemical Society,* 2013, 160, A15-A24.

141. J. Song and M. Z. Bazant, "*Electrochemical Impedance of a Battery Electrode with Anisotropic Active Particles*," *Electrochimica Acta,* 2014, 131, 214-227.

142. B. Tribollet and J. Newman, "*Impedance Model for a Concentrated-Solution - Application to the Electrodissolution of Copper in Chloride Solutions*," *Journal of the Electrochemical Society,* 1984, 131, 2780-2785.

143. B. Tribollet and J. Newman, "*Analytic-Expression of the Warburg Impedance for a Rotating-Disk Electrode*," *Journal of the Electrochemical Society,* 1983, 130, 822-824.

144. R. W. J. M. Huang, F. Chung, and E. M. Kelder, "*Impedance Simulation of A Li-Ion Battery with Porous Electrodes and Spherical Li+ Intercalation Particles*," *Journal of the Electrochemical Society,* 2006, 153, A1459-A1465.

145. A. M. Johnson and J. Newman, "*Desalting by Means of Porous Carbon Electrodes*," *Journal of the Electrochemical Society,* 1971, 118, 510-&.

146. J. Newman and W. Tiedemann, "*Porous-Electrode Theory with Battery Applications*," *Aiche Journal,* 1975, 21, 25-41.

147. L. Wang, J. S. Zhao, X. M. He, and C. R. Wan, "*Kinetic Investigation of Sulfurized Polyacrylonitrile Cathode Material by Electrochemical Impedance Spectroscopy*," *Electrochimica Acta,* 2011, 56, 5252-5256.

148. V. S. Kolosnitsyn, E. V. Kuzmina, E. V. Karaseva, and S. E. Mochalov, "*A Study of The Electrochemical Processes in Lithium–Sulphur Cells by Impedance Spectroscopy*," *Journal of Power Sources,* 2011, 196, 1478-1482.

149. Q. Zhang, E. Uchaker, S. L. Candelaria, and G. Cao, "*Nanomaterials for Energy Conversion and Storage*," *Chemical Society Reviews,* 2013, 42, 3127-3171.

150. M. Guo, G. Sikha, and R. E. White, "*Single-Particle Model for a Lithium-Ion Cell: Thermal Behavior*," *Journal of the Electrochemical Society,* 2011, 158, A122-A132.

151. B. S. Haran, B. N. Popov, and R. E. White, "*Determination of the Hydrogen Diffusion Coefficient in Metal Hydrides by Impedance Spectroscopy*," *Journal of Power Sources*, 1998, 75, 56-63.

152. G. Ning and B. N. Popov, "*Cycle Life Modeling of Lithium-Ion Batteries*," *Journal of the Electrochemical Society,* 2004, 151, A1584-A1591.

153. K. C. Smith, P. P. Mukherjee, and T. S. Fisher, "*Columnar Order In Jammed LiFePO4 Cathodes: Ion Transport Catastrophe and Its Mitigation*," *Physical Chemistry Chemical Physics,* 2012, 14, 7040-7050.

154. M. V. Paukshto, "*Diffusion-Induced Stresses in Solids*," *International Journal of Fracture,* 1999, 97, 227-236.

155. I. V. Belova and G. E. Murch, "*Thermal and Diffusion Induced Stresses in Crystalline Solids*," *Journal of Applied Physics,* 1995, 77, 127-134.

156. P. K. V. V. Nukala, S. Zapperi, and S. Simunovic, "*Statistical Properties of Fracture in a Random Spring Model*," *Physical Review E,* 2005, 71, 066106.

157. P. Barai, R. Sampath, P. K. V. V. Nukala, and S. Simunovic, "*Scaling of Surface Roughness in Perfectly Plastic Disordered Media*," *Physical Review E,* 2010, 82,

158. P. K. V. V. Nukala, S. Zapperi, M. J. Alava, and S. Šimunović, "*Crack Roughness in the Two-Dimensional Random Threshold Beam Model*," *Physical Review E,* 2008, 78, 046105.

159. P. K. V. V. Nukala, P. Barai, S. Zapperi, M. J. Alava, and S. Simunovic, "*Fracture Roughness in Three-Dimensional Beam Lattice Systems*," *Physical Review E,* 2010, 82,

160. S. Zapperi, P. K. Nukala, and S. Simunovic, "*Crack Roughness and Avalanche Precursors in The Random Fuse Model*," *Phys Rev E Stat Nonlin Soft Matter Phys,* 2005, 71, 026106.

161. G.-F. Zhao, J. Fang, and J. Zhao, "*A 3D Distinct Lattice Spring Model for Elasticity and Dynamic Failure*," *International Journal for Numerical and Analytical Methods in Geomechanics,* 2011, 35, 859 - 885.

162. H. J. Zhang, K. X. Wang, X. Y. Wu, Y. M. Jiang, Y. B. Zhai, C. Wang, *et al.*, "*MoO2/Mo2C Heteronanotubes Function as High-Performance Li-Ion Battery Electrode*," *Advanced Functional Materials,* 2014, 24, 3399-3404.

163. L. X. Liao, P. J. Zuo, Y. L. Ma, X. Q. Chen, Y. X. An, Y. Z. Gao, *et al.*, "*Effects of Temperature on Charge/Discharge Behaviors of LiFePO4 Cathode for Li-Ion Batteries*," *Electrochimica Acta,* 2012, 60, 269-273.

164. M. Vynnycky, "*Analysis of a Model for the Operation of a Vanadium Redox Battery*," *Energy,* 2011, 36, 2242-2256.

165. X. Li, M. Xiao, and S.-Y. Choe, "*Reduced Order Model (ROM) of a Pouch Type Lithium Polymer Battery Based on Electrochemical Thermal Principles for Real Time Applications*," *Electrochimica Acta,* 2013, 97, 66-78.

166. V. Senthil Kumar, "*Reduced Order Model for a Lithium Ion Cell with Uniform Reaction Rate Approximation*," *Journal of Power Sources,* 2013, 222, 426-441.

167. T.-S. Dao, C. P. Vyasarayani, and J. McPhee, "*Simplification and Order Reduction of Lithium-Ion Battery Model Based on Porous-Electrode Theory*," *Journal of Power Sources,* 2012, 198, 329-337.

168. J. A. Astrom, "*Statistical Models of Brittle Fragmentation*," *Advances in Physics,* 2006, 55, 247-278.

169. M. Zaiser, "*Scale Invariance in Plastic Flow of Crystalline Solids*," *Advances in Physics,* 2006, 55, 185-245.

170. A. Hansen and J. Schmittbuhl, "*Origin of the Universal Roughness Exponent of Brittle Fracture Surfaces: Stress-Weighted Percolation in the Damage Zone*," *Physical Review Letters,* 2003, 90,

171. K. An, P. Barai, K. Smith, and P. P. Mukherjee, "*Probing the Thermal Implications in Mechanical Degradation of Lithium-Ion Battery Electrodes*," *Journal of The Electrochemical Society,* 2014, 161, A1058-A1070.

172. P. Barai and P. P. Mukherjee, "*Mechano-Electrochemical Model for Acoustic Emission Characterization in Intercalation Electrodes*," *Journal of the Electrochemical Society,* 2014, 161, F3123-F3136.

173. L. O. Valøen and J. N. Reimers, "*Transport Properties of LiPF6-Based Li-Ion Battery Electrolytes*," *Journal of The Electrochemical Society,* 2005, 152, A882-A891.

174. A. Awarke, S. Pischinger, and J. Ogrzewalla, "*Pseudo 3D Modeling and Analysis of the SEI Growth Distribution in Large Format Li-Ion Polymer Pouch Cells*," *Journal of the Electrochemical Society,* 2013, 160, A172-A181.

175. K. E. Thomas and J. Newman, "*Heats of Mixing and of Entropy in Porous Insertion Electrodes*," *Journal of Power Sources,* 2003, 119, 844-849.

176. P. P. Mukherjee, Q. J. Kang, and C. Y. Wang, "*Pore-Scale Modeling of Two-Phase Transport in Polymer Electrolyte Fuel Cells-Progress and Perspective*," *Energy & Environmental Science,* 2011, 4, 346-369.

177. S. Cho, C.-F. Chen, and P. P. Mukherjee, "*Influence of Microstructure on Impedance Response in Intercalation Electrodes*," *Journal of The Electrochemical Society,* 2015, 162, A1202-A1214.

178. C.-F. Chen and P. P. Mukherjee, "*Probing the Morphological Influence on Solid Electrolyte Interphase and Impedance Response in Intercalation Electrodes*," *Physical Chemistry Chemical Physics,* 2015, 17, 9812-9827.

179. K. Kumaresan, Y. Mikhaylik, and R. E. White, "*A Mathematical Model for A Lithium-Sulfur Cell*," *Journal of the Electrochemical Society,* 2008, 155, A576-A582.

180. R. E. White, S. E. Lorimer, and R. Darby, "*Prediction of the Current Density at an Electrode at Which Multiple Electrode Reactions Occur under Potentiostatic Control*," *Journal of The Electrochemical Society,* 1983, 130, 1123-1126.

181. H. H. Girault, *Analytical and Physical Elecrochemistry*, 1st ed. New York: Marcel Dekker, 2004.